SPECTROSCOPIC INVESTIGATIONS OF THE VIBRATIONAL POTENTIAL ENERGY SURFACES IN ELECTRONIC GROUND AND EXCITED STATES

A Dissertation

by

JUAN YANG

Submitted to the Office of Graduate Studies of
Texas A&M University
in partial fulfillment of the requirements for the degree of

DOCTOR OF PHILOSOPHY

May 2006

Major Subject: Chemistry

SPECTROSCOPIC INVESTIGATIONS OF THE VIBRATIONAL POTENTIAL ENERGY SURFACES IN ELECTRONIC GROUND AND EXCITED STATES

A Dissertation

by

JUAN YANG

Submitted to the Office of Graduate Studies of
Texas A&M University
in partial fulfillment of the requirements for the degree of

DOCTOR OF PHILOSOPHY

Approved by:

Chair of Committee,	Jaan Laane
Committee Members,	John P. Fackler
	Robert R. Lucchese
	Stephen A. Fulling
Head of Department,	Emile A. Schweikert

May 2006

Major Subject: Chemistry

ABSTRACT

Spectroscopic Investigations of the Vibrational Potential Energy Surfaces

in Electronic Ground and Excited States. (May 2006)

Juan Yang, B.S., Beijing University

Chair of Advisory Committee: Dr. Jaan Laane

The vibrational potential energy surfaces in electronic ground and excited states of several ring molecules were investigated using several different spectroscopic methods, including far-infrared (IR), Raman, ultraviolet (UV) absorption, fluorescence excitation (FES), and single vibronic level fluorescence (SVLF) spectroscopies.

Based on new information obtained from SVLF and millimeter wave spectra, the far-IR spectra of coumaran were reassigned and the one-dimensional ring-puckering potential energy functions for several vibrational states in the S_0 ground state were determined. The barrier was found to be 154 cm^{-1} and the puckering angles to be ± 25°, in good agreement with the millimeter wave barrier of 152 cm^{-1} and puckering angles of ± 23°. Moreover, the UV absorption and FES spectra of coumaran allowed the one-dimensional ring-puckering potential energy functions in the S_1 excited state to be determined. The puckering barrier is 34 cm^{-1} for the excited state and the puckering

angles are ± 14°.

Several calculations with different basis sets have been carried out to better understand the unusual vibrational frequencies of cyclopropenone. It was shown that there is strong interaction between the C=O and symmetric C-C stretching vibrations. These results differ quantitatively from a previous normal coordinate calculation and interpretation.

The vapor-phase Raman spectrum of 3,7-dioxabicyclo[3.3.0]oct-1,5-ene was analyzed and compared to the predicted spectrum from DFT calculations. The spectrum further shows it has D_{2h} symmetry, in which the skeletons of both rings are planar.

The infrared and Raman spectra of vapor-phase and liquid-phase 1,4-benzodioxan and 1,2,3,4-tetrahydronaphthalene were collected and the complete vibrational assignments for both molecules were made. Theoretical calculations predicted the barriers to planarity to be 4809 cm^{-1} for 1,2,3,4-tetrahydonaphthalene and 4095 cm^{-1} for 1,4-benzodioxan. The UV absorption, FES, and SVLF spectra of both molecules were recorded and assigned. Both one and two-dimensional potential energy functions of 1,4-benzodioxan for the ring-twisting and ring-bending vibrations were carried out for the S_0 and $S_1(\pi,\pi^*)$ states, and these were consistent with the high barriers calculated for both states. The low-frequency spectra of 1,2,3,4-tetrahydronaphthalene in both S_0 and $S_1(\pi,\pi^*)$ states were also analyzed.

DEDICATION

To my father Xiangfeng Yang, my mother Xiaochun Zuo, and my husband Shaohui Wang, for their love and support.

ACKNOWLEDGEMENTS

First, I would like to thank my research advisor, Dr. Jaan Laane, for his guidance, patience, and support throughout my Ph.D. studies. He is not only a great mentor in science but also a nice person to work with.

I would also like to thank Dr. John P. Fackler, Dr. Robert R. Lucchese, and Dr. Stephen A. Fulling for serving on my advisory committee. Also Dr. Rand L. Watson is acknowledged to kindly be a substitute for Dr. Lucchese on my final defense.

Many thanks to the research associates for their support in this work. I would like to thank Dr. Kristjan Haller for teaching me how to record Raman spectra and how to do optical alignment, Dr. Niklas Meinander for writing the two-dimensional kinetic and potential energy programs, Dr. Jaebum Choo and Dr. Ohyun Kwon for carrying out the theoretical calculations for coumaran excited state, Dr. Katsuhiko Okuyama for showing me how to do the assignments for FES and UV absorption spectra, Dr. Daniel Autrey for explaining the theory and experimental details to me when I just joined the group and also for his nice work in recording some infrared and Raman spectra of 1,4-benzodioxan, and Dr. Martin Wagner for together with me collecting the FES and SVLF spectra of coumaran, 1,4-benzodioxan, and tetralin, and also for training me to independently operate the OPO laser system.

Thanks also go to my fellow group members: Kathleen McCann, Abdul-aziz Al-Saadi, and Mohammed Rishard, for their friendship and help. Special appreciation goes to Mrs. Linda Redd for her friendship and support.

Finally, I want to thank my parents, Xiangfeng Yang and Xiaochun Zuo, and my husband Shaohui Wang. Without their love and support, this work could not have been done.

TABLE OF CONTENTS

CHAPTER Page

CHAPTER Page

LIST OF FIGURES

FIGURE Page

FIGURE Page

FIGURE Page

FIGURE Page

FIGURE Page

LIST OF TABLES

TABLE Page

TABLE Page

TABLE Page

CHAPTER I

INTRODUCTION

The investigation of the vibrational potential energy surfaces (PESs) in electronic ground and excited states is one of the most interesting research areas in physical chemistry since PESs can provide a great amount of information on molecular structures, energy barriers, photochemical and photophysical processes, reaction pathways, etc. However, as is well known, a non-linear molecule with N atoms has 3N-6 vibrations. Solving a (3N-6)-dimensional Schrödinger equation to obtain a (3N-6)-dimensional vibrational PES is not practically feasible especially when N becomes large. For a non-rigid cyclic molecule with a saturated M-membered ring, there are M-3 out-of-plane ring vibrations that are normally low-frequency, large-amplitude, anharmonic motions. These are the motions that typically associated with the conformational changes of the molecule. Based on the high-low frequency separation assumption, those low-frequency large-amplitude vibrations can be separated from other high-frequency vibrations since they interact very little. Thus the (3N-6)-dimensional problem can be reduced to a good approximation as only a one or two-dimensional calculation.[1] To determine the one or two-dimensional vibrational PESs in terms of one or two vibrational coordinates,

---

This dissertation follows the style of The Journal of Chemical Physics.

experimental spectroscopic techniques in conjunction with rigorous quantum mechanical computations can be used. The transitions between the quantum levels in the electronic ground state can be observed by far-infrared (IR) and low-frequency Raman spectroscopies. The transitions that involve the vibronic levels in the electronic excited state can be studied by ultraviolet (UV) absorption, jet-cooled fluorescence excitation (FES) and single vibronic level fluorescence (SVLF) spectroscopies. In this dissertation the vibrational PESs in the electronic ground and excited states of several cyclic or bicyclic molecules have been investigated by spectroscopic approaches and these molecules are briefly discussed below.

COUMARAN

Coumaran (COU) is a bicyclic molecule that can be included in the indan family. The far-infrared spectra of COU along with a one-dimensional analysis of the ring-puckering potential energy function were previously reported by Bondoc *et al*.[2] in 2000. However, a band observed at -95 cm^{-1} in the SVLF spectra[3] with the 0_0^0 excitation clearly showed the inconsistence with this old assignments, which had placed the first level (v = 2) above the nearly degenerate ground-state levels (v = 0 and 1) at 127.8 cm^{-1}. In 2005 Ottoviani and Caminati[4] determined that the ground state splitting between v = 0 and 1 was 3.12 cm^{-1} by millimeter wave spectra. This had previously been assigned to

the splitting between v = 2 and 3. In this work the far-infrared spectrum of COU has been reassigned based on this new information. The one-dimensional ring-puckering potential functions for the ground state as well as for the ring-twisting and ring-flapping vibrationally excited states have been determined. Moreover, the UV absorption, jet-cooled FES and SVLF spectra of COU associated with its $S_1(\pi,\pi^*)$ electronic excited state have been recorded and analyzed. The one-dimensional puckering potential functions for the electronic excited state have also been determined.

CYCLOPROPENONE

The vibrational spectra of cyclopropenone (CPO) and its d_2 isotopomer were published by Brown *et al*.[5] in 1975, as was the normal coordinate analysis.[6] The infrared and Raman spectra reported from this paper were recorded almost exclusively for the liquid and solid phases although two vapor-phase bands were observed for each isotopomer. The C=O stretch at 1883 cm^{-1} in the vapor-phase infrared spectrum and the C=C stretch at 1483 cm^{-1} for the liquid-phase are unusual since the values for typical C=O and C=C stretches are about 1700 and 1600 cm^{-1}, respectively. Brown *et al*.[5] attributed this to a strong C=O bond and a weak C=C bond. In this work several calculations with different basis sets have been carried out to better understand the unusual vibrational frequencies of CPO.

3,7-DIOXABICYCLO[3.3.0]OCT-1,5-ENE

The vibrational spectra and theoretical calculations for bicyclo[3.3.0]oct-1,5-ene (BCO) were previously reported.[7] It is structurally interesting since the two five-member rings can pucker in either the same or opposite directions, producing either *cis* (C_{2v}) or *trans* (C_{2h}) structures. The ring-puckering spectra of BCO are expected to be very complicated, and because the vibrations do not have much of dipole moment changes, they are also expected to be weak.[8] The molecule 3,7-dioxabicyclo[3.3.0]oct-1,5-ene (DOBO), on the other hand, will have a larger dipole moment change for the in-phase puckering vibration and its spectra should be simpler as the planar form should be the most stable form.

The DOBO molecule has been synthesized in small quantities (~ 15 mg) by Mlynek and Hopf in Technical University of Braunschweig, Germany. Due to the lack of sample only the vapor-phase Raman spectrum was recorded. Together with density functional (DFT) calculations, the Raman spectrum was used to determine the symmetry and structure of the DOBO molecule.

1,2,3,4-TETRAHYDRONAPHTHALENE AND 1,4-BENZODIOXAN

1,2,3,4-Tetrahydronaphthalene (tetralin or TET) and 1,4-benzodioxan (14BZD) are related to the previously studied molecules cyclohexene[9] and 2,3-dihydro-1,4-dioxin,[10]

respectively. The PESs for both cyclohexene and 2,3-dihydro-1,4-dioxin are two-dimensional functions of the ring-bending coordinate x and the ring-twisting coordinate τ, with very high barriers to planarity due to the CH_2-CH_2 torsional interactions as expected. With a planar benzene ring attached to the six-membered ring instead of the double bond, similar PESs and high barriers to planarity for TET and 14BZD are also expected.

In this work the infrared and Raman spectra of both vapor and liquid phases TET and 14BZD have been collected and the complete vibrational assignments have been made. Furthermore, the UV absorption, jet-cooled FES, and SVLF spectra of both molecules have been recorded and assigned.

1,3-DITHIOLANE

Similar to previously studied molecules such as cyclopentane,[11] 1,3-dioxolane,[12,13] and 1,3-oxathiolane,[14,15] a very interesting feature for the 1,3-dithiolane (13DTL) molecule is its pseudorotational vibration.[16] A saturated five-membered ring molecule has two out-of-plane ring vibrations: a twisting mode (half-chair, C_2 symmetry) and a bending mode (envelope, C_s symmetry), which can also be described as radial and pseudorotational vibrations because it is possible to convert from one structure to another without surmounting the barrier to planarity. A previous study[13] assigned the

pseudorotational energy levels of 13DTL in the ground and first radial excited states and showed that 13DTL has a pseudorotation barrier of 296 cm^{-1}. However later microwave spectra[17] showed a peak at 185.5 GHz, or 6.18 cm^{-1}, to be the $2 \leftarrow 0$ transition for the pseudorotation. Therefore, a careful reexamination of the potential energy function of the pseudorotational vibration of 13DTL is needed. The complete vibrational analysis has been performed based on the vapor and liquid phases infrared and Raman spectra of 13DTL. Density functional theory (DFT) calculations for planar (C_{2v}), twist (C_2), bent (C_s), and non-symmetric (C_1) structures were carried out and compared with the experimental frequencies.

CHAPTER II

THEORY AND COMPUTATIONAL METHODS

Structural and conformational changes in non-rigid molecules often occur via vibrational pathways that are governed by vibrational potential energy surfaces (PESs). To determine these vibrational potential energy surfaces, quantum mechanics as well as experimental data are used.[18-21]

THE VIBRATIONAL HAMILTONIAN OPERATOR $\hat{\mathbf{H}}_{vib}$

The Schrödinger equation for a molecular vibration is

$$\hat{\mathbf{H}}_{vib}\Psi = E_{vib}\Psi , \tag{2.1}$$

where E_{vib} are the eigenvalues and Ψ are the eigenfunctions corresponding to each E_{vib}. $\hat{\mathbf{H}}_{vib}$ is the vibrational Hamiltonian operator, defined as

$$\hat{\mathbf{H}}_{vib} = \hat{\mathbf{T}}_{vib} + \hat{\mathbf{V}}_{vib} , \tag{2.2}$$

where $\hat{\mathbf{T}}_{vib}$ and $\hat{\mathbf{V}}_{vib}$ are the vibrational kinetic and potential energy operators, respectively.

THE VIBRATIONAL KINETIC ENERGY OPERATOR $\hat{\mathbf{T}}_{vib}$

The vibrational kinetic energy operator for the internal motions of a molecule with N

atoms in the center of mass coordinate system is given by

$$\hat{\mathbf{T}}_{vib} = -\frac{\hbar^2}{2}\sum_{i=1}^{3N-6}\sum_{j=1}^{3N-6}\left(\frac{\partial}{\partial q_i} + \frac{1}{4}\frac{\partial \ln g}{\partial q_i}\right)g_{ij}\left(\frac{\partial}{\partial q_j} - \frac{1}{4}\frac{\partial \ln g}{\partial q_j}\right), \tag{2.3}$$

where q_i and q_j are the vibrational coordinates, g_{ij} are elements of the **G** matrix in terms of the vibrational coordinates, and g is the determinant of the **G** matrix.

The **G** matrix is given by

$$\mathbf{G} = \begin{pmatrix} \mathbf{I} & \mathbf{X} \\ \mathbf{X}^t & \mathbf{Y} \end{pmatrix}^{-1}. \tag{2.4}$$

In Equation (2.4) **I** is the 3×3 dimensional moment of inertia tensor matrix defined as

$$\mathbf{I} = \begin{pmatrix} I_{xx} & I_{xy} & I_{xz} \\ I_{yx} & I_{yy} & I_{yz} \\ I_{zx} & I_{zy} & I_{zz} \end{pmatrix}, \tag{2.5}$$

where

$$I_{ii} = \sum_{\alpha=1}^{N} m_\alpha(\mathbf{r}_\alpha \cdot \mathbf{r}_\alpha - \mathbf{r}_{\alpha i}^2),\ i = x, y, \text{or } z, \tag{2.6a}$$

$$I_{ij} = -\sum_{\alpha=1}^{N} m_\alpha(\mathbf{r}_{\alpha i} \cdot \mathbf{r}_{\alpha j}),\ i \neq j,\ i, j = x, y, \text{or } z, \tag{2.6b}$$

where $\mathbf{r}_\alpha$ is the coordinate vector from the α^{th} atom to the center-of-mass of the molecule, and $\mathbf{r}_{\alpha i}$ and $\mathbf{r}_{\alpha j}$ are the coordinate vectors from the α^{th} atom to the i^{th} and j^{th} atoms, respectively.

In Equation (2.4) **X** is the $3\times(3N-6)$ dimensional matrix that represents the

vibration-rotation interactions defined as

$$X_{ij} = \sum_{\alpha=1}^{N} m_\alpha \left[\mathbf{r}_\alpha \times \left(\frac{\partial \mathbf{r}_\alpha}{\partial q_j} \right) \right]_i , \tag{2.7}$$

and **Y** is the symmetric $(3N-6)\times(3N-6)$ dimensional pure vibrational matrix defined as

$$Y_{ij} = \sum_{\alpha=1}^{N} m_\alpha \left(\frac{\partial \mathbf{r}_\alpha}{\partial q_i} \right) \cdot \left(\frac{\partial \mathbf{r}_\alpha}{\partial q_j} \right), \tag{2.8}$$

where q_i and q_j are the vibrational coordinates.

In general, planar or near-planar saturated cyclic molecules with M members (M > 3) have M-3 out-of-plane ring vibrations. These out-of-plane ring vibrations are typically of low frequency and large amplitude and cannot be well described by harmonic potential functions. Since they interact little with higher frequency motions, they can be treated separately from higher frequency vibrations of the ring molecules. In most cases, one or two out-of-plane vibrations of low-frequency and large-amplitude are considered.

1) The One-Dimensional Vibrational Kinetic Energy Operator

For four-membered ring molecules or “pseudo-four-membered” ring molecules, such as cyclobutane, cyclopentene, or 1,4-cyclohexadiene, which have a ring-puckering vibration that is separable from all other vibrations, as shown in Figure 1(a), (b), and (c), respectively, the **G** matrix is given by

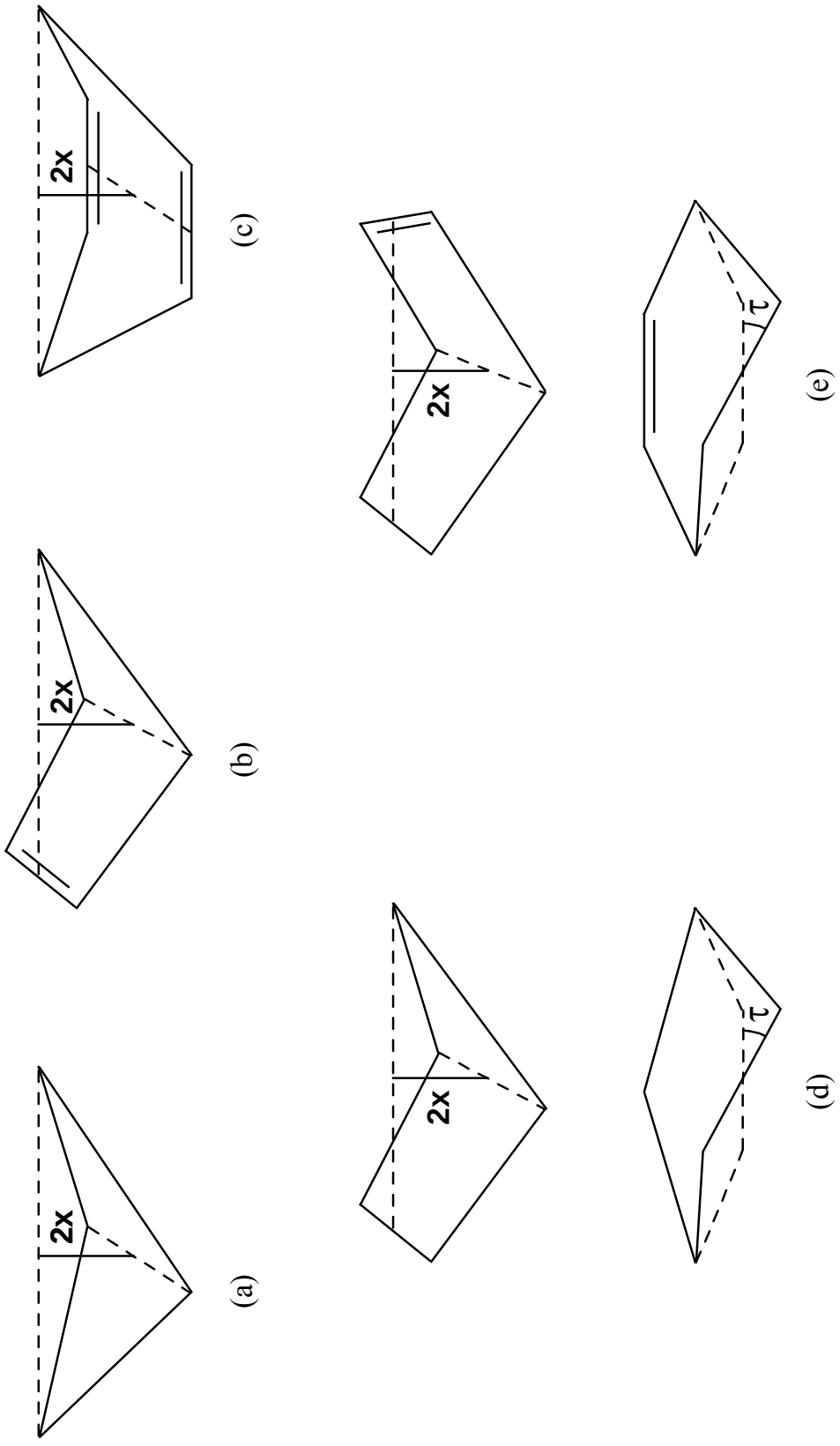

Figure 1. The ring-puckering coordinate x of (a) cyclobutane, (b) cyclopentene, and (c) 1,4-cyclohexadiene and the ring-bending coordinate x and the ring-twisting coordinate τ of (d) cyclopentane and (e) cyclohexene.

$$\mathbf{G} = \begin{pmatrix} I_{xx} & I_{xy} & I_{xz} & X_{11} \\ I_{yx} & I_{yy} & I_{yz} & X_{21} \\ I_{zx} & I_{zy} & I_{zz} & X_{31} \\ X_{11} & X_{21} & X_{31} & Y_{11} \end{pmatrix}^{-1}, \tag{2.9}$$

and after matrix inversion the **G** matrix becomes

$$\mathbf{G} = \begin{pmatrix} g_{11} & g_{12} & g_{13} & g_{14} \\ g_{21} & g_{22} & g_{23} & g_{24} \\ g_{31} & g_{32} & g_{33} & g_{34} \\ g_{41} & g_{42} & g_{43} & g_{44} \end{pmatrix}, \tag{2.10}$$

where g_{44} is the reciprocal reduced mass for the ring-puckering vibration and is the pure vibrational contribution to the kinetic energy. Here the matrix elements g_{ij}, with indices i,j = 1,2,3, are used to describe the rotations of the molecule by convention.

Because of the large amplitude of this ring-puckering motion, the reciprocal reduced mass g_{44} is dependent on the vibrational coordinate, and it can be expressed as a polynomial expansion in terms of the ring-puckering coordinate x, as given by

$$g_{44}(x) = \sum_{i=0}^{n} g_{44}^{(i)} x^i = g_{44}^{(0)} + g_{44}^{(1)} x + g_{44}^{(2)} x^2 + \ldots = \frac{1}{\mu(x)}, \tag{2.11}$$

where $\mu(x)$ is the coordinate-dependent reduced mass for the ring-puckering vibration and $g_{44}^{(i)}$ are the expansion coefficients. Since the ring-puckering vibration is assumed to be symmetric about a planar conformation, $g_{44}^{(i)}$ with all odd i numbers equal zero.

Derived from Equation (2.3), the one-dimensional vibrational kinetic energy operator $\hat{\mathbf{T}}_{vib}$, is given by

$$\hat{\mathbf{T}}_{\text{vib}} = -\frac{\hbar^2}{2}\left[\frac{\partial}{\partial \text{x}} \text{g}_{44}(\text{x}) \frac{\partial}{\partial \text{x}}\right] + \hat{\mathbf{V}}', \tag{2.12}$$

where x is the vibrational coordinate and $\hat{\mathbf{V}}'$ is called the pseudo potential because some of the terms resemble the potential energy. It is defined as

$$\hat{\mathbf{V}}' = -\frac{\hbar^2}{8}\left[\frac{\partial \ln g}{\partial \text{x}} \text{g}_{44}(\text{x}) \frac{\partial}{\partial \text{x}} - \frac{\partial}{\partial \text{x}} \text{g}_{44}(\text{x}) \frac{\partial \ln g}{\partial \text{x}}\right] + \frac{\hbar^2}{32}\left[\frac{\partial \ln g}{\partial \text{x}} \text{g}_{44}(\text{x}) \frac{\partial \ln g}{\partial \text{x}}\right]. \tag{2.13}$$

The pseudo potential $\hat{\mathbf{V}}'$ is small compared to the potential and usually can be omitted.[18,19]

2) The Two-Dimensional Vibrational Kinetic Energy Operator

For five-membered ring molecules or "pseudo-five-membered" ring molecules, such as cyclopentane or cyclohexene, which have a ring-bending and a ring-twisting vibrations that are separable from all other vibrations and have significant interaction between each other, as shown in Figure 1(d) and (e), respectively, the **G** matrix is given by

$$\mathbf{G} = \begin{pmatrix} \text{I}_{\text{xx}} & \text{I}_{\text{xy}} & \text{I}_{\text{xz}} & \text{X}_{11} & \text{X}_{12} \\ \text{I}_{\text{yx}} & \text{I}_{\text{yy}} & \text{I}_{\text{yz}} & \text{X}_{21} & \text{X}_{22} \\ \text{I}_{\text{zx}} & \text{I}_{\text{zy}} & \text{I}_{\text{zz}} & \text{X}_{31} & \text{X}_{32} \\ \text{X}_{11} & \text{X}_{21} & \text{X}_{31} & \text{Y}_{11} & \text{Y}_{12} \\ \text{X}_{12} & \text{X}_{22} & \text{X}_{32} & \text{Y}_{21} & \text{Y}_{22} \end{pmatrix}^{-1}, \tag{2.14}$$

and the inverted **G** matrix is

$$\mathbf{G} = \begin{pmatrix} g_{11} & g_{12} & g_{13} & g_{14} & g_{15} \\ g_{21} & g_{22} & g_{23} & g_{24} & g_{25} \\ g_{31} & g_{32} & g_{33} & g_{34} & g_{35} \\ g_{41} & g_{42} & g_{43} & g_{44} & g_{45} \\ g_{51} & g_{52} & g_{53} & g_{54} & g_{55} \end{pmatrix}, \tag{2.15}$$

where g_{44} and g_{55} are the reciprocal reduced masses for the ring-bending and ring-twisting vibrations, respectively, and are the pure vibrational contribution to the kinetic energy. The g_{45} term is the interaction cross term for these two vibrations. Similar to the one-dimensional vibrational kinetic energy expansion in Equation (2.11), the two-dimensional vibrational kinetic energy terms, g_{44}, g_{55}, and g_{45}, can be expressed as polynomial expansions of the ring-bending coordinate q_4 and the ring-twisting coordinate q_5, as given by

$$g_{ij}(q_4, q_5) = \sum_{k=0}^{m} \sum_{l=0}^{n} g_{ij}^{(k,l)} q_4^k q_5^l, \;\; i, j = 4,5, \tag{2.16}$$

where $g_{ij}^{(k,l)}$ are the expansion coefficients. For symmetric vibrations, the only terms included in the expansions are those with even k+l numbers. For molecules in which the two out-of-plane ring vibrations are of different symmetry, the interaction between these two motions is small; therefore the cross term g_{45} usually can be omitted. The coordinate-dependent reduced masses for these two out-of-plane vibrations are

$$\mu_4(q_4, q_5) = \frac{1}{g_{44}(q_4, q_5)}, \;\; \mu_5(q_4, q_5) = \frac{1}{g_{55}(q_4, q_5)}. \tag{2.17}$$

Derived from Equation (2.3), the two-dimensional vibrational kinetic energy

operator $\hat{\mathbf{T}}_{vib}$, is given by

$$\hat{\mathbf{T}}_{vib} = -\frac{\hbar^2}{2}\left[\frac{\partial}{\partial q_4} g_{44}(q_4,q_5)\frac{\partial}{\partial q_4} + \frac{\partial}{\partial q_4} g_{45}(q_4,q_5)\frac{\partial}{\partial q_5} + \frac{\partial}{\partial q_5} g_{45}(q_4,q_5)\frac{\partial}{\partial q_4} + \frac{\partial}{\partial q_5} g_{55}(q_4,q_5)\frac{\partial}{\partial q_5}\right] + \hat{\mathbf{V}}' \quad (2.18)$$

where q_4 and q_5 are the vibrational coordinates. The pseudo potential $\hat{\mathbf{V}}'$ is defined as

$$\hat{\mathbf{V}}' = -\frac{\hbar^2}{8}\sum_{i,j=4}^{5}\left(\frac{\partial \ln g}{\partial q_i} g_{ij}\frac{\partial}{\partial q_j} - \frac{\partial}{\partial q_i} g_{ij}\frac{\partial \ln g}{\partial q_j}\right) + \frac{\hbar^2}{32}\sum_{i,j=4}^{5}\left(\frac{\partial \ln g}{\partial q_i} g_{ij}\frac{\partial \ln g}{\partial q_j}\right). \quad (2.19)$$

$\hat{\mathbf{V}}'$ is small compared to the potential and usually omitted.[18,19]

If the two coupled vibrational coordinates q_4 and q_5 are simply denoted by x and y, the two-dimensional kinetic energy operator is then written as

$$2\hat{\mathbf{T}} = \hat{\mathbf{p}}_x g_{44}(x,y)\hat{\mathbf{p}}_x + \hat{\mathbf{p}}_x g_{45}(x,y)\hat{\mathbf{p}}_y + \hat{\mathbf{p}}_y g_{45}(x,y)\hat{\mathbf{p}}_x + \hat{\mathbf{p}}_y g_{55}(x,y)\hat{\mathbf{p}}_y, \quad (2.20)$$

where

$$\hat{\mathbf{p}}_x = -i\hbar\frac{\partial}{\partial x}, \quad \hat{\mathbf{p}}_y = -i\hbar\frac{\partial}{\partial y}. \quad (2.21)$$

THE VIBRATIONAL POTENTIAL ENERGY OPERATOR $\hat{\mathbf{V}}_{vib}$

1) The One-Dimensional Vibrational Potential Energy Operator

In 1945 R. P. Bell[22] proposed that the potential energy for the ring-puckering vibration in a molecule whose equilibrium configuration is planar, could be represented as a quartic oscillator, as given by

$$V(x) = ax^4, \quad (2.22)$$

where x is the ring-puckering coordinate.

However, in the case of cyclobutane and many other ring molecules, the equilibrium configuration is non-planar. As an example, the dihedral angle for cyclobutane[23] is about 33°. Therefore the potential curve for the puckering vibration has two identical minima corresponding to the ring being puckered up or down. There is clearly an energy barrier between these two minima and this corresponds to the planar configuration of the molecule. To introduce such a barrier, a quadratic term is added to the potential function, giving

$$V(x) = ax^4 + bx^2 . \tag{2.23}$$

The sign of the coefficient *a* is always positive. The sign of the coefficient *b* determines the shape of the potential curve and the equilibrium configuration of the molecule. If *b* is positive, the potential curve has a single minimum, corresponding to the planar equilibrium configuration. If *b* is negative, the potential curve shows a 'W-shape' and has two minima and a barrier, indicating a bent equilibrium configuration of the molecule. In this case, the barrier to planarity (BP) is given by

$$BP = \frac{b^2}{4a}, \tag{2.24}$$

and the energy minima, x_{min}, are at

$$x_{min} = \pm\sqrt{\frac{-b}{2a}} . \tag{2.25}$$

The equilibrium conformation of cyclic molecules that contain four or five-membered rings is determined by the competition between the torsional strain and the ring-angle strain. The torsional strain is resulting from the adjacent methylene groups ($-CH_2-CH_2-$) becoming eclipsed in a planar structure. On one hand, as the ring puckers, the adjacent methylene groups become staggered and the torsional strain decreases, and this makes the molecule prefer being puckered. However, on the other hand, the ring angles decrease as the ring puckers, resulting in an increase in the ring-angle strain since the natural C-C-C bond angle is tetrahedral. As is well known, in Equation (2.23) the coefficient *a* arises primarily from the ring-angle strain whereas the coefficient *b* results from the torsional strain along with contributions from the ring-angle strain. If the ring-angle strain is stronger than the torsional strain, the coefficient *b* is positive and the molecule tends to stay planar. Otherwise the coefficient *b* becomes negative and the molecule will have a bent equilibrium conformation.

2) The Two-Dimensional Vibrational Potential Energy Operator

For molecules that have two strongly coupled large-amplitude vibrations, such as the ring-bending and ring-twisting vibrations in cyclohexene, the two-dimensional vibrational potential energy operator can be written as

$$\hat{\mathbf{V}}(q_4, q_5) = \hat{\mathbf{V}}_1(q_4) + \hat{\mathbf{V}}_2(q_5) + \hat{\mathbf{V}}_{12}(q_4, q_5), \tag{2.26}$$

where q_4 and q_5 are the ring-bending and ring-twisting coordinates, respectively, and

$$\hat{\mathbf{V}}_1(q_4) = \sum_i C_{i0} q_4^i \quad \text{and} \quad \hat{\mathbf{V}}_2(q_5) = \sum_j C_{0j} q_5^j \tag{2.27}$$

represent the potentials of one-dimensional vibrations, and

$$\hat{\mathbf{V}}_{12}(q_4, q_5) = \sum_{i,j} C_{ij} q_4^i q_5^j \tag{2.28}$$

represents the coupling between the two vibrations.

If the two coupled vibrational coordinates q_4 and q_5 are simply denoted by x and y, a typical potential energy function is of the form

$$\hat{\mathbf{V}}(x, y) = a_1 x^4 + b_1 x^2 + a_2 y^4 + b_2 y^2 + c x^2 y^2 + d_1 x^3 y + d_2 x y^3 , \tag{2.29}$$

where the coefficients a_i are the ring-angle strain force constants, the coefficients b_i are the torsional strain force constants, the coefficient c is the force constant for the symmetric bending-twisting interaction, and the coefficients d_i are the force constants for the asymmetric bending-twisting interaction.

If both vibrations are symmetric, such that $V(\pm x, \pm y) = V(x, y)$, the two asymmetric terms in Equation (2.29) are not necessary and the potential energy function can be written as

$$\hat{\mathbf{V}}(x, y) = a_1 x^4 + b_1 x^2 + a_2 y^4 + b_2 y^2 + c x^2 y^2 . \tag{2.30}$$

The signs of the coefficients a_1, a_2, and c are always positive. As is the case for the one-dimensional potential function, the signs of the coefficients b_1 and b_2 determine the shape of the potential surface and the equilibrium configuration of the molecule.

To calculate the energy barrier and the extrema positions, the first order partial derivatives are set to be zero, giving

$$\begin{cases} \dfrac{\partial \mathrm{V}}{\partial \mathrm{x}} = 0 = 2\mathrm{x}\left(2a_1\mathrm{x}^2 + b_1 + c\mathrm{y}^2\right) \\ \dfrac{\partial \mathrm{V}}{\partial \mathrm{y}} = 0 = 2\mathrm{y}\left(2a_2\mathrm{y}^2 + b_2 + c\mathrm{x}^2\right) \end{cases}. \tag{2.31}$$

If both $b_1 \geq 0$ and $b_2 \geq 0$, the only solution for the above equations will be $\mathrm{x} = 0$ and $\mathrm{y} = 0$. It is obviously an energy minimum and corresponds to the planar form of the molecule. There is no barrier in the potential energy surface.

If $b_1 \geq 0$ and $b_2 < 0$, the solutions of Equations (2.31) will be

$$\begin{cases} \mathrm{x}_1 = 0 \\ \mathrm{y}_1 = 0 \end{cases} \quad \text{and} \quad \begin{cases} \mathrm{x}_2 = 0 \\ \mathrm{y}_2 = \pm\sqrt{-b_2/2a_2} \end{cases}, \tag{2.32}$$

which correspond to a saddle point at the planar conformation and two energy minima at the twisting conformations, respectively. The barrier to planarity is given by

$$\mathrm{BP} = \frac{b_2^2}{4a_2}. \tag{2.33}$$

If $b_1 < 0$ and $b_2 \geq 0$, the solutions are

$$\begin{cases} \mathrm{x}_1 = 0 \\ \mathrm{y}_1 = 0 \end{cases} \quad \text{and} \quad \begin{cases} \mathrm{x}_2 = \pm\sqrt{-b_1/2a_1} \\ \mathrm{y}_2 = 0 \end{cases}, \tag{2.34}$$

which correspond to a saddle point at the planar conformation and two energy minima at the bending conformations, respectively. The barrier to planarity is given by

$$\mathrm{BP} = \frac{b_1^2}{4a_1}. \tag{2.35}$$

If both $b_1 < 0$ and $b_2 < 0$, Equations (2,31) have four sets of solutions as given below

$$\begin{cases} x_1 = 0 \\ y_1 = 0 \end{cases}, \quad \begin{cases} x_2 = 0 \\ y_2 = \pm\sqrt{-\dfrac{b_2}{2a_2}} \end{cases}, \quad \begin{cases} x_3 = \pm\sqrt{-\dfrac{b_1}{2a_1}} \\ y_3 = 0 \end{cases} \text{ and } \quad \begin{cases} x_4 = \pm\sqrt{\dfrac{2a_2b_1 - b_2c}{c^2 - 4a_1a_2}} \\ y_4 = \pm\sqrt{\dfrac{2a_1b_2 - b_1c}{c^2 - 4a_1a_2}} \end{cases}, \tag{2.36}$$

where (x_4, y_4) becomes imaginary if $\dfrac{2a_2b_1 - b_2c}{c^2 - 4a_1a_2} < 0$ or $\dfrac{2a_1b_2 - b_1c}{c^2 - 4a_1a_2} < 0$. The corresponding V values are

$$V_1 = 0, \quad V_2 = -\frac{b_2^2}{4a_2}, \quad V_3 = -\frac{b_1^2}{4a_1}, \quad \text{and } V_4 = \frac{a_1b_2^2 + a_2b_1^2 - b_1b_2c}{c^2 - 4a_1a_2}. \tag{2.37}$$

The solution of $(x_1, y_1) = (0,0)$ is always an energy maximum in this case, while the other three sets of solutions could possibly correspond to either an energy minimum or a saddle point, with different values of the coefficients a_i, b_i, and c.

Assuming there are three positive c values c_1, c_2, and c_3, defined as

$$2a_2b_1 - b_2c_1 = 0, \text{ or } c_1 = 2a_2b_1/b_2, \tag{2.38}$$

$$2a_1b_2 - b_1c_2 = 0, \text{ or } c_2 = 2a_1b_2/b_1, \tag{2.39}$$

$$c_3^2 - 4a_1a_2 = 0, \text{ or } c_3 = \sqrt{4a_1a_2}. \tag{2.40}$$

Since $c_1c_2 = c_3^2$ or $\dfrac{c_1}{c_3} = \dfrac{c_3}{c_2}$, the value of c_3 will always be between c_1 and c_2. Assuming $c_1 \geq c_2$, then $c_1 \geq c_3 \geq c_2$. If $c \geq c_1$, (x_2, y_2) and (x_3, y_3) are energy minima and (x_4, y_4) corresponds to a saddle point in the two-dimensional surface. The barrier to

planarity is $\frac{b_1^2}{4a_1}$ in this case. If $c_1 \geq c \geq c_2$, (x_2, y_2) becomes a saddle point and (x_3, y_3) is still an energy minimum whereas (x_4, y_4) becomes imaginary. The barrier to planarity is still $\frac{b_1^2}{4a_1}$. If $c < c_2$, (x_4, y_4) becomes real again and corresponds to four identical energy minima. (x_2, y_2) and (x_3, y_3) are saddle points. The barrier to planarity in this case, is $\frac{a_1 b_2^2 + a_2 b_1^2 - b_1 b_2 c}{4a_1 a_2 - c^2}$. These results are summarized in Table 1.

As an example, a set of coefficients is used to demonstrate these results. The coefficients a_i and b_i are fixed as the following arbitrary values

$$a_1 = 2.0 \times 10^4,\ b_1 = -2.0 \times 10^4,\ a_2 = 3.0 \times 10^4,\ \text{and}\ b_2 = -1.0 \times 10^4.$$

The resulting c_1, c_2, and c_3 values are

$$c_1 = 1.2 \times 10^5,\ c_2 = 2.0 \times 10^4,\ \text{and}\ c_3 = 4.9 \times 10^4,$$

respectively. Figure 2 shows the potential energy surfaces and contours with four arbitrarily chosen c values: (a) $c_A = 1.5 \times 10^5$, (b) $c_B = 1.0 \times 10^5$, (c) $c_C = 4.0 \times 10^4$, and (d) $c_D = 5.0 \times 10^3$. The maxima, minima, and saddle points are indicated in the figures by MAX, MIN, and S, respectively.

TABLE 1: Summary of the Extrema Positions and Barriers to Planarity for A Two-Dimensional Surface Given by $\hat{V}(x,y) = a_1x^4 + b_1x^2 + a_2y^4 + b_2y^2 + cx^2y^2$ with Different Ranges of *c* Values.

c Value Range:	$c > c_1$	$c = c_1$	$c_1 > c > c_2$	$c = c_2$	$c < c_2$
$(x_1, y_1) = (0,0)$	Maximum	Maximum	Maximum	Maximum	Maximum
$(x_2, y_2) = \left(0, \pm\sqrt{-\frac{b_2}{2a_2}}\right)$	Minimum	Saddle point	Saddle point	Saddle point	Saddle point
$(x_3, y_3) = \left(\pm\sqrt{-\frac{b_1}{2a_1}}, 0\right)$	Minimum	Minimum	Minimum	Minimum	Saddle point
$(x_4, y_4) = \left(\pm\sqrt{\frac{2a_2b_1 - b_2c}{c^2 - 4a_1a_2}}, \pm\sqrt{\frac{2a_1b_2 - b_1c}{c^2 - 4a_1a_2}}\right)$	Saddle point	Saddle point	Imaginary	Minimum	Minimum
Barrier to Planarity (BP)	$\frac{b_1^2}{4a_1}$	$\frac{b_1^2}{4a_1}$	$\frac{b_1^2}{4a_1}$	$\frac{b_1^2}{4a_1}$	$\frac{a_1b_2^2 + a_2b_1^2 - b_1b_2c}{4a_1a_2 - c^2}$
Example Figure	Figure 2(a)		Figure 2(b) and (c)		Figure 2(d)

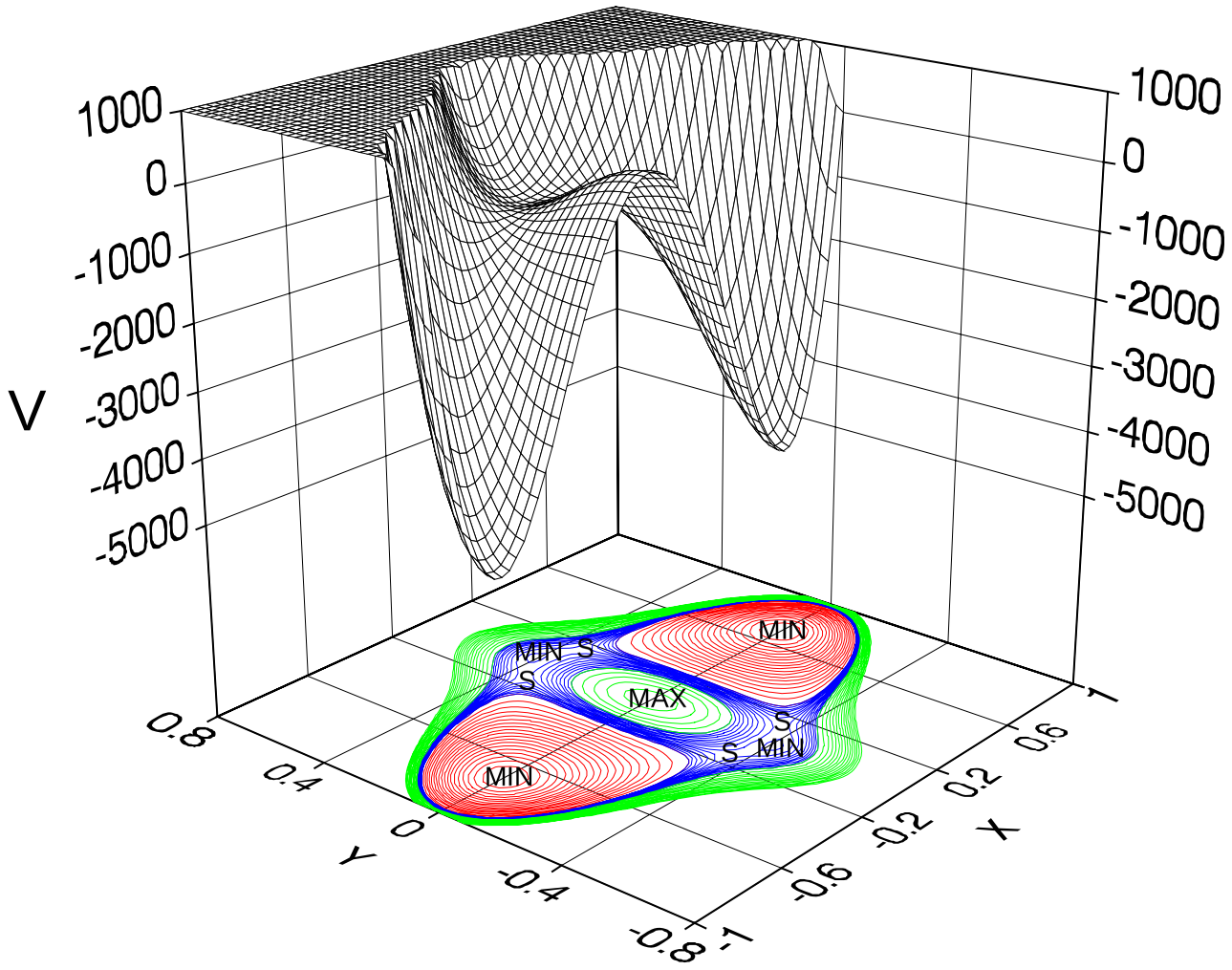

Figure 2. The two-dimensional surface and contours for given potential functions. (a) The two-dimensional function is given by $V = (2.0\times10^4)x^4 - (2.0\times10^4)x^2 + (3.0\times10^4)y^4 - (1.0\times10^4)y^2 + (1.5\times10^5)x^2y^2$.

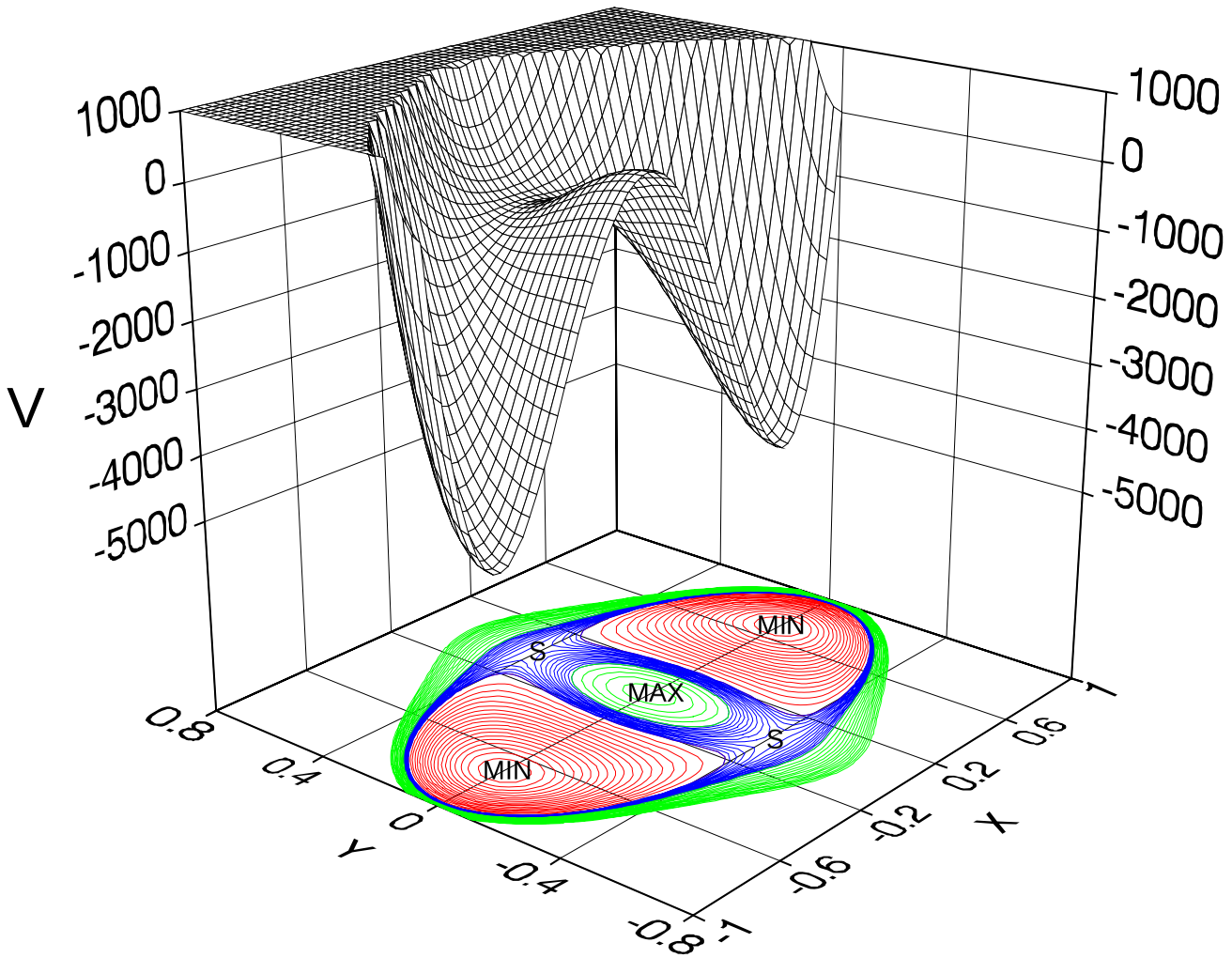

Figure 2. The two-dimensional surface and contours for given potential functions. (b) The two-dimensional function is given by $V = (2.0\times10^4)x^4 - (2.0\times10^4)x^2 + (3.0\times10^4)y^4 - (1.0\times10^4)y^2 + (1.0\times10^5)x^2y^2$.

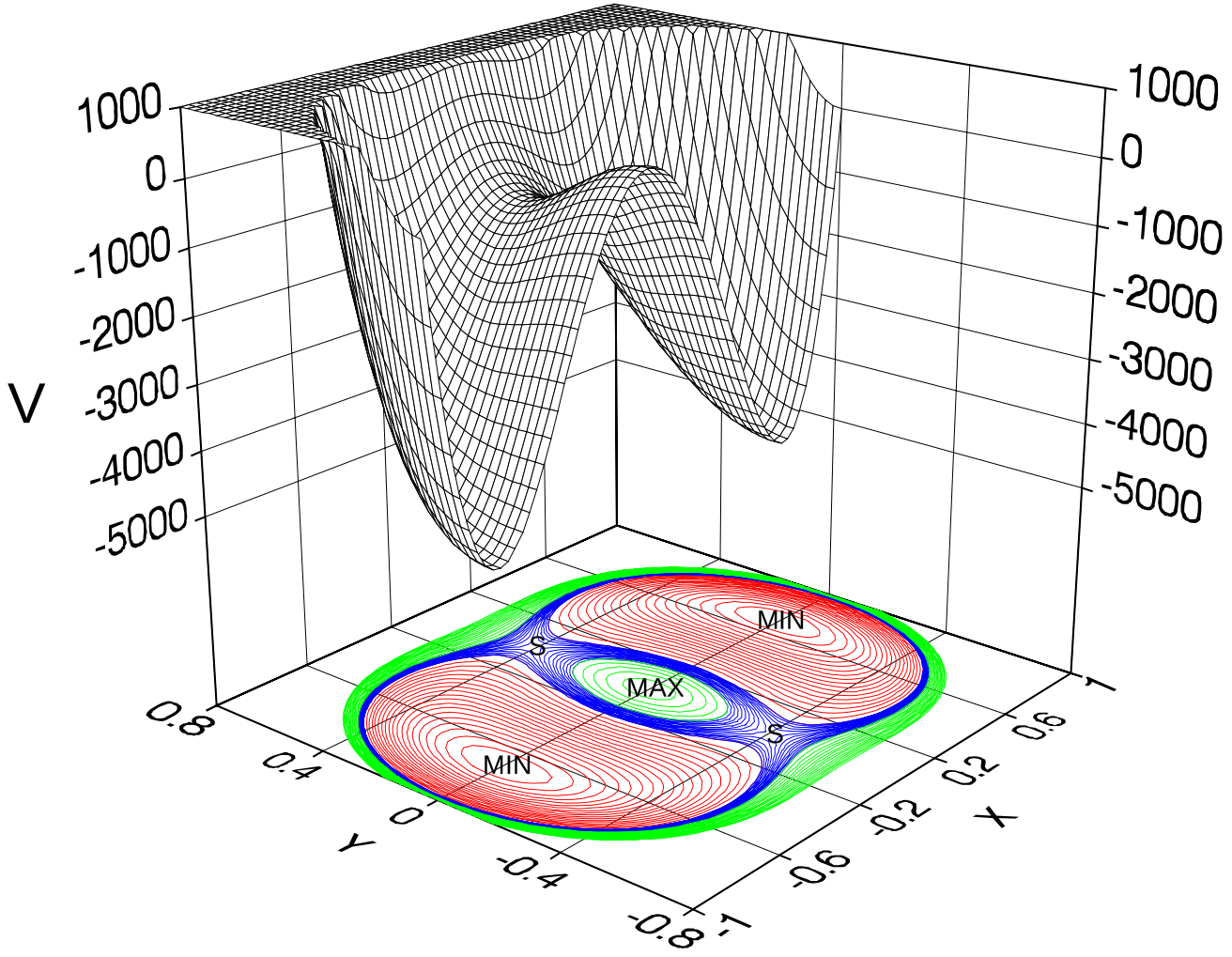

Figure 2. The two-dimensional surface and contours for given potential functions. (c) The two-dimensional function is given by $V = (2.0\times10^4)x^4 - (2.0\times10^4)x^2 + (3.0\times10^4)y^4 - (1.0\times10^4)y^2 + (4.0\times10^4)x^2y^2$.

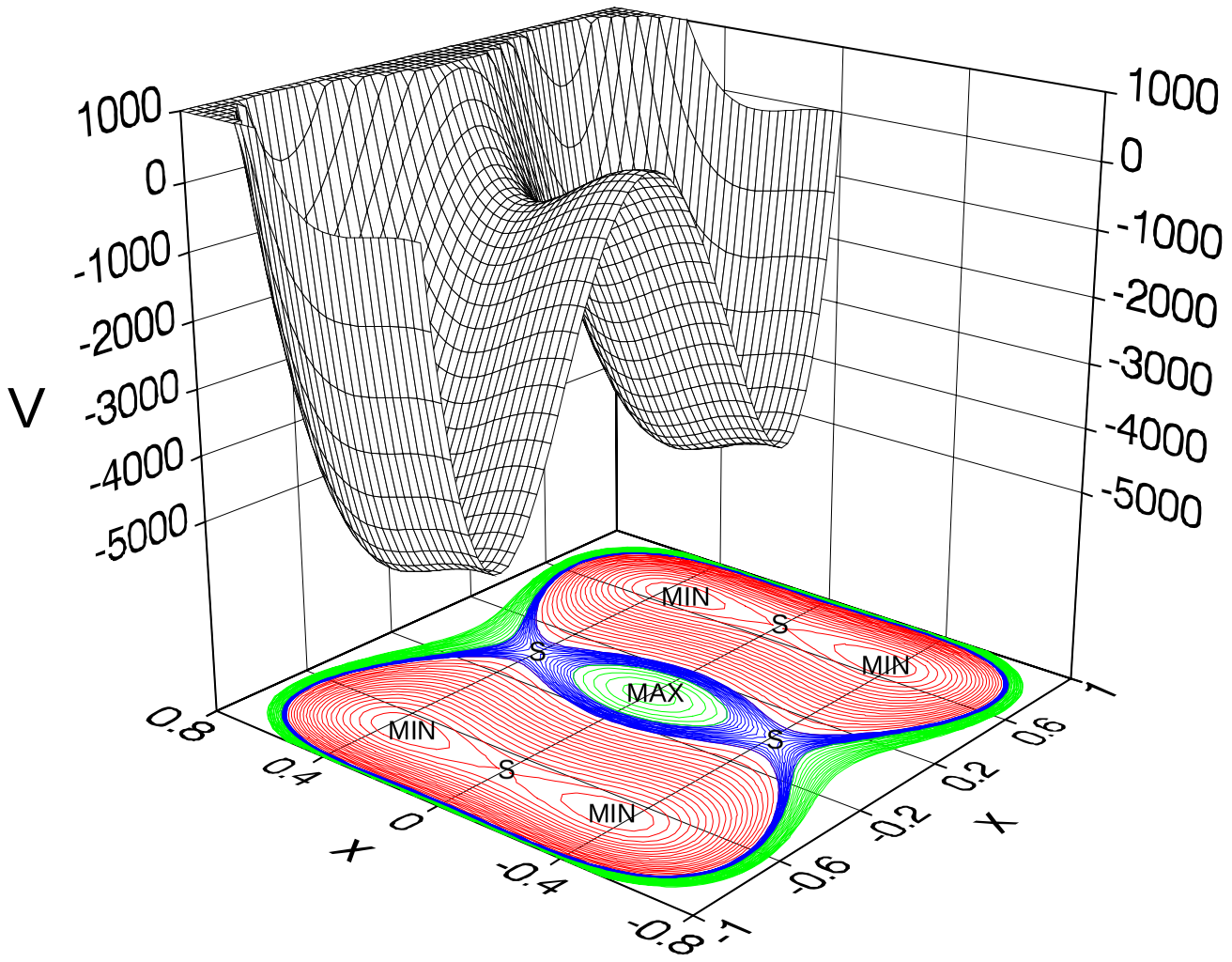

Figure 2. The two-dimensional surface and contours for given potential functions. (d) The two-dimensional function is given by $V = (2.0\times10^4)x^4 - (2.0\times10^4)x^2 + (3.0\times10^4)y^4 - (1.0\times10^4)y^2 + (5.0\times10^3)x^2y^2$.

CHAPTER III

EXPERIMENTAL METHODS

The experimental spectroscopic techniques utilized for investigating the vibrational potential energy surfaces (PESs) in the electronic ground and excited states are shown in Figure 3. These are infrared (IR), Raman, ultraviolet (UV) absorption, fluorescence excitation (FES), also called laser induced fluorescence (LIF), and single vibronic level fluorescence (SVLF), also called dispersed fluorescence (DF) spectroscopies. Of these five spectroscopic techniques, IR, Raman, and SVLF are used to determine the vibrational energy levels in the electronic ground state while FES and UV absorption provide information about the vibronic energy levels in the electronic excited state.

INFRARED SPECTRA

Liquid-phase mid-infrared spectra were recorded on a Biorad FTS-60 Fourier-transform infrared spectrometer equipped with a globar source, a potassium bromide (KBr) beamsplitter, and a triglycine sulfate detector. A drop of the sample was placed between two polished KBr windows. 64 scans at 1 cm^{-1} resolution were typically averaged.

Vapor-phase mid-infrared spectra were recorded on a Bomem DA8.02 Fourier-

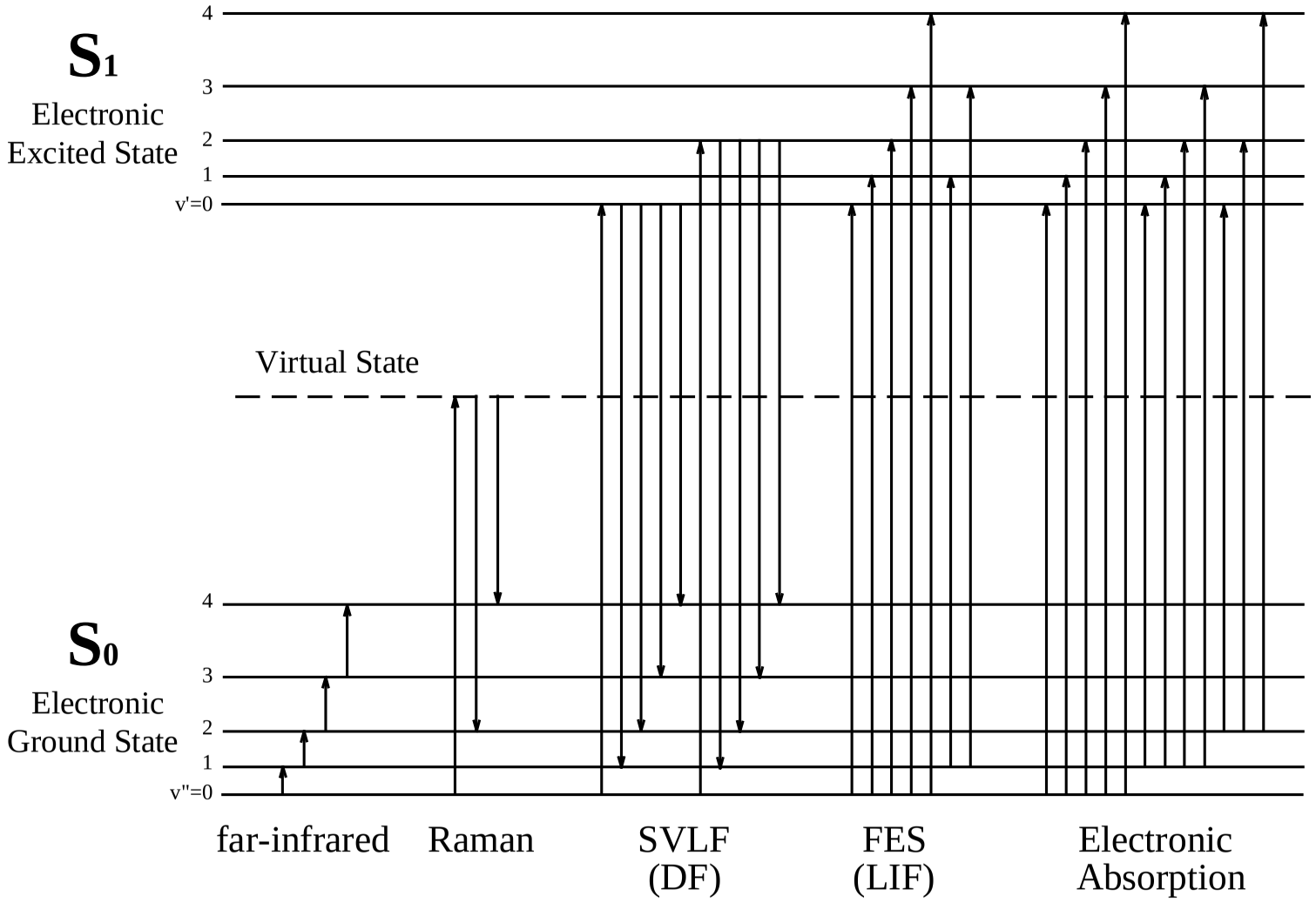

Figure 3. Spectroscopic techniques for investigation of the vibronic energy levels in the electronic ground (S_0) and excited (S_1) states.

transform spectrometer equipped with a globar source, a KBr beamsplitter, and a DTGS detector. A 10 cm heatable cell fitted with KBr windows was heated up to the boiling point of the sample, usually in the 200-250 °C range. Vapor-phase spectra were recorded at 0.25 cm^{-1} resolution and 1024 scans were typically averaged.

Vapor-phase far-infrared spectra were recorded on a Bomem DA8.02 Fourier-transform spectrometer using a globar source, a hyper beamsplitter, and a DTGS/POLY detector. The sample was contained in a multi-reflection long path glass cell with an optical pathlength of 22 m. The cell can be put into a heatable jacket and heated up to 200 °C. For temperatures below 60 °C, polyethylene windows that had been pounded to eliminate interference fringes were used. For temperatures higher than 60 °C, wedged silicon windows were used. The spectra were recorded at 0.1, 0.25, and 0.5 cm^{-1} resolutions and more than ten thousand scans were typically averaged.

RAMAN SPECTRA

Raman spectra were recorded at the right angle scattering geometry using an Instruments SA Jobin Yvon U-1000 spectrometer with a double monochromator equipped with 1800 grooves mm^{-1} holographic gratings. A Coherent Radiation Innova 20 argon ion laser operating at 514.5 nm was used as the excitation source. The output laser power was adjusted to be about 0.5 W for liquid-phase spectra and 5 W for vapor-phase

spectra. At the sample, the laser power was reduced by approximately 50%. A liquid nitrogen-cooled charge-coupled device (CCD) or a photomultiplier-tube (PMT) was used as detectors. The CCD is generally used in the spectra region higher than 150 cm^{-1}.

Liquid-phase Raman spectra were recorded at ambient temperatures. The sample was contained in an NMR glass tube. Depolarization measurements were taken using a polarizer and a scrambler ($\lambda/4$ plate) to separate the scattered light into its parallel and perpendicular components. Vapor-phase Raman spectra were collected at temperatures about the boiling point of the sample, usually in the 200-250 °C range, and at pressures typically 700-900 Torr. The sample was contained in a thermostatically controlled high-temperature Raman cell as previously described.[24,25] Resolutions for the vapor-phase Raman spectra were in the 0.5-2.0 cm^{-1} range with the PMT and 0.7 cm^{-1} with the CCD.

ULTRAVIOLET ABSORPTION SPECTRA

Ultraviolet absorption spectra were recorded on a Bomem DA8.02 Fourier-transform spectrometer using a deuterium lamp source, a quartz beamsplitter, and a silicon detector in the 20,000-50,000 cm^{-1} region. The vapor-phase sample was contained in a 20 cm glass cell with quartz windows. Ultraviolet absorption spectra were collected at ambient temperatures and the vapor pressure within the cell was about 200 mTorr. Resolutions of 0.25 and 0.5 cm^{-1} were used and more than ten thousand scans were averaged.

JET-COOLED FLUORESCENCE EXCITATION AND SINGLE VIBRONIC LEVEL FLUORESCENCE SPECTRA

Both fluorescence excitation and single vibronic level fluorescence spectroscopies involve the excitation of the sample molecules to the electronic excited state (S_1), and this was accomplished using a tunable UV laser system. This laser system consists of a Continuum Sunlite EX optical parametric oscillator (OPO) pumped by a Continuum Powerlite 9020 20 Hz Nd:YAG laser. Using the non-linear properties of the barium borate (BBO) crystals the OPO laser can be tuned across the whole visible region, from 710 nm to 450 nm. The outlet visible beam from the OPO laser is then frequency doubled by a Continuum FX-1 UV extension unit, resulting in a continuously tunable UV radiation from 355 nm to 225 nm. A photomultiplier-tube (PMT) was used as the detector for the FES spectra. The SVLF spectra were recorded using an Instruments SA HR-640 monochromator and a Spex Spectrum One charge-coupled device (CCD) detector with a 2000 × 800 pixel chip. Helium was used as backing gas with stated purity of 99.99% at pressures up to 60 psi. FES spectra were taken with a spectral resolution of ± 0.5 cm^{-1} and SVLF spectra were obtained at ± 1 cm^{-1} resolution. More details can be found elsewhere.[26-30]

For both fluorescence techniques the sample molecules are cooled down to very low temperature through a supersonic jet expansion. In the jet-cooled chamber the sample

molecules are allowed to expand freely through an orifice into a vacuum (~10^{-6} Torr). Since the sample is flowing with noble carrier gas at high pressure and the orifice diameter (0.025 inch) is much greater than the mean free path of the sample molecule, numerous collisions will occur in and immediately beyond the orifice and convert the random motions of the particles into a mass flow, forming a molecular beam with a small range of velocities. After the jet expansion process, the translational temperatures of the sample molecules can be reduced to below 1 K. Rotational temperatures can be as low as 10-20 K and vibrational temperatures can reach about 30-50 K. At such low temperatures, most of the molecules will occupy only the ground vibrational level and most hot bands in the spectra are eliminated.

The FES technique involves scanning a tunable UV laser over the vibronic levels in the molecule's electronic excited state and recording the total fluorescence emitted by the sample no matter to which level it fluoresces back to in the electronic ground state. Since almost all molecules are cooled down to the ground vibrational level, FES gives information about the vibronic levels in the electronic excited state. The selection rules for FES transitions are the same as those for the electronic absorption spectroscopy. However, the fluorescence intensities may be quite different.

In the SVLF process a laser is tuned to a specific resonance frequency to induce a transition from the ground vibrational level in the S_0 state to a specific excited vibronic

level of interest. The fluorescence emitted to various vibrational levels is then separated by a monochromator and recorded by a CCD detector. SVLF spectra can help to identify the assignment of FES bands. Moreover, they also give information about the energy levels in the electronic ground state. The selection rule for SVLF involves both an allowed transition to the excited vibronic level and an allowed transition back to a particular ground vibrational level.

Jet-cooled FES spectra were always considered and compared together with the room temperature ultraviolet absorption spectra, which contain numerous transitions originating from a great number of vibrational levels and thus are generally very congested. As a method to simplify the assignment, the jet-cooled FES spectra are more valuable in distinguishing cold bands from hot bands in the UV absorption spectra since they clearly show which transitions originate from the ground vibrational level.

In addition to the very low temperature FES spectra that contain all cold bands, sometimes it is also useful to increase the vibrational temperature of the sample a small amount to investigate the hot bands originating from the first or second vibrational excited states of some low-frequency vibrations. This can be done by reducing the helium backing pressure and decreasing the distance from the nozzle to the laser beam.

CHAPTER IV

S_0 RING-PUCKERING POTENTIAL ENERGY FUNCTION FOR COUMARAN*

INTRODUCTION

In recent years spectroscopic methods have been used to investigate the potential energy surfaces of various molecules in their electronic ground and excited states.[31] These have included the bicyclic molecules in the indan family. In 2000 Bondoc *et al*.[2] reported the analysis of the far-infrared and Raman spectra of coumaran along with a one-dimensional analysis of the ring-puckering potential energy function. In the further process of investigating the vibronic energy levels in the electronic excited state of coumaran via jet-cooled fluorescence spectra as well as the ultraviolet absorption spectra, the recorded single vibrational level fluorescence (SVLF or dispersed fluorescence) spectra[3] clearly showed that there was a vibrational level near -95 cm^{-1}, and this was inconsistent with the old assignments, which placed the first level (v = 2) above the nearly degenerate ground state levels (v = 0 and 1) at 127.8 cm^{-1}. Later Ottoviani and Caminati[4] have reported their results from the millimeter wave spectra and indeed have

---

*Reprinted with permission from "S_0 Ring-Puckering Potential Energy Function for Coumaran" by J. Yang, K. Okuyama, K. Morris, Z. Arp, and J. Laane, 2005. *J. Phys. Chem. A*, **109**, 8290-8292. 2005 by American Chemical Society.

shown that the original assignment needed revision. They determined that the ground state splitting between v = 0 and 1 was 3.12 cm^{-1}, which had previously been assigned to the splitting between v = 2 and 3. In this chapter the revised assignment of the far-infrared spectrum of coumaran along with the one-dimensional ring-puckering potential energy function that does a very good job of fitting the data is presented.

EXPERIMENTAL

The far-infrared and the ultraviolet absorption spectra were recorded on a Bomem DA3.02 instrument using sampling techniques previously described.[2] The recording of the single vibronic level fluorescence spectra have also been previously described[28-32] on the basis of a Continuum Nd:YAG Powerlite Model 9020 laser and a Sunlite EX OPO system with the FX-1 ultraviolet frequency doubling extension unit.

RESULTS AND DISCUSSION

Figure 4 shows the far-infrared spectrum of coumaran that was reported previously.[2] This new figure reflects the revised assignments for the puckering transitions, which are also listed in Table 2. Figure 5 shows the energy level diagram for the ring-puckering levels when none of the other vibrations are excited and in the first excited states of the ring-flapping (v_F = 1) and ring-twisting (v_T = 1). These energy levels were derived from

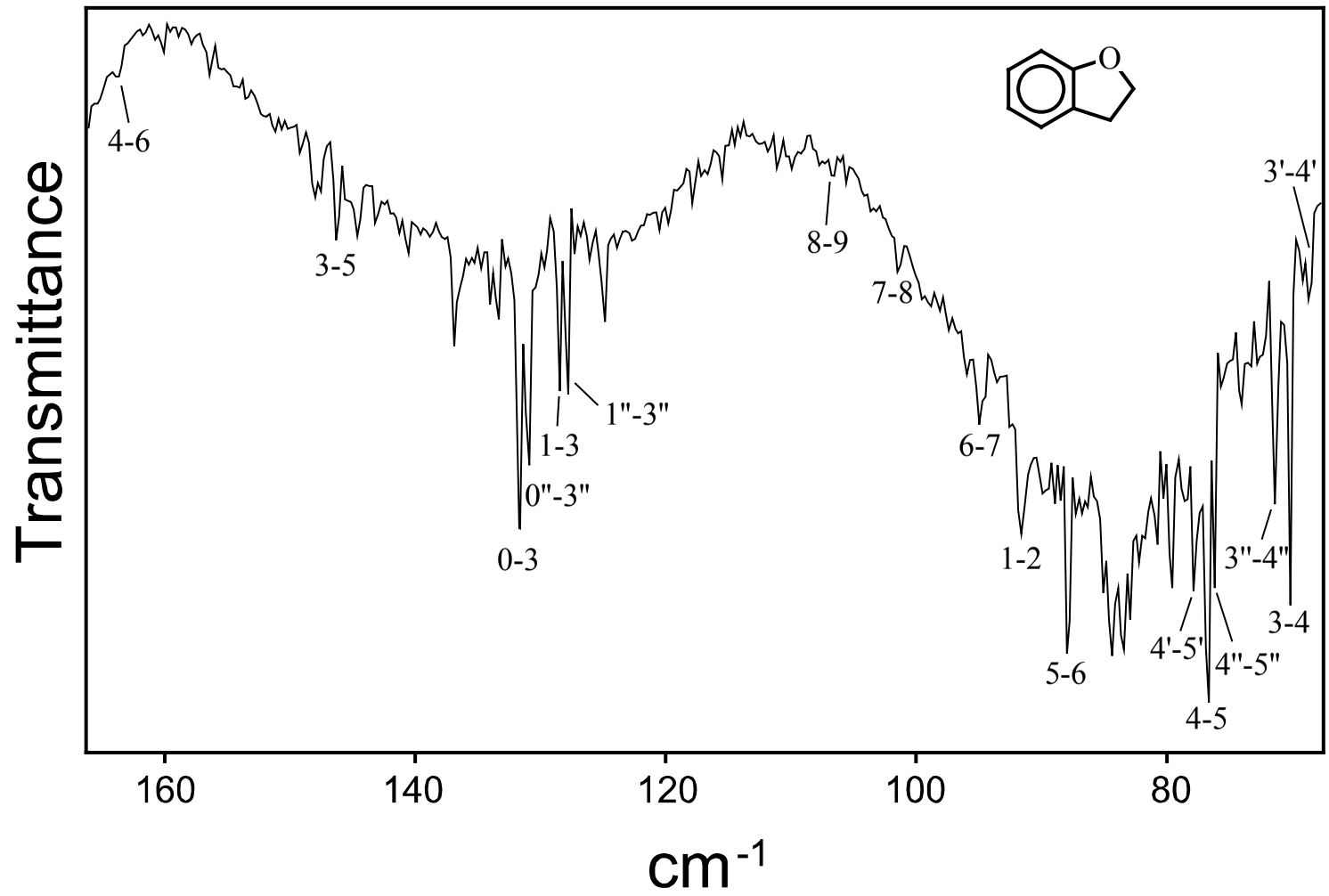

Figure 4. Far-infrared spectrum and assignments for the ring-puckering transitions of coumaran. Primes indicate puckering transitions in the flapping excited state ($v_F = 1$) and double primes indicated those in the twisting excited state ($v_T = 1$).

TABLE 2: Ring-Puckering Transitions of Coumaran.

Transition	Observed		Calculated		Previous
	Freq. (cm^{-1})	Rel. Int.	Freq. (cm^{-1})	Rel. Int.	Assign.[a]
0-1	3.1[b]	---	2.4	0.001	2-3
1-2	91.7	0.4	92.1	0.8	2-4
2-3	36.7	---	36.9	0.3	4-5
3-4	70.1	(1.0)	71.8	(1.0)	5-6
4-5	76.7	0.8	77.0	1.0	6-7
5-6	87.9	0.5	87.1	0.9	3-4
6-7	95.0	0.3	94.8	0.8	3'-4'
7-8	101.4	0.2	101.7	0.6	
8-9	106.7	0.1	107.8	0.5	
0-2	(95.0)[c]	0.3	94.5	0.2	3'-4'
1-3	128.4	0.4	129.0	0.4	
2-4	(106.7)[c]	0.1	108.8	0.2	4-6
3-5	146.3	0.2	148.8	0.4	5-7
4-6	163.7	0.1	164.1	0.4	6-8
5-7	183.2	w	181.9	0.4	
0-3	131.7	0.8	131.4	0.7	0-3
1-4	Obscured	---	200.9	0.2	
2-5	183.9	w	185.8	0.2	
3-6	235.3	0.1	235.9	0.2	

[a] From Reference 2.

[b] From Reference 4.

[c] Frequency used twice.

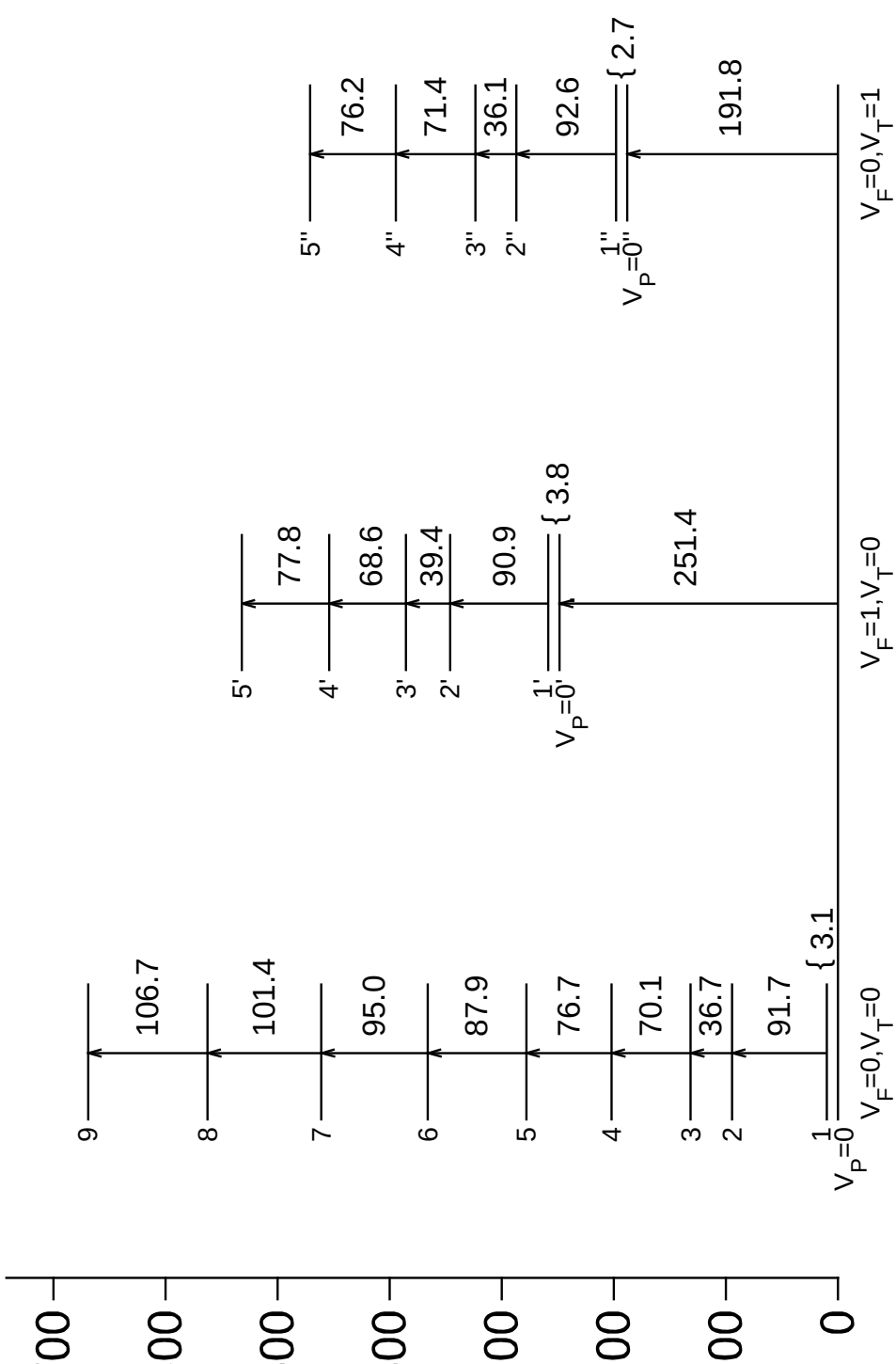

Figure 5. Energy level diagram for the ring-puckering quantum states for the ground state and the flapping (v_F = 1) and twisting (v_T = 1) vibrational excited states.

the far-infrared spectra,[2] Raman spectra,[2] ultraviolet absorption spectra, and single vibronic level fluorescence spectra.[3] Table 3 lists some of the transition frequencies from which the energy levels were derived. The ring-puckering level data were fitted using the one-dimensional ring-puckering Hamiltonian

$$H = -\frac{\hbar^2}{2}\frac{d}{dx}g_{44}(x)\frac{d}{dx} + V(x), \tag{4.1}$$

where the potential function has the form

$$V(x) = ax^4 + bx^2, \tag{4.2}$$

and where x is the ring-puckering coordinate as previously defined.[2] The coordinate dependent kinetic energy function (the reciprocal reduced mass), $g_{44}(x)$, was calculated in the previous work. Utilizing the revised assignments, the potential energy function was determined to be

$$V(cm^{-1}) = (8.91\times10^5)x^4 - (2.34\times10^4)x^2, \tag{4.3}$$

where x is in units of Å. This function, along with the observed transitions, is shown in Figure 6. The barrier to planarity is 154 ± 4 cm^{-1} and the minima are at x = ± 0.11 Å, which correspond to puckering angles of ± 25°. The ring-puckering frequencies calculated with this potential function are compared to the observed ones in Table 2, and the average difference is 0.7 cm^{-1} or less than 1%. In the previous paper with the previous assignments, a barrier to planarity of 279 cm^{-1} had been calculated, and this had agreed fortuitously well with the *ab initio* (MP2/6-31G*) result of 258 cm^{-1}. Ottoviani

TABLE 3: Selected Spectroscopic Transitions Involving ν_{45}, ν_{44}, and ν_{43} of Coumaran[a].

Transition[b]	Method	Frequency (cm^{-1})	
		Experimental	Inferred[c]
0-0"	IR, Raman	191.8	191.8
0-0'	IR	251.4	251.4
45_2^0	SVLF	-95	-94.5
$43_1^0 45_1^0 / 45_6^2$	UV	-255.2	-255.2
45_5^1	UV	-242.8	-243.1
45_4^0	UV	-201.8	-201.8
$44_1^1 45_2^0 / 44_1^1 45_3^1$	UV	-164.8	-164.8
$44_1^0 45_0^1$	UV	-157.0	-156.8
45_3^1	UV	-96.3	-96.5
45_2^0	UV	-94.5	-94.5
$44_1^0 45_1^2$	UV	-83.7	-83.7
$43_1^1 / 44_1^1$	UV	-70.0	-70.5/-69.5
$43_1^1 45_1^1$	UV	-38.7	-38.7
$44_1^1 45_1^1$	UV	-36.3	-36.1
45_1^1	UV, FES	31.9	31.9
45_0^2	UV, FES	110.8	110.8
$44_0^1 45_1^0$	UV, FES	119.2	119.2
$44_0^1 45_0^1$	UV, FES	158.4	158.4
$43_0^1 45_1^0$	UV, FES	177.8	177.8

[a] ν_{45}: ring-puckering; ν_{44}: ring-twisting; ν_{43}: ring-flapping.

[b] Quantum numbers indicate puckering states; single primes indicate transitions in the ν_{43} ($v_F = 1$) excited state; double primes indicate transitions in the ν_{44} ($v_T = 1$) state. UV absorption and SVLF values are relative to the 0_0^0 excitation frequency of 34,965.9 cm^{-1}.

[c] Inferred from energy levels in Figure 5.

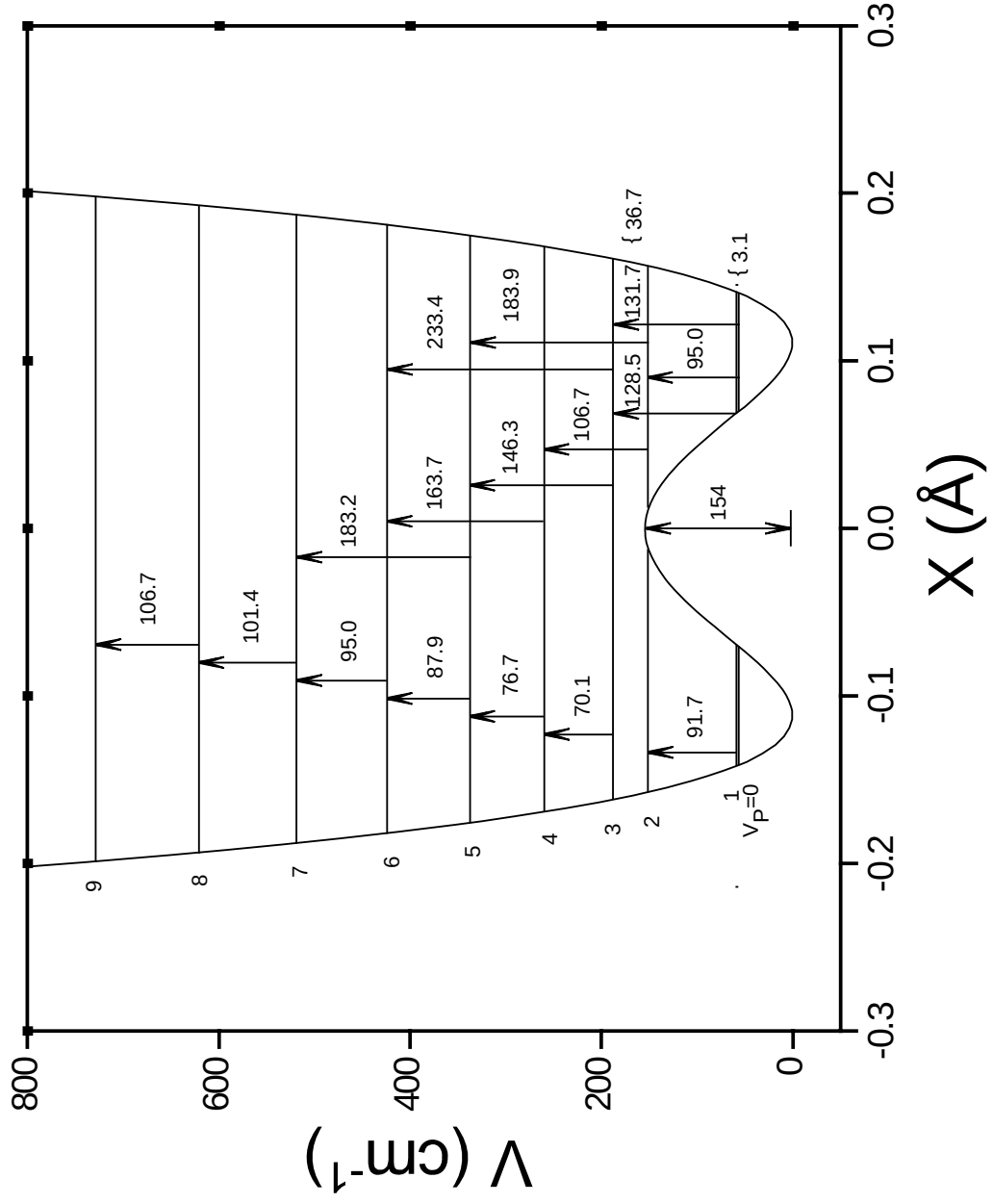

Figure 6. One-dimensional potential energy function for the ring-puckering of coumaran in the S_0 state.

and Caminati[4] also reported *ab initio* calculations which produced barriers in the 52 to 270 cm^{-1} range. They calculated a potential function of the form

$$V(\tau) = B_2[1-(\tau/\tau_e)^2]^2, \qquad (4.4)$$

where B_2 is the barrier and τ_e is the equilibrium puckering angle. On the basis of the ground state splitting and inertial defect, and not utilizing any far-infrared data, they calculated a barrier of 152 cm^{-1} and a puckering angle of 23°, totally consistent with the results reported in this work. It is interesting to note that these barriers and puckering angles, which agree almost perfectly, derive from totally different data. Although it is true that the value of the ground state splitting was invaluable in revising the far-infrared spectra, its exact value was not that critical for the calculation. In fact, as can be seen in Table 2, the calculated value of 2.37 cm^{-1} in this work for the v = 0,1 splitting differs from the observed value of 3.12 cm^{-1}. This splitting is extremely sensitive to not only the barrier height but also to the shape of the potential energy function near the energy minima. The far-infrared spectra, unlike the microwave data, are very sensitive near the top of the barrier, and thus are very reliable for determining the magnitude of the barrier, assuming the assignments are correct. To test how important the exact value of the ground state splitting is for determining the barrier height in this case here, the 0-1 splitting of 3.12 cm^{-1} and the 0-3 far-infrared transition at 131.7 cm^{-1} are forced to be fit exactly. This resulted in a calculated barrier of 143 cm^{-1}. Because the use of this

approach relies on data near the bottom of the potential energy well rather than near the top of the barrier, the 154 cm^{-1} barrier height is thought to be the more accurate value.

A higher level basis set (MP2/cc-pVTZ) was also used to calculate the barrier to planarity. This resulted in a barrier of 238 cm^{-1} and a dihedral angle of 26.5°. If the benzene ring is forced to stay planar during the puckering, a barrier of 204 cm^{-1} is predicted, which is closer to the real value.

The ring-puckering levels shown in Figure 5 for the excited vibrational states of the ring-flapping (v_F = 1) and ring-twisting (v_T = 1) can also be used to determine the one-dimensional ring-puckering functions for these states. The functions determined are for the ring-flapping

$$V_F(cm^{-1}) = (8.63\times10^5)x^4 - (2.27\times10^4)x^2, \quad (4.5)$$

and for the ring-twisting

$$V_T(cm^{-1}) = (8.80\times10^5)x^4 - (2.34\times10^4)x^2. \quad (4.6)$$

The observed and calculated energy spacings for these excited states are shown in Table 4. In the flapping excited state (v_F = 1) the barrier to planarity is 149 cm^{-1} and in the twisting excited state (v_T = 1) it is 156 cm^{-1}. The change in the observed 0-1 splitting reflects the fact that a higher barrier produces a smaller splitting and *vice-versa*.

The ultraviolet absorption, fluorescence excitation (FES), and single vibronic level fluorescence (SVLF) spectra of coumaran as well as the potential energy function for the

TABLE 4: Observed and Calculated Ring-Puckering Transition Frequencies (cm^{-1}) of Coumaran in Its Flapping and Twisting Excited States.

Flapping ($v_F = 1$)			Twisting ($v_T = 1$)		
Transition	Observed	Calculated[a]	Transition	Observed	Calculated[b]
0'-1'	3.8	2.6	0"-1"	2.7	2.3
1'-2'	90.0	90.0	1"-2"	92.6	92.6
2'-3'	39.4	37.8	2"-3"	36.1	36.1
3'-4'	68.6	71.1	3"-4"	71.4	71.5
4'-5'	77.8	76.7	4"-5"	76.2	76.4

[a] From Equation (4.5).

[b] From Equation (4.6).

$S_1(\pi,\pi^*)$ state will be presented in the next chapter. It is worth noting at this time, however, that the ultraviolet absorption spectra show bands at -96.3 and -94.5 cm^{-1} (see Table 3) relative to the electronic origin at 34,965.9 cm^{-1}, and these correspond to the 45_3^1 and 45_2^0 transitions (ν_{45} is the ring-puckering vibration). The SVLF spectrum shows the 45_2^0 band at -95 cm^{-1}. Thus it would appear that between the millimeter-wave and far-infrared spectrum, the coumaran puzzle is now clearly resolved.

A valid question is why the previous assignment[2] could be fit so well with a potential energy calculation. This can be understood to some extent by examining Table 2 where the earlier assignment is also shown. In the previous assignment, the 3.1 cm^{-1} spacing was identified but assigned as the 2-3 splitting rather than the 0-1. From its intensity the 131.7 cm^{-1} band was correctly assigned as the 0-3. Because the *ab initio* calculations predicted a barrier near 260 cm^{-1}, the assignment of the 3.1 cm^{-1} to the 0-1 splitting seemed less plausible because it yielded a considerably smaller barrier. It should also be noted that the sequence of transitions near the top of the barrier of 36.7, 70.1, and 76.7 cm^{-1} is the same for both the new and previous assignments, reflecting the effect of the barrier as well as the quartic nature of the potential function above it.

CONCLUSIONS

It is reassuring that analysis of the millimeter wave spectra[4] and the far-infrared

spectra lead to essentially the same results for the barrier to planarity and puckering angle despite using different data. It is somewhat disappointing that the *ab initio* calculations are not as accurate as expected, but the barrier is calculated as the difference between two very large numbers.

The energy levels in Figure 5 provide additional data for studying the interactions between the three lowest frequency out-of-plane modes, and those data can be used for fitting a two-dimensional potential energy surface. The frequency changes in the $v_F = 1$ and $v_T = 1$ states reflect the degree of interaction between the ring-puckering and the ring-flapping or ring-twisting modes. These frequency changes are modest but do indicate that the accuracy of the one-dimensional potential function used here is limited somewhat by the interactions.

CHAPTER V

FLUORESCENCE AND ULTRAVIOLET ABSORPTION SPECTRA AND STRUCTURE OF COUMARAN AND ITS RING-PUCKERING POTENTIAL ENERGY FUNCTION IN THE $S_1(\pi,\pi^*)$ EXCITED STATE

INTRODUCTION

The out-of-plane ring vibrations and structures of several molecules in the indan family in their ground and $S_1(\pi,\pi^*)$ excited states using far-infrared, Raman, jet-cooled fluorescence, and ultraviolet absorption spectroscopies have been investigated over the past ten years.[31] The focus of the work has been to understand what effect the $\pi \rightarrow \pi^*$ transition on the benzene ring has on the overall structure of the molecule. Understanding electronic excited states is the key to understanding photochemical processes. The molecules previously studied include indan[30] (IND), phthalan[33-35] (PHT), coumaran[2] (COU), and 1,3-benzodioxole[32,36] (BZD). Indan is puckered in both the S_0 and $S_1(\pi,\pi^*)$ states with barriers of 488 and 441 cm^{-1}, respectively. The non-planarity arises from the CH_2-CH_2 torsional interactions, which try to make the adjacent methylene groups be staggered relative to their neighbors. Phthalan has a tiny barrier to planarity of 35 cm^{-1} in the ground state but becomes more rigid with no barrier for S_1.

1,3-Benzodioxole is puckered in both states with barriers of 164 cm^{-1} in S_0 and 264 cm^{-1} in S_1. For 1,3-benzodioxole these barriers arise due to the anomeric effect, which arises from the $–O–CH_2–O–$ configuration. In S_0 the anomeric effect is somewhat suppressed due to interactions involving the benzene ring and, hence, the barrier is lower. Coumaran, the subject of the current chapter, has a single CH_2-CH_2 torsional interaction, so in analogy with 2,3-dihydrofuran with its 93 cm^{-1} barrier,[37] it is expected to have a small barrier to inversion.

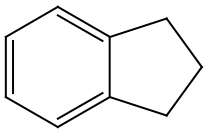

IND

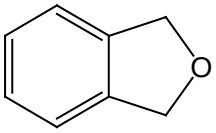

PHT

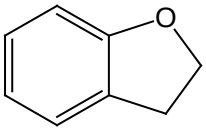

COU

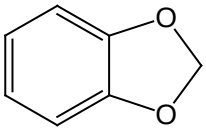

BZD

When the far-infrared spectra of coumaran was first examined by Bondoc *et al*,[2] a ring-puckering potential energy function for S_0 with a 279 cm^{-1} barrier was postulated, and in that work an energy level splitting of 3.2 cm^{-1} was assigned to the v = 2,3 pair of levels. However, recent millimeter wave spectra of Ottoviani and Caminati[4] showed that it was the v = 0,1 splitting that was at 3.12 cm^{-1}. This information allowed a reassessment of the far-infrared assignments and the determination of the one-dimensional ring-puckering potential energy function for coumaran in its S_0 state, as described in Chapter IV. This reassignment also explained the apparent anomalous single vibronic level fluorescence band[3] at -95 cm^{-1}, which had not previously been assigned.

Moreover, the revised S_0 assignment has now helped to clarify much of the ultraviolet absorption spectra so that it is possible to map out the $S_1(\pi,\pi^*)$ levels and to determine the ring-puckering potential function for that state. These results will be presented in this chapter. Watkins and co-workers[38] have studied the REMPI and ZEKE spectra of coumaran and proposed assignments and a potential function for the $S_1(\pi,\pi^*)$ state. However, their S_1 assignments require revision, in part because they had relied upon the previously published S_0 potential energy function.

EXPERIMENTAL

Coumaran (2,3-dihydrobenzofuran, b.p. 188°) was obtained from Sigma Aldrich with a stated purity of 99%. It was further purified using trap to trap vacuum transfer. The ultraviolet spectra at 0.1, 0.25, and 0.5 cm^{-1} resolutions were recorded on a Bomem DA8.02 Fourier-transform spectrometer using a 20 cm glass cell with quartz windows at ambient temperatures. The fluorescence excitation spectra and the single vibronic level fluorescence spectra were recorded using a Continuum Powerlite 9020 Nd:YAG laser which pumped a Continuum Sunlite OPO and FX-1 ultraviolet extension unit. FES spectra were obtained at a ± 0.5 cm^{-1} resolution and SVLF spectra were taken with a spectral resolution of ± 1 cm^{-1}. More details are provided elsewhere.[28-32]

ASSIGNMENTS OF SPECTRA

As will be shown later in this chapter, coumaran is a quasi-planar molecule with a small barrier to planarity. It therefore has C_1 symmetry but closely follows C_s selection rules, which would apply to a planar molecule. Molecules of C_s symmetry have A' modes for totally symmetric in-plane vibrations and A" modes for out-of-plane motions. A complete vibrational assignment will be presented in the next chapter. The focus of this current chapter will concentrate only on the low-frequency vibrations, which are responsible for the conformational changes. For the most part, the transitions from the S_0 vibrational levels to the $S_1(\pi,\pi^*)$ vibronic levels, where both electronic states have A' symmetry, follow the selection rules $A' \leftrightarrow A'$, $A'' \leftrightarrow A''$, and $A' \not\leftrightarrow A''$. In the S_0 state the barrier of 154 cm^{-1} gives rise to the two lowest ring-puckering levels being only 3.12 cm^{-1} apart,[4] and these have A' and A" symmetry for $v_P = 0$ and $v_P = 1$ levels, respectively. Both of these levels are significantly populated even under jet-cooled conditions, and thus the $A' \leftrightarrow A'$ and $A'' \leftrightarrow A''$ transitions can be readily distinguished and are of great value in making the assignments. The transition frequencies from the $v_P = 0$ A' ground state therefore correspond exactly to the vibronic energy values for the S_1 electronic state. The transitions from $v_P = 1$ A" state, however, are all 3.1 cm^{-1} lower than the vibronic energy levels. More than seventy transitions in the ultraviolet absorption spectra very nicely follow these selection rules. However, in a few cases, two for S_0 and

one for S_1, there are quantum states which should behave as A" modes but appear to have A' character or *vice-versa*. These occur in the ring-flapping vibrational excited state (v_F = 1) and can be attributed to the strong interaction between the puckering and flapping vibrations and to the fact that the molecule actually has C_1 symmetry where all quantum states are totally symmetric. These will be discussed below.

Figures 7 and 8 shows the jet-cooled fluorescence excitation spectrum (FES) and the room-temperature ultraviolet absorption spectrum of coumaran in the 0-500 cm^{-1} and 500-1000 cm^{-1} regions, respectively, relative to the electronic origin at 34,965.9 cm^{-1}. Table 5 lists the frequencies and assignments in the FES and UV absorption spectra. Figure 9 shows the single vibrational level fluorescence (SVLF) spectra collected from exciting the 0_0^0 band at 34,965.9 cm^{-1} and the 45_0^2 band at 110.8 cm^{-1} higher. Figure 10 shows the SVLF spectrum from exciting the 45_1^1 band that is 31.9 cm^{-1} higher than the 0_0^0 band. The corresponding ultraviolet spectrum arising from hot band transitions is also shown. The SVLF spectra were recorded from eleven different excitation lines, and the application of symmetry rules expedited the assignment of the $S_1(\pi,\pi^*)$ bands. Tables 6 and 7 provide a listing of the SVLF spectra along with the values inferred from the far-infrared and ultraviolet absorption spectra. As can be seen, the assignments have little ambiguity. Table 6 presents the SVLF data for the A' symmetry levels in the S_1 state, which were excited from the S_0 ground vibrational level (v_P = 0). These are the $A' \leftrightarrow A'$

transitions since the vibronic levels prefer to fluoresce back to the same symmetry. The SVLF data in Table 7 result from the A"↔ A" transitions as these originate from the A" v_P = 1 level, which lies 3.1 cm^{-1} above the v_P = 0 level. Figure 11 shows the energy level diagram for both the S_0 and $S_1(\pi,\pi^*)$ states, based on those spectra. The energy levels were derived from the FES and absorption spectra shown in Table 5.

In Figure 11, following conventions adopted in previous works,[2,30-36] the ring-puckering (ν_{45}) levels (v_P) in the flapping (ν_{43}) first vibrational excited state (v_F = 1) are labeled with single primes, and those in the twisting (ν_{44}) first vibrational excited state (v_T = 1) with double primes. Since all these three vibrations have A" symmetry, the quantum states alternate between A" and A' symmetry. Figure 11 also shows the puckering levels in several other states and these were determined for the most part from the SVLF and UV absorption spectra. The vibrational numbering is based on C_s symmetry. In this figure the 2' and 3' levels for the flapping (ν_{43}) in S_0 are labeled by * to indicate that they show anomalous symmetry behavior. This is also true for 2' in the S_1 state. Although each of these levels would appear to have the wrong symmetry, at least in part, which likely results from the fact that the puckering and flapping are strongly coupled and that the actual molecular symmetry is only C_1, the energies of these states do correspond to the values expected.

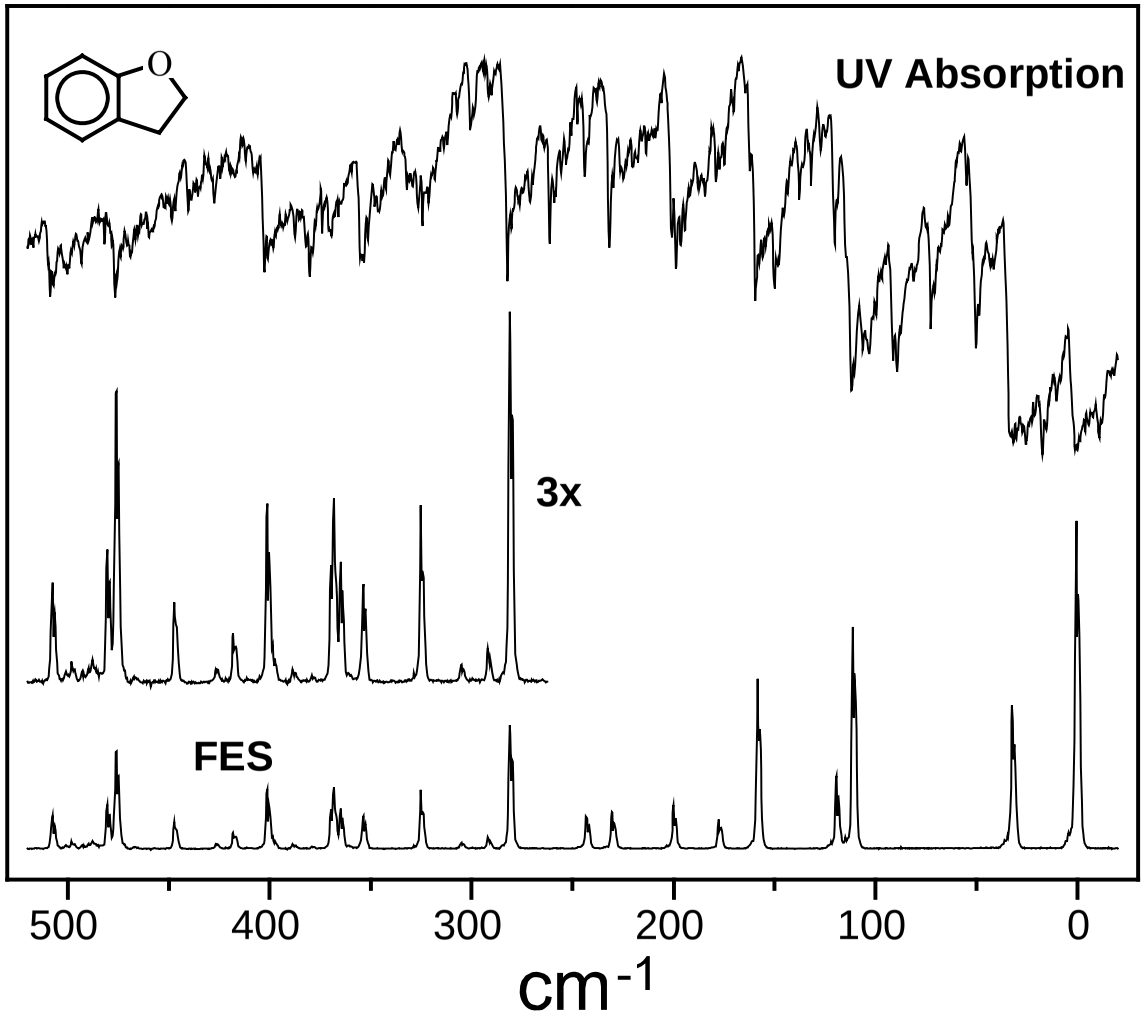

Figure 7. Fluorescence excitation spectra of jet-cooled coumaran and the ultraviolet absorption spectra at ambient temperature in the 0-500 cm^{-1} region.

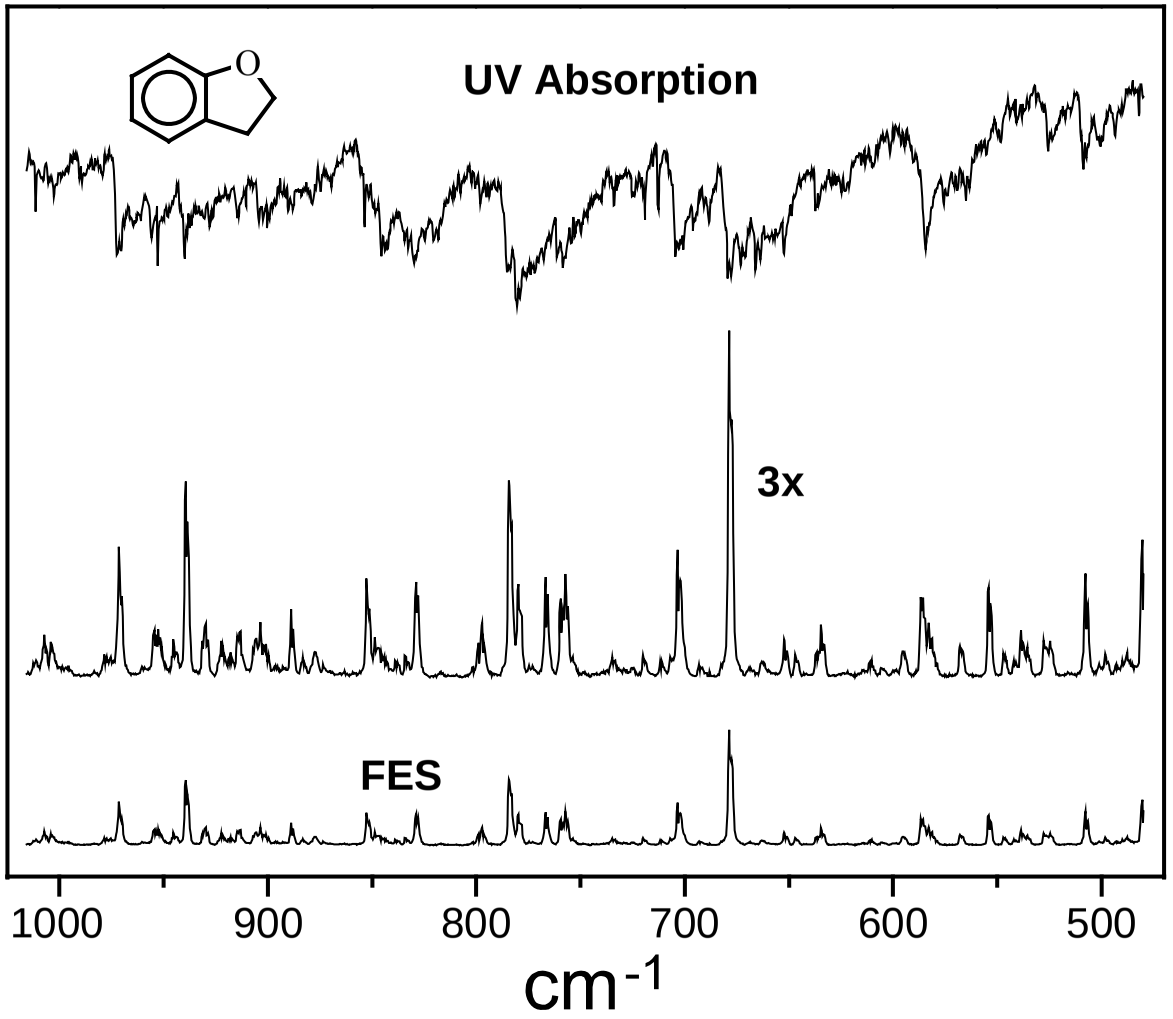

Figure 8. Fluorescence excitation spectra of jet-cooled coumaran and the ultraviolet absorption spectra at ambient temperature in the 500-1000 cm^{-1} region.

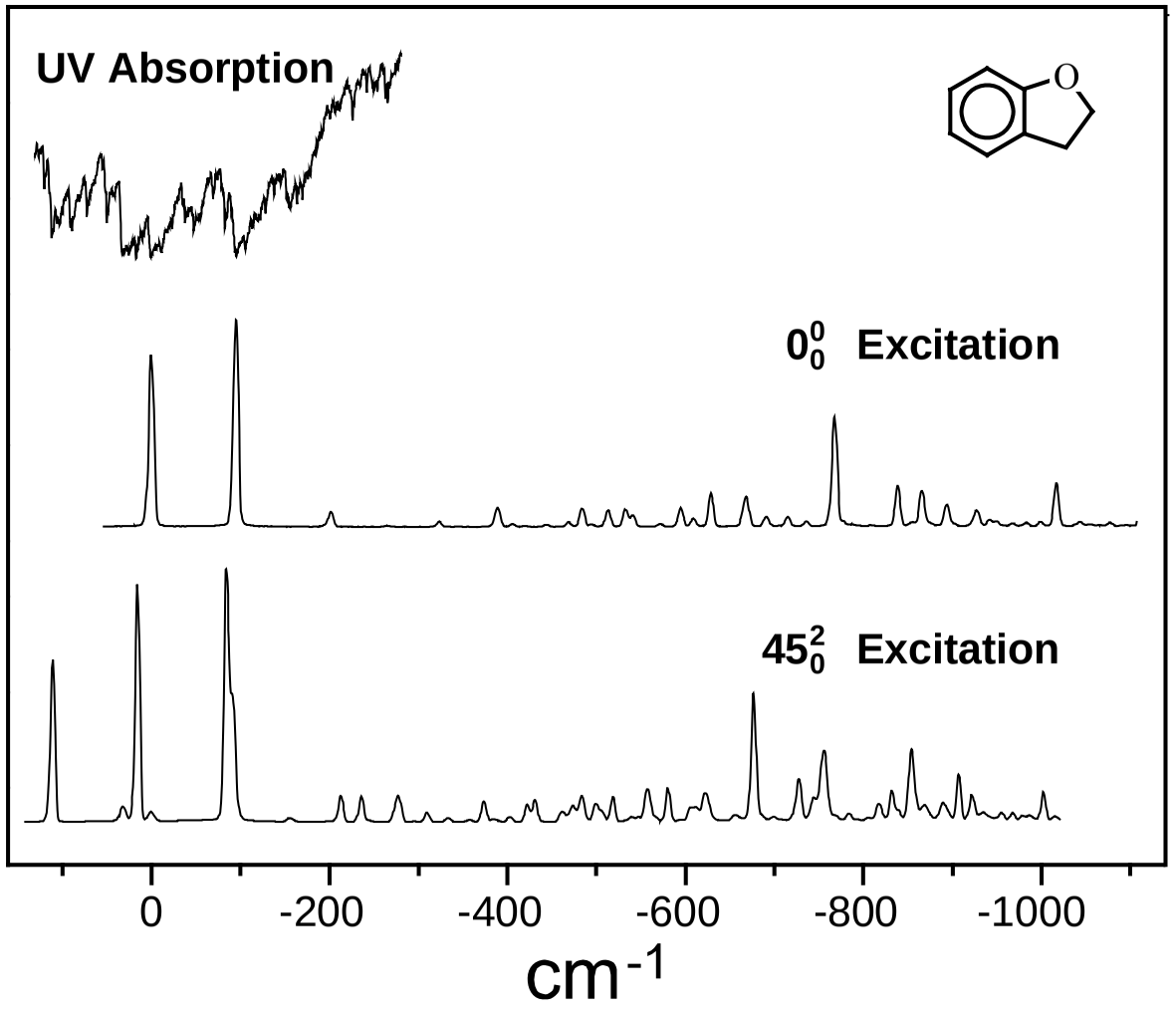

Figure 9. Single vibronic level fluorescence spectra of coumaran with excitation of the 0_0^0 band at 34,965.9 cm^{-1} and the 45_0^2 band at 110.8 cm^{-1} higher.

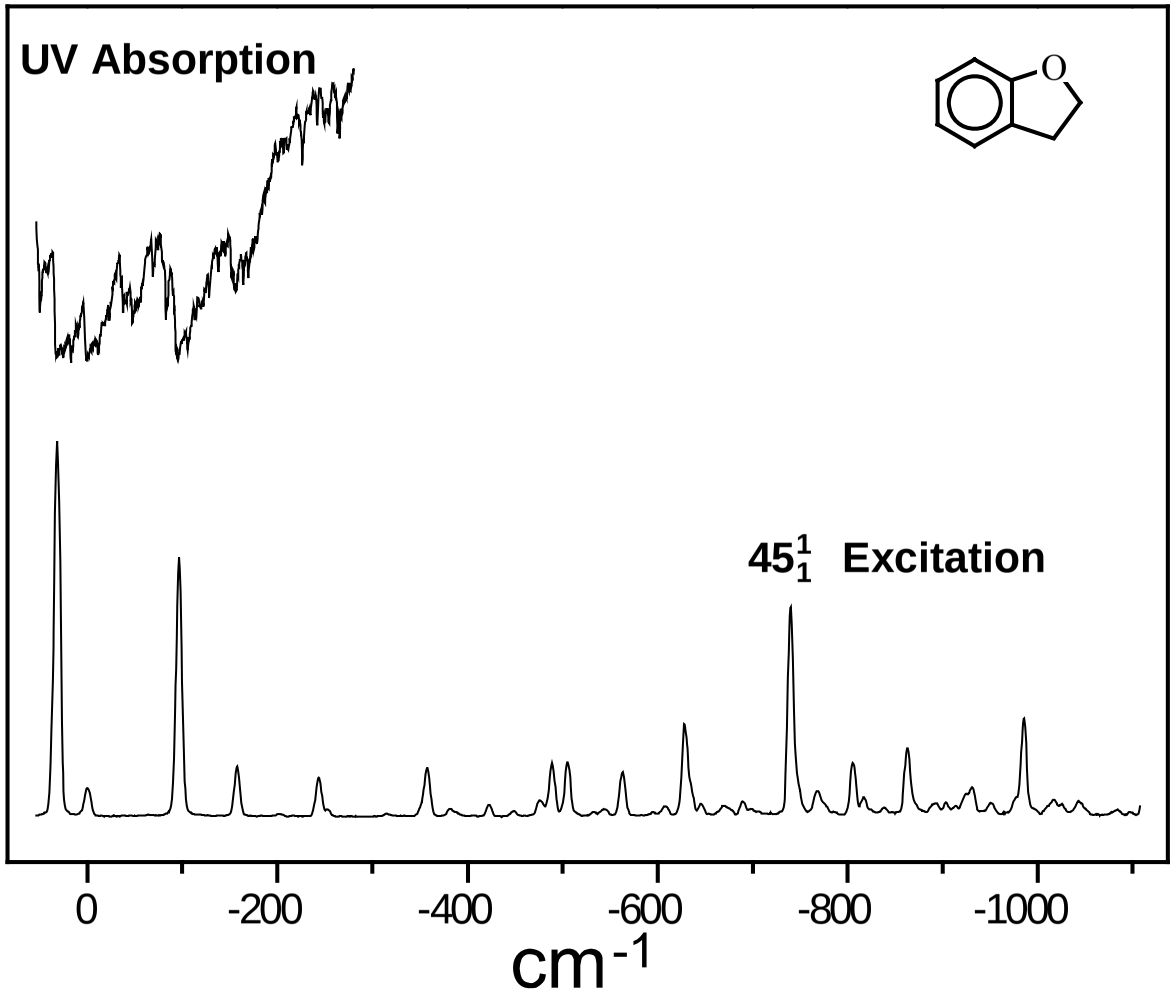

Figure 10. Single vibronic level fluorescence spectra of coumaran with excitation of the 45_1^1 band at 31.9 cm^{-1} higher than the 0_0^0 band.

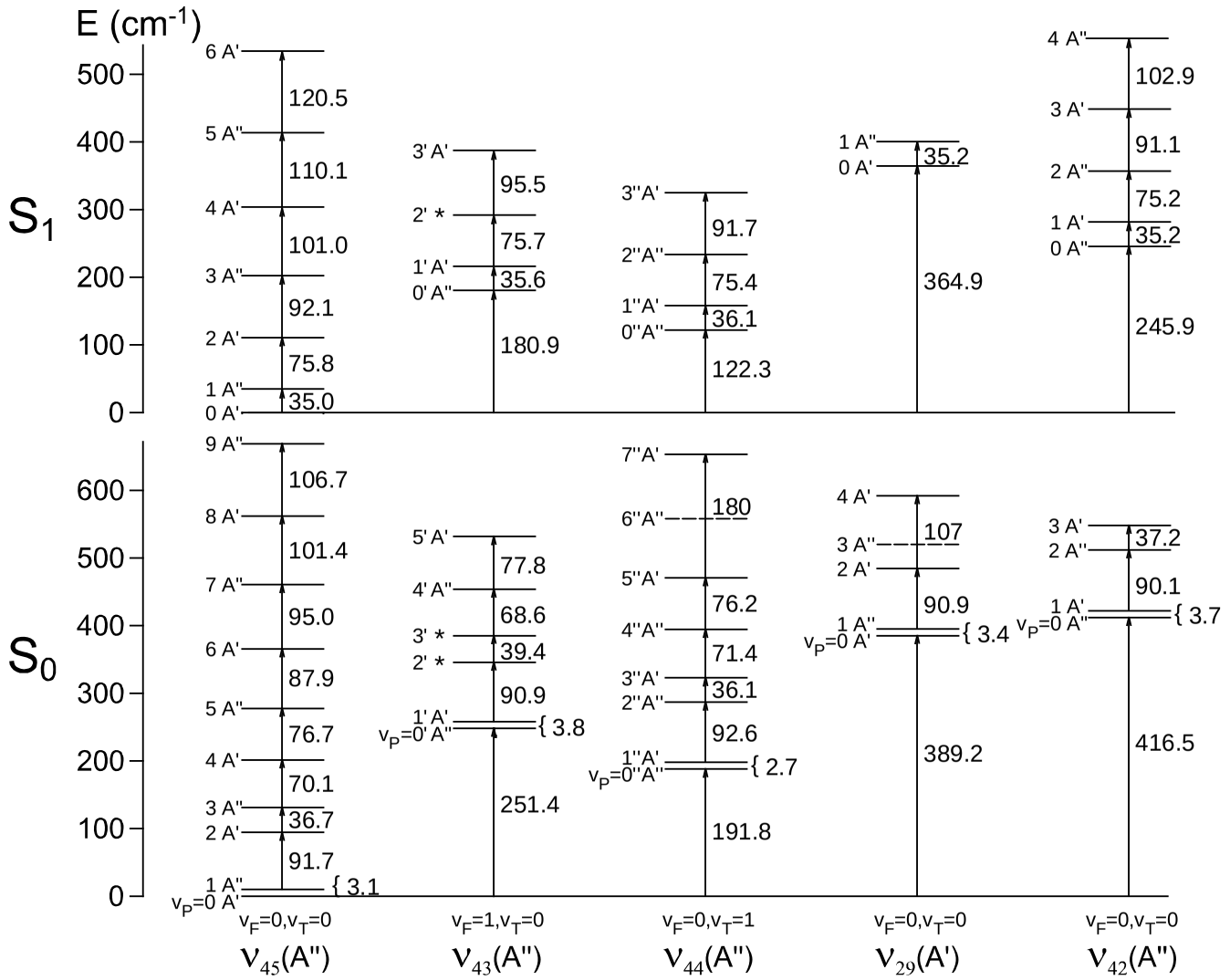

Figure 11. Energy level diagram for the low-frequency modes of coumaran in its S_0 and $S_1(\pi,\pi^*)$ states.

Table 5: Ultraviolet (UV) Absorption and Fluorescence Excitation (FES) Frequencies (cm^{-1}) and Assignments for Coumaran.

Experimental		In This Work		WBC[c]	
UV[a]	FES[a]	Inferred[b]	Assignment	REMPI	Assignment
-266.4 s		-266.4	$42_1^1 45_3^1$		
-255.2 m		-255.2	$43_1^0 45_1^0 / 45_6^2$		
-250.4 m		-250.8	$42_0^1 43_1^0 45_5^1$		
-242.8 m		-243.1	45_5^1		
-227.1 s		-227.1	$43_1^0 44_0^1 45_3^1$		
-201.8 m		-201.8	45_4^0		
-170.6 m		-170.6	42_1^1		
-168.4 m		-168.4	$44_1^1 45_2^0 / 44_1^1 45_3^1$		
-157.0 s		-156.8	$44_1^0 45_0^1$		
-155.7 s		-155.8	$44_0^1 45_5^0$		
-139.1 m		-139.1	$42_1^1 45_1^1$		
-129.2 m		-129.1	$43_1^0 44_0^1$		
-118.6 w		-118.6	$29_1^1 45_2^0$		
-106.6 s		-106.2	$43_0^1 44_1^0 45_2^0$		
-97.9 m		-97.2	$43_0^1 45_5^0$		
-96.3 vs		-96.5	45_3^1		
-94.5 vs		-94.5	45_2^0		
-91.0 w		-91.0	45_4^2		
-83.7 vs		-83.7	$44_1^0 45_1^2$		
-75.3 w		-75.2	45_5^3		
-70.0 s		-70.5/-69.5	$43_1^1 / 44_1^1$		
-48.4 vs		-48.5	$43_1^0 45_0^3$		
-38.7 s		-38.7	$43_1^1 45_1^1$		
-36.3 m		-36.1	$44_1^1 45_1^1$		
-31.5 m		-31.0	$43_0^1 44_1^0 45_3^2$ [d]		
-24.3 s		-24.3	29_1^1		
-19.4 m		-19.3	$44_1^0 45_3^4$		
-11.9 s		-10.9	$43_0^1 44_1^0$		
-5.0 m		-5.5	$42_0^1 43_1^0$		

Table 5: Continued.

Experimental		In This Work		WBC[c]	
UV[a]	FES[a]	Inferred[b]	Assignment	REMPI	Assignment
0.0 vs	0 vs	0.0	0_0^0	0	0^0
9.2 m		10.2	$42_0^1 43_1^0 45_2^2$		
14.3 m		14.7	$43_0^1 45_4^1$		
16.2 vs		16.3	45_2^2		
24.5 m		25.9	$42_0^1 43_1^0 45_1^1$		
31.9 vs	32 vs	31.9	45_1^1	32	$45^1 45_1^0$ / $44^1 45_2^0$
41.3 m		41.7	$29_0^1 44_1^0 45_3^0$		
47.5 s		48.7	$43_1^0 45_1^4$		
49.2 vs		49.4	$43_0^1 45_3^0$		
53.7 m		54.1	$42_0^1 44_1^0$		
71.4 vs		71.4	45_3^3		
88.2 vs		86.6	$42_0^1 44_1^0 45_1^1$		
90.2 s		90.4	$43_0^1 45_4^{2\,d}$		
102.1 s		102.1	45_4^4		
105.2 m		104.9	$42_0^1 43_1^0 45_0^2$		
109.3 m		109.4	$44_1^0 45_1^4$		
110.8 vs	111 vs	110.8	45_0^2	112	45^2
119.2 s	119 s	119.2	$44_0^1 45_1^0$	120	$45^3 45_1^0$
130.7 m		131.0	$44_1^1 45_1^3$		
136.6 m		135.9	45_5^5		
148.9 s			?		
158.4 vs	158 vs	158.4	$44_0^1 45_0^1$	160	44^1
163.4 m		163.1	$29_0^1 45_4^0$		
168.9 m		168.5	45_6^6		
177.8 m	177 m	177.8	$43_0^1 45_1^0$	179	…
197.6 vs		197.7	$43_0^1 45_2^{2\,d}$		
199.8 vs	200 m	199.8	45_1^3	202	43^1 / $44^2 45_2^0$
230.7 vs	230 m	230.7	$44_0^1 45_1^2$	232	…
242.8 s	243 m	242.8	$42_0^1 45_1^0$	245	$40^2 45_2^0$

Table 5: Continued.

Experimental		In This Work		WBC[c]	
UV[a]	FES[a]	Inferred[b]	Assignment	REMPI	Assignment
260.3 vs			?		
270.0 m		270.4	$29_0^1 45_2^0$		
281.1 vs	281 s	281.1	$42_0^1 45_0^1$	283	42^1
	292 w	292.2	$43_0^1 45_0^{2\,d}$	294	…
299.2 m			?		
304.9 w	305 vw	303.9	45_0^4	307	45^6
323.2 m			?		
325.5 m	325 s	325.5	$44_0^1 45_0^3$	327	44^2
353.2 vs	353 m	353.2	$42_0^1 45_1^2$	356	…
364.9 w	365 m	364.9	29_0^1	367	41^1
368.5 m	369 s	368.5	$42_0^1 44_0^1$	371	40^1
379.1 s	379 vw		?		
	388 vw	387.7	$43_0^1 45_0^3$		
401.7 vs	401 s	401.7	$42_0^1 44_0^1 45_1^1$	403	…
417.9 m	418 w	417.9	$41_0^1 45_1^0$	419	…
426.3 m	426 vw	426.4	$42_0^1 43_0^1$	428	$42^2 45_2^0$
439.4 m		440.0	45_2^6		
447.4 m	447 m	447.4	$42_0^1 45_0^3$	449	$42^1 44^1$
475.6 s	476 s	475.6	42_0^2	478	$39^1 / 45^2 41^1$
480.8 m	481 m	480.8	$42_0^1 44_0^1 45_0^2$	483	$44^3 / 45^2 40^1$
507.7 s	508 m	507.7	$42_0^2 45_1^1$	510	38^1
524.6 m	525 w	524.6	27_0^1	526	$37^1 / 44^1 41^1$
547.2 m	547 w	550.3	$42_0^1 45_1^4$	585	…
583.5 vs	583 m	583.5	26_0^1	585	…
586.5 m	586 m	586.5	$42_0^2 45_0^2$	589	$45^2 39^1$
678.2 s	679 s		Fundamental		
784.0 s	784 s		Fundamental		
939.1 s	939 s		Fundamental		
971.2 s	971 m		$939+45_1^1$		

Table 5: Continued.

[a] The fluorescence excitation spectra are of supersonic jet-cooled molecules; the ultraviolet absorption spectra were recorded at ambient temperature; for intensities: s-strong, m-medium, w-weak, v-very.

[b] Frequency values inferred from the energy level diagrams in Figure 11.

[c] From Reference 38.

[d] Transitions with anomalous symmetry characteristics.

Table 6: Frequencies (cm^{-1}) and Assignments of Single Vibronic Level Fluorescence (SVLF) Spectra with Excitation of the A' Vibronic Levels of Coumaran.

Excitation: 0_0^0		45_0^2		$44_0^1 45_0^1$		A'↔ A'
FES Bands: 0.0[a] vs		+110.8 s		+158.4 s		Inferred[b]
-95 vs	45_2^0	-95 vs	45_2^2	-96 w	$44_0^1 45_2^1$	-94.5
		-195 vs	$44_1^0 45_1^2$	-194 s	$44_1^1 45_1^1$	-194.5
-202 m	45_4^0	-202 sh	45_4^2			-201.8
-266 vw		-266 w		-265 vs		?
-323 w	$44_1^0 45_3^0$	-323 m	$44_1^0 45_3^2$	-323 s	$44_1^1 45_3^1$	-323.2
		-346 m	$43_1^0 45_2^2$	-346 w	$43_1^0 44_0^1 45_2^1$	-346.1[c]
-389 m	29_1^0	-388 m	$29_1^0 45_0^2$	-386 m	$29_1^0 44_0^1 45_0^1$	-389.2
		-420 m	$42_1^0 45_1^2$	-420 ms	$42_1^0 44_0^1 45_1^1$	-420.2
-444 w	$43_1^0 44_1^0$	-444 w	$43_1^0 44_1^0 45_0^2$	-443 vw	$43_1^0 44_1^1 45_0^1$	-443.2
-469 w		-468 vw		-469 ms		(-266-202) ?
-484 m	$29_1^0 45_2^0$	-484 m	$29_1^0 45_2^2$			-483.5
-514 m	$41_1^0 45_1^0$	-513 w	$41_1^0 45_1^2$			-513
-533 m	28_1^0	-533 m	$28_1^0 45_0^2$	-533 m	$28_1^0 44_0^1 45_0^1$	-533
-541 m	$43_1^0 44_1^0 45_2^0$	-541 m	$43_1^0 44_1^0 45_2^2$	-541 m	$43_1^0 44_1^1 45_2^1$	-539
						-547
-595 m	27_1^0	-594 m	$27_1^0 45_0^2$	-595 w	$27_1^0 44_0^1 45_0^1$	-595
-629 s	$28_1^0 45_2^0$	-629 m	$28_1^0 45_2^2$			-629
-668 s	26_1^0	-668 m	$26_1^0 45_0^2$	-668 m	$26_1^0 44_0^1 45_0^1$	-668
-691 w	$27_1^0 45_2^0$	-691 m	$27_1^0 45_2^2$			-691
-768 vs	25_1^0	-767 w	$25_1^0 45_0^2$	-769 m	$25_1^0 44_0^1 45_0^1$	-768
		-787 vs	$27_1^0 44_1^0 45_1^2$	-788 m	$27_1^0 44_1^1 45_1^1$	-788
-839 s	24_1^0	-838 m	$24_1^0 45_0^2$	-836 m	$24_1^0 44_0^1 45_0^1$	-839
-866 s	$38_1^0 45_1^0$	-866 s	$38_1^0 45_1^2$			-866
		-964 s	$35_1^0 45_1^2$			-964
-1017 s	21_1^0	-1017 m	$21_1^0 45_0^2$			-1017

Table 6: Continued.

Excitation:	$42_0^1 45_0^1$	29_0^1		A'↔ A'
FES Bands:	+281.1 s	+364.9 m		Inferred[b]
-94 w	$42_0^1 45_2^1$	-95 m	$29_0^1 45_2^0$	-94.5
-193 w	$42_0^1 44_1^0 45_1^1$	-194 sh	$29_0^1 44_1^0 45_1^0$	-194.5
		-202 w	$29_0^1 45_4^0$	-201.8
-264 m		-265 m		?
-323 ms	$42_0^1 44_1^0 45_3^1$	-323 m	$29_0^1 44_1^0 45_3^0$	-323.2
		-346 m	$29_0^1 43_1^0 45_2^0$	-346.1[c]
-386 vw	$42_0^1 29_1^0 45_0^1$	-388 vs	29_1^1	-389.2
-420 vs	$42_1^1 45_1^1$	-420 s	$42_1^0 29_0^1 45_1^0$	-420.2
-443 w	$42_0^1 43_1^0 44_1^0 45_0^1$	-444 m	$29_0^1 43_1^0 44_1^0$	-443.2
-469 m		-469 w		(-266-202) ?
		-483 vs	$29_1^1 45_2^0$	-483.5
		-513 m	$29_0^1 41_1^0 45_1^0$	-513
-532 vw	$28_1^0 42_0^1 45_0^1$	-533 m	$28_1^0 29_0^1$	-533
		-540 m	$29_0^1 43_1^0 44_1^0 45_2^0$	-539
-547 s	$42_1^1 45_3^1$			-547
-594 m	$27_1^0 42_0^1 45_0^1$	-591 m	$27_1^0 29_0^1$	-595
		-628 m	$28_1^0 29_0^1 45_2^0$	-629
-666 w	$26_1^0 42_0^1 45_0^1$	-669 m	$26_1^0 29_0^1$	-668
-692 m	$27_1^0 42_0^1 45_2^1$	-693 m	$27_1^0 29_0^1 45_2^0$	-691
-767 w	$25_1^0 42_0^1 45_0^1$	-767 s	$25_1^0 29_0^1$	-768
-787 m	$27_1^0 42_0^1 44_1^0 45_1^1$			-788
-836 vw	$24_1^0 42_0^1 45_0^1$	-838 w	$24_1^0 29_0^1$	-839
		-865 m	$29_0^1 38_1^0 45_1^0$	-866
				-964
		-1015 m	$21_1^0 29_0^1$	-1017

[a] The excitation of 0_0^0 is at 34,965.9 cm^{-1}; the frequencies of all other excitation bands are relative to 0_0^0; for intensities: s-strong, m-medium, w-weak, v-very, sh-shoulder.

[b] Frequency values inferred from the energy levels in Figure 11.

[c] Transitions with anomalous symmetry characteristics.

Table 7: Frequencies (cm^{-1}) and Assignments of Single Vibronic Level Fluorescence (SVLF) Spectra with Excitation of the A'' Vibronic Levels of Coumaran.

Excitation: 45_1^1		$44_0^1 45_1^0$		$43_0^1 45_1^0$		A''↔ A''
FES Bands: +31.9 s		+119.2 ms		+177.8 m		Inferred[b]
-128 vs	45_3^1			-129 s	$43_0^1 45_3^0$	-128.4
-189 m	$44_1^0 45_0^1$	-189 s	44_1^1	-190 vs	$43_0^1 44_1^0$	-188.7
		-249 s	$43_1^0 44_0^1$	-249 w	43_1^1	-248.3
-275 m	45_5^1	-275 vs	$44_0^1 45_5^0$	-275 vs	$43_0^1 45_5^0$	-275.0
-285 w	$44_1^0 45_2^1$	-284 s	$44_1^1 45_2^0$	-284 s	$43_0^1 44_1^0 45_2^0$	-284.0
		-347 s		-347 m		?
-383 w	$43_1^0 45_3^1$			-383 m	$43_1^1 45_3^0$	-382.4[c]
-389 m	$29_1^0 45_1^1$					-389.5
		-391 m	$44_1^1 45_4^0$			-391.5
-413 w	$42_1^0 45_0^1$	-414 m	$42_1^0 44_0^1$	-414 w	$42_1^0 43_0^1$	-413.4
-508 w	$42_1^0 45_2^1$			-508 m	$42_1^0 43_0^1 45_2^0$	-508

Excitation: 45_1^3		$44_0^1 45_1^2$		$42_0^1 45_1^0$		A''↔ A''
FES Bands: +199.8 m		+230.7 m		+242.8 m		Inferred[b]
-128 s	45_3^3	-128 m	$44_0^1 45_3^2$	-127 w	$42_0^1 45_3^0$	-128.4
		-189 w	$44_1^1 45_0^2$	-188 s	$42_0^1 44_1^0$	-188.7
-248 s	$43_1^0 45_0^3$	-248 m	$43_1^0 44_0^1 45_0^2$			-248.3
-275 w	45_5^3					-275.0
-284 m	$44_1^0 45_2^3$	-284 m	$44_1^1 45_2^2$	-284 m	$42_0^1 44_1^0 45_2^0$	-284.0
-346 m		-346 s				?
-382 w	$43_1^0 45_3^3$	-383 s	$43_1^0 44_0^1 45_3^2$			-382.4[c]
						-389.5
-391 m	$44_1^0 45_4^3$	-391 m	$44_1^1 45_4^2$			-391.5
-413 w	$42_1^0 45_0^3$			-413 vs	42_1^1	-413.4
		-509 w	$42_1^1 45_2^2$	-508 vs	$42_1^1 45_2^0$	-508

[a] The excitation of 0_0^0 is at 34,965.9 cm^{-1}; the frequencies of all other excitation bands are relative to 0_0^0; for intensities: s-strong, m-medium, w-weak, v-very.

[b] Frequency values inferred from the energy levels in Figure 11.

[c] Transitions with anomalous symmetry characteristics.

CALCULATIONS

The ring-puckering energy level data shown for the $S_1(\pi,\pi^*)$ state in Figure 11 were used to determine the one-dimensional ring-puckering potential energy function for coumaran. The Hamiltonian has the form

$$H = -\frac{\hbar^2}{2}\frac{d}{dx}g_{44}(x)\frac{d}{dx} + V(x), \tag{5.1}$$

where x is the ring-puckering coordinate in Å as previously defined[2] and the potential energy function has the form

$$V(x) = ax^4 + bx^2. \tag{5.2}$$

The coordinate dependent reciprocal reduced mass expression, $g_{44}(x)$, was calculated as previously described.[2] The structure for the $S_1(\pi,\pi^*)$ excited state was calculated using time-dependent density functional theory (TDDFT) calculations at the B3LYP level with the TZVP basis set in the TURBOMOLE V5-6 program package.[39,40] This calculation was carried out by Dr. Ohyun Kwon in Samsung Advanced Institute of Technology, Korea. Figure 12 shows this calculated excited structure along with the ground state structure. Gaussian 03[41] was also used for computations. The kinetic energy expressions g_{44} for the S_0 and S_1 were calculated based on the structures in Figure 12, giving

$$g_{44}(S_0) = 0.006501 - 0.03544x^2 + 0.01844x^4 + 0.1579x^6, \tag{5.3}$$

and

$$g_{44}(S_1) = 0.006419 - 0.03526x^2 + 0.01917x^4 + 0.1563x^6. \tag{5.4}$$

Very small coefficients for x, x^3, and x^5 were also calculated, but these are nearly negligible. It can also be noted that $g_{44}(S_0)$ and $g_{44}(S_1)$ have very similar magnitudes although the increased benzene bond lengths for the S_1 state result in a higher reduced mass of 155.78 au (reciprocal of 0.006419) vs. 153.82 au for S_0. The calculated potential energy function which best fits the data for S_1 state is

$$V(cm^{-1}) = (1.554 \times 10^6)x^4 - (1.460 \times 10^4)x^2 . \quad (5.5)$$

This one-dimensional function is shown in Figure 13. The barrier to planarity is 34 cm^{-1} and the energy minima are at x = ± 0.0685 Å, which correspond to puckering dihedral angles of ± 14°. Figure 14 compares this function to that in the ground state, where the minima are at ± 25° and the barrier is 154 cm^{-1}. Table 8 compares the calculated and observed energy spacings for the ring-puckering in the $S_1(\pi,\pi^*)$ state, and the fit is excellent, especially in view of the fact that there is expected to be substantial coupling between the puckering and flapping modes. To a lesser extent, the ring-twisting vibration can also couple as this is not precluded by symmetry selection rules.

In the flapping excited state (v_F = 1) of S_1, the potential function for the ring-puckering vibration that best fits the data is

$$V_F(cm^{-1}) = (1.68 \times 10^6)x^4 - (1.54 \times 10^4)x^2 , \quad (5.6)$$

whereas in the twisting excited state (v_T = 1) it is

$$V_T(cm^{-1}) = (1.55 \times 10^6)x^4 - (1.42 \times 10^4)x^2 . \quad (5.7)$$

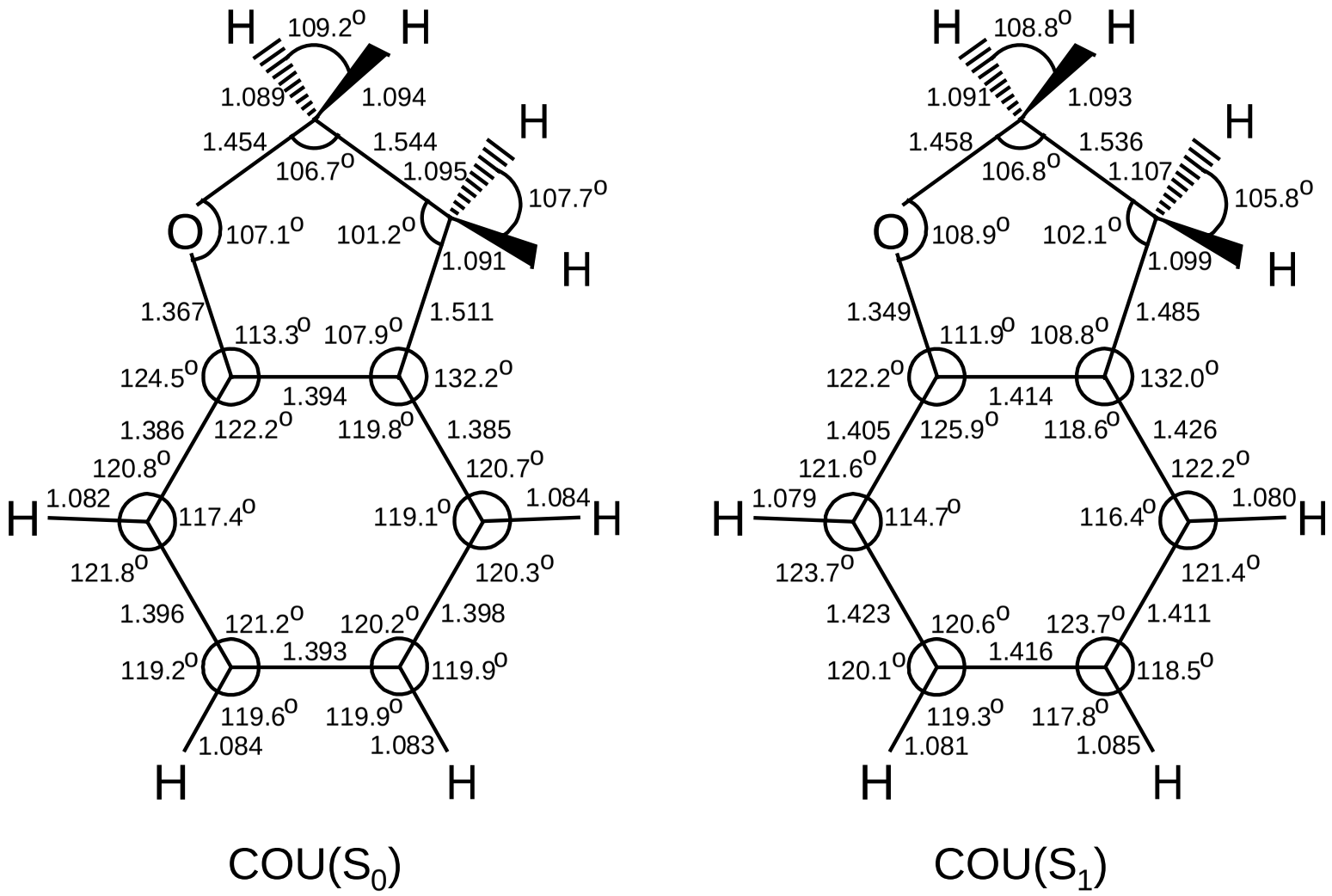

Figure 12. Calculated structures for the S_0 and $S_1(\pi,\pi^*)$ states of coumaran.

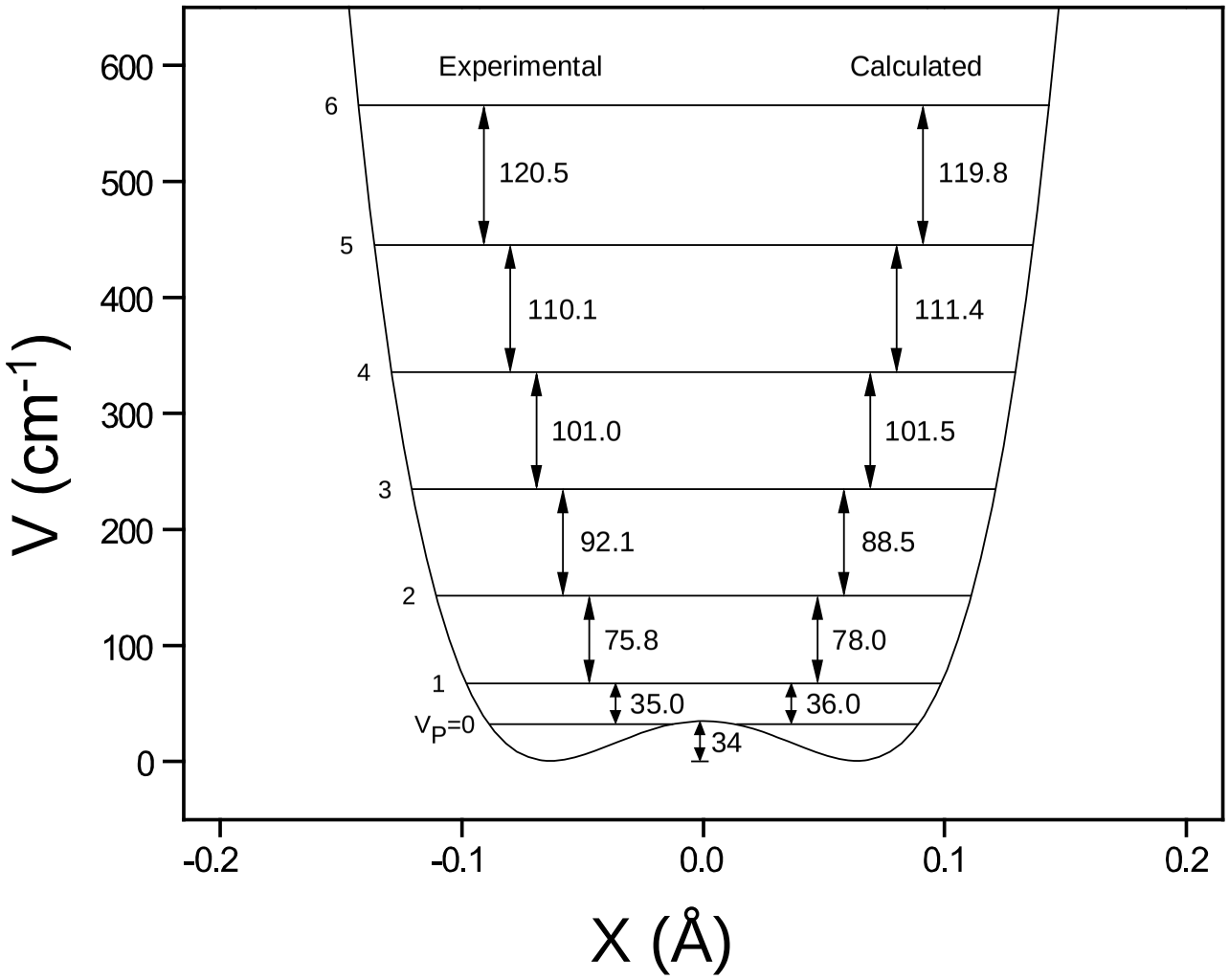

Figure 13. One-dimensional potential energy function for the ring-puckering of coumaran in its $S_1(\pi,\pi^*)$ state.

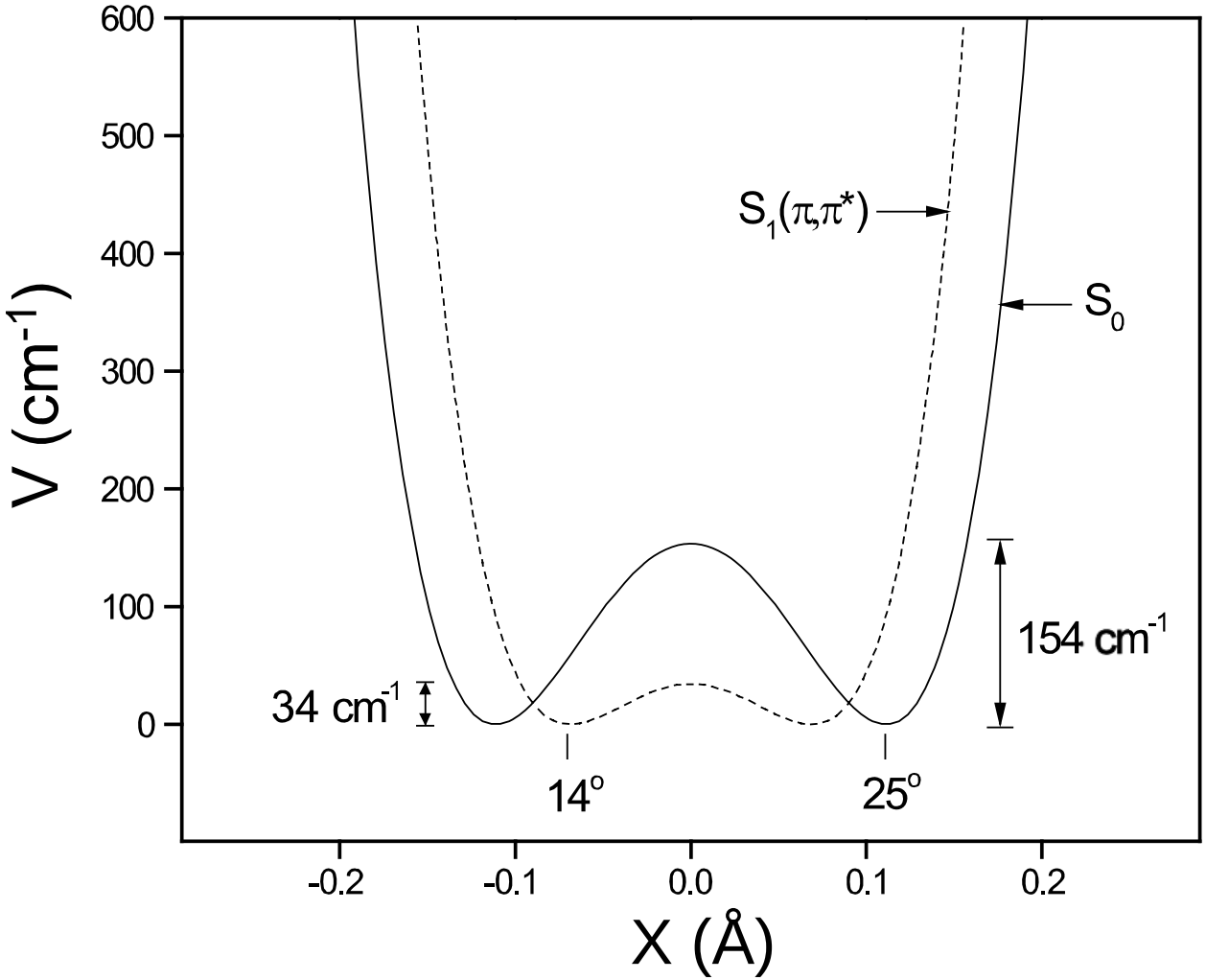

Figure 14. Comparison of the ring-puckering potential energy functions of coumaran in its S_0 and $S_1(\pi,\pi^*)$ states.

Table 8: Experimental and Calculated Energy Level Spacings (cm^{-1}) for the Ring-Puckering of Coumaran in Its $S_1(\pi,\pi^*)$ State.

State	Spacing	Experimental	Calculated	Difference
$v_F = 0$, $v_T = 0$[a]	0-1	35.0	36.0	-1.0
	1-2	75.8	78.0	-2.2
	2-3	92.1	88.5	3.6
	3-4	101.0	101.5	-0.5
	4-5	110.1	111.4	-1.3
	5-6	120.5	119.8	0.7
$v_F = 1$, $v_T = 0$[b]	0'-1'	35.6	37.1	-1.5
	1'-2'	75.7	80.1	-4.4
	2'-3'	95.5	91.0	4.5
$v_F = 0$, $v_T = 1$[c]	0"-1"	36.1	37.0	-0.9
	1"-2"	75.4	78.1	-2.7
	2"-3"	91.7	89.0	2.7

[a] $V(cm^{-1}) = (1.554\times10^{6})x^{4} - (1.460\times10^{4})x^{2};\ v_F = 0, v_T = 0.$

[b] $V_F(cm^{-1}) = (1.68\times10^{6})x^{4} - (1.54\times10^{4})x^{2};\ v_F = 1, v_T = 0.$

[c] $V_T(cm^{-1}) = (1.55\times10^{6})x^{4} - (1.42\times10^{4})x^{2};\ v_F = 0, v_T = 1.$

The barriers are 35 and 32.5 cm^{-1}, respectively. Table 8 also compares the observed and calculated values for the energy spacings of these two excited states. Since the data for these two states ($v_F = 1$ and $v_T = 1$) are very limited, the functions and barriers are likely not very accurate.

Theoretical calculations predicted a barrier to planarity of 21 cm^{-1} for the S_1 state as compared to the experimental value of 35 cm^{-1}. The calculation also predicted the vertical excitation energy to be 38,965 cm^{-1} vs. 34,966 cm^{-1} observed. The adiabatic excitation energy was calculated to be 36,158 cm^{-1} (4.483 eV).

DISCUSSION

Table 9 compares the experimental and calculated barriers for the four molecules in the indan family in their S_0 and $S_1(\pi,\pi^*)$ state. The table also compares the potential energy parameters *a* and *b* used for Equation (5.2). As is well known,[2,30-37,42] the constant *a* arises primarily from angle strain forces whereas *b* results from torsional forces along with contributions from angle strain. A negative *b* value leads to a barrier to planarity. This is the case whenever the torsional forces exceed the angle strain contributions to this quadratic coefficient. As expected, indan has the highest barriers for both the S_0 and S_1 states due to its two CH_2-CH_2 torsional interactions, which want to stagger the methylene groups and thus bend the five-membered ring out of plane. This is similar to

Table 9: The Ring-Puckering Potential Energy Parameters and the Experimental and Calculated Potential Energy Barriers from the One-Dimensional Approximations[a] for the Indan Family.

Molecule	S_0 Ground State				$S_1(\pi,\pi^*)$ Excited State				Ref.
	Parameter		Barrier (cm^{-1})		Parameter		Barrier (cm^{-1})		
	a ($\times 10^5$)	b ($\times 10^4$)	Exp.[b]	Calc.	a ($\times 10^5$)	b ($\times 10^4$)	Exp.[b]	Calc.	
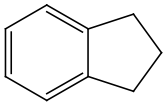	NA[c]	NA	488	662	NA	NA	441	528	2
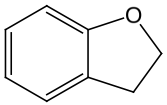	10.0	-24.8	154	238	15.5	-1.46	34	21	This work 5,6
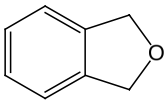	3.78	-7.10	35	91	5.47	0.386	0	11	3,4
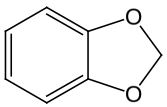	12.9	-2.57	164	171	18.3	-3.15	264	369	7,8

[a] $V(cm^{-1}) = ax^4 + bx^2$, for x in Å; a in cm^{-1} / Å^4; b in cm^{-1} / Å^2.

[b] Calculated from two-dimensional model for indan, phthalan, and 1,3-benzodioxole.

[c] Only a two-dimensional calculation was carried out for indan.

the case for cyclopentene,[43] which has a barrier to planarity of 232 cm^{-1}. The barrier for indan in the S_1 electronic excited state drops from 488 to 441 cm^{-1} and this indicates an increase in angle strain within the five-membered ring. The one-dimensional potential energy parameters for indan are not shown in Table 9 since no one-dimensional function that would satisfactorily fit the data was determined. However, for the other three molecules these parameters are listed in the table. In each case the parameter *a* increases by about 50% from the S_0 state to the S_1 state, as a result of the increased angle strain, which also tends to make the *b* coefficient more positive (or less negative). The exception to this is 1,3-benzodioxole for which the angle strain and *a* parameter increase, but for which the increased anomeric effect greatly increases the negative magnitude of *b* as well as the barrier height. Phthalan has a tiny 35 cm^{-1} barrier in S_0, apparently from oxygen p orbital interactions with the methylene groups, but this disappears as the molecule becomes much more rigid in the S_1 state. Coumaran has only one CH_2-CH_2 interaction, and hence its 154 cm^{-1} barrier for S_0 is considerably less than the 488 cm^{-1} barrier of indan. For S_1 the barrier of coumaran nearly disappears (34 cm^{-1}) as the increased angle strain virtually cancels out the torsional forces.

The $\pi \rightarrow \pi^*$ transition on the benzene ring, which reduces the total π bond contribution from three to two, has the effect of increasing the C-C bond lengths in the benzene ring in coumaran. As can be seen in Figure 12, these C-C bond lengths increase

from approximately 1.39 Å to 1.41 Å. Figure 15 shows all the bond length changes calculated for both coumaran and 1,3-benzodioxole. While the benzene ring bonds lengthen, the two bonds of the five-membered rings joining the benzene ring are shortened: 1.367 to 1.349 Å for the C-O bond and 1.511 to 1.485 Å for the C-C bond for coumaran. Thus, the five-membered rings get a bit wider and a bit shorter. These changes are not unexpected, but the sizable increase in angle strain in the five-membered ring upon the electron excitation is somewhat surprising. This is present for all four molecules and in each case tends to make the molecule planar or more nearly planar in the $S_1(\pi,\pi^*)$ state. The angle strain is also increased in the S_1 state of 1,3-benzodioxole as reflected in its *a* potential energy parameter, but the barrier to planarity is increased due to the fact that the anomeric effect is less suppressed in S_1 as compared to S_0.

Further examination of Figure 15 shows why the angle strain increases in the five-membered rings of these types of molecules upon excitation to the excited $S_1(\pi,\pi^*)$ state. The angle strain primarily results from the fact that the average angle in a planar five-membered ring (pentagon) is 108° and the angles about the carbon atoms that are part of both rings nominally prefer to be 120°. These angles also have the largest angle-bending force constants. There is also a small amount of strain in the other angles within the five-membered ring. In the S_1 state the C-C bond at the bridgehead is increased by 0.020 Å for coumaran and this has the effect of increasing the net angle

strain adjacent to this bond. Figure 15 also shows the changes in these angles.

Figure 16 shows a qualitative molecular orbital diagram for the HOMO π and LUMO π* orbitals of benzene (D_{6h} symmetry) correlated to those of coumaran (C_s symmetry) and to the other C_{2v} molecules in the indan family. The doubly-degenerate E_{1g} orbital of benzene splits upon substitution to two A" π bonding orbitals which have different but similar energies. Similarly, the antibonding E_{2u} π* orbitals of benzene also split into two A" orbitals. Figure 16 shows the atomic p orbitals which make up these π and π* molecular orbitals. While it is not obvious which A" levels are involved in the $\pi \rightarrow \pi^*$ transition that produces the $S_1(\pi,\pi^*)$ state, it can be seen that the C-C bonds in benzene should be weakened. This is, of course, also the intuitive expectation.

What this work has shown is that modest structural changes in the adjacent benzene ring can be accompanied by significant structural and conformational changes of the five-membered ring. The increased angle strain for coumaran, phthalan, and indan in the $S_1(\pi,\pi^*)$ states results in more rigid molecules which tend to become planar or more nearly planar. The change is the least for indan and this is likely due to the fact that the torsional CH_2-CH_2 interactions continue to dominate in the S_1 as well as the S_0 states. As we demonstrated previously, 1,3-benzodioxole is the oddball in this series as its anomeric effect (O-CH_2-O interaction) becomes less suppressed in the excited state and thus results in a more puckered molecule.

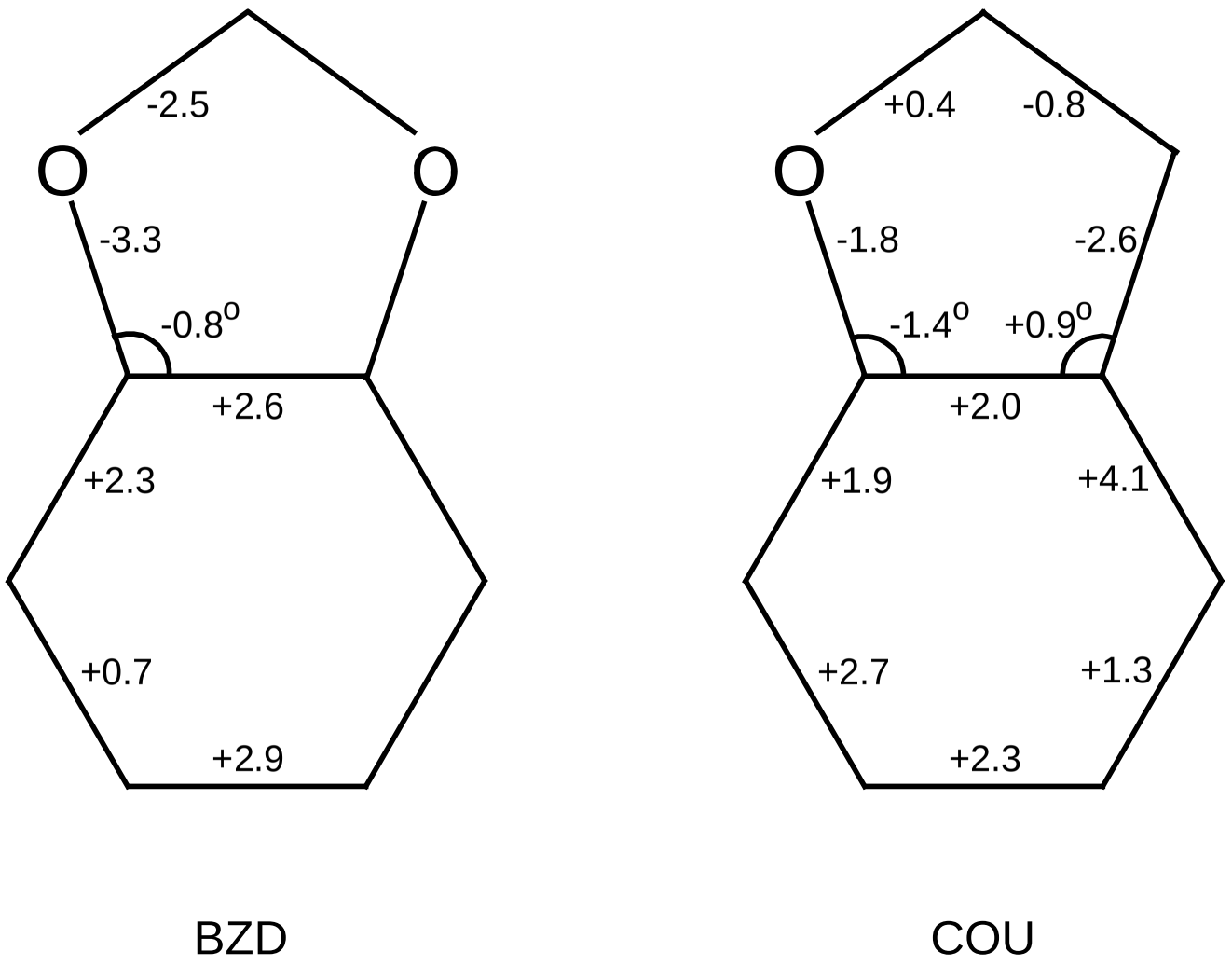

Figure 15. Calculated bond angle and bond length (pm) changes for coumaran arising from the $\pi \rightarrow \pi^*$ transition to the $S_1(\pi,\pi^*)$ states.

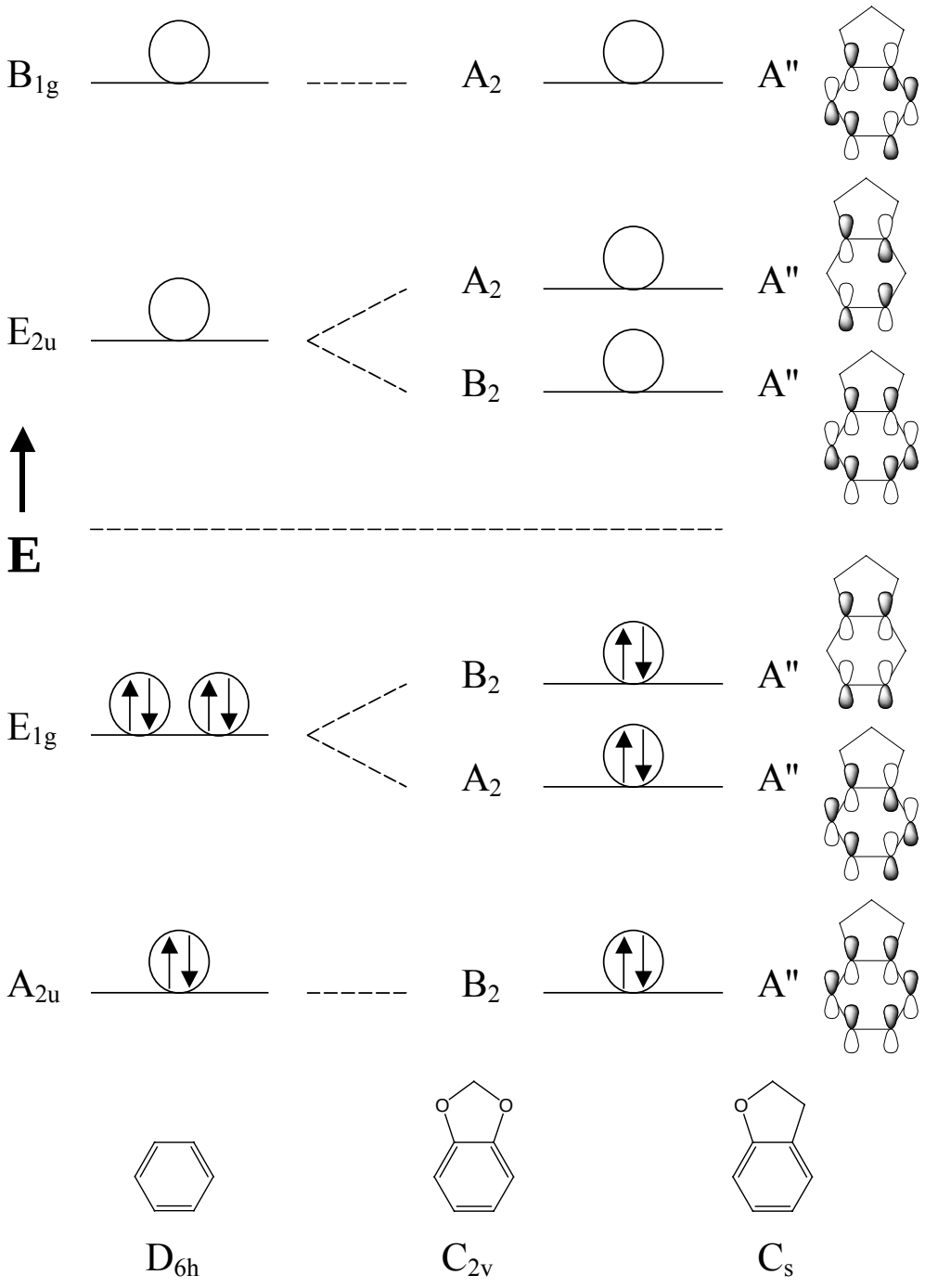

Figure 16. Qualitative molecular orbital diagram correlating the benzene π orbitals to a C_{2v} molecule such as 1,3-benzodioxole or to the C_s coumaran molecule. The signs of the atomic p orbitals are indicated by dark or light shading.

CHAPTER VI

VIBRATIONAL ASSIGNMENTS FOR COUMARAN IN ITS S_0 AND $S_1(\pi,\pi^*)$ STATES

INTRODUCTION

In Chapters IV and V the one-dimensional ring-puckering potential energy functions for the S_0 ground and $S_1(\pi,\pi^*)$ excited electronic states of coumaran (COU) have been determined. In S_0 state the barrier to planarity is 154 cm^{-1} and the dihedral angle for puckering is ± 25°. These results agree well with the millimeter wave spectra[4] values of 152 cm^{-1} and ± 23°, which were calculated based on the ground state splitting and inertial defect and a different type of potential function. In the $S_1(\pi,\pi^*)$ excited state coumaran is quasi-planar with a barrier to planarity of 34 cm^{-1} and with energy minima at puckering angles of ± 14°.

Although the fit of the observed energy levels and the calculated ones from the one-dimensional puckering potential function is good, there is evidence to show that the puckering (ν_{45}) and flapping (ν_{43}) modes have strong interaction. As more than seventy transitions from the S_0 vibrational levels to the $S_1(\pi,\pi^*)$ vibronic levels follow the C_s symmetry selection rules $A' \leftrightarrow A'$, $A'' \leftrightarrow A''$, and $A' \not\leftrightarrow A''$, however, there are three quantum states, two for S_0 and one for S_1, turn out to have anomalous symmetry

characteristics. These all occur in the ring-flapping vibrational excited state ($v_F = 1$), and thus indicate substantial coupling between the puckering and flapping vibrations. Moreover, the far-infrared spectra provide transitions corresponding to quantum jumps from the puckering levels to the flapping levels and also to several flapping-puckering combinational levels. Therefore, a two-dimensional analysis of the ring-puckering (ν_{45}) and ring-flapping (ν_{43}) motions is necessary to carry out for the coumaran molecule. Only preliminary results have been obtained so far and these are present in this chapter. At the same time, the complete vibrational assignments of coumaran for both the S_0 ground and the $S_1(\pi,\pi^*)$ excited electronic states based on the experimental spectra as well as the theoretical calculations have been made and will also be included in this chapter.

EXPERIMENTAL

The far-infrared spectra were recorded on a Bomem DA3.02 instrument using sampling techniques previously described.[2] The liquid and vapor-phase Raman spectra were collected with an Instruments SA Jobin Yvon U-1000 spectrometer, a Coherent Radiation Innova 20 argon ion laser operating at 514.5 nm, and a liquid nitrogen-cooled charge-coupled device (CCD) detector. The single vibronic level fluorescence spectra were recorded using a Continuum Sunlite OPO laser pumped by a Continuum Powerlite

9020 Nd:YAG laser and a FX-1 ultraviolet frequency doubling extension unit, as previously described.[28-32]

CALCULATIONS

Theoretical calculations were carried out using time-dependent density functional theory (TDDFT) at the B3LYP level and with the TZVP basis set in the TURBOMOLE V5-6 program package[39,40] for both S_0 and $S_1(\pi,\pi^*)$ states. These calculations were carried out by Dr. Ohyun Kwon in Samsung Advanced Institute of Technology, Korea. Gaussian 03[41] with B3LYP/6-311++G(d,p) basis set was also used for frequency calculations in the S_0 state. The scaling factors used were 0.985 for frequencies below 1700 cm^{-1} and 0.964 for frequencies in the 2900-3100 cm^{-1} region, based on previous work.[7,44,45]

MOLECULAR VIBRATIONS AND ASSIGNMENTS

As discussed in Chapter V, coumaran is a quasi-planar molecule with a small barrier to planarity. It possesses C_1 symmetry but can be considered to have perturbed C_s (planar structure) symmetry for the purpose of analyzing its vibrations. A planar coumaran molecule would have 45 vibrations distributing as

29A' + 16A".

The A' vibrations are the totally symmetric motions and they will produce infrared type A, B hybrids and Raman polarized bands. The A" vibrations are the out-of-plane motions and these will produce infrared type C bands and Raman depolarized bands.

Figure 17 shows the relative motions for the three lowest frequency out-of-plane ring vibrations of coumaran. These are the ring-puckering (ν_{45}), ring-twisting (ν_{44}), and ring-flapping (ν_{43}) vibrations, all of which are of A" symmetry in the C_s group. The twisting motion can also couple with the puckering motion, but this coupling is to a lesser extent than that between the puckering and flapping motions.

Figure 18 compares the liquid and vapor-phase Raman spectra of coumaran to the computed Raman spectrum from B3LYP/6-311++G(d,p) calculation in the 0-1700 cm^{-1} region with the scaling factor of 0.985. Figure 19 compares the vapor-phase Raman spectrum to the single vibronic level fluorescence spectrum shifted with respect to the 0_0^0 excitation at 34,965.9 cm^{-1}. In the vapor-phase Raman spectrum, all the sharp intense bands clearly correspond to the totally symmetric A' vibrations in C_s symmetry. As can be seen, the Raman spectrum can help to distinguish the fundamental bands in the SVLF spectrum. The SVLF spectrum with 0_0^0 excitation shows the $A' \leftrightarrow A'$ transitions involving the $v_P = 0$ A' level in S_1 state. For the A' fundamental vibrations the relative transition frequencies correspond exactly to the vibrational frequencies. However, for the A" fundamental vibrations, the fluorescence follows the C_s symmetry selection rule

$A' \leftrightarrow A'$ and thus goes to the A' levels that are the combination levels of one quantum puckering (A") and one quantum the corresponding A" fundamental vibrations. Therefore, the relative transition frequencies are about 3 cm^{-1} higher than the fundamental frequencies. Table 10 summaries the experimental and calculated frequencies as well as the vibrational assignments of coumaran in the S_0 state. Table 11 summaries those in the $S_1(\pi,\pi^*)$ excited state. Similarly, for the $A' \leftrightarrow A'$ transitions in FES and UV absorption spectra, the relative transition frequencies correspond exactly to the vibrational frequencies. For the $A'' \leftrightarrow A''$ transitions, however, since the excitation is originating from the $v_P = 1$ A" level, which is 3.1 cm^{-1} above the ground $v_P = 0$ level, the relative transition frequencies are all 3.1 cm^{-1} lower than the corresponding A" vibronic energy level.

TWO-DIMENSIONAL ANALYSIS

When analyzing the far-infrared spectra of coumaran in Chapter IV, Table 2 lists only the observed transitions for the pure puckering vibration. Transitions for the pure twisting and pure flapping vibrations as well as transitions corresponding to quantum jumps between the energy levels of different types of ring vibrations are also observed in the far-infrared spectra. Table 12 presents the full assignments of the far-infrared spectra for coumaran, again with primes indicating the puckering energy levels in the flapping

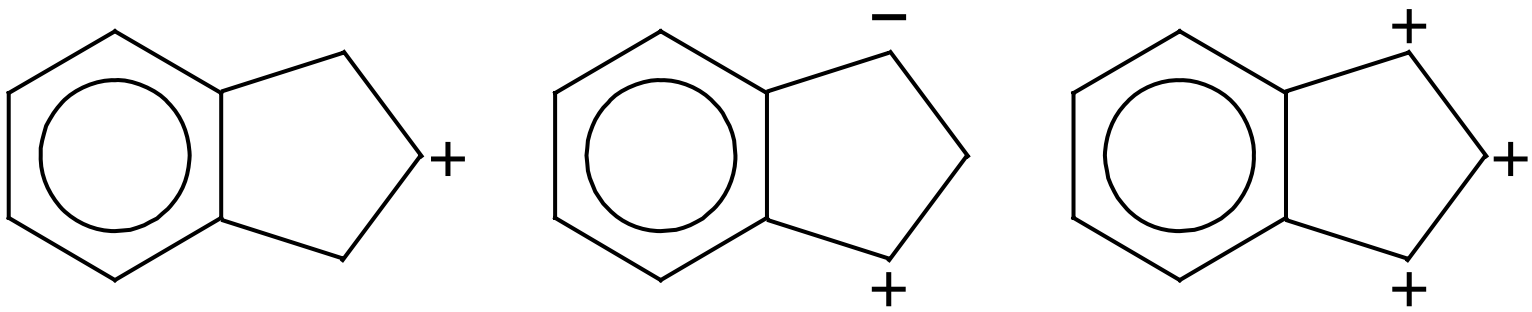

ring-puckering
(A")
ν_{45}

ring-twisting
(A")
ν_{44}

ring-flapping
(A")
ν_{43}

Figure 17. The relative motions for the three lowest frequency ring vibrations of coumaran.

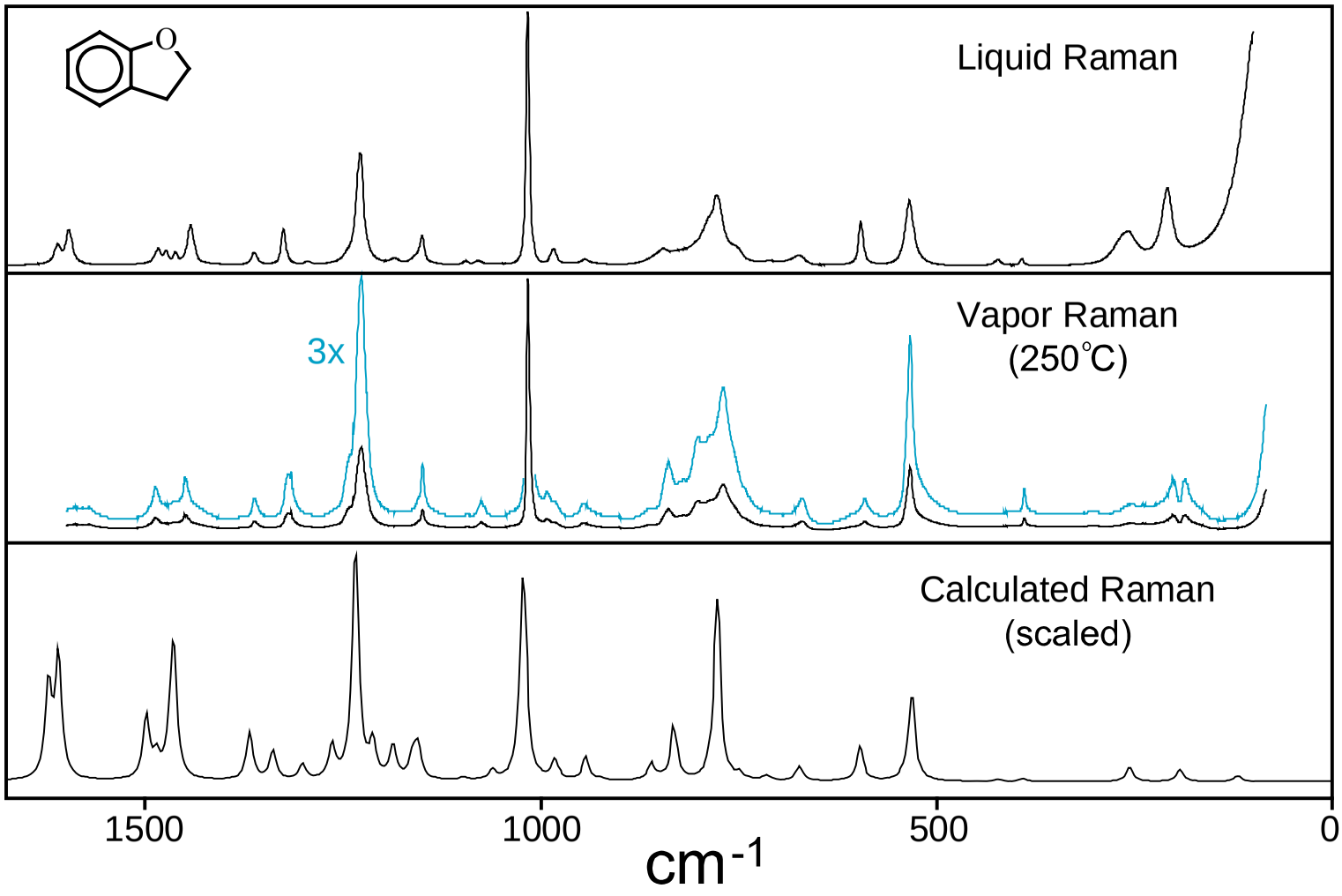

Figure 18. Liquid (top) and vapor (middle) phase Raman spectra of coumaran compared to the calculated DFT spectrum with scaled frequencies (bottom).

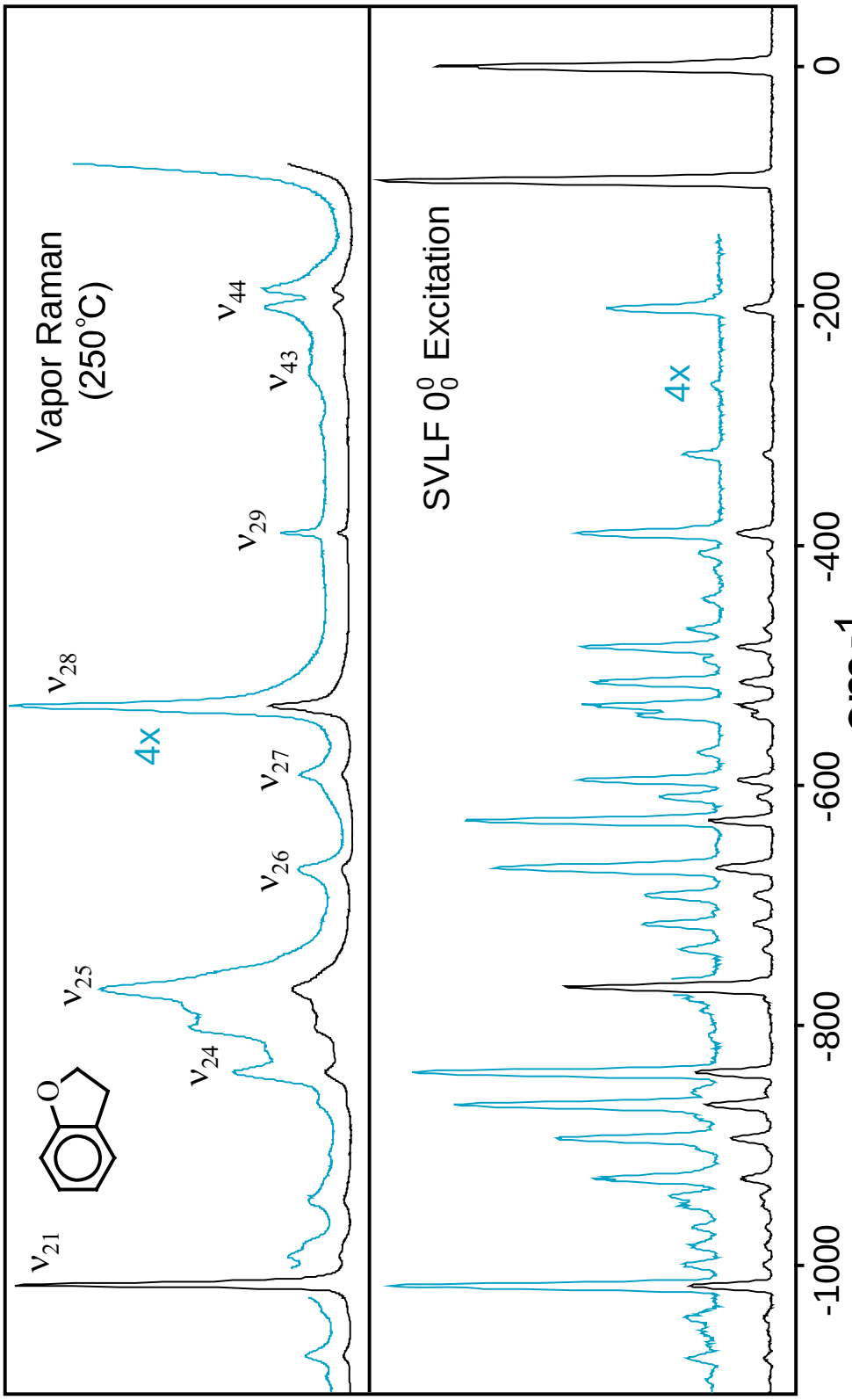

Figure 19. The vapor-phase Raman spectra (top) and single vibronic level fluorescence spectrum with the 0_0^0 excitation at 34,965.9 cm^{-1} (bottom) of coumaran.

TABLE 10: The Experimental (Raman and SVLF) and Calculated Frequencies (cm^{-1}) and Vibrational Assignments of Coumaran in the S_0 State.

Symmetry	ν		Approximate Description	Experimental			Calculated[a]		
C_s	C_s	C_1		Raman		0_0^0 SVLF	C_s[b]	C_1[b]	C_1[c]
A'(P)	1	1	C-H stretch	---		---	3082	3083	3086
	2	2	C-H stretch	---		---	3073	3073	3075
	3	3	C-H stretch	---		---	3056	3057	3060
	4	4	C-H stretch	---		---	3047	3048	3052
	5	7	CH_2 symmetric stretch	---		---	2947	2924	2925
	6	8	CH_2 symmetric stretch	---		---	2926	2914	2917
	7	9	benzene ring stretch	---		---	1622	1622	1623
	8	10	benzene ring stretch	---		---	1610	1610	1610
	9	11	CH_2 deformation	---		---	1503	1498	1504
	10	12	benzene ring stretch	1486	m	---	1490	1486	1490
	11	13	CH_2 deformation	---		---	1472	1471	1475
	12	14	benzene ring stretch	1450	m	---	1468	1464	1469
	13	15	CH_2 wag	1362	w	---	1370	1368	1374
	14	16	benzene ring stretch	1319	m	---	1338	1339	1338
	15	17	CH_2 wag	---		---	1300	1301	1305
	16	19	sat. ring C-C stretch	1127	s	---	1244	1234	1234
	17	20	sat. ring C-O stretch	---		---	1232	1212	1215
	18	22	C-H wag (ip)	---		---	1164	1162	1166
	19	23	C-H wag (ip)	1150	m	---	1156	1155	1159
	20	24	C-H wag (ip)	1094	vw	---	1100	1098	1101
	21	26	C-H wag (ip)	1016	vs	1017	1023	1022	1025

TABLE 10: Continued.

Symmetry	ν		Approximate Description	Experimental			Calculated[a]		
C_s	C_s	C_1		Raman		0_0^0 SVLF	C_s[b]	C_1[b]	C_1[c]
A'(P)	22	27	sat. ring O-C-C stretch	---		---	983.1	982.1	968.5
	23	29	sat. ring O-C-C stretch	945	w	---	943.0	943.1	919.5
	24	33	benzene ring deformation	838	m	839	846.8	832.0	832.7
	25	34	bridgehead C-C stretch	769	s,br	768	795.3	777.3	778.1
	26	37	ring deformation	670	m	668	700.9	673.4	680.4
	27	38	benzene ring deformation	591	m	595	598.6	597.1	597.5
	28	40	benzene ring deformation	533	s	533	533.0	531.4	534.1
	29	42	ring deformation	389	m	389	389.5	390.3	391.6
A"(D)	30	5	CH_2 antisym. stretch	---		---	2988	3004	3005
	31	6	CH_2 antisym. stretch	---		---	2950	2968	2971
	32	18	CH_2 twist	---		---	1230	1263	1268
	33	21	CH_2 twist	---		---	1190	1186	1191
	34	25	CH_2 rock	1075	w	---	1055	1061	1062
	35	28	C-H wag (op)	---		964-3[d]	947.8	958.8	942.5
	36	30	C-H wag (op)	---		---	919.6	924.7	908.8
	37	32	C-H wag (op)	---		---	813.2	851.1	844.1
	38	31	CH_2 rock	864	w	866-3[d]	845.7	860.6	862.1
	39	35	C-H wag (op)	---		---	744.6	748.7	743.1
	40	36	benzene ring bend (op)	---		---	681.6	715.2	642.3
	41	39	benzene ring twist (op)	---		513-3[d]	532.0	539.4	519.1
	42	41	benzene ring bend (op)	---		420-3[d]	417.4	423.5	417.5

TABLE 10: Continued.

Symmetry	ν		Approximate Description	Experimental		Calculated[a]		
C_s	C_s	C_1		Raman	0_0^0 SVLF	C_s[b]	C_1[b]	C_1[c]
A"(D)	43	43	sat. ring flap	250.7 w	---	234.6	256.2	255.8
	44	44	sat. ring twist	192.5 m	195-3[d]	188.9	192.8	193.1
	45	45	sat. ring pucker	---	---	*i*	119.4	126.4

Abbreviations: P, polarized; D, depolarized; ip, in-plane; op, out-of-plane; s, strong; m, medium; w, weak; v, very; br, broad.

[a] The scaling factors used are 0.985 for frequencies below 1700 cm^{-1} and 0.964 for frequencies in the 2900-3100 cm^{-1} region.

[b] Calculated using the B3LYP/6-311++G(d,p) basis set with GAUSSIAN 03.

[c] Calculated using the B3LYP/TZVP basis set with the TURBOMOLE V5-6 program package.

[d] For the A" vibrations, the fluorescence follows the symmetry selection rule A' ↔ A' and thus goes to the A' levels, which are the combination levels of one quantum puckering (A") and one quantum the corresponding A" vibrations. Therefore, the relative transition frequencies are about 3 cm^{-1} higher than the fundamental frequencies.

TABLE 11: The Experimental (FES and UV) and Calculated Frequencies (cm^{-1}) and Vibrational Assignments of Coumaran in the S_1 State.

Symmetry	ν		Approximate Description	Experimental		Calculated[a]
C_s	C_s	C_1		FES	UV	C_1[b]
A'(P)	1	1	C-H stretch	---	---	3235.3
	2	2	C-H stretch	---	---	3221.1
	3	3	C-H stretch	---	---	3204.9
	4	4	C-H stretch	---	---	3171.9
	5	7	CH_2 symmetric stretch	---	---	2961.9
	6	8	CH_2 symmetric stretch	---	---	2841.5
	7	9	benzene ring stretch	---	---	1520.3
	8	10	benzene ring stretch	---	---	1459.8
	9	11	CH_2 deformation	---	---	1504.2
	10	12	benzene ring stretch	---	---	1452.2
	11	13	CH_2 deformation	---	---	1481.9
	12	14	benzene ring stretch	---	---	1430.1
	13	15	CH_2 wag	---	---	1374.7
	14	16	benzene ring stretch	---	---	1423.6
	15	17	CH_2 wag	---	---	1297.8
	16	19	sat. ring C-C stretch	---	---	1257.8
	17	20	sat. ring C-O stretch	---	---	1172.4
	18	22	C-H wag (ip)	---	---	1235.5
	19	23	C-H wag (ip)	---	---	1165.6
	20	24	C-H wag (ip)	---	---	1071.1
	21	26	C-H wag (ip)	---	---	989.6

TABLE 11: Continued.

Symmetry	ν		Approximate Description	Experimental				Calculated[a]
C_s	C_s	C_1		FES		UV		C_1[b]
A'(P)	22	27	sat. ring O-C-C stretch	---		---		980.6
	23	29	sat. ring O-C-C stretch	---		---		933.0
	24	33	benzene ring deformation	---		---		780.9
	25	34	bridgehead C-C stretch	---		---		698.9
	26	37	ring deformation	583	m	583.5	vs	569.8
	27	38	benzene ring deformation	525	w	524.6	m	524.4
	28	40	benzene ring deformation	---		---		497.2
	29	42	ring deformation	365	m	364.9	w	382.9
A"(D)[c]	30	5	CH_2 antisym. stretch	---		---		3098.5
	31	6	CH_2 antisym. stretch	---		---		3050.3
	32	18	CH_2 twist	---		---		1214.3
	33	21	CH_2 twist	---		---		1159.5
	34	25	CH_2 rock	---		---		1032.3
	35	28	C-H wag (op)	---		---		868.9
	36	30	C-H wag (op)	---		---		862.5
	37	32	C-H wag (op)	---		---		677.6
	38	31	CH_2 rock	---		---		834.5
	39	35	C-H wag (op)	---		---		531.4
	40	36	benzene ring bend (op)	---		---		594.8
	41	39	benzene ring twist (op)	418+3	w	417.9+3.1	m	403.0
	42	41	benzene ring bend (op)	243+3	m	242.8+3.1	s	290.9

TABLE 11: Continued.

Symmetry	ν		Approximate Description	Experimental				Calculated[a]
C_s	C_s	C_1		FES		UV		C_1[b]
A"(D)[c]	43	43	sat. ring flap	177+3	m	177.8+3.1	m	234.2
	44	44	sat. ring twist	119+3	s	119.2+3.1	s	149.1
	45	45	sat. ring pucker	32+3	vs	31.9+3.1	vs	148.0
				(111)[d]	vs	(110.8)[d]	vs	

Abbreviations: P, polarized; D, depolarized; ip, in-plane; op, out-of-plane; s, strong; m, medium; w, weak; v, very.

[a] The scaling factors used are 0.985 for frequencies below 1700 cm^{-1} and 0.964 for frequencies in the 2900-3100 cm^{-1} region.

[b] Calculated using the B3LYP/TZVP basis set with the TURBOMOLE V5-6 program package.

[c] For the A" vibrations, the transitions are originating from the $v_P = 1$ A" level, therefore, the transition frequencies are all 3.1 cm^{-1} lower than the corresponding A" vibronic energy level.

[d] Overtone (A') transition frequencies are shown in parenthesis.

vibrationally excited state (v_F = 1) and double primes indicating those in the twisting vibrationally excited state (v_T = 1). The previous assignment[2] for the far-infrared spectra is also listed in Table 12 for comparison. There are altogether twelve puckering-flapping difference or summation bands observed in the far-infrared spectra, which indicate strong interactions between the puckering and flapping motions. Figure 20 shows the energy levels and transitions for the pure puckering and flapping bands as well as the puckering-flapping difference and summation bands for coumaran.

TABLE 12: The Far-IR and Inferred Frequencies (cm^{-1}) and Assignments for Coumaran.

Transition[a]	Far-infrared		Inferred[b]	Previous Assign.[c]
	Freq.	Int.		
3-1"	62.7	m	63.0	
3'-4'	68.6	m	68.6	
$3"-29_{1}45_{1}$	69.2	w	69.4	
3-4	70.1	s	70.3	5-6
3"-4"	71.4	s	71.4	5'-6'
$2'-42_{1}45_{1}$	74.0	m	74.1	
4"-5"	76.2	m	76.2	
4-5	76.7	s	76.3	6-7
4'-5'	77.8	m	77.8	6'-7'
2"-6	79.7	m	78.9	
?	82.9	m	---	
1"-5	83.5	s	83.6	7-8
?	84.4	s	---	
4-2"	85.1	m	85.3	7'-8'
5-6	87.9	s	87.9	3-4
1-2	91.7	m	91.4	2-4
1"-2"	92.5	vw	92.6	
6-7 / 0-2	95.0	m	94.5/95.0	3'-4'
0"-2"	96.0	w	95.3	
2-0"	97.4	vw	97.3	2'-4'
7-8	101.4	w	101.4	
8-9 / 2-4	106.7	w	106.7/107.3	4-6
$5-29_{1}$	111.1	w	111.1	
$6-29_{1}45_{2}$	117.8	w	117.5	
3-0'	119.8	w	119.9	
3-1'	123.8	vw	123.7	
2'-5"	124.9	m	124.7	3-5
1"-3"	127.8	s	128.7	1-2
1-3	128.4	s	128.4	0-2
1'-3'	129.7	w	130.3	
0"-3"	130.9	s	131.4	1-3
0-3	131.7	s	131.5	0-3
$2"-42_{1}45_{1}$	133.4	m	133.1	1'-2'
0'-3'	134.0	m	134.1	0'-2'

TABLE 12: Continued.

Transition[a]	Far-infrared		Inferred[b]	Previous Assign.[c]
	Freq.	Int.		
$1'-29_145_1$	136.9	m	137.4	0'-3'
4-2'	144.6	m	144.3	
3-5	146.3	m	146.6	5-7
3"-5"	147.8	m	147.6	5'-7'
2-0'	156.4	w	156.9	
$3"-29_145_2$	160.1	w	160.3	6-8
2-1'	160.8	vw	160.7	
4-6	163.7	w	164.2	6'-8'
5-7 / 4-3'	183.2	w	182.9/183.7	
2-5	183.9	vw	183.6	
0-0"	191.8	vvs,br	191.8	
3-2'	214.8	vw	214.6	
$1"-42_1$	221.8	m	222.0	
$0"-29_145_2$	232.5	w	232.1	
3-6	235.3	m	234.5	
?	243.1	m	---	0-0' / 1-1'
1-0'	248.1	m	248.3	3-3'
0-0' / 2-2'	251.4	s	251.4/251.6	5-5'
1-1'	252.1	w	252.1	6-6'
3-3'	253.9	w	254.0	
0-1'	254.8	m	255.2	4-4'
1"-4'	262.0	m	262.3	

Abbreviations: s, strong; m, medium; w, weak; v, very, br, broad.

[a] Primes indicate puckering transitions in the flapping vibrationally excited state ($v_F = 1$) and double primes indicate puckering transitions in the twisting vibrationally excited state ($v_T = 1$).

[b] Frequency values inferred from the energy level diagrams in Figure 11.

[c] From reference 2.

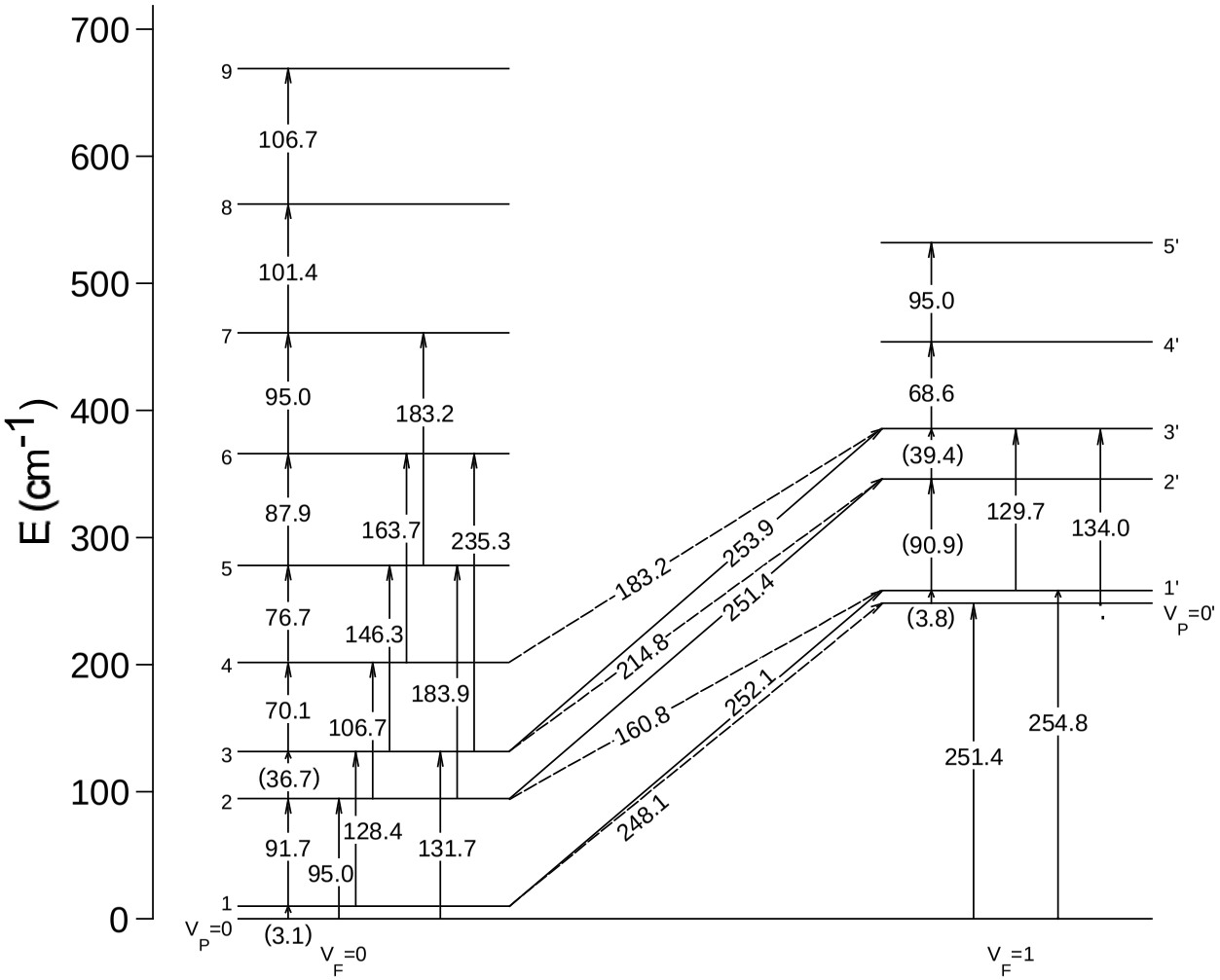

Figure 20. The energy levels and transitions for the pure puckering and pure flapping bands and the puckering-flapping difference and summation bands for coumaran.

CHAPTER VII

VIBRATIONAL FREQUENCIES AND STRUCTURE OF CYCLOPROPENONE FROM THEORETICAL CALCULATIONS*

INTRODUCTION

The preparation of the highly strained molecule cyclopropenone (CPO) was first reported in 1967 in solution[46] and then in pure form[47] in 1972 by the Breslow group. In 1974 the vibrational spectra of cyclopropenone and its d_2 isotopomer were published,[5] as was the normal coordinate analysis.[6] The microwave spectrum, from which the geometry of the molecule was determined, was reported in 1973.[48]

The infrared and Raman spectra reported for this molecule were recorded almost exclusively for the liquid and solid phases although two vapor-phase bands were observed for each isotopomer. An unusual feature of the spectra is the high value for the C=O stretch at 1883 cm^{-1} in the vapor-phase infrared spectrum, and this was initially interpreted as being due to a very strong C=O bond[49] since a value near 1700 cm^{-1} would be more typical. Similarly, the C=C stretch at 1483 cm^{-1} for the liquid-phase is quite far from an expected value of about 1600 cm^{-1} for the typical C=C stretch. In their 1974

---

*Reprinted with permission from "Vibrational Frequencies and Structure of Cyclopropenone from *Ab Initio* Calculations" by J. Yang, K. McCann, and J. Laane, 2004. *J. Mol. Struct.*, **695-696**, 339-344. 2004 by Elsevier B.V.

paper Brown *et al*.[5] reasoned that this must be due to a weak C=C stretch. The normal coordinate calculation,[6] carried out with limited symmetrized force constants by the same group, also argued that the C=C bond was weaker even though its bond distance differs little from that of cyclopropene. However, as part of the exercises for a course lectured by Jaan Laane,[50] it was found that the utilization of normal valued force constants for the C=O, C=C, and C-C stretches produced frequencies close to where they were experimentally observed. In other words, the unusual frequencies appear to arise from vibrational interactions rather than unusual force constants.

In this chapter, theoretical calculations are carried out to predict the structure and vibrational frequencies for both cyclopropenone and its d_2 isotopomer. In particular, the focus of this chapter is put on examining the A_1 vibrations ν_3, ν_4, and ν_5, which result from combinations of the C=O, C=C, and symmetric C-C stretching motions so that the origin of these unusual stretching frequencies can be found.

CALCULATIONS

Theoretical calculations were carried out using the Gaussian 98 package.[51] Both structure and the vibrational frequencies were calculated at the density functional (B3LYP) level of theory with three different basis sets: the cc-pVTZ (triple-zeta) basis set, the 6-311++G(d,p) basis set, and the 6-31G(d) basis set.

RESULTS

1) Molecular Structure

The molecule cyclopropenone is shown in Figure 21 along with the definition of its internal coordinates, which will be utilized later. Table 13 compares the experimentally determined structure[48] of cyclopropenone to those from several different theoretical calculations. The agreement can be seen to be good but certainly not perfect. Interestingly, the triple zeta calculation is in slightly poorer agreement with the experimental values than the smaller basis sets. Figure 22 shows the structure calculated from the triple zeta computation. Table 14 compares the experimental rotational constants[48] to those calculated for both isotopomers using two different basis sets. Again the agreement is good but not perfect.

2) Vibrational Frequencies

Table 15 and 16 present the calculated frequencies and intensities for three different computations and compare these to experimental values for cyclopropenone-d_0 and cyclopropenone-d_2, respectively. The calculations correspond to vapor-phase values, but only two vapor-phase frequencies were reported for each isotopomer and these differed from the liquid-phase values by an average of over 50 cm^{-1}. Hence, because of the large phase dependence of the experimental values, the agreements between observed and

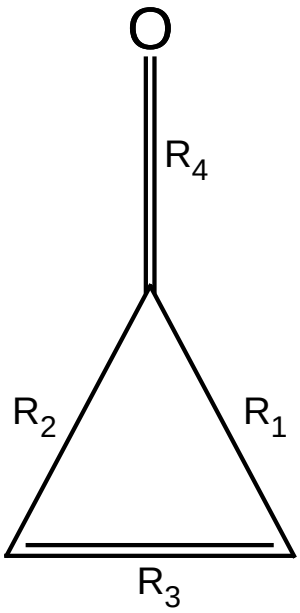

Figure 21. Cyclopropenone and its bond stretching internal coordinates.

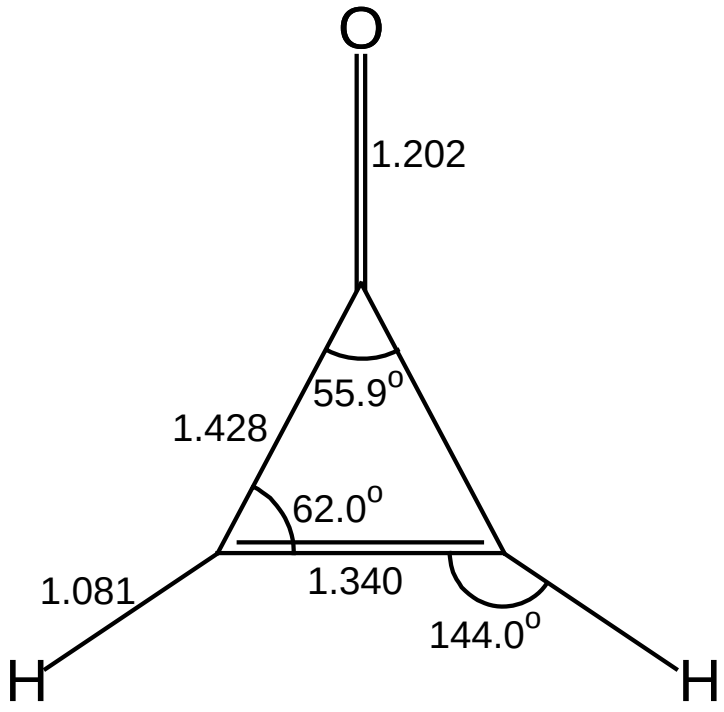

Figure 22. Calculated structure of cyclopropenone from B3LYP/cc-pVTZ calculation.

TABLE 13: Experimental and Calculated Structure (Bond Length in Å) of Cyclopropenone.

Parameter	Microwave[a]	B3LYP Calculations		
		cc-pVTZ	6-311++G(d,p)	6-31G(d)
C=O	1.212	1.202	1.203	1.207
C-C	1.412	1.428	1.431	1.436
C=C	1.302	1.340	1.344	1.346
C-H	1.097	1.081	1.083	1.086
$\angle HC_2C_3$	144.92°	144.00°	144.18°	144.14°
$\angle C_2C_3C_1$	62.55°	62.03°	61.99°	62.06°
$\angle C_2C_1C_3$	54.90°	55.94°	56.02°	55.88°

[a] From Reference 48.

TABLE 14: Experimental and Calculated Rotational Constants for Cyclopropenone and Cyclopropenone-d_2.

Constant		Microwave[a] (MHz)	B3LYP Calculations (MHz)	
			cc-pVTZ	6-311++G(d,p)
CPO-d_0	A	32046.0	32447.4	32228.2
	B	7825.0	7852.9	7826.4
	C	6280.7	6322.7	6297.2
CPO-d_2	A	24538.9	24805.6	24633.2
	B	7254.9	7276.8	7253.8
	C	5591.8	5626.3	5603.7

[a] From Reference 48.

TABLE 15: Observed and Calculated Frequencies (cm^{-1}), Intensities, and Scaling Factors for Cyclopropenone.

	ν	Approximate Description[b]	Observed[a]					B3LYP Calculations				
			IR			Raman		cc-pVTZ			6-311++G(d,p)	6-31G(d)
			Liquid[c]		Vapor	Liquid		Freq.	SF[d]	Int.[e]	Freq.	Freq.
A_1	1	C-H sym. stretch	3088	s	---	3100	160	3216	0.963	(1, 1000)	3216	3241
	2	C=O stretch	1856	vs	1883	1840	10	1933	0.952	(1000, 70)	1924	1964
	3	C=C stretch	1467	s	---	1480	1000	1564	0.948	(16, 180)	1558	1582
	4	C-C sym. stretch	1046	w,b	---	1026	180	1045	0.982	(7, 48)	1040	1054
	5	C-H wag (ip)	886	m	---	855	240	855	0.998	(0.2, 66)	852	861
A_2	6	C-H wag (op)	---	---	---	---	---	989	---	(0, 0.002)	981	980
B_1	7	C-H wag (op)	788	s	742	---	---	767	1.027	(82, 2)	764	760
	8	C=O wag (op)	500	m	---	---	---	473	1.042	(19, 2)	470	470
B_2	9	C-H antisym. stretch	3062	s	---	3069	80	3182	0.964	(3, 594)	3182	3208
	10	C-C antisym. stretch	1178	m	---	1163	27	1156	1.004	(23, 3)	1146	1160
	11	C-H wag (ip)	904	m,b	---	~900	50	823	1.084	(56, 39)	823	822
	12	C=O wag (ip)	536	w	---	528	230	525	1.008	(0.5, 49)	523	524

[a] From Reference 5.

[b] ip, in-plane; op, out-of-plane.

[c] For intensities: s, strong; m, medium; w, weak; v, very; b, broad.

[d] Scaling factor.

[e] Relative intensities (IR, Raman).

TABLE 16: Observed and Calculated Frequencies (cm^{-1}), Intensities, and Scaling Factors for Cyclopropenone-d_2.

	ν	Approximate Description[b]	Observed[a]					B3LYP Calculations				
			IR			Raman		cc-pVTZ			6-311++G(d,p)	6-31G(d)
			Liquid[c]		Vapor	Liquid		Freq.	SF[d]	Int.[e]	Freq.	Freq.
A_1	1	C-D sym. stretch	2392	s	---	2392	130	2444	0.979	(25, 1000)	2445	2463
	2	C=O stretch	1780	vs	1886	1780	19	1918	0.928	(1000, 217)	1908	1949
	3	C=C stretch	1409	s	---	1409	950	1484	0.949	(6, 699)	1477	1500
	4	C-C sym. stretch	969	w	---	967	1000	986	0.982	(5, 252)	984	992
	5	C-D wag (ip)	658	m	---	656	130	645	1.019	(1, 75)	641	652
A_2	6	C-D wag (op)	---	---	---	---	---	800	---	(0, 9)	793	793
B_1	7	C-D wag (op)	697	s	679	---	---	700	0.996	(39, 0.4)	695	695
	8	C=O wag (op)	409	w	---	---	---	387	1.057	(15, 1)	386	384
B_2	9	C-D antisym. stretch	2288	s	---	2292	90	2344	0.977	(2, 821)	2345	2363
	10	C-C antisym. stretch	1074	w,b	---	1078	130	1044	1.031	(2, 70)	1039	1051
	11	C-D wag (ip)	786	s	---	788	65	755	1.042	(45, 32)	752	753
	12	C=O wag (ip)	486	m	---	478	400	464	1.039	(1, 144)	462	464

[a] From Reference 5.

[b] ip, in-plane; op, out-of-plane.

[c] For intensities: s, strong; m, medium; w, weak; v, very; b, broad.

[d] Scaling factor.

[e] Relative intensities (IR, Raman).

calculated values are not expected to be very good. Table 15 and 16 also list the scaling factors for each vibration. The typical scaling factors are 0.964 for C-H stretches and 0.985 for lower frequency vibrations.[7,44,45] As can be seen, the liquid phase frequencies can require scaling factors in the 0.948 to 1.084 range. The latter value for the C-H in-plane wag (B_2) suggests in fact that this particular assignment may be in error.

Table 15 and 16 also compare the relative calculated intensities to the observed magnitudes. Although these tend to agree qualitatively, the quantitative agreement is not good. For one thing, the experimental values have not been corrected for instrumental factors. Secondly, calculated intensities are always much more sensitive than frequencies to the potential energy surface of the molecule. Nonetheless, the calculated two most intense bands for the infrared spectrum of cyclopropenone-d_0 at 1840 and 788 cm^{-1} (1883 and 742 cm^{-1} in the vapor) are indeed the two strongest in the observed spectrum. In the Raman spectrum, aside from the C-H stretching modes which are calculated to be extremely intense, the strongest bands observed at 1483, 853, and 529 cm^{-1} are all also calculated to be among the strongest. However, a medium band observed at 1026 cm^{-1} is calculated to have negligible intensity for the infrared spectrum.

3) Characterization of the A_1 Stretching Modes

The unusual frequencies for the A_1 stretching modes have been of considerable

interest. The triple zeta calculation is utilized to examine the nature of the 1840, 1483, and 1026 cm^{-1} modes. Unlike the conclusion in the normal coordinate calculation by Tuazan *et al*.[6], in this work the C-H in-plane wag is found to contribute primarily to the 853 cm^{-1} vibration, although there is some mixing with the 1026 cm^{-1} vibration. Hence, the three higher frequency bands result mostly from the C=O, C=C, and symmetric C-C stretching modes. Based on the computed vectors and only considering the stretching motions, the vibrations can be described as the following

$$\nu_2(1933\ \mathrm{cm}^{-1}) = 0.49(\Delta R_1 + \Delta R_2) + 0.06\Delta R_3 - 0.72\Delta R_4, \quad (7.1)$$

$$\nu_3(1564\ \mathrm{cm}^{-1}) = 0.19(\Delta R_1 + \Delta R_2) + 0.96\Delta R_3 + 0.10\Delta R_4, \quad (7.2)$$

and

$$\nu_4(1045\ \mathrm{cm}^{-1}) = 0.63(\Delta R_1 + \Delta R_2) - 0.06\Delta R_3 + 0.44\Delta R_4. \quad (7.3)$$

Figure 23 shows the vector diagrams for these skeletal motions. Based on the result above, the contribution of each type of stretching motion to each of the three vibrations can be calculated and these results are shown in Table 17 and 18, where they are compared to the conclusions from the referred normal coordinate calculation. Similar calculations were carried out for the cyclopropenone-d_2 molecule and these are shown below

$$\nu_2(1917\ \mathrm{cm}^{-1}) = 0.48(\Delta R_1 + \Delta R_2) - 0.04\Delta R_3 - 0.74\Delta R_4, \quad (7.4)$$

$$\nu_3(1483\ \mathrm{cm}^{-1}) = 0.19(\Delta R_1 + \Delta R_2) + 0.96\Delta R_3 + 0.05\Delta R_4, \quad (7.5)$$

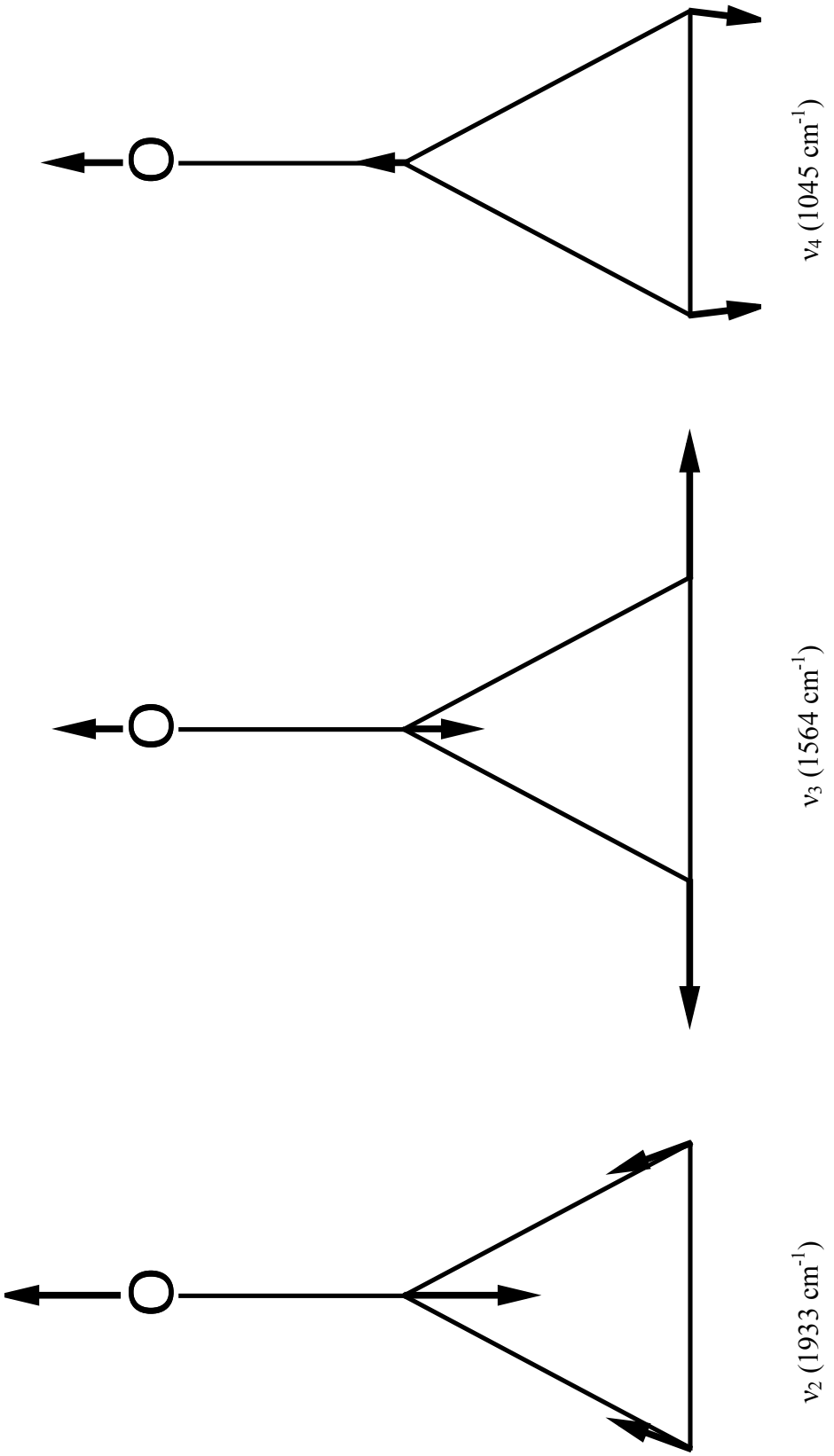

Figure 23. Vector diagrams for the A_1 stretching modes of cyclopropenone.

TABLE 17: Contribution of the A_1 Skeletal Modes to the Three Vibrations ν_2, ν_3, and ν_4 of Cyclopropenone.

Motion	This Work			From Ref. 6		
	ν_2	ν_3	ν_4	ν_2	ν_3	ν_4
C=O stretch	0.68	0.01	0.33	0.48	0.16	0.16
C=C stretch	0.004	0.95	0.006	0.07	0.78	0.00
C-C sym. stretch	0.32	0.04	0.67	0.51	0.00	0.16

TABLE 18: Contribution of the A_1 Skeletal Modes to the Three Vibrations ν_2, ν_3, and ν_4 of Cyclopropenone-d_2.

Motion	This Work			From Ref. 6		
	ν_2	ν_3	ν_4	ν_2	ν_3	ν_4
C=O stretch	0.70	0.003	0.21	0.56	0.08	0.32
C=C stretch	0.002	0.96	0.03	0.00	0.78	0.04
C-C sym. stretch	0.30	0.04	0.76	0.44	0.00	0.42

and

$$\nu_4(986\ \mathrm{cm}^{-1}) = 0.66(\Delta R_1 + \Delta R_2) - 0.13\Delta R_3 + 0.35\Delta R_4\,. \qquad (7.6)$$

There is general agreement with the normal coordinate calculation[6] that ν_2, ν_3, and ν_4 modes are primarily the C=O, C=C, and C-C stretches, respectively. However, since the normal coordinate calculation arbitrarily sets several interaction constants to zero, the representation in this work is more accurate. The calculations show that the high C=O stretching band results from interactions with the C-C symmetric stretch while the low C=C stretch results from a small interaction with the C-C stretching. The earlier force constant calculation ascribed the 1483 cm^{-1} ν_3 band to C=O and C=C interactions with essentially no C-C stretching. The ν_4 vibration involves the interaction between both C-C and C=O stretches, and this is also the conclusion in the previous work. However, the force constant calculation concluded that the C-H wagging also contributed to ν_4.

DISCUSSION

As compared to some of the previous studies,[44,45] the density functional calculations for cyclopropenone do a poorer job of matching the observed frequencies. This is likely due to the fact that the observed values correspond to the liquid phase whereas the computations are for individual non-interacting molecules. The phase dependence of the bands has been reported to be large[5] as vapor-phase bands at 1883 and 742 cm^{-1} shift to

1840 and 788 cm^{-1}, respectively, for the liquid.

The computations do a fairly good job of predicting the bond distances and angles as compared to the microwave work.[48] However, discrepancies up to 0.038 Å and 1.04° are present.

The primary result of this chapter is to show that the unusual A_1 stretching frequencies do not result from unusual bonding forces. Rather, they occur from coupling of the C=O, C=C, and C-C stretches. The band at 1840 cm^{-1} is due to the C=O stretch (68%) mixed with C-C stretching (32%) while the band at 1483 cm^{-1} results from C=C (95%) and C-C (4%) coupling. The 1026 cm^{-1} band is 67% C-C and 33% C=O.

CHAPTER VIII

RAMAN SPECTRUM, THEORETICAL CALCULATIONS, AND STRUCTURE OF 3,7-DIOXABICYCLO[3.3.0]OCT-1,5-ENE*

INTRODUCTION

The vibrational spectra and theoretical calculations for bicyclo[3.3.0]oct-1,5-ene (BCO) were previously reported in 2004.[7] The BCO molecule is structurally interesting since the two five-member rings can pucker in either the same or opposite directions, producing either *cis* (C_{2v}) or *trans* (C_{2h}) structures. Because the barriers to inversion of BCO are small, the vibrational spectra can be described quite well on the basis of a planar (D_{2h}) structure. Nonetheless, the spectra and theoretical calculations both show the *cis* C_{2v} conformation to be the lowest energy form. The C_{2h} *trans* form is slightly higher in energy but still about 1 kcal/mole more stable than the planar structure.

The ring-puckering spectra of BCO are expected to be very complicated, and because the vibrations do not have much of dipole moment changes, they are expected to be weak.[7,8] The molecule 3,7-dioxabicyclo[3.3.0]oct-1,5-ene (DOBO), on the other hand, will have a larger dipole moment change for the in-phase puckering vibration and its

---

*Reprinted with permission from "Synthesis, Raman Spectrum, *Ab Initio* Calculations, and Structure of 3,7-dioxabicyclo[3.3.0]oct-1,5-ene" by C. Mlynek, H. Hopf, J. Yang, and J. Laane, 2005. *J. Mol. Struct.*, **742**, 161-164. 2005 by Elsevier B.V.

spectra should be simpler as the planar form should be the most stable form. This chapter will present the study of the vibrational spectrum, structure, and the nature of the ring-puckering motions of the DOBO molecule.

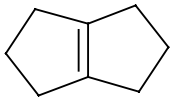

BCO

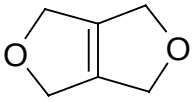

DOBO

At this moment, only 15 mg of DOBO were prepared and this only allowed its vapor-phase Raman spectrum to be recorded. Because of the small amount of sample, no other spectra were recorded. Together with theoretical calculations, the Raman spectrum was used to determine the symmetry and structure of this molecule.

EXPERIMENTAL

The 3,7-dioxabicyclo[3.3.0]oct-1,5-ene (DOBO) compound was synthesized in small quantities (~ 15 mg) by Mlynek and Hopf in Technical University of Braunschweig, Germany, and has been shown to be analytically pure by NMR and mass spectra.[52] The vapor-phase Raman spectra of DOBO at a temperature of 250 ^{o}C were recorded using an Instruments SA Jobin Yvon U-1000 spectrometer and a Coherent Radiation Innova 20 argon ion laser with excitation at 514.5 nm and 4 W laser power. A liquid-nitrogen cooled charge-coupled device (CCD) was used as the detector. The spectral resolution was 0.7 cm^{-1}. The sample was contained in a thermostatically

controlled high-temperature Raman cell as previously described.[24,25] The sample pressure was about 700 Torr.

CALCULATIONS

Theoretical calculations were carried out using the GAUSSIAN 03 package[41] at both the Moller-Plesset second-order perturbation (MP2) and the density functional (B3LYP) levels of theory with various basis sets. Energies and structural parameters were calculated using the MP2 method with the cc-pVTZ (triple zeta) basis set, while the vibrational frequencies along with both the infrared and Raman intensities were obtained with the density functional (B3LYP) theory and the 6-311++G(d,p) basis set. The frequency scaling factors are 0.964 for the 2800-3000 cm^{-1} region and 0.985 for the region below 1800 cm^{-1}, based on previous work.[7,44,45]

RESULTS AND DISCUSSION

Figure 24 shows the vapor-phase Raman spectrum of DOBO recorded at 250 °C. In this figure, the sharp, more intense bands all correspond to the totally symmetric A_g vibrations in D_{2h} symmetry. The broader band types correspond to B_{1g}, B_{2g}, and B_{3g} modes. All other vibrations are Raman inactive. Due to lack of sample, no infrared spectra were recorded and thus the frequencies for the infrared active ungerade modes

were not determined experimentally. Density functional theory (B3LYP) with the 6-311++G(d,p) basis set was used to calculate the Raman spectrum of this molecule. Figure 24 also compares the calculated spectrum to the experimental one. The computed spectrum assumes Lorentzian band shapes and therefore makes no attempt to predict the vapor-phase band types. The frequency agreement between the recorded spectrum and calculated spectrum is excellent. The intensity agreement is fairly good but certainly not close to perfect. Table 19 lists the vapor-phase Raman frequencies for DOBO and compares these to the BCO values. The calculated vibrational frequencies and Raman intensities are also listed. The observed and calculated frequencies agree on average within 9 cm^{-1}.

Table 20 lists the Raman inactive vibrations and their DFT calculated frequencies for DOBO. These are also compared to the experimental values of BCO. The frequencies are fairly similar except that the ring modes for DOBO are higher since C-O bond stretching force constants are greater than those for C-C bonds. No experimental data for the infrared active vibrations are shown since there was not enough sample to record the infrared spectra.

Figure 25 shows the optimized structure for DOBO from the MP2/cc-pVTZ (triple zeta) calculation. The skeletal atoms, unlike the case for BCO, which has puckered rings, all lie within a plane resulting in D_{2h} symmetry. The recorded Raman spectrum, which

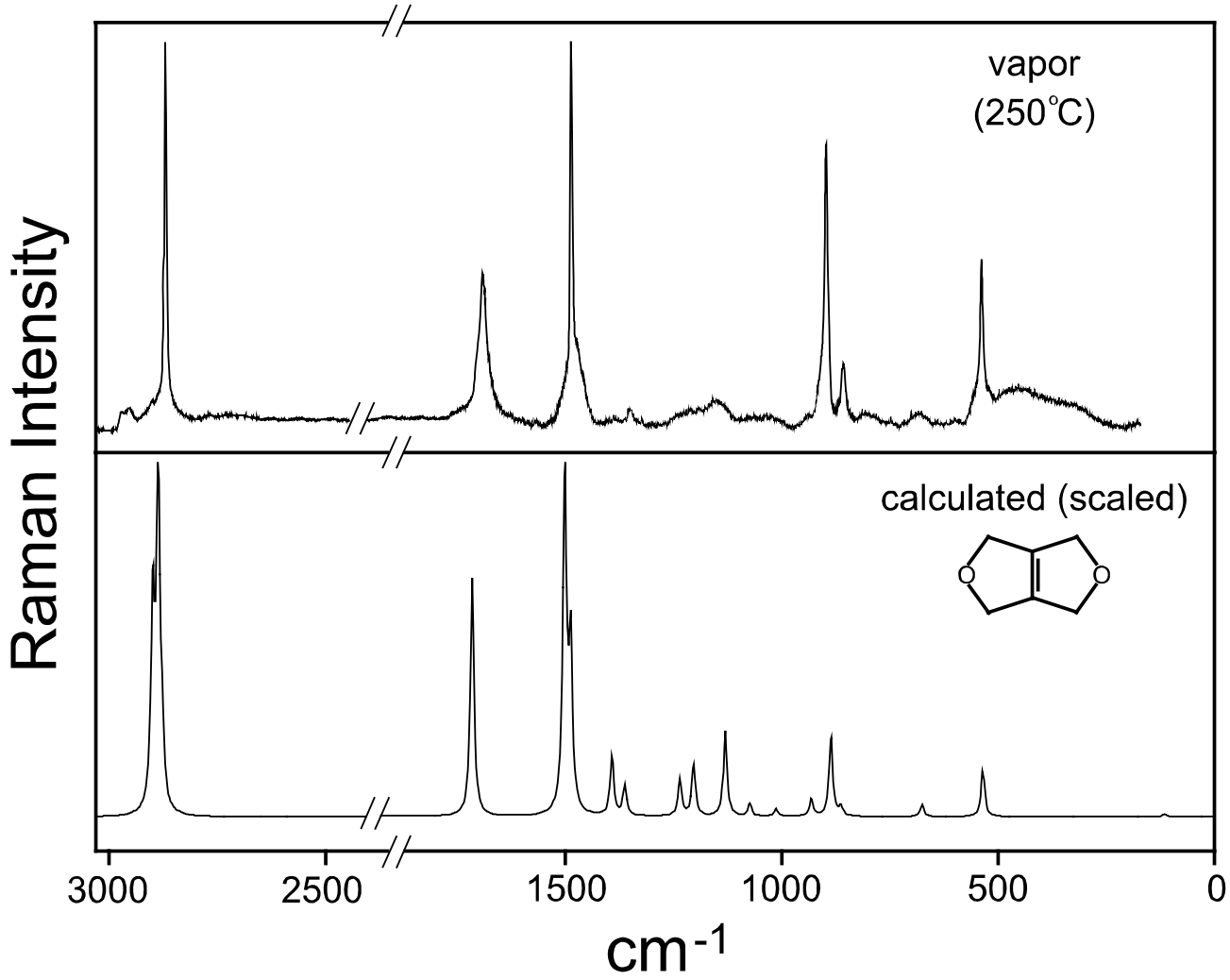

Figure 24. Vapor-phase Raman spectrum of 3,7-dioxabicyclo[3.3.0]oct-1,5-ene at 250 °C (top) and calculated Raman spectrum using the B3LYP/6-311++G(d,p) basis set with appropriate scaling factors (bottom).

TABLE 19: Vibrational Assignments (cm^{-1}) for the Raman Active Gerade Modes of 3,7-Dioxabicyclo[3.3.0]oct-1,5-ene (DOBO).

Symmetry D_{2h}	ν	Description	DOBO Vapor Raman		BCO Vapor Raman[a]		DFT[b] (D_{2h})	
			Freq.	Int.	Freq.	Int.	Freq.[c]	Int.
A_g	1	CH_2 sym. stretch (ip, ip')	2870	(100)	2857	(100)	2887	(100)
(R: P)	2	C=C stretch	1690	(4)	1677	(27)	1716	(5)
	3	CH_2 deformation (ip, ip')	1486	(10)	1473	(17)	1501	(8)
	4	CH_2 wag (ip, op')	1350	w	1287	(5)	1363	(0.7)
	5	ring stretch	897	(7)	889	(22)	887	(2)
	6	ring breath (ip')	857	(2)	852	(14)	863	(0.2)
	7	ring bend (ip, ip')	537	(4)	522	(7)	535	(1)
B_{1g}	8	CH_2 sym. stretch (op, op')	(2870)[d]	---	(2857)[d]	---	2877	(18)
(R: D)	9	CH_2 deformation (op, op')	1469 sh	(4)	---	---	1488	(4)
	10	CH_2 wag (op, ip')	1385	vw	---	---	1392	(1)
	11	ring stretch	1237	(1)	---	---	1235	(0.8)
	12	ring stretch	1018	w	968	vw	1013	(0.2)
	13	skeletal bend (op, op')	683	(1)	676	vw	676	(0.3)
B_{2g}	14	CH_2 antisym. stretch (ip, op')	2902	(5)	2954	(42)	2900	(10)
(R: D)	15	CH_2 twist (ip, ip')	1148	(2)	---	---	1130	(2)
	16	CH_2 rock (ip, op')	941	w	---	---	932	(0.4)
	17	ring pucker (op')	---	---	---	---	115	(0.1)
B_{3g}	18	CH_2 antisym. stretch (op, ip')	2886	(5)	2874	vw	2899	(57)
(R: D)	19	CH_2 twist (op, op')	1201	(1)	---	---	1203	(1)
	20	CH_2 rock (op, ip')	1071	vw	---	---	1074	(0.3)
	21	ring twist (ip')	450	(2)	---	---	449	(0.0)

TABLE 19: Continued.

Abbreviations: ip, in-phase; op, out-of-phase; w, weak; v, very; sh, should; R, Raman; P, polarized; D, depolarized.

[a] From Reference 7.

[b] Calculated using the B3LYP/6-311++G(d,p) basis set.

[c] Frequencies scaled with a scaling factor of 0.985 for frequencies less than 1800 cm^{-1} and 0.964 for frequencies in the 2800-3000 cm^{-1}.

[d] Frequencies used twice.

TABLE 20: Calculated Vibrational Frequencies (cm^{-1}) for the Ungerade Modes of 3,7-Dioxabicyclo[3.3.0]oct-1,5-ene (DOBO) Compared to the Experimental Frequencies (cm^{-1}) for Those of Bicyclo[3.3.0]oct-1,5-ene (BCO).

Symmetry D_{2h}	ν	Description	B3LYP/6-311++G(d,p)			
			DOBO (D_{2h})		BCO (C_{2v})[a]	
			Freq.[b]	Int.[c]	Freq.	Int.
A_u	22	CH_2 antisym. stretch (op, op')	2898	(0)	2901	(0.03)
	23	CH_2 twist (op, ip')	1189	(0)	1222	(0)
	24	CH_2 rock (op, op')	999	(0)	866	(0)
	25	ring twist (op')	209	(0)	194	(0)
B_{1u}	26	CH_2 antisym. stretch (ip, ip')	2901	(54)	2896	(0.43)
	27	CH_2 twist (ip, op')	1172	(1.6)	1212	(2.1)
	28	CH_2 rock (ip, ip')	1025	(2.8)	1073	(1.9)
	29	ring flap (ip')	166	(0.78)	229	(4.7)
	30	ring pucker (ip')	100	(8.7)	112	(0.01)
B_{2u}	31	CH_2 sym. stretch (op, ip')	2883	(100)	2859	(100)
	32	CH_2 deformation (op, ip')	1493	(0.47)	1465	(1.7)
	33	CH_2 wag (op, op')	1311	(2.1)	1309	(1.1)
	34	ring stretch	1069	(31)	1005	(0.43)
	35	ring stretch	1008	(27)	971	(0.08)
	36	skeletal bend (op, ip')	367	(0.61)	362	(1.4)
B_{3u}	37	CH_2 sym. stretch (ip, op')	2881	(8.2)	2855	(14)
	38	CH_2 deformation (ip, op')	1496	(0.57)	1455	(0.62)
	39	CH_2 wag (ip, ip')	1375	(8.4)	1313	(0.45)

TABLE 20: Continued.

Symmetry D_{2h}	ν	Description	B3LYP/6-311++G(d,p)			
			DOBO (D_{2h})		BCO (C_{2v})[a]	
			Freq.[b]	Int.[c]	Freq.	Int.
B_{3u}	40	ring stretch	1211	(1.0)	1162	(0.07)
	41	ring breath (op')	864	(20)	878	(0.44)
	42	ring bend (ip, op')	785	(7.7)	630	(0.03)

Abbreviations: ip, in-phase; op, out-of-phase.

[a] From Reference 7.

[b] Frequencies scaled with a scaling factor of 0.985 for frequencies less than 1800 cm^{-1} and 0.964 for frequencies in the 2800-3000 cm^{-1}.

[c] Calculated relative infrared intensity in parenthesis.

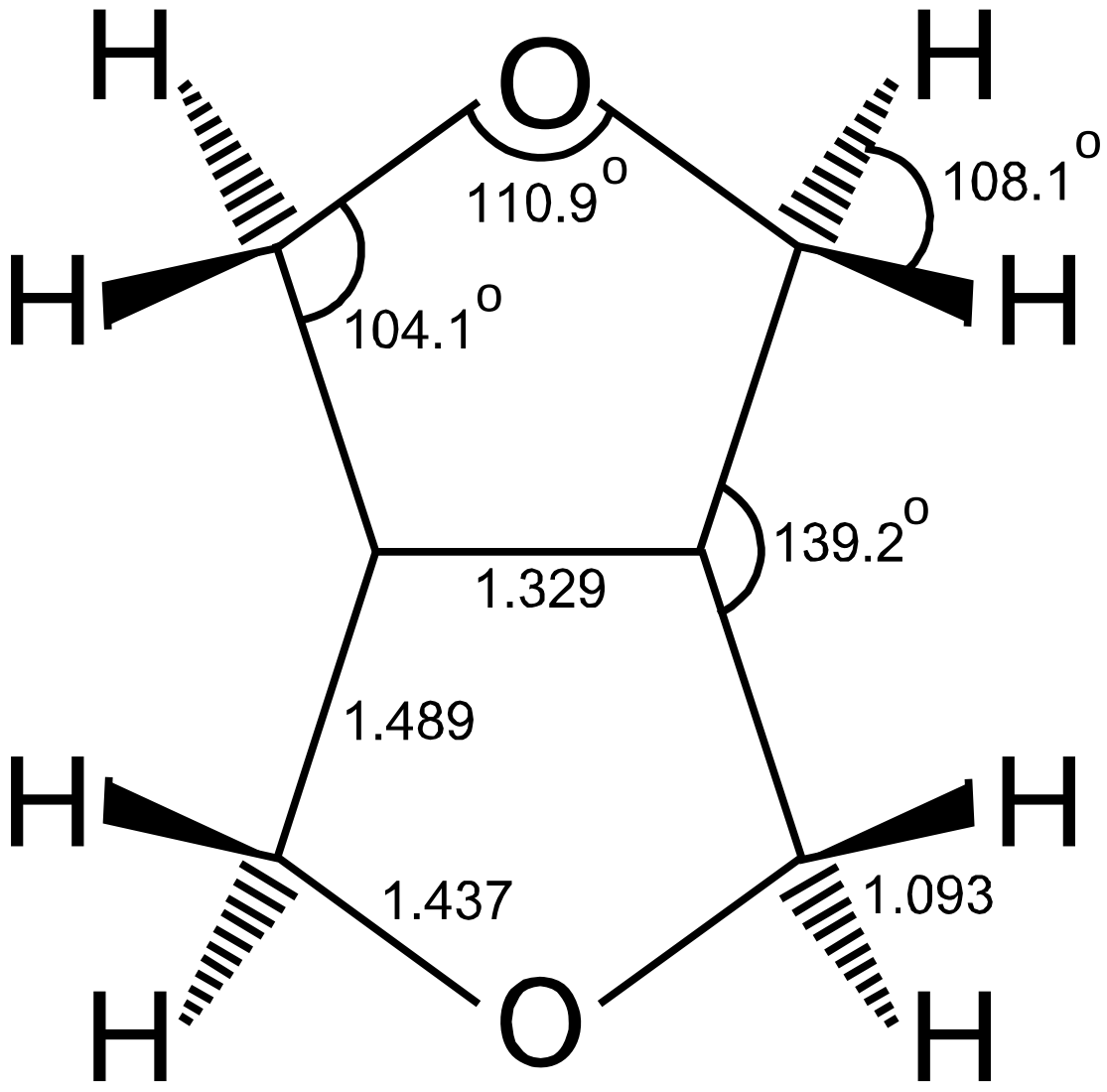

Figure 25. Structure of 3,7-dioxabicyclo[3.3.0]oct-1,5-ene from the MP2/cc-pVTZ calculation.

shows only the gerade vibrations, provides further evidence that the molecule has D_{2h} symmetry with a center of symmetry.

CONCLUSIONS

The vapor-phase Raman spectrum of DOBO presented in this chapter is in good agreement with the calculated spectrum. The observed bands in the Raman spectrum all correspond to the gerade modes, and this further verifies the molecular structure of DOBO. Both Raman spectrum and theoretical calculations show that both rings for this bicyclic molecule are planar.

CHAPTER IX

VIBRATIONAL SPECTRA AND DFT CALCULATIONS OF TETRALIN AND 1,4-BENZODIOXAN*

INTRODUCTION

In the process of analyzing the low-frequency modes of non-rigid molecules to determine the vibrational potential energy surfaces in their electronic ground and excited states,[31,53-55] it is necessary to assign the vibrational frequencies for many of the other vibrations in order to distinguish them from the quantum states of these low-frequency, large-amplitude motions. In Chapter IV, V, and VI the one-dimensional potential energy curves for the puckering vibration and the two-dimensional potential energy surfaces for the puckering and flapping modes of coumaran have been presented. The results for other indan family molecules such as indan,[30] phthalan,[33-35] and 1,3-benzodioxole[32,36] have also been previously reported. This work is now being extended to molecules with a six-membered ring attached to a benzene ring. Two of these molecules are 1,2,3,4-tetrahydronaphthalene (TET), also called tetralin, and 1,4-benzodioxan (14BZD). In the current chapter, the infrared and Raman spectra of these two molecules in both liquid

---

*Reprinted with permission from "Vibrational Spectra and DFT Calculations of Tetralin and 1,4-Benzodioxan" by D. Autrey, J. Yang, and J. Laane, 2003. *J. Mol. Struct.*, **661-662**, 23-32. 2003 by Elsevier B.V.

and vapor phases, as well as the comparison of the experimental frequencies to the values calculated from density functional theory (DFT) will be presented.

EXPERIMENTAL

Samples of tetralin (99% purity) and 1,4-benzodioxan (97% purity) were purchased from Aldrich Chemical Company and further purified by vacuum distillation.

The infrared spectra were recorded on the Biorad FTS-60 Fourier-transform infrared spectrometer. Liquid-phase mid-IR spectra were recorded at 1 cm^{-1} resolution and 64 scans were typically averaged. Vapor-phase mid-IR spectra were recorded using a 10 cm heatable cell, fitted with KBr windows, operated at temperatures in the 200-220 °C range. Vapor-phase IR spectra were recorded at 0.25 cm^{-1} resolution and one thousand scans were typically averaged.

Raman spectra were recorded on an ISA Jobin-Yvon U-1000 monochromator, using either a photomultiplier-tube (PMT) or a liquid-nitrogen cooled charge-coupled device (CCD) detection. Liquid-phase Raman spectra were recorded at ambient temperatures. Excitation at 514.5 nm was achieved with a Coherent Radiation Innova 20 argon ion laser with a lasing power of 1 W. Depolarization measurements were taken using a polarizer and a scrambler to separate the scattered light into its parallel and perpendicular components. Vapor-phase Raman spectra were collected at temperatures in

the 250-300 °C range and at pressures typically 700-900 Torr. The sample was contained in a thermostatically controlled high-temperature Raman cell previously described.[24,25] The laser power was about 5 W for the vapor-phase spectra. Spectral resolutions in the 0.5 to 2.0 cm^{-1} range with the PMT and 0.7 cm^{-1} with the CCD were used. This work is done in conjunction with Daniel Autrey.[56]

CALCULATIONS

Theoretical calculations were carried out using the Gaussian 98 package[51] at both the Moller-Plesset second-order perturbation (MP2) and the density functional theory (B3LYP) with a variety of basis sets. Structural parameters and energies were obtained using the MP2 method with the cc-pVTZ (triple-zeta) basis set, while the vibrational frequencies with the infrared and Raman intensities were obtained with the density functional (B3LYP) method and the 6-311++G(d,p) basis set. Based on previous work,[7,44,45] scaling fractions of 0.964 for the 2800-3100 cm^{-1} region and 0.985 for the region below 1700 cm^{-1} were used.

MOLECULAR STRUCTURE

Both TET and 14BZD are expected to have twisted conformations with C_2 symmetry and the MP2 calculations confirm that. Figure 26 shows the bond lengths and

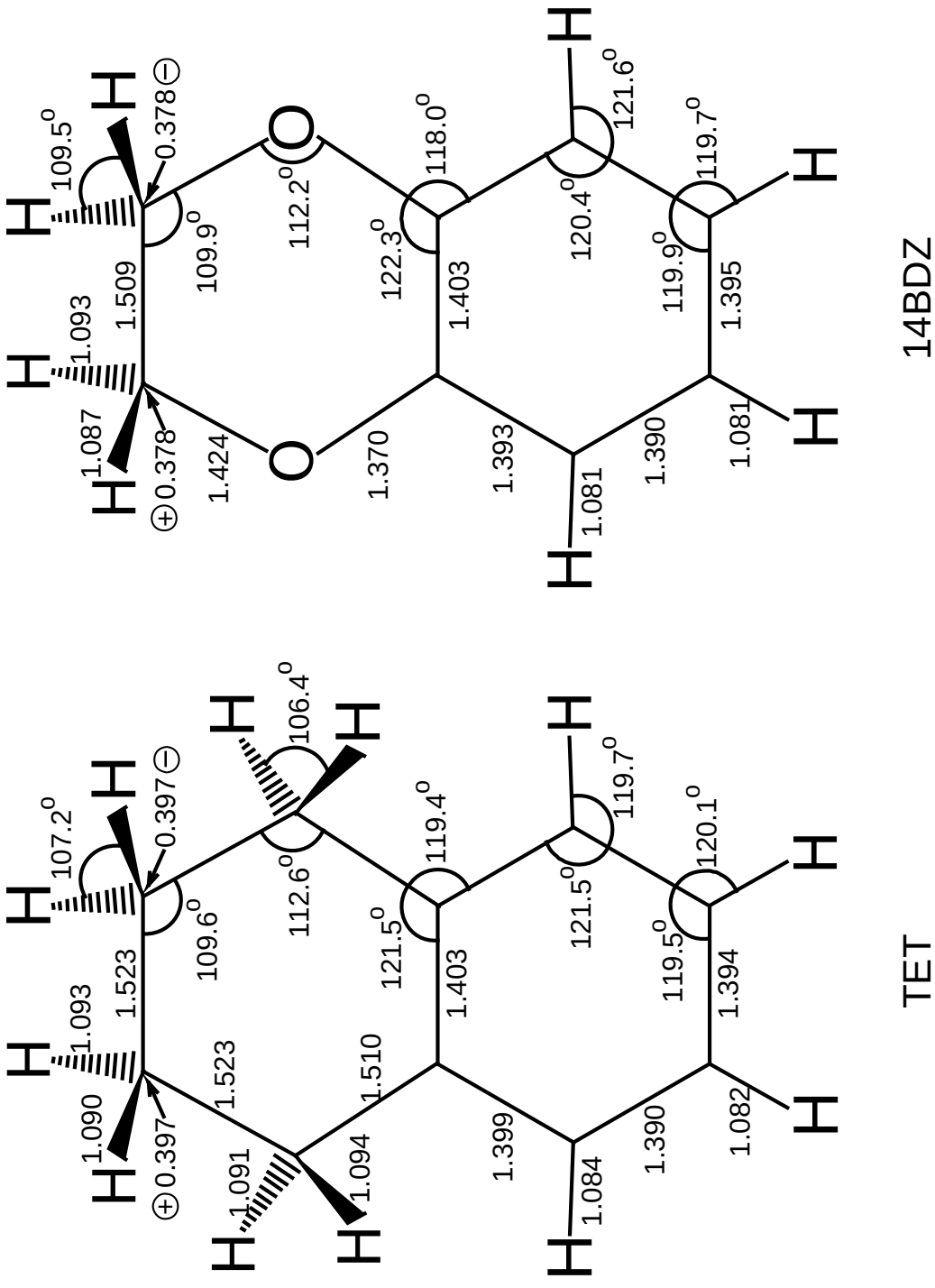

Figure 26. The calculated structures for tetralin and 1,4-benzodioxan from the MP2/6-311++G(d,p) calculations.

bond angles for both molecules calculated with the MP2/cc-pVTZ basis set. The twisting angles were calculated to be 31.4° for TET and 30.1° for 14BZD. The barriers to planarity were calculated to be 4809 and 4095 cm^{-1}, respectively. The larger twisting angle and higher barrier to planarity for TET are expected since it has more CH_2-CH_2 torsional interactions than 14BZD.

MOLECULAR VIBRATIONS

Although both molecules possess C_2 symmetry, it is useful to consider them to have perturbed C_{2v} symmetry (planar structure) for the purpose of classifying their vibrations. A planar tetralin molecule would have a vibrational distribution of

$$19A_1 + 12A_2 + 18B_1 + 11B_2 . \qquad (C_{2v}\ \text{TET})$$

In the twisted C_2 symmetry the A_1 and A_2 symmetry species merge to become A symmetry species whereas B_1 and B_2 merge to become B symmetry. Hence, the vibrations are

$$31A + 29B . \qquad (C_2\ \text{TET})$$

Similarly, for 1,4-benzodioxan the vibrations in C_{2v} symmetry are

$$16A_1 + 9A_2 + 15B_1 + 8B_2 , \qquad (C_{2v}\ \text{14BZD})$$

and in C_2 symmetry

$$25A + 23B . \qquad (C_2\ \text{14BZD})$$

For both molecules the A_1, B_1, and B_2 vibrations will produce Type A, Type B, and Type C infrared bands, respectively. Upon twisting to C_2 symmetry the A symmetry produces Type A bands while those of symmetry species B produce B, C hybrids. The A_1 bands will be Raman polarized. The A_2 bands, which would be depolarized in C_{2v} symmetry, tend to become polarized as the molecule twists. The A_2 vibrations, which are infrared forbidden for a planar structure, begin to have some intensity in their absorption spectra as the molecule twists.

Figure 27 shows the relative motions for the four lowest frequency ring vibrations of these molecules. A comprehensive analysis of these is necessary for determining the potential energy surfaces governing the computational dynamics of these molecules.

RESULTS AND DISCUSSION

Figure 28 compares the vapor-phase infrared spectrum of TET to the computed spectrum, and Figure 29 compares the vapor-phase Raman spectra to its calculated spectrum. Figure 30 presents the infrared and Raman spectra (with both parallel and perpendicular polarizations) of 14BZD liquid while Figures 31 and 32 compare the infrared and Raman spectra of the vapor to the computed spectra. Table 21 summarizes the results for TET, and Table 22 presents the data for 14BZD. Vibrational assignments have previously been made for TET[57] on the basis of C_2 symmetry for the liquid phase

molecules. These results are in good agreement with the previous assignments. Table 23 presents a comparison of the skeletal vibrations TET and 14BZD.

Figure 33 shows the vapor-phase Raman spectrum of 14BZD in the low-frequency region. From this figure the assignments of the four low-frequency ring modes shown in Figure 27 can be readily made. As vibrations ν_{24} and ν_{25} are polarized A modes in C_2 symmetry, the ring-flapping vibration ν_{47}, which is obscured in the non-polarized Raman spectrum, can be clearly seen in the perpendicular-polarized spectrum where the ν_{24} intensity is nearly eliminated. Figure 34 shows the low-frequency vapor phase Raman spectrum of TET, from which ν_{30}, ν_{31}, ν_{59}, and possibly ν_{60} could be assigned.

Analysis of the spectra of both TET and 14BZD shows that the utilization of both C_{2v} and C_2 symmetry point groups is useful. Many of the A_2 vibrations for C_{2v}, which are infrared inactive, can be observed as weak infrared bands, demonstrating that the molecule has the C_2 structure where they are allowed. However, these are some of the weakest bands in the spectra. In addition, approximately half of the A_2 bands are clearly Raman polarized, again demonstrating that the molecules have C_2 symmetry. The other A_2 bands should also be polarized but their depolarization ratios are close to 0.75 and thus cannot be clearly distinguished from depolarized bands.

The calculated frequencies, after scaling, do an excellent job of fitting the observed frequencies, especially for the lower frequencies. For TET the calculated C-H

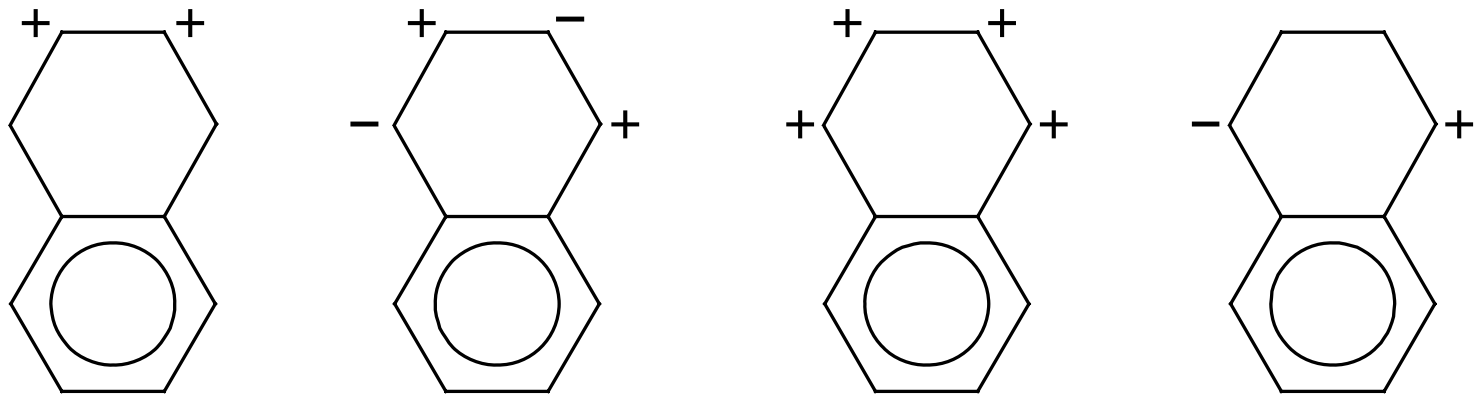

Figure 27. The relative motions for the four lowest frequency ring vibrations for tetralin and 1,4-benzodioxan.

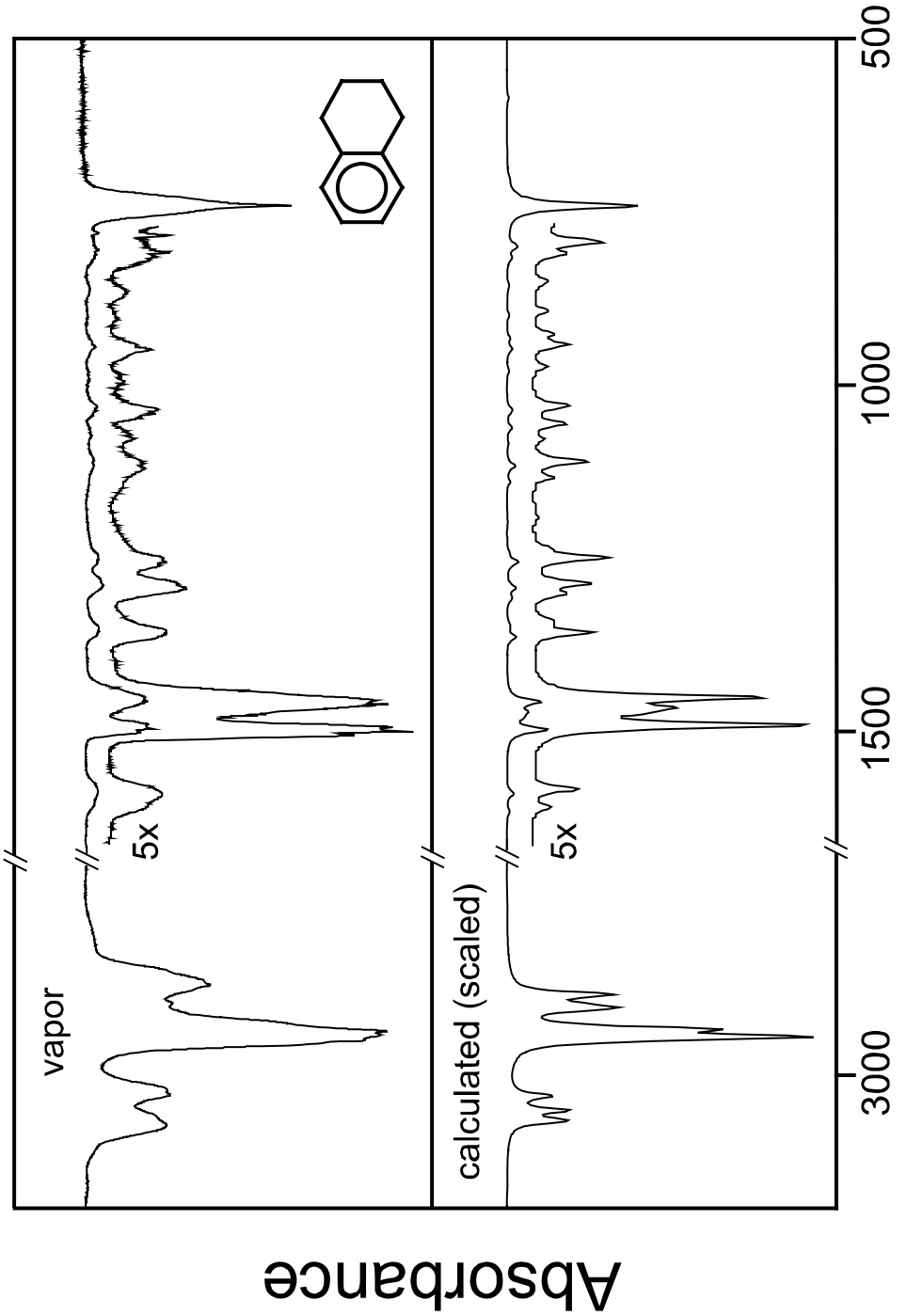

Figure 28. Vapor-phase infrared spectrum (top) of tetralin compared to the computed DFT spectrum with scaled frequencies (bottom).

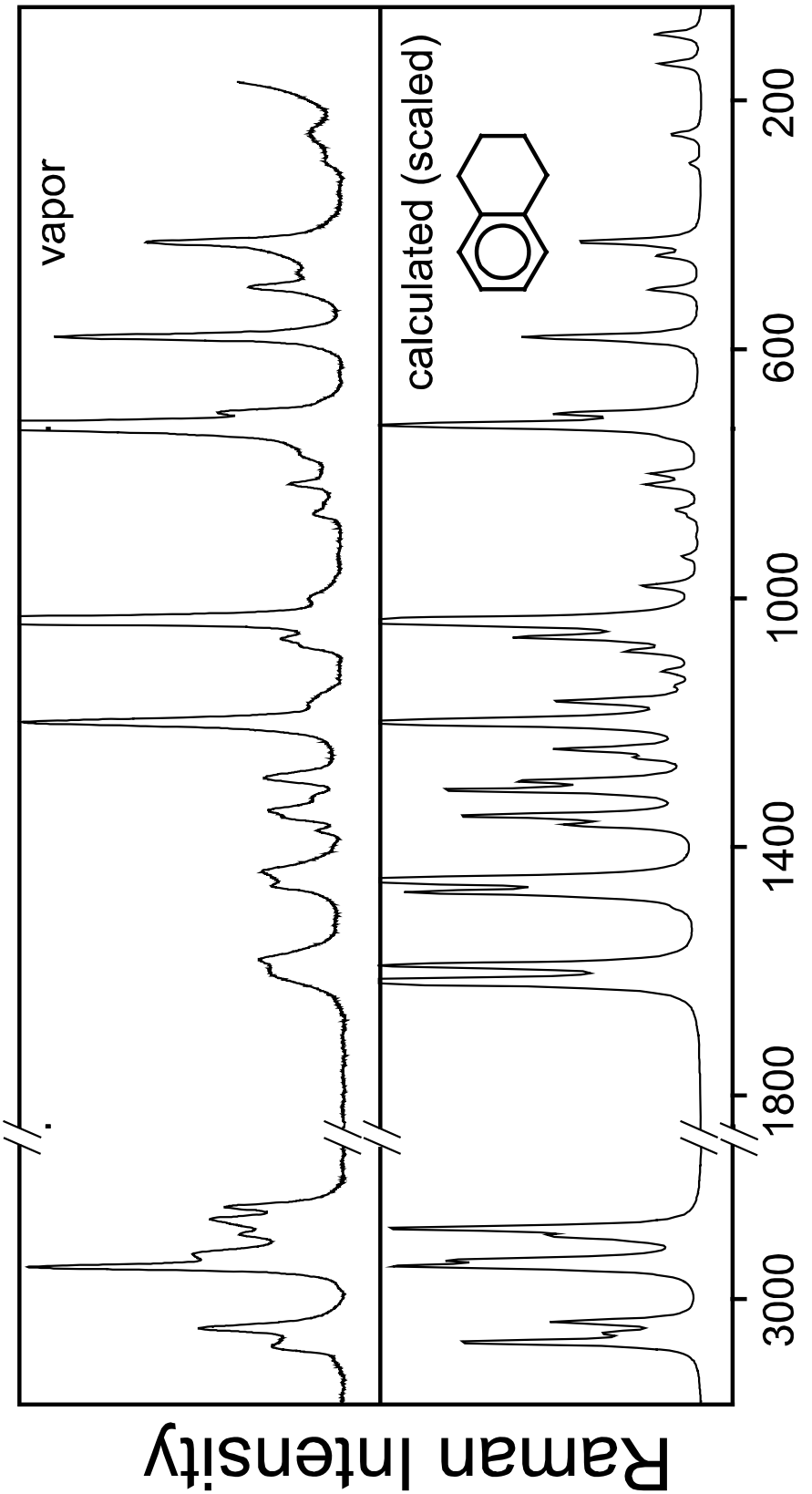

Figure 29. Vapor-phase Raman spectrum (top) of tetralin compared to the calculated DFT spectrum with scaled frequencies (bottom).

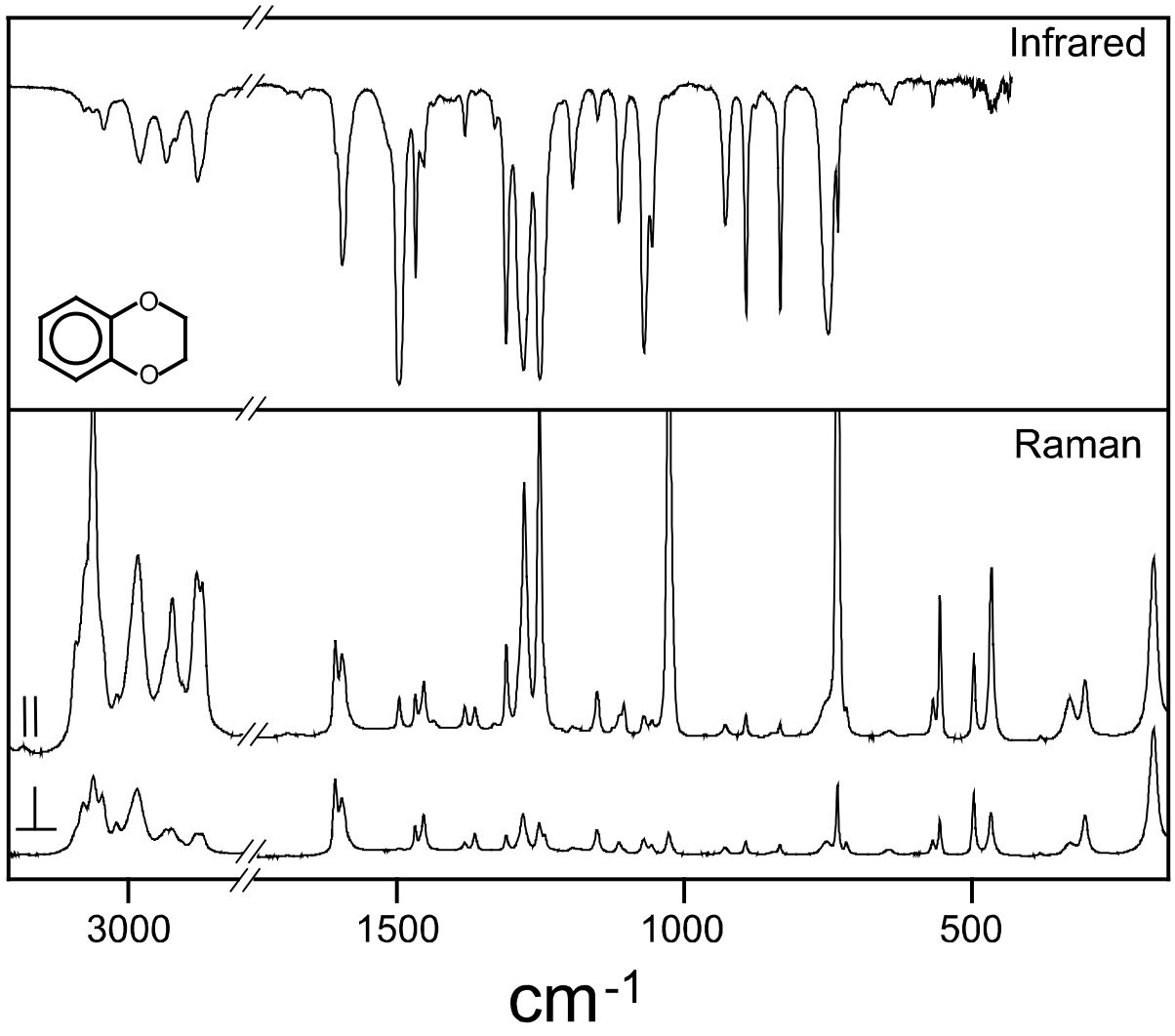

Figure 30. Infrared (top) and Raman (bottom) spectra with both parallel and perpendicular polarizations of 1,4-benzodioxan liquid.

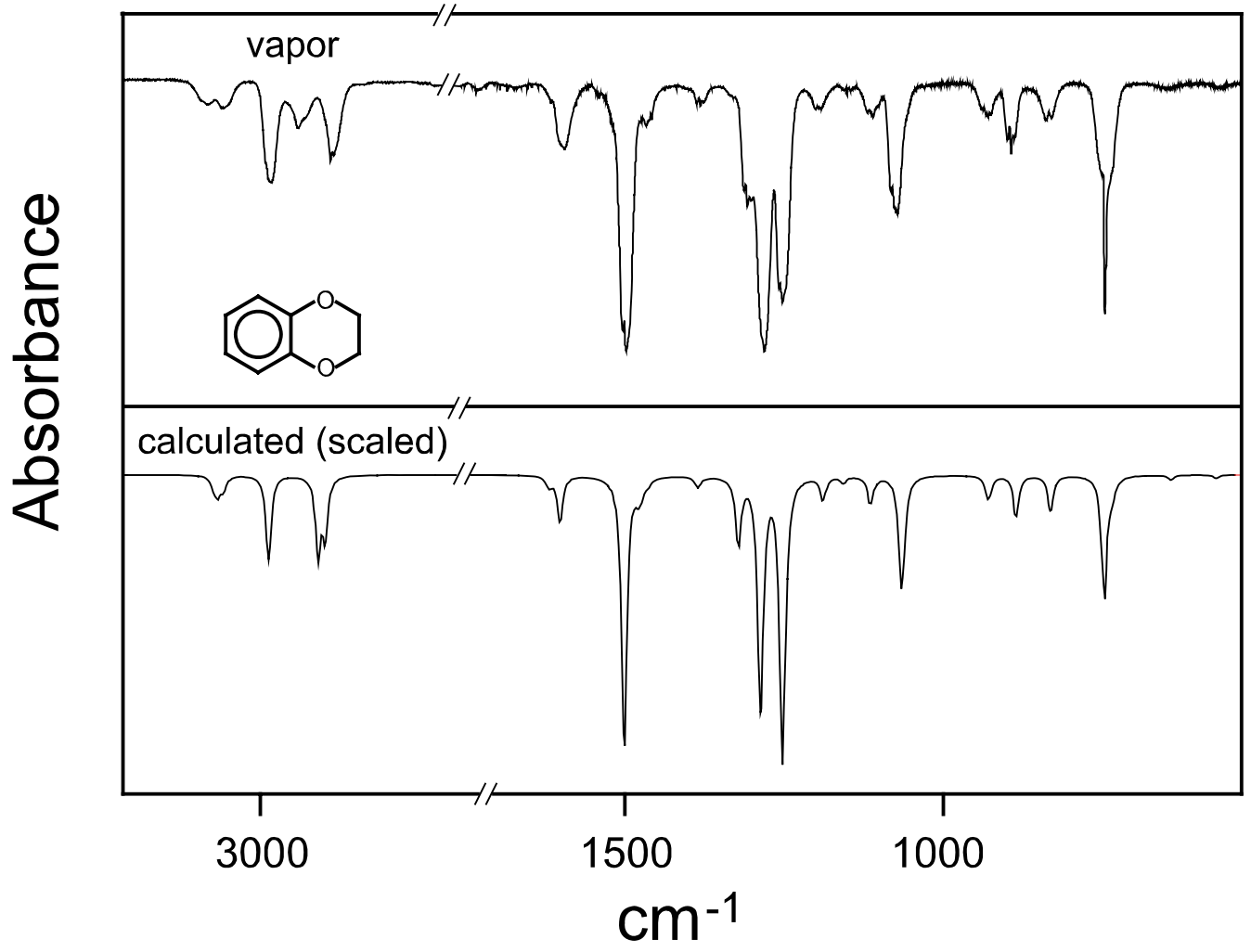

Figure 31. Vapor-phase infrared spectrum (top) of 1,4-benzodioxan compared to the computed DFT spectrum with scaled frequencies (bottom).

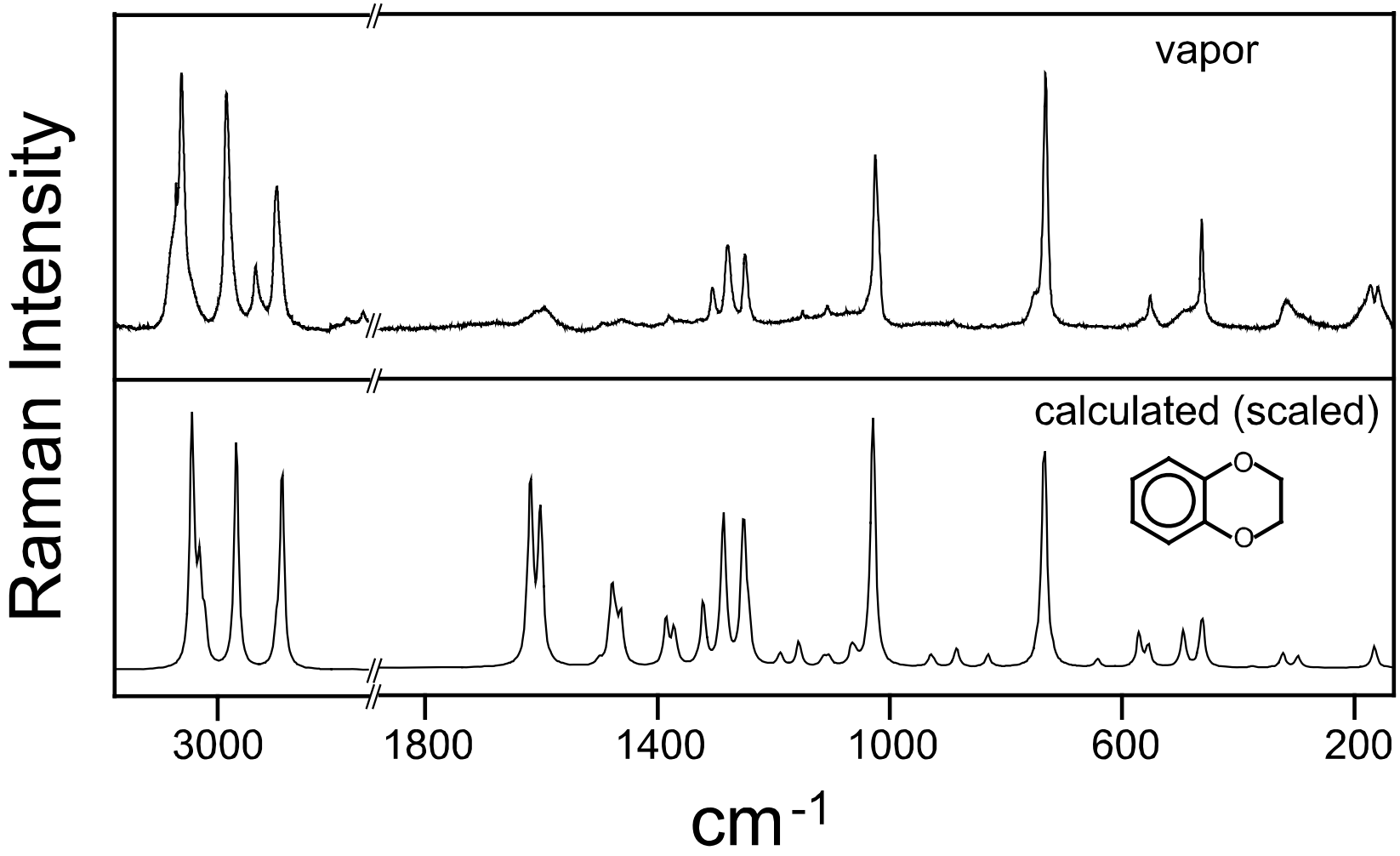

Figure 32. Vapor-phase Raman spectrum (top) of 1,4-benzodioxan compared to the calculated DFT spectrum with scaled frequencies (bottom).

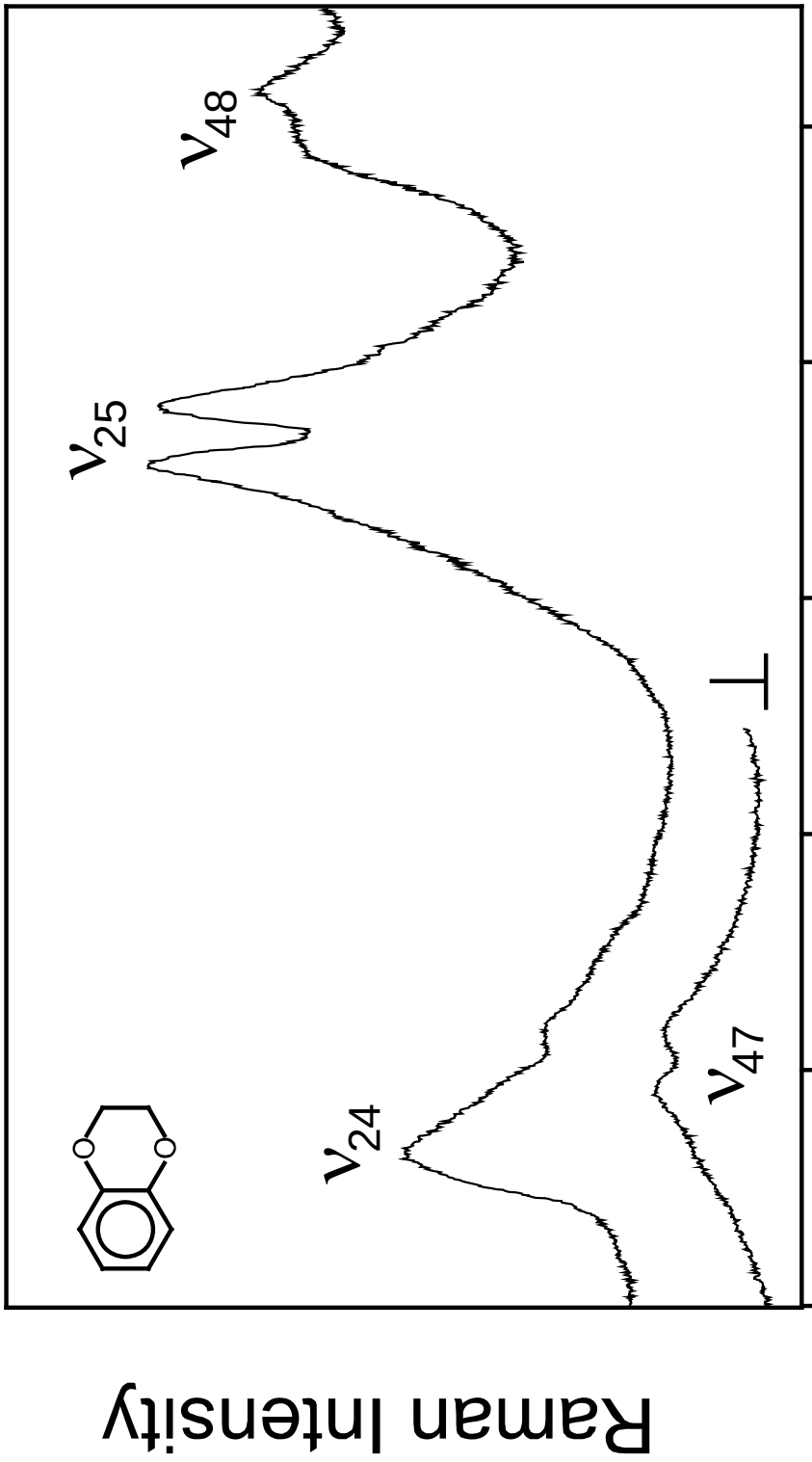

Figure 33. The low-frequency Raman spectrum of 1,4-benzodioxan vapor (250 °C).

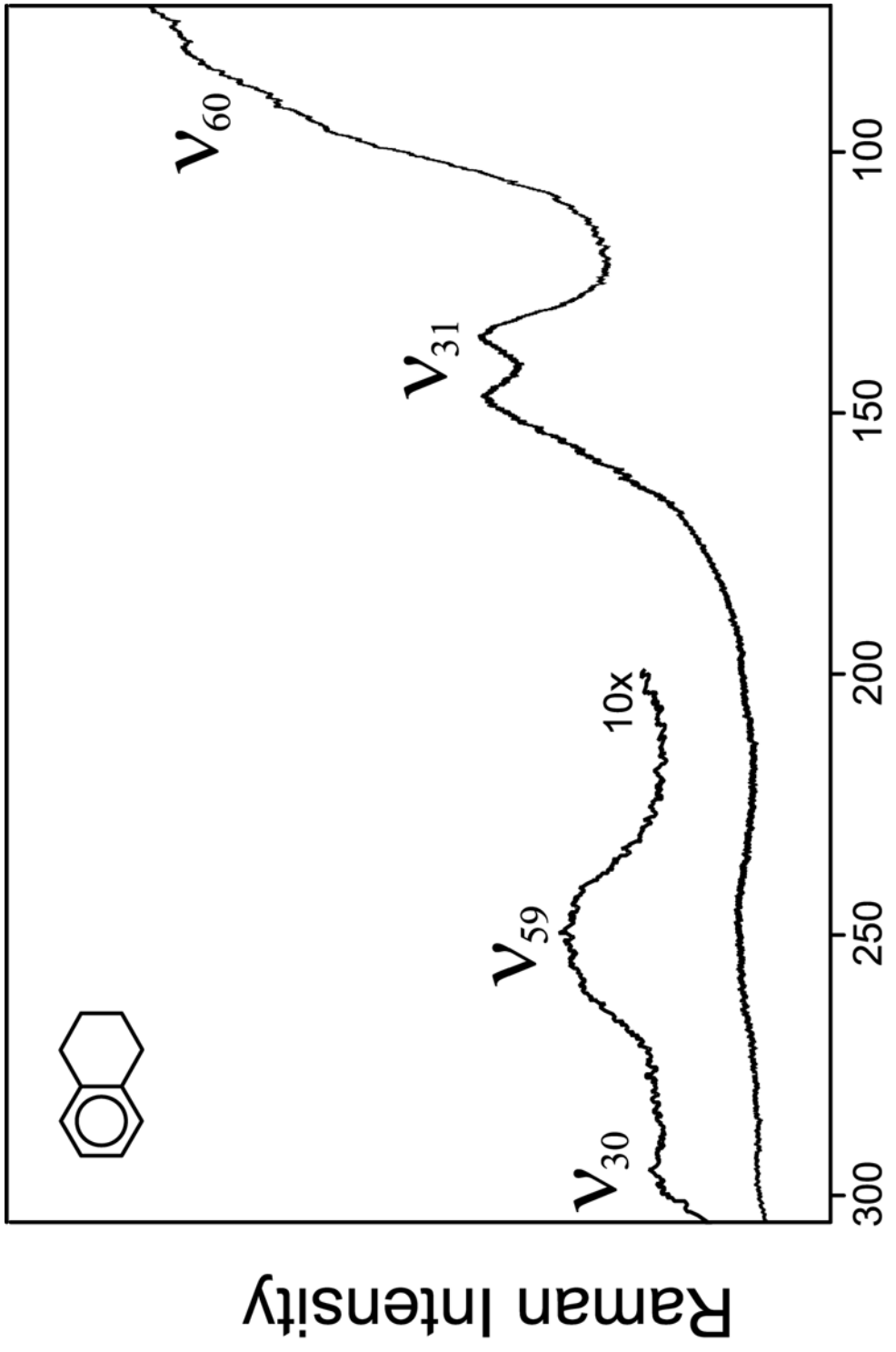

Figure 34. The low-frequency Raman spectrum of tetralin vapor (250 °C).

TABLE 21: The Experimental and Calculated Frequencies (cm^{-1}) and Vibrational Assignments of Tetralin.

Sym.	ν		Description	Infrared		Raman				B3LYP/6-311++G(d,p)			
$C_{2v}(C_2)$	C_{2v}	C_2		Liquid	Vapor	Liquid[a]		Vapor[a]		HF[b]	C_{2v}[c]	C_2[c,d]	
A_1 (A)	1	1	C-H sym. stretch (ip)	3075 m	3073 m	3075 P	(13)	3077 P	(23)	3028	3069	3069	(34, 86)
	2	2	C-H sym. stretch (op)	3040 w	-----	3041 P	(38)	3047 P	(46)	2996	3034	3037	(1.9, 49)
	3	5	CH_2 sym. stretch (ip, op')	2882 m	(2896)	2883 P	(17)	2895[e] P	(33)	2893	2906	2899	(22, 36)
	4	6	CH_2 sym. stretch (ip, ip')	2858 m	2870	2859 P	(13)	2871 P	(42)	2899	2943	2886	(5.2,100)
	5	7	benzene C-C stretch	1579 s	1582 w	1580 D	(5.2)	1581 D	(5.5)	1600	1602	1592	(4.1, 4.5)
	6	8	benzene C-C stretch	1493 s	1496 m	1495 D	(0.3)	-----	-----	1475	1504	1499	(25, 0.1)
	7	9	CH_2 deformation (ip, ip')	1459 sh	1465 w	1460 P	(4.2)	1463 P	(4.6)	1496	1507	1481	(5.9, 0.5)
	8	10	CH_2 deformation (ip, op')	-----	-----	1431 D	(12)	1440 D	(5.3)	1448	1460	1453	(0.2, 5.1)
	9	11	CH_2 wag (op, ip')	1353 m	1354 w	1354 P	(8.0)	1353 P	(1.5)	1370	1372	1365	(5.4, 1.4)
	10	13	benzene C-C stretch	1294 mw	1295 sh	1295 P	(6.8)	-----	-----	1358	1336	1309	(2.7, 3.3)
	11	15	sat. ring (C-C) stretch	1201 w	-----	1202 P	(35)	1199 P	(22)	1222	1196	1200	(0.6, 7.1)
	12	16	CH_2 wag (op, op')	1161 vvw	-----	1161 D	(1.4)	1166 D	(1.3)	1247	1268	1167	(0, 1.1)
	13	17	C-H wag (op, op')	1155 vw	-----	1155 D	(2.1)	1157 D	(1.4)	1040	1165	1164	(0, 0.8)
	14	19	sat. ring (C-C) stretch	1067 m	1067 w	1067 D	(4.4)	1065 D	(2.6)	1016	1113	1064	(2.9, 2.2)
	15	20	C-H wag (op,ip')	1037 m	1038 w	1037 P	(100)	1035 P	(57)	1004	1043	1038	(3.5, 9.0)
	16	23	sat. ring (C-C) stretch	864[e] mw	864[e] w	867 P	(2.1)	864 P	(1.8)	887	839	858	(1.4, 0.3)
	17	25	benzene C-C stretch	724 sh	-----	724 P	(81)	721 P	(83)	713	713	723	(0.5, 5.1)
	18	27	benzene ring bend	580 vw	-----	580 P	(19)	578 P	(19)	568	584	581	(0.1, 2.2)
	19	29	sat. ring bend	-----	-----	431 P	(13)	427 P	(13)	418	442	427	(0.7, 1.6)
A_2 (A)	20	3	CH_2 asym. stretch (op, ip')	(2927) vs br	2949 s	2938 P	(42)	2948[e] P	(100)	2855	2948	2946	(100, 78)
	21	4	CH_2 asym. stretch (op, op')	(2927) vs br	2925 w	2913 P	(18)	2927 P	(47)	2849	2918	2936	(0.9, 65)
	22	12	CH_2 twist (ip, ip')	(1341) w	-----	(1341) D	(5.6)	(1342) D	(4.9)	1188	1291	1351	(0.3, 0.4)
	23	14	CH_2 twist (ip, op')	1248 m	1251 w	1248 D	(0.5)	-----	-----	1155	1259	1257	(7.0, 0.6)

TABLE 21: Continued.

Sym.	ν		Description	Infrared		Raman				B3LYP/6-311++G(d,p)			
$C_{2v}(C_2)$	C_{2v}	C_2		Liquid	Vapor	Liquid[a]		Vapor[a]		HF[b]	C_{2v}[c]	C_2[c,d]	
A_2 (A)	24	28	CH_2 rock (op, op')	1079 w	1074 w	1079 D	(2.8)	1076 D	(1.7)	1088	1056	1085	(0.9, 0.8)
	25	21	C-H wag (op, op')	1005 vw	-----	1005 P	(0.7)	1000 P	(1.1)	1075	969	973	(0, 0.02)
	26	22	C-H wag (op, ip')	(864)	868 w	867 D	(2.1)	-----	-----	837	871	869	(0.2, 0.1)
	27	24	CH_2 rock (op, ip')	817 mw	817 w	817 D	(5.6)	815 P	(2.6)	813	818	819	(2.4, 0.7)
	28	26	benzene ring bend	700 vw	-----	700 P	(6.2)	699 P	(5.9)	695	688	703	(0.6, 1.7)
	29	28	benzene ring bend	504 w	-----	504 P	(7.9)	498 P	(6.2)	502	483	504	(0.2, 0.7)
	30	30	skeletal twist	-----	-----	309 P	(0.8)	298 P	(0.6)	296	*i*	301	(0.2, 0.2)
	31	31	sat. ring twist	-----	-----	161 D	(10)	142	(11)	144	125	141	(0, 0.6)
B_1 (B)	32	32	C-H asym. stretch (ip)	3059 s	3064	3061 P	(8.8)	~3066 sh	-----	3012	3054	3054	(33, 24)
	33	33	C-H asym. stretch (op)	3026 vw	3024	3026 D	(12)	-----	-----	2991	3031	3033	(24, 1.8)
	34	36	CH_2 sym. stretch (op, op')	2896 w	2896	2894 D	(7.1)	(2895)	(33)	2891	2905	2905	(51, 7.4)
	35	37	CH_2 sym. stretch (op, ip')	-----	2874	2866 P	(28)	~2880 sh	-----	2904	2927	2885	(52, 13)
	36	38	benzene C-C stretch	1601 mw	1598 w	1603 D	(9.7)	1598 D	(4.7)	1630	1618	1618	(1.6, 7.6)
	37	40	CH_2 deformation (op, ip')	1452 s	1456 m	-----	-----	-----	-----	1461	1482	1474	(8.7, 3.3)
	38	39	CH_2 deformation (op, op')	1448 sh	1448 w	1448 D	(4.9)	1447 D	(4.7)	1457	1459	1459	(20, 0.9)
	39	41	benzene C-C stretch	1436 s	1437 m	1436 D	(4.1)	-----	-----	1435	1454	1457	(0.1, 1.1)
	40	42	CH_2 wag (ip, op')	1341[e] w	-----	1341[e] D	(5.6)	1342[e] D	(4.9)	1359	1361	1350	(0.9, 2.6)
	41	43	CH_2 wag (ip, ip')	1334 w	-----	-----	-----	-----	-----	1341	1351	1346	(0.7, 0)
	42	45	C-H wag (ip, ip')	1235 mw	1246 w	1235 D	(2.2)	1241 D	vw	1281	1251	1243	(1.0, 1.8)
	43	46	sat. ring (C-C) stretch	1189 w	-----	-----	-----	-----	-----	1231	1204	1184	(0.3, 0)
	44	48	C-H wag (ip, op')	1111 m	1112 w	1112 D	(0.9)	-----	-----	1103	1118	1118	(5.1, 0.4)
	45	49	sat. ring (C-C) stretch	985 mw	986 w	986 D	(2.3)	982 D	(0.9)	959	1007	981	(1.4, 0.7)
	46	53	benzene ring bend	804 s	805 w	805 D	(2.2)	805 D	(0.7)	899	854	801	(6.1, 0.6)

TABLE 21: Continued.

Sym.	ν		Description	Infrared		Raman				B3LYP/6-311++G(d,p)			
$C_{2v}(C_2)$	C_{2v}	C_2		Liquid	Vapor	Liquid[a]		Vapor[a]		HF[b]	C_{2v}[c]	C_2[c,d]	
B_1 (B)	47	55	benzene ring bend	587 w	-----	588 D sh	-----	-----	-----	576	728	587[f]	(1.3, 0.4)
	48	56	sat. ring bend	453 w	-----	454 D	(2.2)	453 D	(2.1)	430	477	450	(1.1, 0.5)
	49	58	sat. ring bend	-----	-----	343 D	(0.1)	-----	-----	331	334	339	(0.4, 0)
B_2 (B)	50	34	CH_2 asym. stretch (ip, ip')	(2927) vs br	(2949)	(2938) P	(42)	(2948) P	(100)	2857	2974	2949	(77, 26)
	51	35	CH_2 asym. stretch (ip, op')	(2927) vs br	2936 vs	2917 D	(13)	~2933 sh	-----	2848	2922	2935	(100,7.0)
	52	44	CH_2 twist (op, ip')	1283 m	1287 w	1284 D	(3.4)	1289[e] D	(5.1)	1165	1287	1294	(5.2, 2.1)
	53	47	CH_2 twist (op, op')	1134 mw	1137 vw	1134 D	(0.2)	-----	-----	1129	1219	1142	(1.8, 0.2)
	54	50	C-H wag (ip, op')	945 ms	944 w	947 D	(0.1)	-----	-----	921	955	950	(3.2, 0)
	55	51	CH_2 rock (ip,ip')	938 w	938 sh	938 D	(0.4)	-----	-----	756	709	934[f]	(1.7, 0.2)
	56	52	CH_2 rock (ip,op')	898 mw	902 w	899 D	(0.3)	-----	-----	899	910	900	(1.5, 0)
	57	54	C-H wag (ip, ip')	742 vs	741 vs	743 D	(0.7)	-----	-----	786	749	743	(82, 0.2)
	58	57	benzene ring bend	432 ms	-----	-----	-----	436 D	(3.9)	443	429	432	(7.2, 0.1)
	59	59	sat. ring flap	-----	-----	264 D	(3.8)	253 D	(1.6)	258	210	255	(7.0, 0.4)
	60	60	sat. ring bend	-----	-----	-----	-----	~90	vw	96	*i*	94	(0.2, 0.6)

Abbreviations: ip, in-phase; op, out-of-phase; s, strong; m, medium; w, weak; v, very; sh, should; br, broad; P, polarized; D, depolarized.

[a] Relative intensity in parenthesis.

[b] From Reference 57; some of the frequencies have been assigned to different motions.

[c] Frequencies scaled with a scaling factor of 0.985 for frequencies less than 1700 cm^{-1} and 0.964 for frequencies greater than 2800 cm^{-1}.

[d] Relative intensities shown as (IR, Raman).

[e] Frequency used twice..

[f] The B_1 ring bending ν_{47} and B_2 CH_2 rocking ν_{55} motions are strongly coupled in C_2 symmetry.

TABLE 22: The Experimental and Calculated Frequencies (cm^{-1}) and Vibrational Assignments of 1,4-Benzodioxan.

Sym.	ν		Description	Infrared		Raman				B3LYP/6-311++G(d,p)		
$C_{2v}(C_2)$	C_{2v}	C_2		Liquid	Vapor	Liquid[a]		Vapor[a]		C_{2v}[b]	C_2[b,c]	
A_1 (A)	1	1	C-H sym. stretch (ip)	3092 vw	3082 ms	3092 P	(7)	3081	(8)	3085	3083	(4, 100)
	2	2	C-H sym. stretch (op)	3062 m	3056 ms	3062 P	(36)	3070	(64)	3069	3067	(4, 36)
	3	4	CH_2 sym. stretch (ip)	2872 sh	~2880 sh	2872 P	(12)	2885[e]	(35)	2938	2905	(21, 82)
	4	5	benzene C-C stretch	1605 w	1609 vw	1607 P	(11)	1609	(4)	1616	1602	(16, 6)
	5	6	benzene C-C stretch	1495 vs	1496 vs	1496 P	(5)	1494	(0.5)	1515	1502	(95, 0.2)
	6	7	CH_2 deformation (ip)[d]	(1466) m	(1465) w	(1468) D	(5)	(1462)	(3)	1504	1473	(4, 1)
	7	8	CH_2 wag (op)	1381 m	1381 w	1382 P	(3)	1381	(4)	1402	1385	(4, 2)
	8	9	benzene C-C stretch	1309 s	1307 ms	1310 P	(10)	1306	(11)	1325	1321	(23, 2)
	9	11	sat. ring (C-O) stretch	1251 s	1250 s	1252 P	(35)	1249	(25)	1272	1252	(100, 5)
	10	12	C-H wag (op,op')	1150 m	1151 w	1152 P	(5)	1151	(3)	1156	1157	(2, 0.9)
	11	14	sat. ring (C-O) stretch	1070 s	1074 s	1071 D	(3)	1074	(1)	1102	1066	(38, 0.7)
	12	15	C-H wag (op,ip')	1027 vw	-----	1028 P	(51)	1025	(65)	1033	1029	(0, 10)
	13	17	sat. ring (C-C) stretch	892 s	893 ms	893 D	(3)	891	(1)	893	886	(14, 0.7)
	14	19	benzene C-C stretch	733 m	733 vw	734 P	(100)	732	(100)	725	734	(5, 9)
	15	21	benzene ring bend	568 w	565 vw	569 D	(4)	566	(2)	560	571	(1, 1)
	16	23	sat. ring bend	465 vw	-----	467 P	(16)	463[e]	(42)	464	462	(0.2, 2)
A_2 (A)	17	3	CH_2 asym. stretch (op)	2981[e]	2991 sh	2984 P[e]	(15)	2983[e]	(59)	2949	2995	(8, 33)
	18	10	CH_2 twist (ip)	1279 s	1280 s	1278 P	(25)	1280	(29)	1250	1286	(84, 5)
	19	13	CH_2 rock (op)	1105 vw	-----	1105 P	(4)	1107	(4)	1112	1105	(0.8, 0.4)
	20	16	C-H wag (op, op')	962 vw	-----	965 D	(6)	-----	-----	942	952	(0, 0.01)
	21	18	C-H wag (op, ip')	-----	-----	845 D	(1)	842	vvw	832	845	(0, 0.01)
	22	20	benzene ring bend	718 vw	-----	719 D	(1)	-----	-----	670	720	(0.3, 0.2)
	23	22	benzene ring bend	556 vw	-----	556 D	(14)	552	(11)	540	555	(0, 0.8)

TABLE 22: Continued.

Sym.	ν		Description	Infrared		Raman				B3LYP/6-311++G(d,p)		
$C_{2v}(C_2)$	C_{2v}	C_2		Liquid	Vapor	Liquid[a]		Vapor[a]		C_{2v}[b]	C_2[b,c]	
A_2 (A)	24	24	skeletal twist	-----	-----	330 D	(4)	317	(4)	i	323	(2, 0.5)
	25	25	sat. ring twist	-----	-----	184 D	(18)	167	(15)	168	165	(0, 0.8)
B_1 (B)	26	26	C-H asym. stretch (ip)	3077 mw	3082 mw	3080 P	(8)	-----	-----	3077	3075	(6, 8)
	27	27	C-H asym. stretch (op)	3045 ms	3058 mw	3046 P	(3)	-----	-----	3059	3057	(0.3, 16)
	28	29	CH_2 sym. stretch (op)	2880 s	2886 s	2881 P	(11)	(2885)	(35)	2927	2916	(27, 12)
	29	30	benzene C-C stretch	1593 ms	1599 ms	1595 D	(9)	1596	(5)	1617	1619	(4, 7)
	30	31	CH_2 deformation (op)	1466 m[e]	1465 w[e]	1468 D[e]	(5)	1462[e]	(3)	1495	1479	(5, 3)
	31	32	benzene C-C stretch	1452 w	1456 w	1453 D	(6)	(1462)	(3)	1465	1463	(2, 2)
	32	33	CH_2 wag (ip)	1363 w	-----	1364 D	(4)	1362	vvw	1404	1371	(0.3, 1)
	33	34	C-H wag (ip, ip')	-----	-----	1282 D	(1)	-----	-----	1278	1285	(0.5, 0.4)
	34	36	sat. ring (C-O) stretch	1194 s	1194 w	1194 D	(1.5)	-----	-----	1215	1189	(8, 0.5)
	35	37	C-H wag (ip, op')	1113 ms	1114 w	1114 D	(0.7)	-----	-----	1119	1114	(9, 0.3)
	36	38	sat. ring (C-O) stretch	1056 ms	-----	1057 D	(2)	-----	-----	1057	1059	(6, 0.3)
	37	41	benzene ring bend	833 s	834 w	834 D	(2)	-----	-----	833	831	(13, 0.5)
	38	43	benzene ring bend	642 w	645 vw	643 D	(1)	-----	-----	760	642[f]	(2, 0.3)
	39	44	sat. ring bend	497 w	-----	497 D	(9)	495	(3)	511	494	(0.4, 1)
	40	46	sat. ring bend	-----	-----	381 D	(0.5)	-----	-----	369	376	(3, 0.05)
B_2 (B)	41	28	CH_2 asym. stretch (ip)	(2981) vs	(2984) vs	(2984) P	(15)	2983	(59)	2978	2995	(21, 61)
	42	35	CH_2 twist (op)	1242 w sh	-----	1243 D	(3)	-----	-----	1280	1243	(3, 1)
	43	39	CH_2 rock (ip)	929 ms[e]	936 w	929 D	(1.6)	-----	-----	826	930[f]	(6, 0.4)
	44	40	C-H wag (ip, op')	(929) ms	924 w	-----		-----	-----	922	925	(3, 0.2)
	45	42	C-H wag (ip, ip')	749 s	746 s	753 D	(0.6)	746	(7)	741	747	(42, 0.3)

TABLE 22: Continued.

Sym.	ν		Description	Infrared		Raman				B3LYP/6-311++G(d,p)		
$C_{2v}(C_2)$	C_{2v}	C_2		Liquid	Vapor	Liquid[a]		Vapor[a]		C_{2v}[b]	C_2[b,c]	
B_2 (B)	46	45	benzene ring bend	461 w	-----	461 D	(0)	(463)	(42)	448	462	(2, 0.1)
	47	47	sat. ring flap	-----	-----	303 D	(6)	297	(4)	258	297	(0.1, 0.4)
	48	48	sat. ring bend	-----	-----	105 D	(1)	105	(8)	i	104	(5, 0.3)

Abbreviations: ip, in-phase; op, out-of-phase; s, strong; m, medium; w, weak; v, very; sh, should; P, polarized; D, depolarized.

[a] Relative intensity in parenthesis.

[b] Frequencies scaled with a scaling factor of 0.985 for frequencies less than 1700 cm^{-1} and 0.964 for frequencies greater than 2800 cm^{-1}.

[c] Relative intensities shown as (IR, Raman).

[d] The ν_6 bands are obscured by the ν_{30} bands or *vice-versa*. Infrared and Raman bands at 1436 cm^{-1} in the vapor are apparently due to $2\nu_{22}$.

[e] Frequency used twice.

[f] ν_{38} and ν_{43} are coupled in C_2 symmetry.

TABLE 23: The Frequencies (cm^{-1}) of the Skeletal Ring Vibrations for Tetralin (TET) and 1,4-Benzodioxan (14BZD).

Symmetry C_{2v}	Description	TET		14BZD	
		ν	Freq.	ν	Freq.
A_1	benzene C-C stretch	5	1581	4	1609
	benzene C-C stretch	6	1495	5	1496
	benzene C-C stretch	10	1295	8	1306
	sat. ring stretch	11	1199	9	1249
	sat. ring stretch	14	1065	11	1074
	sat. ring stretch	16	864	13	893
	benzene C-C stretch	17	721	14	732
	benzene ring bend	18	578	15	566
	sat. ring bend	19	427	16	463
A_2	benzene ring bend	28	699	22	718
	benzene ring bend	29	498	23	552
	skeletal twist	30	298	24	317
	sat. ring twist	31	142	25	167
B_1	benzene C-C stretch	36	1598	29	1596
	benzene C-C stretch	39	1436	31	1456
	sat. ring stretch	43	1189	34	1194
	sat. ring stretch	45	986	36	1057
	benzene ring bend	46	805	37	834
	benzene ring bend	47	588	38	645
	sat. ring bend	48	453	39	495
	sat. ring bend	49	343	40	381
B_2	benzene ring bend	58	432	46	461
	sat. ring flap	59	253	47	297
	sat. ring bend	60	~90	48	105

stretching frequencies differ from the experimental ones by an average of about 7 cm^{-1}, bands in the 1350-1620 cm^{-1} region differ by about 13 cm^{-1}, whereas those below 1350 cm^{-1} differ by about 4 cm^{-1}. For 14BZD the corresponding numbers are 12 cm^{-1}, 9 cm^{-1}, and 4 cm^{-1} respectively. The differences in the C-H stretching region are not surprising considering the frequencies themselves are large. Moreover, Fermi resonance between the C-H stretchings and CH_2 deformations are typically present in organic systems and these shift the observed values. For 14BZD, for example, for ν_3 (in C_{2v} symmetry) the calculated value of 2905 cm^{-1} is 20 cm^{-1} higher than the very strong vapor-phase Raman band at 2885 cm^{-1}, which is likely shifted by a Fermi interaction, perhaps with ν_{31}. Most of the calculated frequencies in the 1350-1620 cm^{-1} region are calculated to be too high suggesting that an intermediate scaling factor between the 0.985 and 0.964 would provide a better fit. In fact, the scaling factor appears to be frequency dependent. The computed frequencies, which fit the experimental data very well in most cases, indicated that some of the initial assignments needed revision. For 14BZD ν_6 was originally assigned to the weak infrared and Raman (polarized) liquid bands at 1436 cm^{-1}, but this vibration is calculated to be at 1473 cm^{-1}. It is probable that 1436 cm^{-1} is the overtone of ν_{22} at 718 cm^{-1} and ν_6 is simply obscured by stronger bands at 1466 cm^{-1}, which is assigned to be ν_{30}. Alternatively, since CH_2 deformations often seem to be depolarized even when they are totally symmetric, ν_6 may be at 1466 cm^{-1} and may be obscuring ν_{30}.

It is also interesting to see how the change in symmetry affects the vibrational frequencies. For C_{2v} symmetry, A_1 and A_2 vibrations cannot interact and neither can B_1 and B_2 vibrations. For C_2 symmetry the A_1 and A_2 modes both become A symmetry species and then the vibrational motions can interact. Similarly the B_1 and B_2 modes can interact as both become B symmetry for C_2. These interactions account for much of the changes seen in the calculations. For example, for TET the vibrations ν_{47} at 728 cm^{-1} and ν_{55} at 709 cm^{-1} cannot interact for C_{2v} symmetry. When the ring is twisted to take on C_2 symmetry, however, the motions interact and the calculated frequencies are pushed apart to 934 and 587 cm^{-1}. The experimental values are in good agreement also. As another example, ν_{38} at 760 cm^{-1} and ν_{43} at 826 cm^{-1} do not couple in C_{2v} symmetry for 14BZD, but are pushed apart to 642 and 930 cm^{-1} for the C_2 structure.

CONCLUSIONS

In this chapter the infrared and Raman spectra for both TET and 14BZD are presented and the DFT calculations for the frequencies are compared to the experimental values. Using appropriate scaling factors, the agreement between computed and observed frequencies is very good. Computations of the frequencies for the C_{2v} (planar) structures make it easier to assign the vibrations but artificially exclude interactions between certain vibrational motions, which are actually present for the twisted C_2

structure. Hence, the calculated C_{2v} frequencies can differ substantially for the C_2 and the experimental values. Thus, when carrying out calculations one must be cautious with imposing a higher symmetry on a molecule for vibrational analysis.

CHAPTER X

FLUORESCENCE AND ULTRAVIOLET ABSORPTION SPECTRA AND THE DETERMINATION OF THE TWO-DIMENSIONAL VIBRATIONAL POTENTIAL ENERGY SURFACES FOR THE RING-TWISTING AND RING-BENDING MODES OF 1,4-BENZODIOXAN IN ITS S_0 AND $S_1(\pi,\pi^*)$ STATES

INTRODUCTION

In Chapter IX the vibrational frequencies of all the vibrations for both 1,2,3,4-tetrahydronaphthalene (tetralin or TET) and 1,4-benzodioxan (14BZD) have been assigned, based on their liquid and vapor phase mid-infrared and Raman spectra as well as on the computed frequencies from the B3LYP/6-311++G(d,p) calculations. These data are helpful in characterizing the electronic ground state and distinguishing the low-frequency, large-amplitude ring vibrations from other higher frequency motions.

In this chapter an investigation of the two-dimensional vibrational potential energy surfaces (PESs) for the ring-twisting and ring-bending vibrations of 14BZD in its ground and excited electronic states is presented. In order to do this the fluorescence excitation (FES) and single vibronic level fluorescence (SVLF) spectra of jet-cooled 14BZD molecules are collected and compared with the vapor-phase ultraviolet (UV) absorption

spectra at room temperature. Both FES and UV absorption spectra have been studied by Gordon and Hollas.[58,59] However, as will be shown later, the signal to noise ratio of their spectra are not very good, and they assigned many bands incorrectly. They also failed to observe some bands reported in this study.

EXPERIMENTAL

The sample of 1,4-benzodioxan (97% purity) was purchased from Aldrich Chemical Company and further purified by vacuum distillation.

Ultraviolet absorption spectra were recorded on a Bomem DA8.02 Fourier-transform spectrometer using a deuterium lamp source, a quartz beamsplitter, and a silicon detector in the 20,000-50,000 cm^{-1} region. The vapor-phase sample was contained in a 20 cm glass cell with quartz windows. Ultraviolet absorption spectra were collected at ambient temperatures and the vapor pressure within the cell was about 200 mTorr. Resolutions of 0.25 and 0.5 cm^{-1} were used and more than ten thousand scans were averaged.

The FES and the SVLF spectra were recorded using a Continuum Powerlite 9020 Nd:YAG laser which pumped a Continuum Sunlite OPO and FX-1 ultraviolet extension unit. FES spectra were obtained at a $\pm$ 0.5 cm^{-1} resolution and SVLF spectra were taken with a spectral resolution of $\pm$ 1 cm^{-1}. More details are provided elsewhere.[28-32]

CALCULATIONS

Theoretical calculations were carried out using the GAUSSIAN 03 package.[41] Structural parameters and vibrational frequencies were calculated for both C_2 and C_1 structures in the $S_1(\pi,\pi^*)$ excited state. The configuration interaction-singles (CIS) method with both 6-31G(d) and 6-311++G(d,p) basis sets were used. Calculations for both S_0 and $S_1(\pi,\pi^*)$ states were also carried out by collaborator Dr. Jaebum Choo in Hanyang University, Korea, but these results are not included in this chapter since full details from his work was not available.

Figure 35 shows the bond lengths and bond angles for 14BZD in the S_0 and $S_1(\pi,\pi^*)$ states calculated with different theories and basis sets. The twisting angles were calculated to be 30.1° for C_2 symmetry in the S_0 ground state and 28.5° and 27.7° for C_2 and C_1 symmetry in the $S_1(\pi,\pi^*)$ excited state, respectively. Table 24 lists the calculated energies for the planar (C_{2v}), bent (C_s), and non-symmetric (C_1) structures of 14BZD in both S_0 and $S_1(\pi,\pi^*)$ states relative to the energy minima at twisted (C_2) conformations. Table 25 compares the calculated frequencies for 14BZD in its S_0 and $S_1(\pi,\pi^*)$ states.

By fixing the dihedral angle D(-O-C-C-O-), the twisting angle τ is confined to be a constant during the structural optimization. The energies for different conformations with different twisting angles are computed from the MP2/cc-pVTZ calculations. These results are listed in Table 26. A one-dimensional calculated potential energy curve for

14BZD S_0 state with respect to the twisting coordinate τ is presented in Figure 36. Similarly, by fixing the dihedral angle D(-C=C-O-C-), the bending angle θ can also be fixed during the optimization. Corresponding relative energies and the one-dimensional potential energy curve with respect to the bending coordinate θ are presented in Table 27 and Figure 37. The twisting angle τ and bending angle θ are referred to page 158 for definition. All energies are relative to the energy minima at twisted conformations.

If both τ and θ are fixed at the same time, the relative energies for conformations with specific twisting and bending coordinates can be calculated. By varying the fixed τ and θ values, a two-dimensional potential energy surface that consists of hundreds of data points can be generated, as shown in Figure 38.

VIBRATIONAL HAMILTONIAN

As previously discussed in Chapter II, for molecules that have two strongly coupled large-amplitude vibrations, in this case for 14BZD, the ring-twisting vibration ν_{25} and the ring-bending vibration ν_{48}, the two-dimensional vibrational Hamiltonian operator is given by

$$\hat{\mathbf{H}}_{\text{vib}} = -\frac{\hbar^2}{2}\left[\frac{\partial}{\partial\tau}g_{44}(q_4,q_5)\frac{\partial}{\partial\tau} + \frac{\partial}{\partial\tau}g_{45}(q_4,q_5)\frac{\partial}{\partial\theta} + \frac{\partial}{\partial\theta}g_{45}(q_4,q_5)\frac{\partial}{\partial\tau} + \frac{\partial}{\partial\theta}g_{55}(q_4,q_5)\frac{\partial}{\partial\theta}\right] + \hat{\mathbf{V}}(\tau,\theta) \quad (10.1)$$

where τ and θ are the ring-twisting and ring-bending coordinates, respectively. The g_{44}

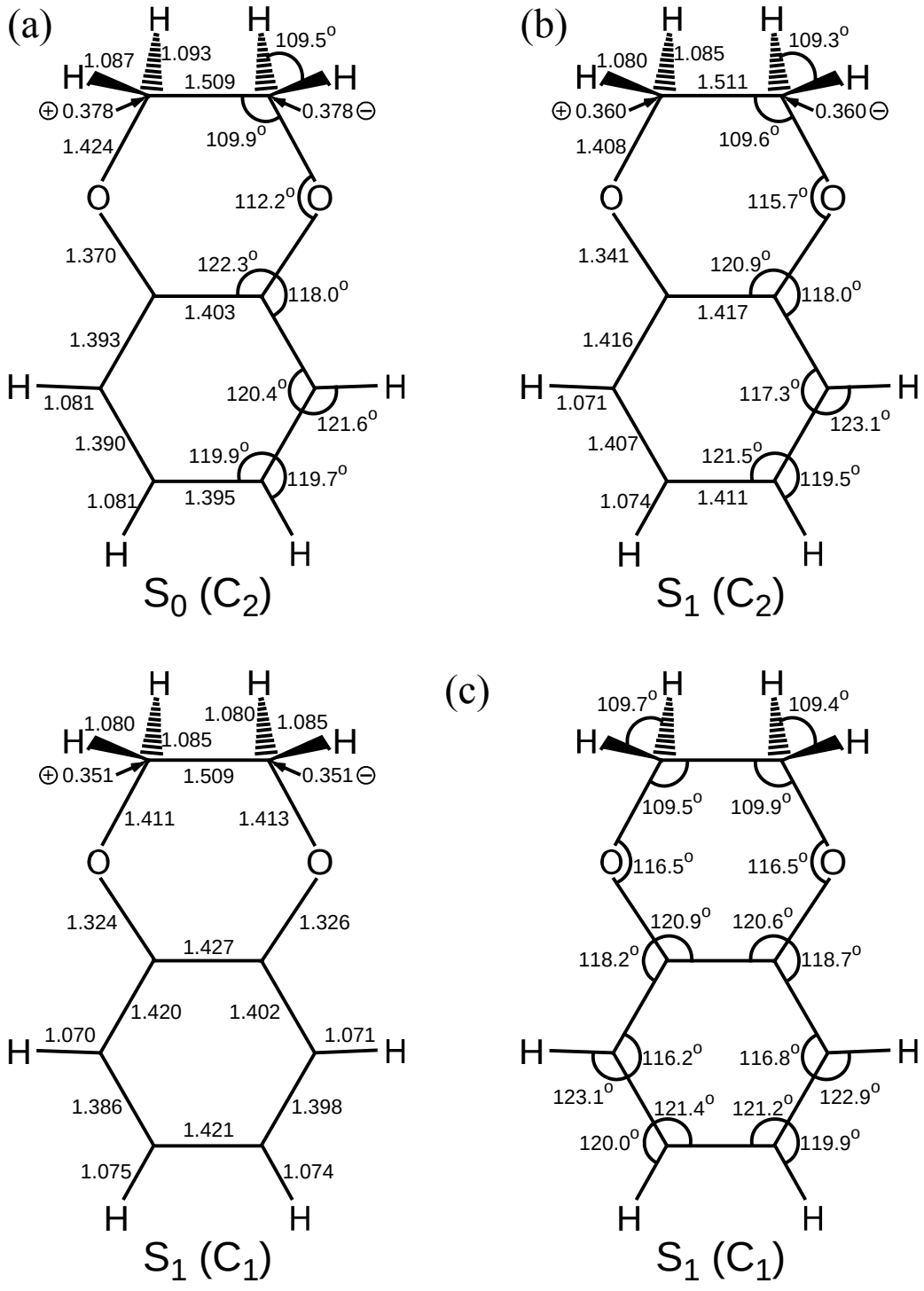

Figure 35. The calculated structures of 1,4-benzodioxan (a) for C_2 symmetry in the S_0 state from MP2/cc-pVTZ calculation; (b) for C_2 symmetry in the $S_1(\pi,\pi^*)$ state from the CIS/6-31G(d) calculation; (c) for C_1 symmetry in the $S_1(\pi,\pi^*)$ state from CIS/6-311++G(d,p) calculation.

TABLE 24: Calculated Relative Energies (cm^{-1}) for Different Structures of 1,4-Benzodioxan in Its S_0 Ground and $S_1(\pi,\pi^*)$ Excited States.

Structure	S_0				S_1
	HF	B3LYP	MP2		CIS
	6-311++G(d,p)	6-311++G(d,p)	6-311++G(d,p)	cc-pVTZ	6-311++G(d,p)
C_{2v} (planar)	3572	3265	4509	4095	7166
C_s (bent)	2219	2360	2576	2722	4698
C_2 (twisted)	0	0	0	0	0
C_1 (twisted & bent)					1318

TABLE 25: Calculated Frequencies (cm^{-1}) for 1,4-Benzodioxan in Its S_0 Ground and $S_1(\pi,\pi^*)$ Excited States.

Sym.	ν		Description	S_0	S_1	
$C_{2v}(C_2)$	C_{2v}	C_2		C_2[a]	C_2[b]	C_1[c]
A_1 (A)	1	1	C-H sym. stretch (ip)	3083	3276	3273
	2	2	C-H sym. stretch (op)	3067	3241	3233
	3	4	CH_2 sym. stretch (ip)	2905	3083	3082
	4	5	benzene C-C stretch	1602	1714	1465
	5	6	benzene C-C stretch	1502	1562	1545
	6	7	CH_2 deformation (ip)	1473	1617	1606
	7	8	CH_2 wag (op)	1385	1519	1562
	8	9	benzene C-C stretch	1321	1806	1682
	9	11	sat. ring (C-O) stretch	1252	1373	1375
	10	12	C-H wag (op,op')	1157	1243	1204
	11	14	sat. ring (C-O) stretch	1066	1170	1163
	12	15	C-H wag (op,ip')	1029	1045	1031
	13	17	sat. ring (C-C) stretch	886	957	951
	14	19	benzene C-C stretch	734	763	752
	15	21	benzene ring bend	571	525	537
	16	23	sat. ring bend	462	485	492
A_2 (A)	17	3	CH_2 asym. stretch (op)	2995	3165	3164
	18	10	CH_2 twist (ip)	1286	1408	1412
	19	13	CH_2 rock (op)	1105	1211	1213
	20	16	C-H wag (op, op')	952	905	957
	21	18	C-H wag (op, ip')	845	622	717
	22	20	benzene ring bend	720	540	646
	23	22	benzene ring bend	555	390	366
	24	24	skeletal twist	323	336	299
	25	25	sat. ring twist	165	155	154
B_1 (B)	26	26	C-H asym. stretch (ip)	3075	3274	3270
	27	27	C-H asym. stretch (op)	3057	3225	3217
	28	29	CH_2 sym. stretch (op)	2916	3089	3089
	29	30	benzene C-C stretch	1619	1557	1578
	30	31	CH_2 deformation (op)	1479	1617	1612
	31	32	benzene C-C stretch	1463	1368	1370
	32	33	CH_2 wag (ip)	1371	1469	1440
	33	34	C-H wag (ip, ip')	1285	1540	1531

TABLE 25: Continued.

Sym.	ν		Description	S_0	S_1	
$C_{2v}(C_2)$	C_{2v}	C_2		C_2[a]	C_2[b]	C_1[c]
B_1 (B)	34	36	sat. ring (C-O) stretch	1189	1232	1257
	35	37	C-H wag (ip, op')	1114	1130	1111
	36	38	sat. ring (C-O) stretch	1059	1149	1151
	37	41	benzene ring bend	831	884	892
	38	43	benzene ring bend	642[d]	665	665
	39	44	sat. ring bend	494	493	483
	40	46	sat. ring bend	376	375	370
B_2 (B)	41	28	CH_2 asym. stretch (ip)	2995	3166	3168
	42	35	CH_2 twist (op)	1243	1345	1348
	43	39	CH_2 rock (ip)	930[d]	1001	1002
	44	40	C-H wag (ip, op')	925	759	834
	45	42	C-H wag (ip, ip')	747	517	633
	46	45	benzene ring bend	462	412	433
	47	47	sat. ring flap	297	153	198
	48	48	sat. ring bend	104	82	107

[a] Calculated using the B3LYP/6-311++G(d,p) basis set with GAUSSIAN 03. The scaling factors are 0.985 for frequencies less than 1800 cm^{-1} and 0.964 for frequencies greater than 2800 cm^{-1}.

[b] Calculated using the CIS/6-31G(d) basis set with GAUSSIAN 03. The scaling factors are 0.976 for frequencies less than 1800 cm^{-1} and 0.955 for frequencies greater than 2800 cm^{-1}.

[c] Calculated using the CIS/6-311++G(d,p) basis set with GAUSSIAN 03. The scaling factors are 0.985 for frequencies less than 1800 cm^{-1} and 0.964 for frequencies greater than 2800 cm^{-1}.

[d] Vibrations that are strongly coupled.

TABLE 26: Relative Energies for the Twisted Conformations (C_2 Structure) of 1,4-Benzodioxan with Fixed Twisting Angle τ from the MP2/cc-pVTZ Calculations.

D(-O-C-C-O-)	τ (degree)	τ (rad)	ΔE (cm^{-1})[a]
-90	-41.67	-0.7272787	3184.5
-85	-39.57	-0.6906268	1928.0
-80	-37.33	-0.6515314	1021.3
-75	-34.98	-0.6105162	425.9
-70	-32.58	-0.5686283	99.6
-65	-30.12	-0.5256932	0
-60	-27.61	-0.4818854	85.2
-55	-25.15	-0.4389503	315.6
-50	-22.70	-0.3961897	655.0
-45	-20.28	-0.3539528	1069.9
-40	-17.90	-0.3124139	1530.8
-35	-15.57	-0.2717478	2009.9
-30	-13.27	-0.2316052	2482.4
-25	-11.00	-0.1919862	2925.9
-20	-8.77	-0.1530654	3319.8
-15	-6.56	-0.1144936	3646.8
-10	-4.36	-0.0760964	3891.9
-5	-2.18	-0.0380482	4043.7
0	0	0	4095.2
5	2.18	0.0380482	4043.7
10	4.36	0.0760964	3891.9
15	6.56	0.1144936	3646.8
20	8.77	0.1530654	3319.8
25	11.00	0.1919862	2925.9
30	13.27	0.2316052	2482.4
35	15.57	0.2717478	2009.9
40	17.90	0.3124139	1530.8
45	20.28	0.3539528	1069.9
50	22.70	0.3961897	655.0
55	25.15	0.4389503	315.6
60	27.61	0.4818854	85.2
65	30.12	0.5256932	0
70	32.58	0.5686283	99.6

TABLE 26: Continued.

D(-O-C-C-O-)	τ (degree)	τ (rad)	ΔE (cm^{-1})[a]
75	34.98	0.6105162	425.9
80	37.33	0.6515314	1021.3
85	39.57	0.6906268	1928.0
90	41.67	0.7272787	3184.5

[a] All energies are relative to the lowest energy twisted conformations at $\tau = \pm 30.1°$

TABLE 27: Relative Energies for the Bent Conformations (C_s Structure) of 1,4-Benzodioxan with Fixed Bending Angle θ from the MP2/cc-pVTZ Calculations.

D(-C=C-O-C-)	θ (degree)	θ (rad)	ΔE (cm^{-1})[a]
-70	-36.98	-0.6454926	7977.3
-65	-34.52	-0.6024178	5475.5
-60	-31.88	-0.5563237	3993.5
-55	-29.18	-0.5092696	3185.7
-50	-26.47	-0.4619188	2814.9
-45	-23.87	-0.4166625	2721.9
-40	-21.06	-0.3675838	2799.9
-35	-18.38	-0.3207741	2975.4
-30	-15.72	-0.2743309	3197.6
-25	-13.07	-0.2281145	3430.9
-20	-10.44	-0.1821775	3649.9
-15	-7.82	-0.1364673	3836.0
-10	-5.21	-0.0908967	3977.3
-5	-2.60	-0.0454484	4065.4
0	0	0	4095.2
5	2.60	0.0454484	4065.4
10	5.21	0.0908967	3977.3
15	7.82	0.1364673	3836.0
20	10.44	0.1821775	3649.9
25	13.07	0.2281145	3430.9
30	15.72	0.2743309	3197.6
35	18.38	0.3207741	2975.4
40	21.06	0.3675838	2799.9
45	23.87	0.4166625	2721.9
50	26.47	0.4619188	2814.9
55	29.18	0.5092696	3185.7
60	31.88	0.5563237	3993.5
65	34.52	0.6024178	5475.5
70	36.98	0.6454926	7977.3

[a] All energies are relative to the lowest energy twisted conformations at $\tau = \pm 30.1°$

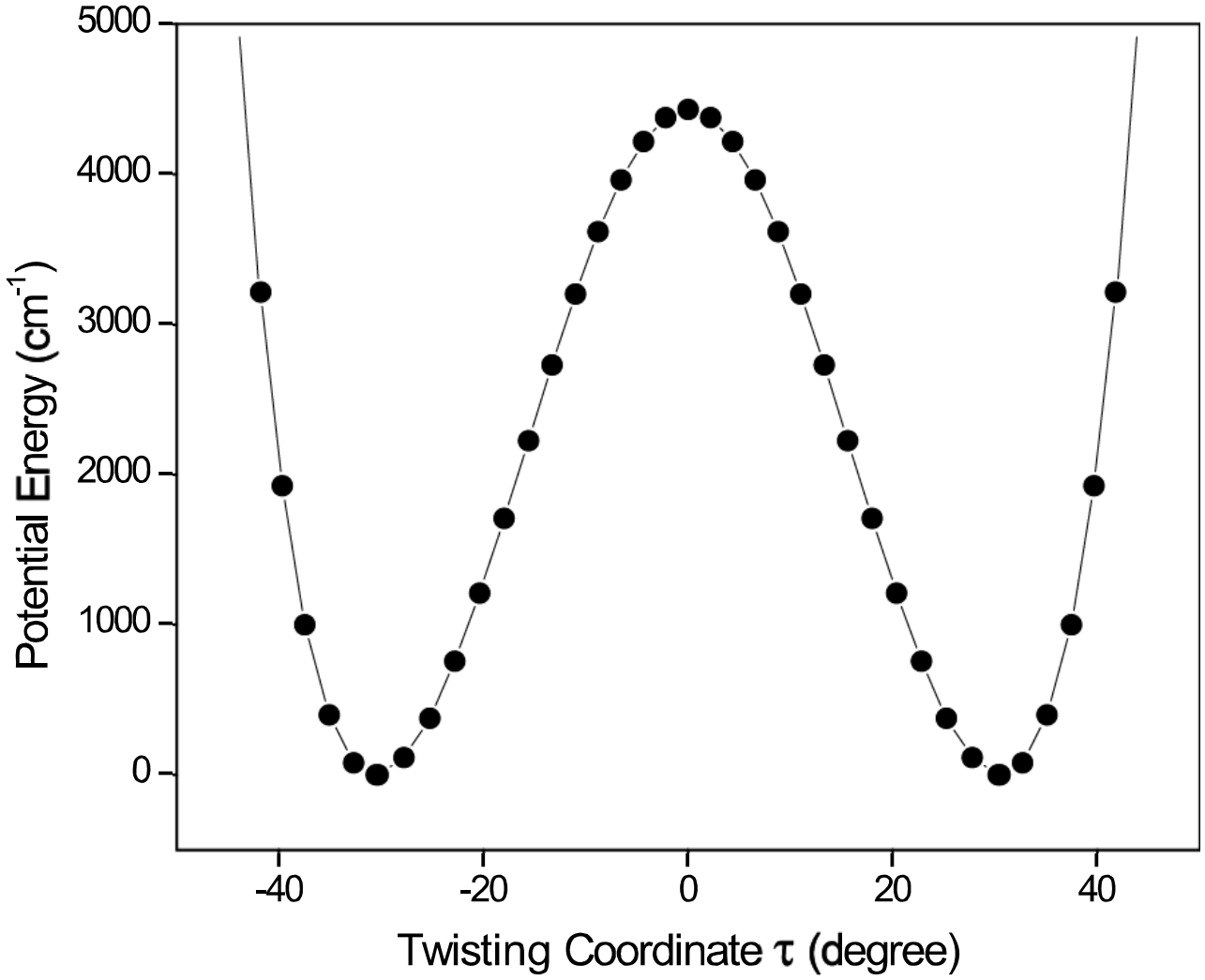

Figure 36. The one-dimensional ring-twisting potential energy curve from MP2/cc-pVTZ calculations for 1,4-benzodioxan.

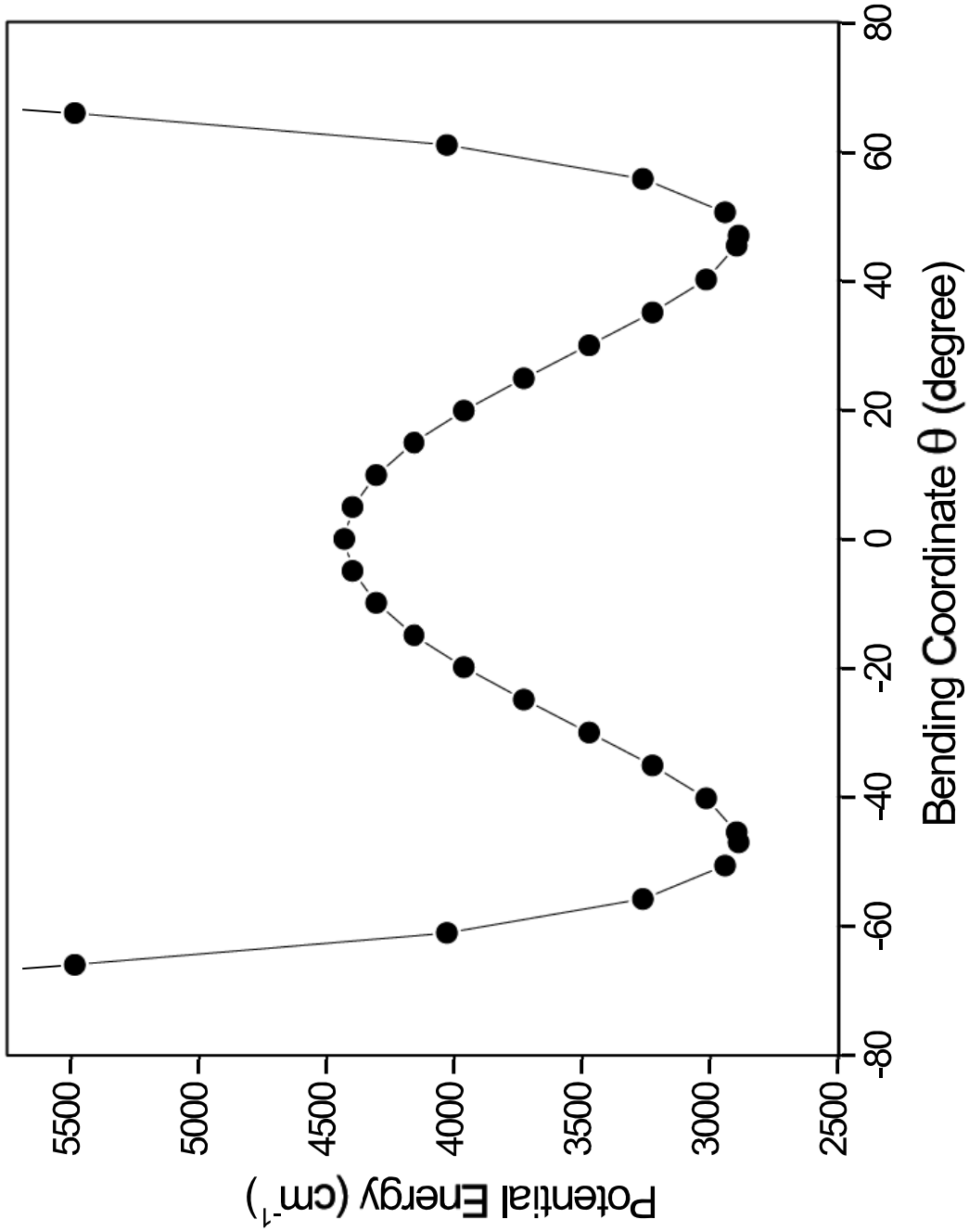

Figure 37. The one-dimensional ring-bending potential energy curve from MP2/cc-pVTZ calculations for 1,4-benzodioxan.

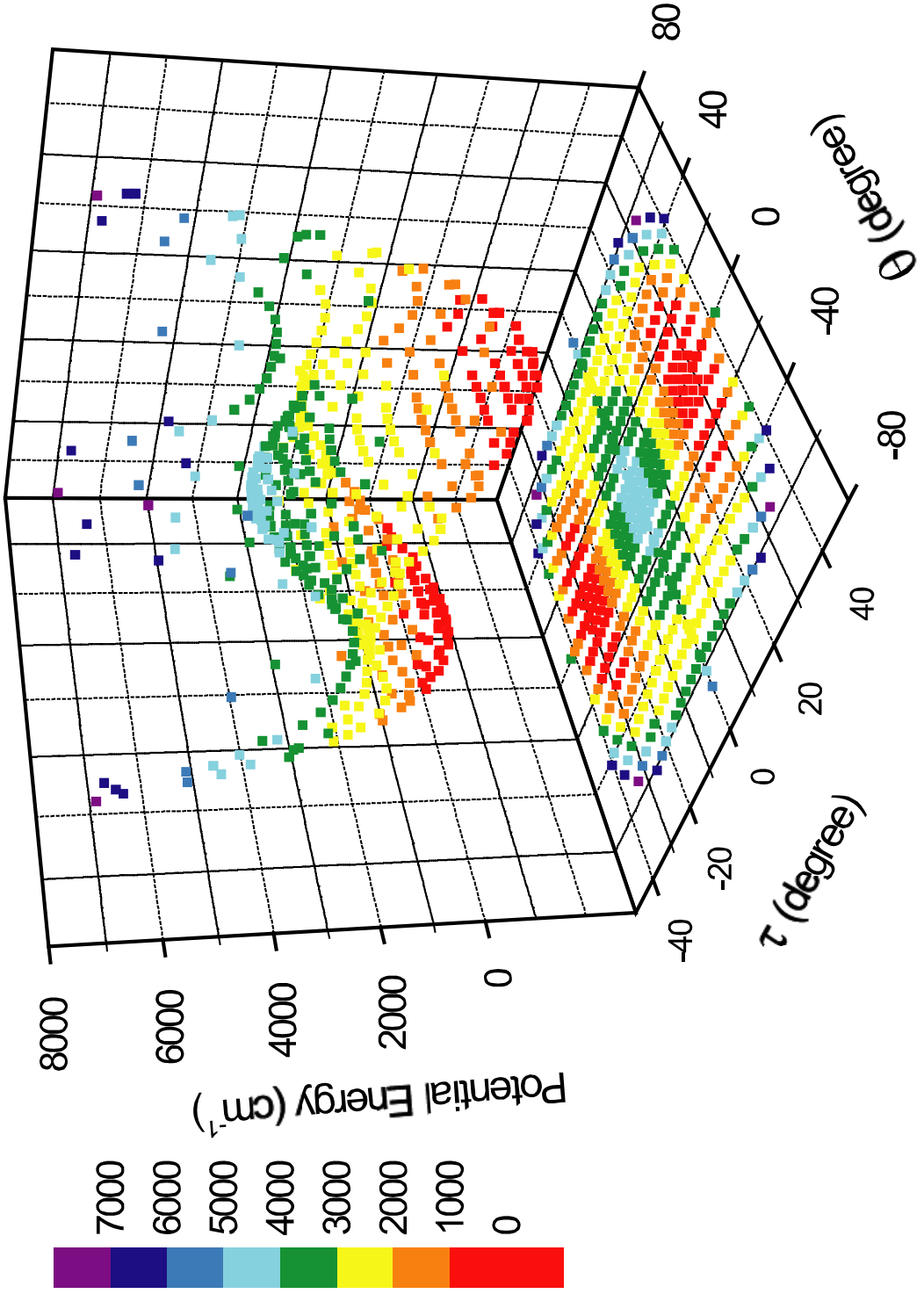

Figure 38. Potential energy data points diagram for 1,4-benzodioxan S_0 state from the MP2/cc-pVTZ calculations.

and g_{55} expressions are the reciprocal reduced masses for the ring-twisting and ring-bending vibrations, respectively. The g_{45} term is the interaction cross term for these two vibrations.

KINETIC ENERGY EXPRESSIONS

The utilization of vector methods for determining the kinetic energy expressions for cyclic molecules in either one or two-dimensional analysis have previously been described.[19-21,60,61] The derivative $\delta\vec{\mathbf{r}}_i / \delta q$ can be calculated. This is the derivative of the atom coordinate vector for the i^{th} atom, $\vec{\mathbf{r}}_i$, in the center-of-mass system with respect to the vibrational coordinate q, in this case, the ring-twisting coordinate τ or the ring-bending coordinate θ. These derivatives can be used to set up the 5×5 G^{-1} matrix, which is then inverted to obtain the g_{ij} (i,j = 4,5) matrix elements.

During the calculation, it is assumed that all bond distances remain fixed during the vibration, that the bisector of each CH_2 group remains coincident with the corresponding C-C-C angle bisector, and that each C-H bond lies along the corresponding C-C-C angle bisector of the benzene ring. Figure 39 shows the definition of the vectors that are used to define the atom positions and the definition of the ring-twisting coordinate τ and the ring-bending coordinate θ for 14BZD. Table 28 presents the components of each bond vector $\vec{\mathbf{u}}_i = a_i\vec{\mathbf{i}} + b_i\vec{\mathbf{j}} + c_i\vec{\mathbf{k}}$. These vectors can be used not only for 14BZD but also for

any molecules with a symmetric saturated six-membered ring attached to a benzene ring.

Using the planar structures from MP2/cc-pVTZ calculations, the kinetic energy expressions for the S_0 ground state of 14BZD was obtained as

$$\begin{aligned} g_{44}^{S_0}(\tau,\theta) = {} & 0.033476535 - 0.006855096\tau^2 - 0.014646045\tau^4 + 0.003929556\tau^6 \\ & - 0.0031163820^2 + 0.0011333620^4 - 0.0001067930^6 \\ & + 0.007942282\tau^2\theta^2 - 0.003060725\tau^4\theta^2 - 0.001319295\tau^2\theta^4 \end{aligned} , \quad (10.2)$$

$$\begin{aligned} g_{55}^{S_0}(\tau,\theta) = {} & 0.044329620 - 0.001141322\tau^2 + 0.002428906\tau^4 + 0.000121541\tau^6 \\ & - 0.0155988390^2 + 0.0051395340^4 - 0.0006862600^6 \\ & + 0.009920440\tau^2\theta^2 - 0.000107406\tau^4\theta^2 - 0.003277779\tau^2\theta^4 \end{aligned} , \quad (10.3)$$

$$\begin{aligned} g_{45}^{S_0}(\tau,\theta) = {} & -0.014930208\tau\theta + 0.0083726413\tau^3\theta \\ & + 0.006351398\tau\theta^3 - 0.0040797066\tau^3\theta^3 \end{aligned} , \quad (10.4)$$

and the kinetic energy expressions for the 14BZD $S_1(\pi,\pi^*)$ excited state are

$$\begin{aligned} g_{44}^{S_1}(\tau,\theta) = {} & 0.035277287 - 0.006634635\tau^2 - 0.012450464\tau^4 + 0.003244677\tau^6 \\ & - 0.0035832930^2 + 0.0014845870^4 - 0.0001735620^6 \\ & + 0.007809779\tau^2\theta^2 - 0.002474722\tau^4\theta^2 - 0.001570280\tau^2\theta^4 \end{aligned} , \quad (10.5)$$

$$\begin{aligned} g_{55}^{S_1}(\tau,\theta) = {} & 0.043567071 - 0.001398840\tau^2 + 0.001948076\tau^4 + 0.000400976\tau^6 \\ & - 0.0155155220^2 + 0.0051310210^4 - 0.0006891750^6 \\ & + 0.009406176\tau^2\theta^2 - 0.000573554\tau^4\theta^2 - 0.003044145\tau^2\theta^4 \end{aligned} , \quad (10.6)$$

$$\begin{aligned} g_{45}^{S_1}(\tau,\theta) = {} & -0.014264471\tau\theta + 0.007050807\tau^3\theta \\ & + 0.0061752092\tau\theta^3 - 0.003623517\tau^3\theta^3 \end{aligned} . \quad (10.7)$$

These g_{ij} (i,j = 4,5) expressions for both S_0 and $S_1(\pi,\pi^*)$ states are presented graphically in Figures 40 and 41, respectively. These figures show that g_{44} and g_{45} depend on both coordinates τ and θ while g_{55} depends mostly only on the ring-bending coordinate θ.

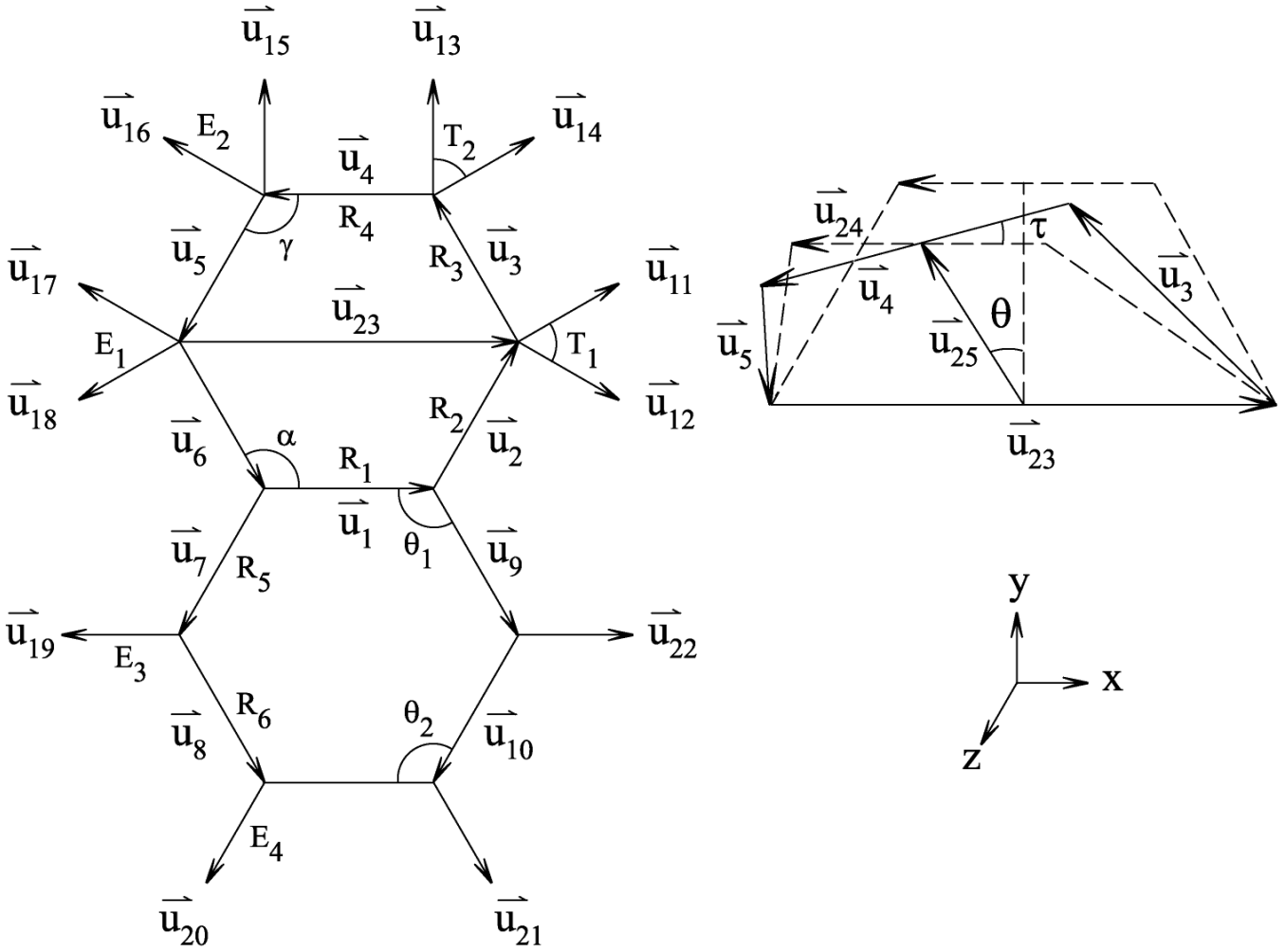

Figure 39. Vectors for defining the atom positions of 1,4-benzodioxan and the definition of the ring-twisting coordinate τ and the ring-bending coordinate θ.

TABLE 28: Components of the Bond Vectors $\vec{u}_i = a_i\vec{i} + b_i\vec{j} + c_i\vec{k}$ for the Ring-Twisting and Ring-Bending Vibrations of 1,4-Benzodioxan.

Vector $\vec{u}_i$	a_i	b_i	c_i
$\vec{u}_1$	R_1	0	0
$\vec{u}_2$	X_2	Y_2	0
$\vec{u}_3$	X_3	Y_3	Z_3
$\vec{u}_4$	X_4	Y_4	Z_4
$\vec{u}_5$	X_5	Y_5	Z_5
$\vec{u}_6$	X_2	$-Y_2$	0
$\vec{u}_7$	X_7	Y_7	0
$\vec{u}_8$	X_8	Y_8	0
$\vec{u}_9$	$-X_7$	Y_7	0
$\vec{u}_{10}$	$-X_8$	Y_8	0
$\vec{u}_{11}$	$p_x + v_x$	$p_y + v_y$	$p_z + v_z$
$\vec{u}_{12}$	$p_x - v_x$	$p_y - v_y$	$p_z - v_z$
$\vec{u}_{13}$	$P_x + V_x$	$P_y + V_y$	$P_z + V_z$
$\vec{u}_{14}$	$P_x - V_x$	$P_y - V_y$	$P_z - V_z$
$\vec{u}_{15}$	$-P_x + V_x$	$-P_y + V_y$	$-P_z + V_z$
$\vec{u}_{16}$	$-P_x - V_x$	$-P_y - V_y$	$-P_z - V_z$
$\vec{u}_{17}$	$-p_x + v_x$	$-p_y + v_y$	$-p_z + v_z$
$\vec{u}_{18}$	$-p_x - v_x$	$-p_y - v_y$	$-p_z - v_z$
$\vec{u}_{19}$	X_{19}	Y_{19}	0
$\vec{u}_{20}$	X_{20}	Y_{20}	0
$\vec{u}_{21}$	$-X_{20}$	Y_{20}	0
$\vec{u}_{22}$	$-X_{19}$	Y_{19}	0
$\vec{u}_{23}$	X_{23}	0	0
$\vec{u}_{24}$	$-R_4$	0	0
$\vec{u}_{25}$	0	Y_{25}	Z_{25}

TABLE 28: Continued.

$X_2 = -R_2 \cos\alpha;\ Y_2 = R_2 \sin\alpha\ ;$

$X_4 = -R_4 \cos\tau;\ Y_4 = -R_4 \sin\tau\sin\theta;\ Z_4 = R_4 \sin\tau\cos\theta\ ;$

$X_7 = R_5 \cos\theta_1;\ Y_7 = -R_5 \sin\theta_1\ ;$

$X_8 = -R_6 \cos\theta_2;\ Y_8 = -R_6 \sin\theta_2\ ;$

$X_{19} = -E_3 \cos\dfrac{\theta_2 - \theta_1}{2};\ Y_{19} = -E_3 \sin\dfrac{\theta_2 - \theta_1}{2}\ ;$

$X_{20} = -E_4 \cos\dfrac{\theta_2}{2};\ Y_{20} = -E_4 \sin\dfrac{\theta_2}{2}\ ;$

$X_{23} = R_1 - 2R_2 \cos\alpha;\ Y_{25} = R_3 \sin\gamma\cos\theta;\ Z_{25} = R_3 \sin\gamma\sin\theta\ ;$

$X_3 = X_5 = -\dfrac{X_4 + X_{23}}{2};$

Y_3, Z_3, Y_5, and Z_5 can be solved from the following equations:

$$\begin{cases} Y_3 + Y_5 = -Y_4 \\ Z_3 + Z_5 = -Z_4 \\ Y_3^2 + Z_3^2 = Y_5^2 + Z_5^2 = R_3^2 - X_3^2 \end{cases};$$

$\vec{\mathbf{p}} = -E_1 \cos\dfrac{T_1}{2} \dfrac{\dfrac{\vec{\mathbf{u}}_2}{R_2} - \dfrac{\vec{\mathbf{u}}_3}{R_3}}{2\cos(\dfrac{\alpha+\gamma}{2})};\ \vec{\mathbf{v}} = -E_1 \sin\dfrac{T_1}{2} \dfrac{\vec{\mathbf{u}}_2 \times \vec{\mathbf{u}}_3}{R_2 R_3 \sin(\alpha+\gamma)}$, where p_x, p_y, and p_z are the components of the vector $\vec{\mathbf{p}}$, and v_x, v_y, and v_z are the components of the vector $\vec{\mathbf{v}}$;

$\vec{\mathbf{P}} = E_2 \cos\dfrac{T_2}{2} \dfrac{\dfrac{\vec{\mathbf{u}}_3}{R_3} - \dfrac{\vec{\mathbf{u}}_4}{R_4}}{2\cos\dfrac{\gamma}{2}};\ \vec{\mathbf{V}} = E_2 \sin\dfrac{T_2}{2} \dfrac{\vec{\mathbf{u}}_3 \times \vec{\mathbf{u}}_4}{R_3 R_4 \sin\gamma}$, where P_x, P_y, and P_z are the components of the vector $\vec{\mathbf{P}}$, and V_x, V_y, and V_z are the components of the vector $\vec{\mathbf{V}}$;

where τ and θ are the ring-twisting and ring-bending coordinates, respectively, as shown in Figure 39.

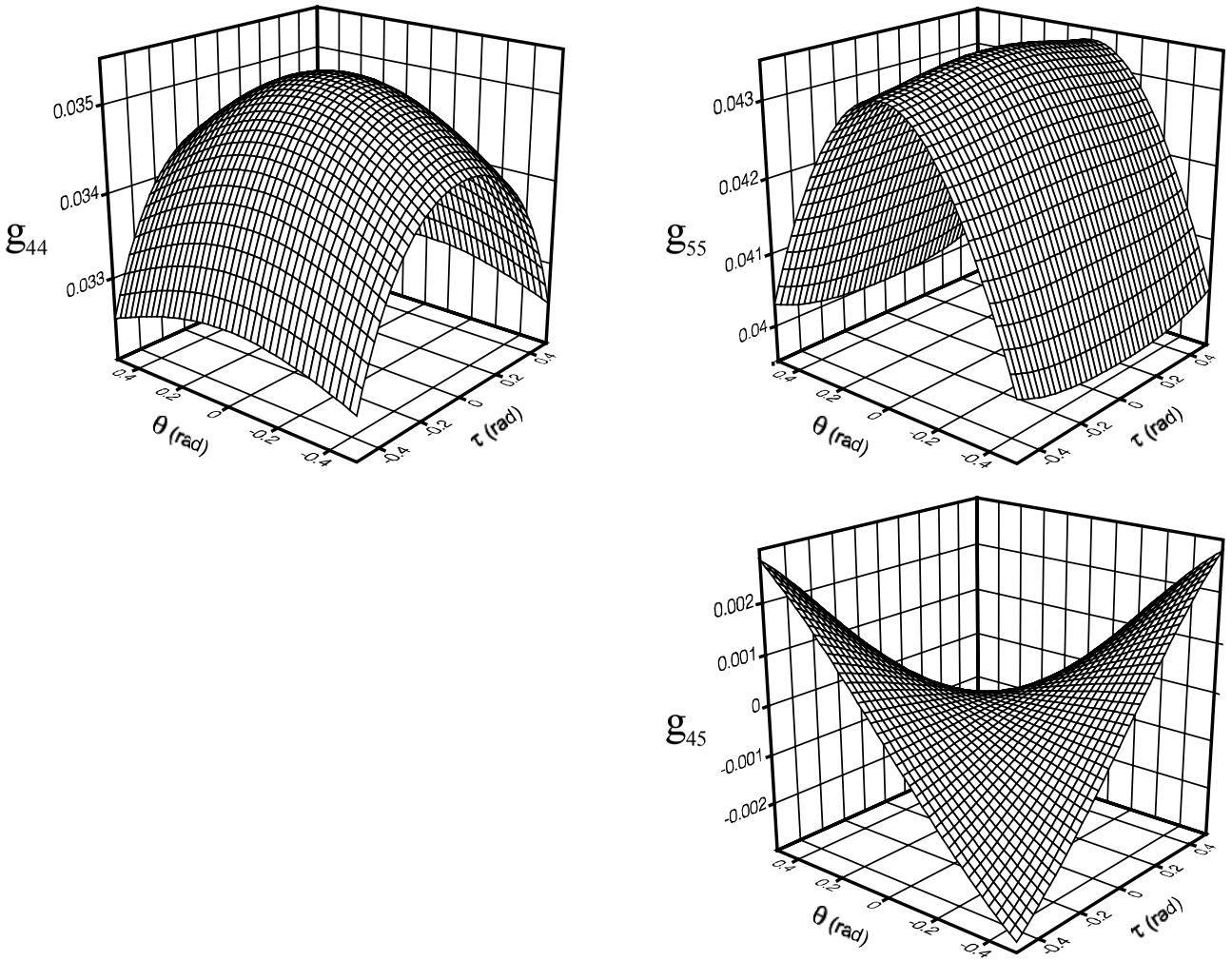

Figure 40. The coordinate dependence of g_{44}, g_{45}, and g_{55} for 1,4-benzodioxan S_0 state. τ and θ are the ring-twisting and ring-bending coordinates, respectively.

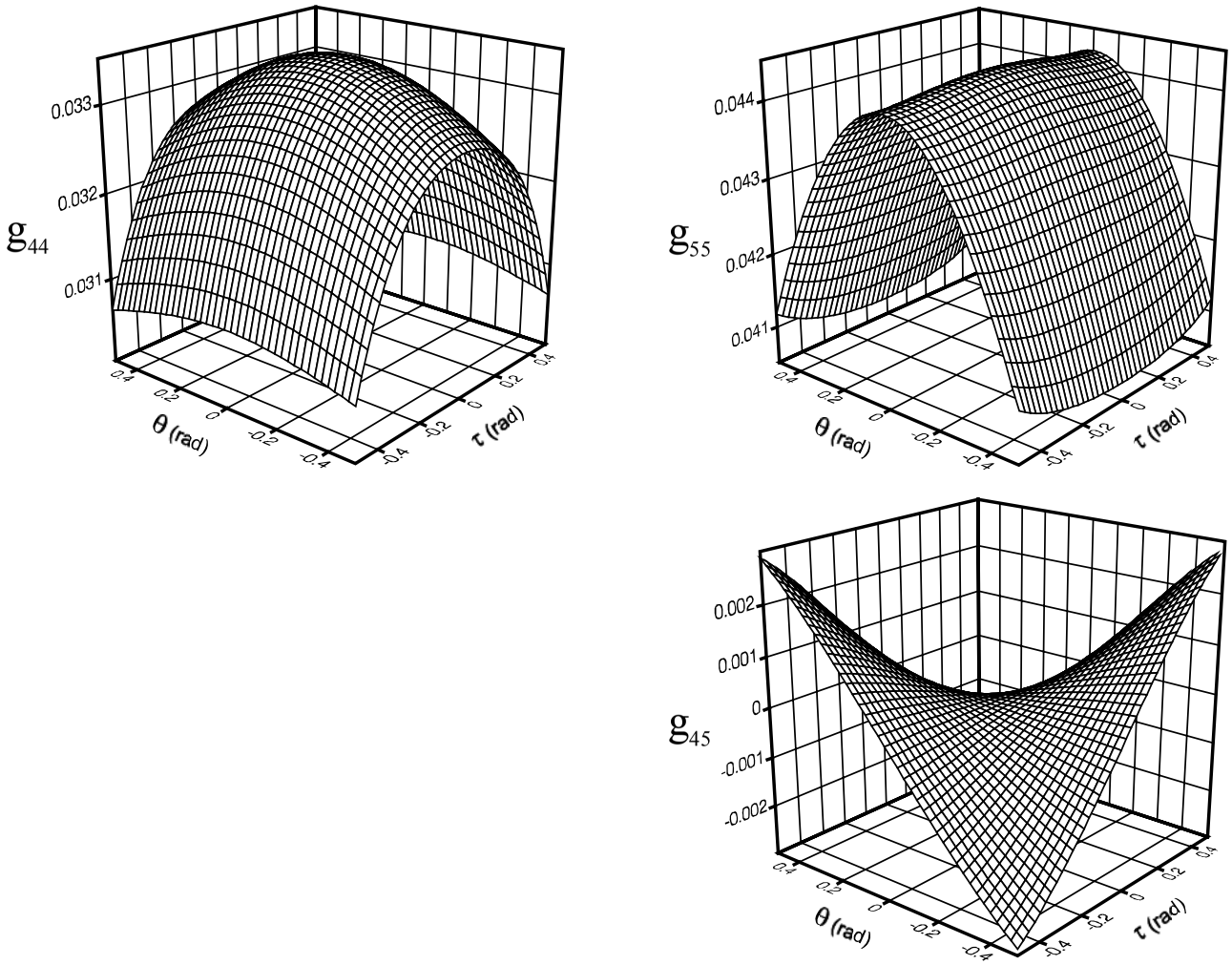

Figure 41. The coordinate dependence of g_{44}, g_{45}, and g_{55} for 1,4-benzodioxan S_1 state. τ and θ are the ring-twisting and ring-bending coordinates, respectively.

ASSIGNMENTS OF SPECTRA

14BZD is related to the previously studied molecule 2,3-dihydro-1,4-dioxin[10] (DHD). With a planar benzene ring replacing the double bond, 14BZD is also expected to have twisted C_2 symmetry with a high barrier to planarity. The MP2/cc-pVTZ calculation predicts the molecule to have a barrier to planarity of 4095 cm^{-1} in the S_0 state. With such a high barrier, the energy levels close to the bottom of the twisting potential energy wells are nearly degenerate. The symmetries of the nearly degenerate ground states (v_T = 0,1) are A_1 and A_2, respectively, assuming the molecule to have perturbed C_{2v} symmetry, as described in Chapter IX.

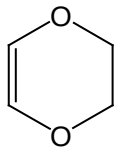

DHD

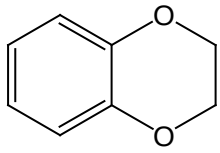

14BZD

Figures 42 and 43 show the jet-cooled fluorescence excitation spectra (FES) and the room-temperature ultraviolet (UV) absorption spectra of 14BZD in the 0-900 cm^{-1} and 900-1800 cm^{-1} regions, respectively, relative to the electronic band origin of 0_0^0 at 35,563.1 cm^{-1}. Figure 44 shows the FES spectra under relatively hot conditions compared with the UV absorption spectra. This was achieved by decreasing the backing pressure of the He carrier gas and by increasing the distance from the nozzle to the laser beam. Table 29 presents the frequencies and assignments in the FES and

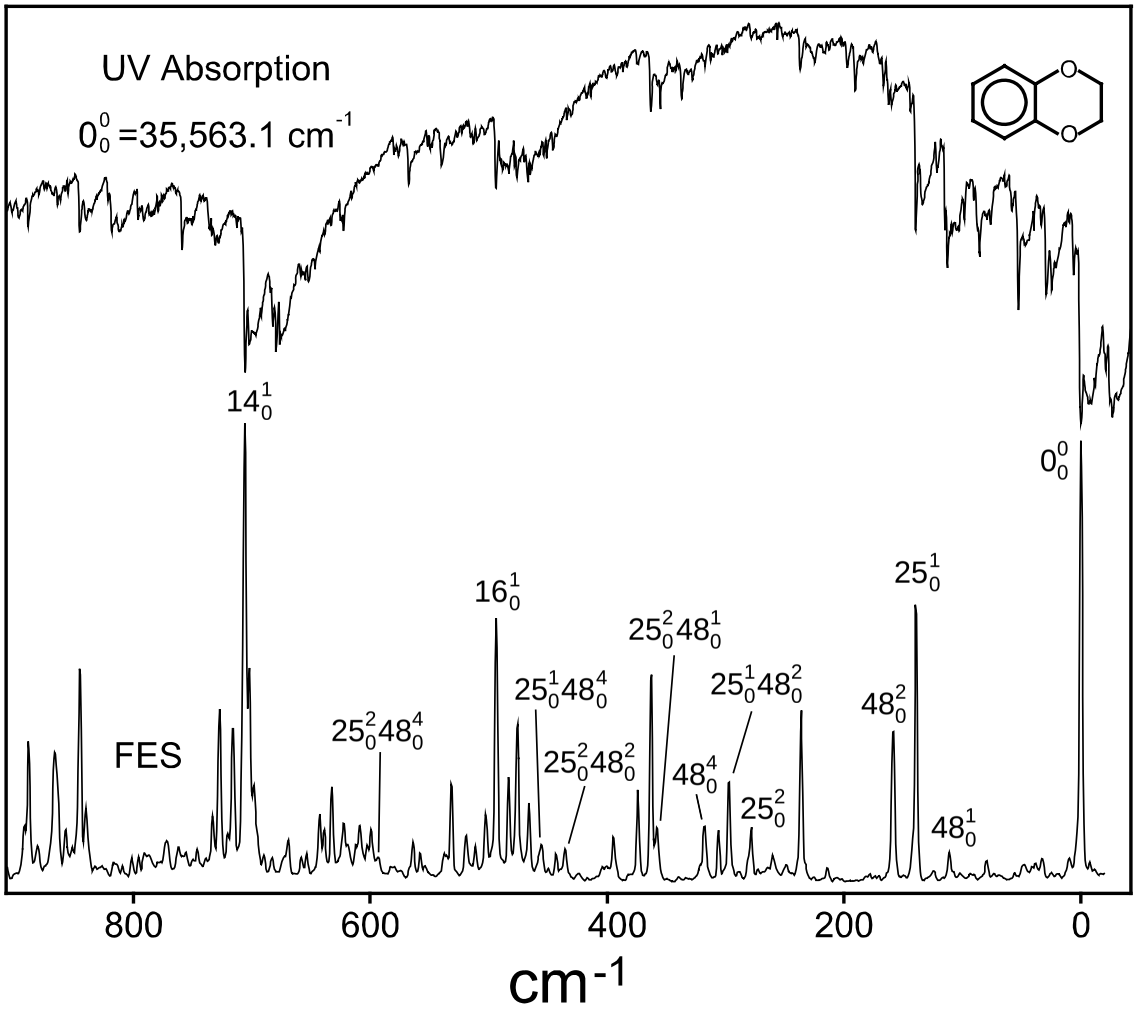

Figure 42. Fluorescence excitation spectra of jet-cooled 1,4-benzodioxan and ultraviolet absorption spectra at ambient temperature in the 0-900 cm^{-1} region.

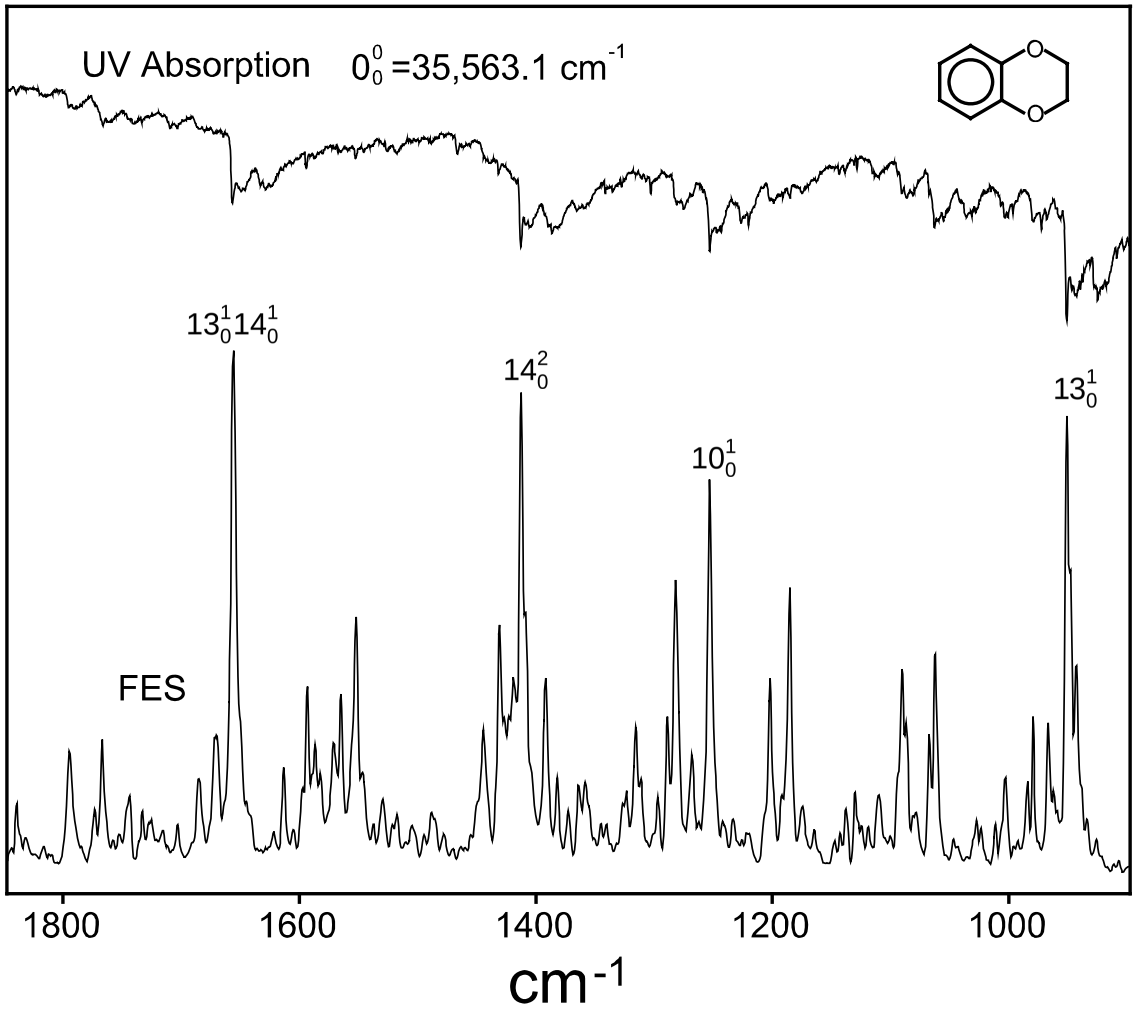

Figure 43. Fluorescence excitation spectra of jet-cooled 1,4-benzodioxan and ultraviolet absorption spectra at ambient temperature in the 900-1800 cm^{-1} region.

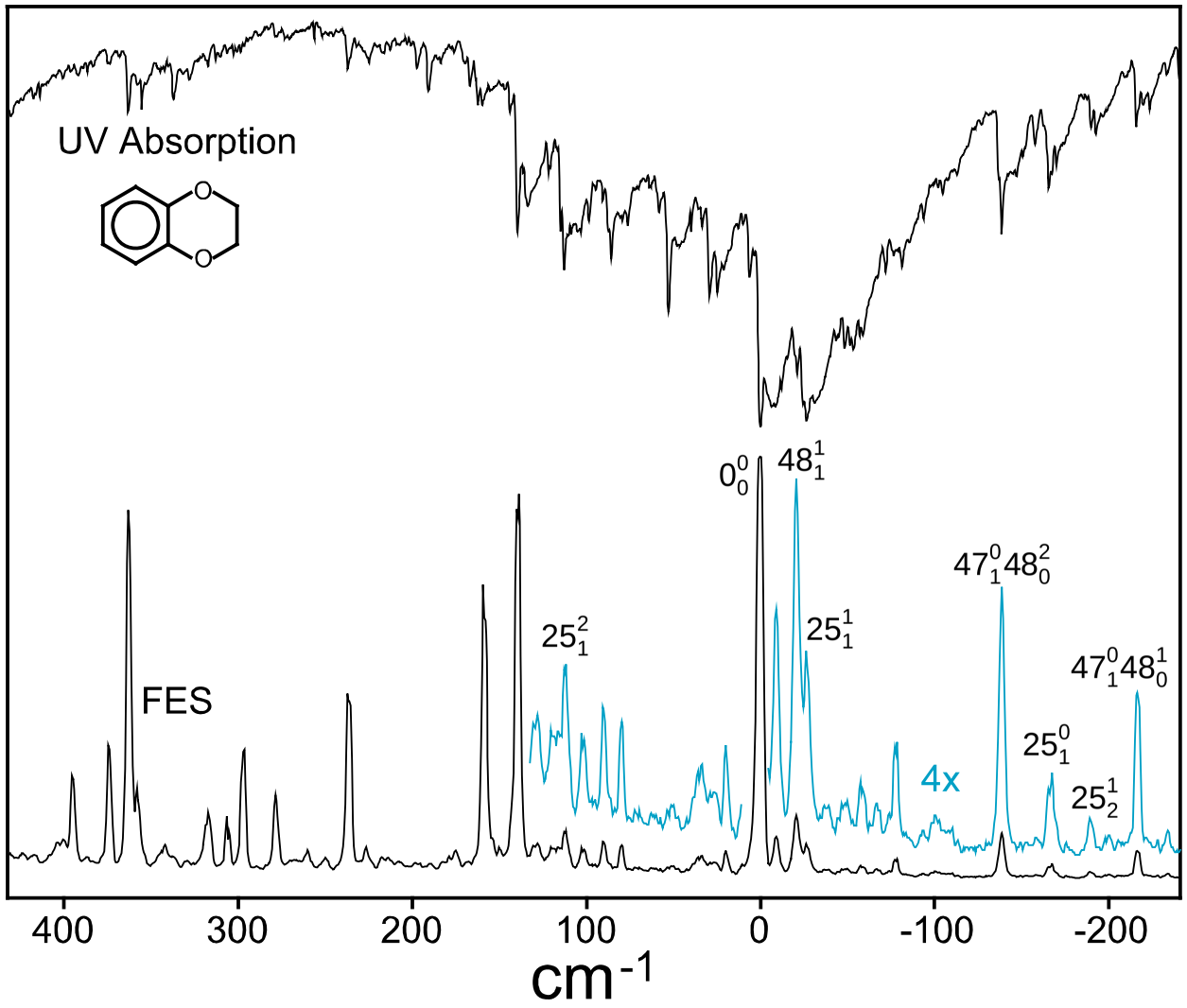

Figure 44. Ultraviolet absorption spectra and fluorescence excitation spectra of hot bands of 1,4-benzodioxan.

TABLE 29: Fluorescence Excitation (FES), Ultraviolet (UV) Absorption Frequencies (cm^{-1}) and Assignments for 1,4-Benzodioxan.

This Work							GH[a]			
FES		UV		Calc.[b]	Inferred[c]	Assignment	FES		UV		Assignment
		-761.8	w		-761.2	$14_1^0 25_1^1$					
		-734.7	m		-734.7	14_1^0					
		-620.5	w		-620.6	$25_1^1 27_2^0$					
		-594.1	m		-594.1	27_2^0					
		-568.4	m		-568.4	15_1^0					
		-561.5	w		-561.5	$46_1^0 48_1^0$					
		-356.6	w		-356.9	27_2^1					
		-246.7	m			?					
		-240.8	m		-241.6	25_4^3			-240.88	vw	$24_2^2 48_1^1$
		-233.7	m		-234.2	$25_1^1 48_2^0$					
		-217.2	w		-217.3	$47_1^0 48_0^1$					
-217	w	-216.0	s		-216.0	25_3^2			-216.10	w	24_2^2
		-192.7	s		-192.1	25_2^1			-193.13	vw	25_2^1
-190	vw	-190.1	m		-190.1	$25_1^0 48_1^1$			-189.98	vw	$25_1^0 48_1^1$
		-170.0	w		-171.0	$25_2^0 48_0^2$					
		-167.3	m			?			-167.87	w	$47_1^0 48_0^1$
-166	vw	-165.6	s		-165.6	25_1^0			-166.06	w	25_1^0
-138	w	-138.4	vs		-137.8	$47_1^0 48_0^2$	-138	vvw	-138.92	m	24_1^1
		-104.6	w		-104.3	48_1^0					
		-93.6	m		-93.1/-94.1	$25_2^0 47_0^2 / 48_4^4$			-94.33	vvw	48_4^4

TABLE 29: Continued.

This Work						GH[a]				
FES		UV		Calc.[b]	Inferred[c]	Assignment	FES		UV		Assignment
		-85.6	w		-85.8	$25_1^0 48_0^1$			-86.08	vvw	
		-81.4	m			?			-81.88	m	25_3^3
-78	vw	---			-78.2	25_3^3			-77.19	m	$25_2^2 48_1^1$
		-71.9	m		-73.0/71.6	$47_0^2 48_3^0 / 48_3^3$			-71.67	m	48_3^3
		-67.4	w		-68.1	$25_0^1 48_2^0$			-68.16	w	$47_0^1 48_4^3$
		-59.0	m		-59.9	47_1^2					
		-52.3	m		-52.0	25_2^2			-53.81	m	25_2^2
		-48.3	w		-48.4	48_2^2			-48.53	m	48_2^2
		-31.1	vs		-28.8	14_1^1					
-26	w	-26.5	vvs		-26.0	25_1^1	-26	vw	-26.91	s	25_1^1
		-24.5	vs		-24.5	48_1^1			-24.66	s	48_1^1
-21	w	-21.0	m			?			-21.57	m	$25_1^1 47_0^1 48_1^0$
		-12.0	w		-12.0	24_1^1					
		-6.3	vs		-6.3	$25_1^0 48_0^2$					
0	vs	0.0	vvs		0.0	0_0^0	0	vs	0	vs	0_0^0
		6.2	m			?			6.03	s	$47_0^1 48_1^0$
		24.7	s			?			24.40	m	$25_1^1 47_0^3 48_3^0$
		29.1	s		30.9/29.5	$48_2^3 / 47_0^2 48_2^0$			28.89	s	$47_0^2 48_2^0$
		52.9	vs		52.9/55.0	$25_1^1 48_0^1 / 48_1^2$			52.61	s	$47_0^3 48_3^0$
							54	vvw	54.13	vw	24_0^1
		58.4	m		58.7	25_3^4					

TABLE 29: Continued.

This Work							GH[a]				
FES		UV		Calc.[b]	Inferred[c]	Assignment	FES		UV		Assignment
80	w	79.5	vw	107	79.8	48_0^1					
		85.8	s		85.8	25_2^3			85.31	m	25_2^3
111	w	112.8	vs		112.7	25_1^2	114	vw	112.39	m	25_1^2
		133.6	s		133.3	$25_1^1 48_0^2$			133.38	vw	
139	s	139.6	vs	154	139.6	25_0^1	139	s	139.30	s	25_0^1
159	s	159.3	w		159.3	48_0^2	159	vw	159.39	w	48_0^2
		166.9	m		168.7	$16_1^1 25_0^1$			166.50	w	$25_0^1 47_0^2 48_2^0$
		190.6	m			?			190.43	w	$25_0^1 47_0^3 48_3^0$
236.5	s	237.2	m	198	237.2/238.6	47_0^2 / 48_0^3	237	vw	236.72	w	47_0^2
278	m	278.3	w		278.3	25_0^2	278	vvw	278.36	vw	25_0^2
297	m	---			298.9	$25_0^1 48_0^2$					
306	m	---		299	306.5	24_0^1					
318	m	317.8	w		317.0/317.8	$47_0^2 48_0^1$ / 48_0^4					
		337.1	m		336.6	$23_0^1 25_1^1$					
		355.4	w		356.8	$23_0^1 25_1^0 48_0^2$					
358	m	357.8	vw		358.1	$25_0^2 48_0^1$					
363	s	363.1	m	366	363.1	23_0^1	363	w	362.88	m	23_0^1
374	m	374.3	w		376.8	$25_0^1 47_0^2$	374	vvw	374.39	vw	$25_0^1 47_0^2$
395	m	---			396.5	$47_0^2 48_0^2$					
435	w	434.2	vw		437.6	$25_0^2 48_0^2$					
443	w	442.8	vw		446.2	$24_0^1 25_0^1$					

TABLE 29: Continued.

This Work							GH[a]		
FES		UV		Calc.[b]	Inferred[c]	Assignment	FES	UV	Assignment
455	w	---			457.4	$25_0^1 48_0^4$			
465	m	465.1	vw		465.8	$24_0^1 48_0^2$			
		467.2	w		467.0	$16_0^1 25_1^1$			
		470.0	vw		469.0	$16_0^1 48_1^1$			
476	s	476.2	w		474.4/475.9	47_0^4 / 48_0^6			
483	m	483.1	w	483	483.1	39_0^1			
493	s	493.5	m	492	493.5	16_0^1			
502	m	503.3	vw		502.7	$23_0^1 25_0^1$			
511	w	510.3	vw		515.5	$25_0^2 47_0^2$			
		513.3	w		513.2	$14_0^1 25_2^1$			
519	m	---			522.4	$23_0^1 48_0^2$			
531.5	m	531.1	vw	537	531.1	15_0^1			
		539.5	m		540.3	$14_0^1 25_1^0$			
553	vw	552.0	vw		553.0	25_0^4			
557	w	---			555.0	$47_0^2 48_0^4$			
564	w	563.6	vw		562.9	$39_0^1 48_0^1$			
		567.4	m		567.5	$14_0^1 47_1^0 48_0^2$			
599	w	---			600.3	$23_0^1 47_0^2$			
609	m	---			612	24_0^2			
622	m	622.8	m		622.7	$25_0^1 39_0^1$			
632	m	633.1	w		633.1	$16_0^1 25_0^1$			

TABLE 29: Continued.

This Work							GH[a]			
FES		UV		Calc.[b]	Inferred[c]	Assignment	FES	UV		Assignment
639	m	638.8	vw		641.4	$23^1_0 25^2_0$				
642.5	m	643.0	vw		642.7	$39^1_0 48^2_0$				
653	w	652.2	m		655.1	$16^1_0 48^2_0$				
658	w	657.3	vw		658.6	$23^1_0 25^1_0 48^2_0$				
669	m	---			670.7	$15^1_0 25^1_0$				
		676.6	s		677.1	14^2_1				
		679.6	vs		679.4	$14^1_0 25^1_1$		678	vs	$18^1_0 25^1_1$
		682.3	s		681.4	$14^1_0 48^1_1$				
690	w	---			690.7	$15^1_0 48^2_0$				
		696.8	m			?				
698	m	---			702.3	$24^1_0 47^2_0 48^2_0$				
702	s	702.0	s	717	702.0	21^1_0				
706	vs	705.9	vs	752	705.9	14^1_0		704	vs	18^1_0
716	m	---				?				
727	m	728.0	m		726.2	23^2_0				
		731.1	m		730.6	?				
		735.9	m		735.0	$14^1_0 47^2_0 48^0_2$				
		758.8	m		758.8	$14^1_0 25^1_1 48^1_0$				
		791.3	m		791.7	$14^1_0 25^3_2$				
		812.3	m		812.9	$13^1_0 47^0_1 48^2_0$				
		818.5	m		818.7	$14^1_0 25^2_1$				

TABLE 29: Continued.

This Work						GH[a]			
FES		UV		Calc.[b]	Inferred[c]	Assignment	FES	UV		Assignment
840	m	840.2	m		839.5	$21^1_0 25^1_0$				
845	s	845.3	m		845.5	$14^1_0 25^1_0$		842	w	$21^1_0 25^1_0$
857	m	857.8	w		856.6	$16^1_0 23^1_0$				
864	m	864.3	w		865.5	$14^1_0 48^2_0$				
867	m	867.5	w		867.6	$23^2_0 25^1_0$				
888	m	888.9	m	892	888.9	37^1_0				
		920.9	m		920.2	$13^1_0 14^1_1$				
		924.9	s		924.8	$13^1_0 25^1_1$		924	s	$14^1_0 25^1_1$
938	m	939.5	w		939.2	$21^1_0 47^2_0$				
943	s	943.0	m		943.1	$14^1_0 47^2_0$				
948	s	947.1	m	957	947.1	20^1_0				
951	vs	951.3	vs	951	951.3	13^1_0		950	s	14^1_0
967	m	967.5	m		966.2	39^2_0				
980	s	979.7	m		980.3	$21^1_0 25^2_0$				
984	m	984.8	vw		984.2	$14^1_0 25^2_0$				
1003	m	1003.4	m		1003	$14^1_0 25^1_0 48^2_0$				
		1036.4	m		1037	$13^1_0 25^3_2$				
1063	s	1062.9	m		1064	$15^2_0 / 13^1_0 25^2_1$				
1067	m	1067.5	m		1069	$14^1_0 23^1_0$				
1087	m	1086.8	m		1087	$20^1_0 25^1_0$				
1090	s	1090.7	m		1091	$13^1_0 25^1_0$				

TABLE 29: Continued.

This Work						GH[a]			
FES		UV		Calc.[b]	Inferred[c]	Assignment	FES	UV		Assignment
		1110.1	w		1111	$13_0^1 48_0^2$				
1186	s	1185.7	w		1188	$13_0^1 47_0^2$				
1202	s	1202.4	w		1200	$14_0^1 16_0^1$				
		1226.8	m		1229	$13_0^1 25_0^2$		1228	m	$12_0^1 25_1^1$
1253	vs	1253.1	s	1204	1253	10_0^1		1251	s	12_0^1
1268	m	1268.1	w			?				
1282	s	1280.8	m			?		1278	m	11_0^1
1289	m	---				?				
1316	m	1315.8	vw		1314	$13_0^1 23_0^1$				
		1386.6	m		1386	$14_0^2 25_1^1$		1385	s	$18_0^2 25_1^1$
1392	s	1392.6	vw		1393	$10_0^1 25_0^1$				
1404	m	1404.3	m		1404	21_0^2				
1409	s	1408.6	m		1408	$14_0^1 21_0^1$				
1413	vs	1412.8	s		1412	14_0^2		1410	s	18_0^2
1419	m	1419.7	vw			?				
1431	s	1431.6	m			?				
1444	m	1444.2	w			?				
1552	s	1552.5	m		1553	$14_0^2 25_0^1$				
1565	m	1565.1	vw		1567	$14_0^1 21_0^1 48_0^2$				
1571	m	---			1572	$14_0^2 48_0^2$				
1594	s	1594.2	m		1594	$14_0^1 37_0^1$				
1613	m	1614.2	vw			?				

TABLE 29: Continued.

This Work						GH[a]			
FES		UV		Calc.[b]	Inferred[c]	Assignment	FES	UV		Assignment
		1629.1	m		1630	$13_0^1 14_0^1 25_1^1$				
1650	m	1649.5	m		1650	$20_0^1 21_0^1$		1642	s	$14_0^1 18_0^1$
1656	vs	1656.5	s		1657	$13_0^1 14_0^1$				
1671	m	---			1672	$14_0^1 39_0^2$				
1685	m	1685.3	w		1686	$14_0^1 21_0^1 25_0^2$				
1767	m	1766.6	m		1769	$14_0^1 15_0^2$				
1794	m	1795.2	m		1797	$13_0^1 14_0^1 25_0^1$				
1839	m	1839.7	w			?				
1897	m	1897.1	m		1902	13_0^2				
		1930.9	m			?				
1957	s	1958.0	m		1959	$10_0^1 14_0^1$				
1987	m	1986.8	m			?				
2013	m	---				?				
2202	m	2202.0	m		2204	$10_0^1 13_0^1$				
2363	m	2363.1	m		2364	$13_0^1 14_0^2$				

Abbreviations: s, strong; m, medium; w, weak; v, very.

[a] From reference 59.

[b] Calculated using the CIS/6-311++G(d,p) basis set with GAUSSIAN 03.

[c] Inferred combination frequencies are based on assignments of individual vibrations.

UV absorption spectra. Assignments up to 2,400 cm^{-1} higher than the 0_0^0 excitation are presented. The results from Gordon and Hollas[59] are also listed for comparison. The difference in assignments is obvious. The spectra in this work are much more comprehensive and thus have allowed a much clearer interpretation to be attained. For example, Gordon and Hollas[59] didn't observe any bands in the 280-360 cm^{-1} region, however, there are four bands clearly shown in the FES spectra and each band has a valid assignment in this work. They assigned the band at -138 cm^{-1} to be 24_1^1 and the band at 54 cm^{-1} to be 24_0^1, which would make the fundamental frequency of the double bond twisting vibration υ_{24} in S_0 state to be 192 cm^{-1}. This is obviously wrong since the vapor Raman spectrum clearly shows the fundamental frequency of υ_{24} to be 317 cm^{-1}. Moreover, there is no band observed near 54 cm^{-1} in this work. The FES band at 306 cm^{-1} is assigned to be 24_0^1, which is close to the computed frequency of 299 cm^{-1} from the CIS/6-311++G(d,p) calculations for the S_1 excited state.

Figure 45 shows the single vibrational level fluorescence (SVLF) spectra collected from exciting the 0_0^0 band at 35,563.1 cm^{-1}. These frequencies and assignments are shown in Table 30. The fundamental frequencies obtained from vapor IR and vapor Raman spectra as well as those from B3LYP/6-311++G(d,p) calculations are also listed for comparison, as referred from Chapter IX. Figures 46 and 47 show the SVLF spectra from exciting the 25_0^1 and 48_0^2 bands, which are 139.2 and 158.6 cm^{-1} higher

than the 0_0^0 band, respectively. The corresponding UV absorption spectra are also shown. The SVLF spectra were recorded from nine different excitation bands including 0_0^0. These corresponding results are summarized in Table 31. Figure 48 presents the energy level diagram for both S_0 and $S_1(\pi,\pi^*)$ states, based on all these spectra. The four lowest-frequency ring vibrations υ_{48}, υ_{25}, υ_{47}, and υ_{24} are labeled as A, B, C, and D, respectively, and the corresponding quantum levels in the S_1 state are indicated by primes in both Table 31 and Figure 48.

PES FOR THE S_0 GROUND STATE

Based upon the assignments of the low-frequency modes presented in Tables 30 and 31 and shown in Figure 48, both a one-dimensional potential energy function in terms of the ring-twisting vibration and a two-dimensional PES in terms of the ring-twisting and ring-bending modes were calculated. Because the barrier to inversion through the twisting mode is very high and because the observed transitions only reach quantum states about 700 cm^{-1} above the energy minima, for both the one and two-dimensional calculations only the lower region of the PESs can be determined with considerable accuracy. Hence, the estimation of the barrier by extrapolation of the potential function in either case cannot be expected to be very accurate.

For the one-dimensional calculation the potential energy function is given by

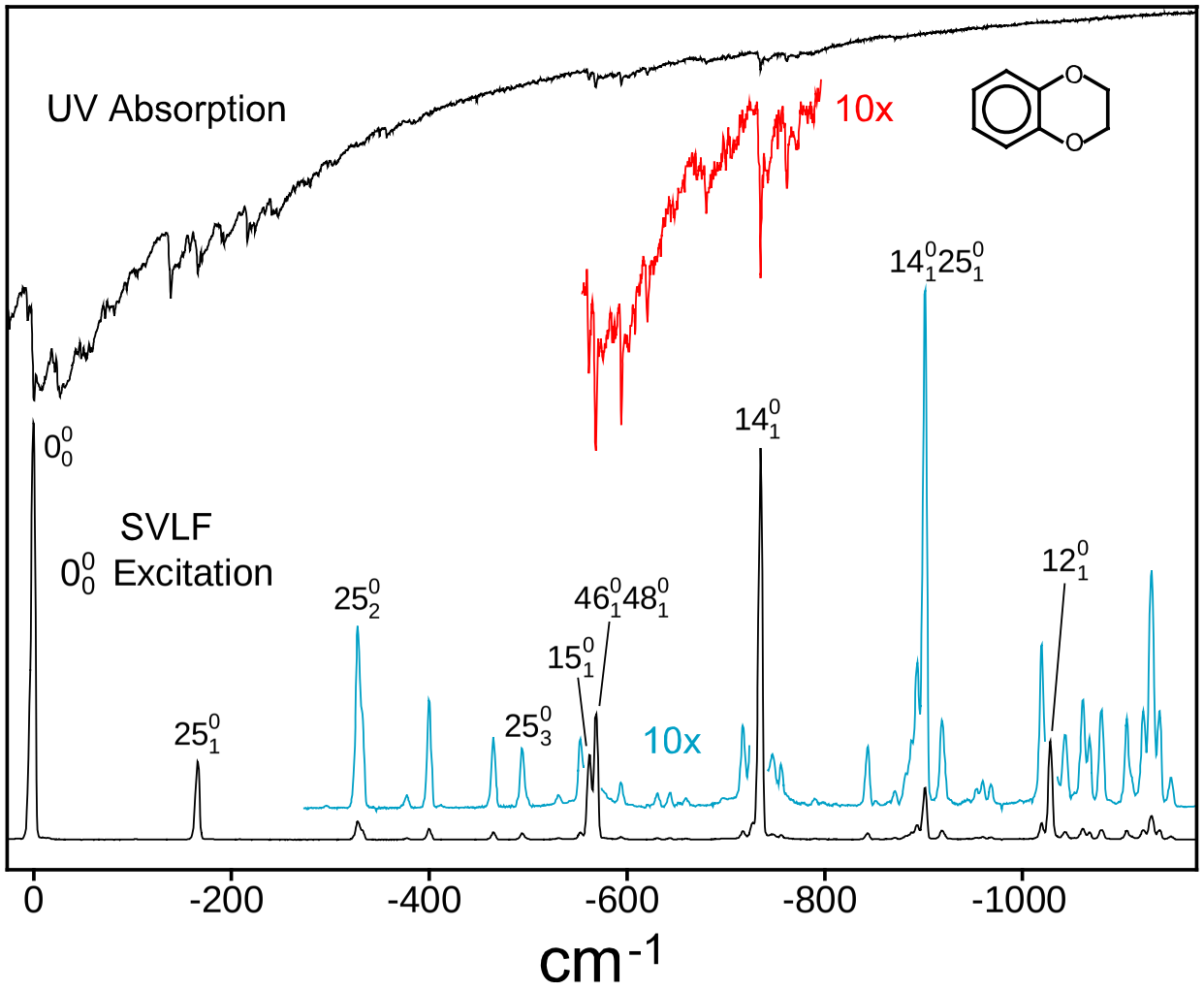

Figure 45. Single vibronic level fluorescence spectra of jet-cooled 1,4-benzodioxan with excitation of the 0_0^0 band at 35563.1 cm^{-1} and the ultraviolet absorption spectra at ambient temperature.

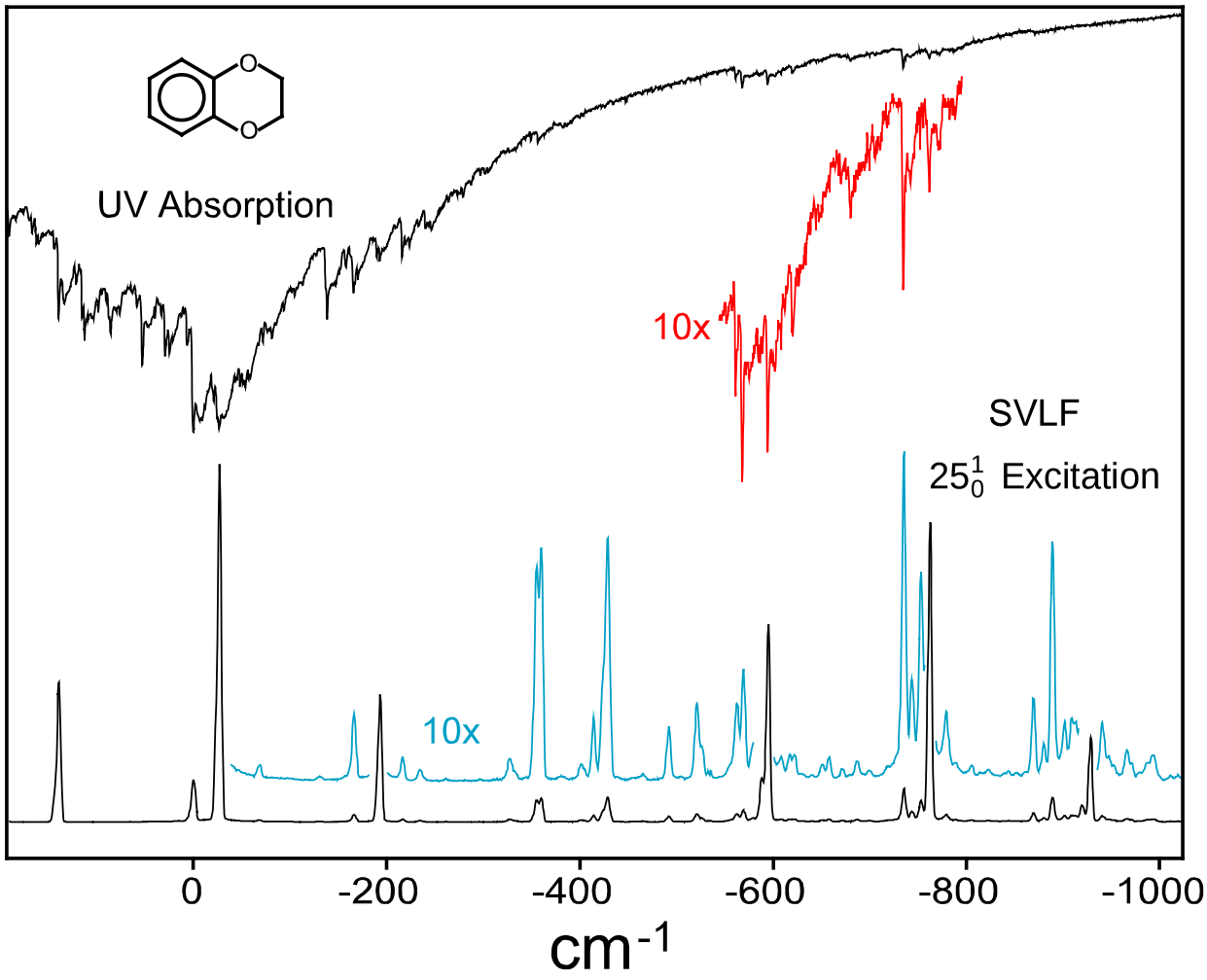

Figure 46. Single vibronic level fluorescence spectra of jet-cooled 1,4-benzodioxan with excitation of the 25_0^1 band at 139.6 cm^{-1} higher than the 0_0^0 band and the ultraviolet absorption spectra at ambient temperature.

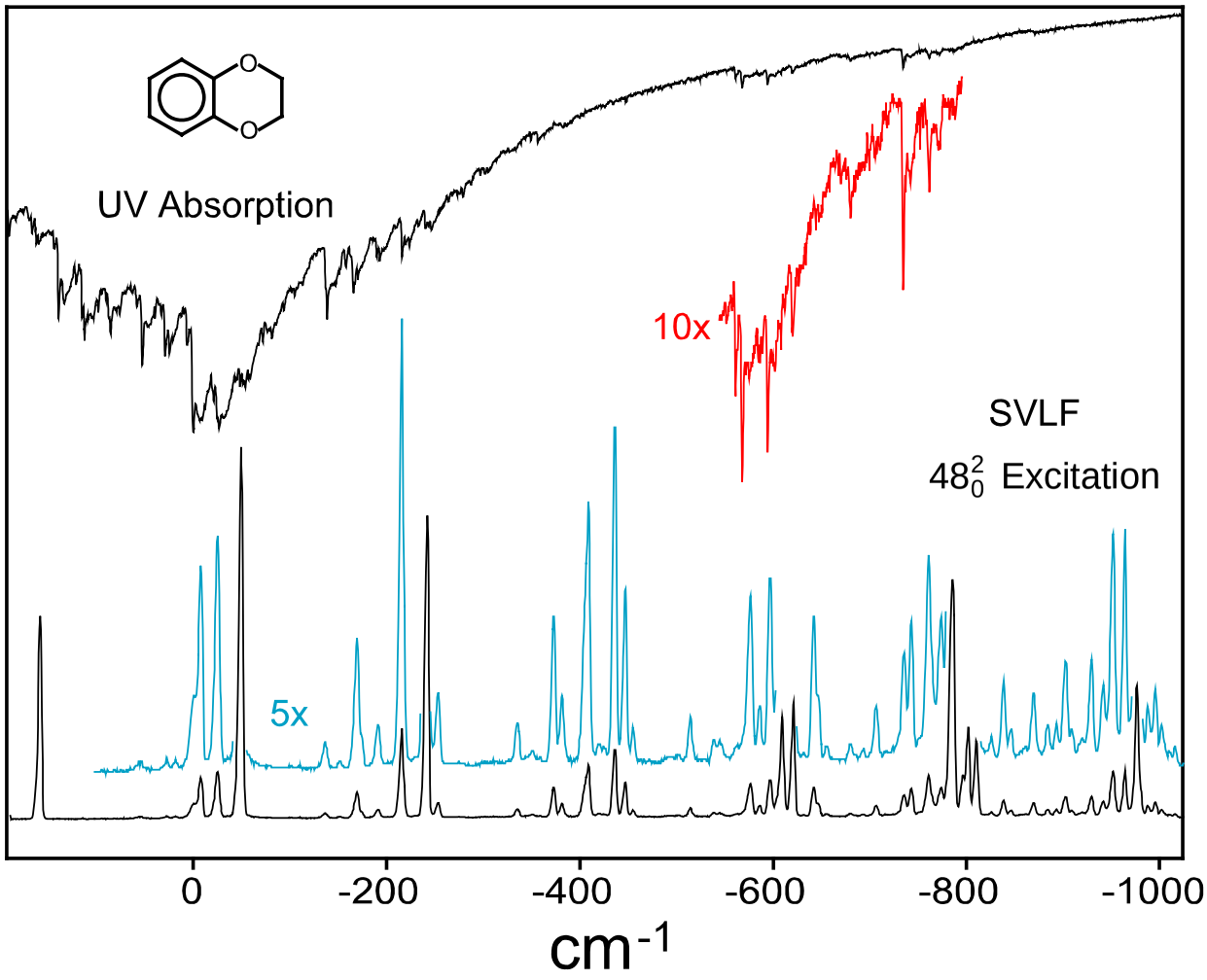

Figure 47. Single vibronic level fluorescence spectra of jet-cooled 1,4-benzodioxan with excitation of the 48_0^2 band at 159.3 cm^{-1} higher than the 0_0^0 band and the ultraviolet absorption spectra at ambient temperature.

TABLE 30: Frequencies (cm^{-1}) and Assignments of Single Vibronic Level Fluorescence (SVLF) Spectra of Jet-Cooled 1,4-Benzodioxan with Excitation of the 0_0^0 band at 35,563.1 cm^{-1}.

This Chapter						From Chapter IX				
SVLF		UV		Inferred[a]	Assignment	Vapor IR		Vapor Raman		Calculated[b]
0	vvs	0.0	vs	0	0_0^0					
-104	vw	-104.6	w		48_1^0	---		105	(8)	104
-166	s	-165.6	s		25_1^0	---		167	(15)	165
-207	vw			-208	48_2^0					
-297	vw	-297.1	w		47_1^0	---		297	(4)	297
-330	ms			-330	25_2^0					
-377	w				40_1^0	---		---		376
-400	m	-400.0	vw	-401	$47_1^0 48_1^0$					
-412	vw			-412	48_4^0					
-464	m	-464.0	vw	-463	$16_1^0 / 46_1^0 / 25_1^0 47_1^0$	---		463	(42)	462
-494	m			-494	$39_1^0 / 25_3^0$	---		495	(3)	494
-553	m	-552.2	vw		23_1^0	---		552	(11)	555
-562	s	-561.5	w		15_1^0	565	vw	566	(2)	571
-569	s	-568.4	m	-568	$46_1^0 48_1^0$					
-594	w	-594.1	m	-594	47_2^0					
-630	w			-630	$16_1^0 25_1^0 / 25_1^0 46_1^0$					
-643	w				38_1^0	645	vw	---		642
-659	w			-660/-658	$25_1^0 39_1^0 / 25_4^0$					
-697	vw			-698	$47_2^0 48_1^0$					
-717	m			-719	$22_1^0 / 23_1^0 25_1^0$	---		---		720
-727	m			-728	$15_1^0 25_1^0$					

TABLE 30: Continued.

This Chapter						From Chapter IX				
SVLF		UV		Inferred[a]	Assignment	Vapor IR		Vapor Raman		Calculated[b]
-735	vs	-734.7	m	-735	$14_1^0 / 25_1^0 46_1^0 48_1^0$	733	vw	732	(100)	734
-747	m				45_1^0	746	s	746	(7)	747
-756	m	-755.5	vw	-754	40_2^0					
-843	m				21_1^0	---		842	vvw	845
-871	w			-871	$39_1^0 40_1^0$					
-881	w			-883	$22_1^0 25_1^0$					
-888	w			-890	47_3^0					
-893	m				13_1^0	893	ms	891	(1)	886
-901	s			-901	$14_1^0 25_1^0$					
-918	m				44_1^0	924	w	---		925
-953	w				20_1^0	---		---		952
-959	w			-958	$16_1^0 39_1^0 / 39_1^0 46_1^0$					
-1019	m			-1017	$16_1^0 23_1^0 / 23_1^0 46_1^0$					
-1028	s				12_1^0	---		1025	(65)	1029
-1043	m			-1044	$45_1^0 47_1^0$					
-1061	m			-1063	$36_1^0 / 39_1^0 46_1^0 48_1^0$	---		---		1059
-1067	m			-1067	$14_1^0 25_2^0$					
-1079	m				11_1^0	1074	s	1074	(1)	1066
-1105	m			-1106	$19_1^0 / 23_2^0$	---		1107	(4)	1105
-1122	m			-1124	15_2^0					
-1130	ms			-1131	$15_1^0 46_1^0 48_1^0$					
-1138	m			-1138	$46_2^0 48_2^0$					

TABLE 30: Continued.

This Chapter					From Chapter IX				
SVLF		UV	Inferred[a]	Assignment	Vapor IR		Vapor Raman		Calculated[b]
-1150	w			10_1^0	1151	w	1151	(3)	1157
-1195	m		-1194	34_1^0 /$12_1^025_1^0$	1194	w	---		1189
-1255	s			9_1^0	1250	s	1249	(25)	1252
-1268	m		-1271	$19_1^025_1^0$					
-1282	s			18_1^0	1280	s	1280	(29)	1286
-1289	s			33_1^0	---		---		1285
-1296	ms		-1297	$14_1^015_1^0$					
-1303	s		-1304	8_1^0 /$14_1^046_1^048_1^0$	1307	ms	1306	(11)	1321
-1421	m		-1421	$9_1^025_1^0$					
-1433	m		-1434	22_2^0					
-1448	m		-1448	$18_1^025_1^0$					
-1469	s		-1470	6_1^0 /14_2^0	1465	w	1462	(3)	1473
-1493	m		-1494	45_2^0					
-1500	m			5_1^0	1496	vs	1494	(0.5)	1502
-1588	m		-1590	$12_1^015_1^0$					
-1602	ms			4_1^0	1609	vw	1609	(4)	1602
-1628	m		-1628	$13_1^014_1^0$					
-1635	m		-1635	$6_1^025_1^0$ /$14_2^025_1^0$					
-1649	m		-1648	$11_1^046_1^048_1^0$					
-1671	m		-1670	$20_1^022_1^0$					
-1686	m		-1686	21_2^0					
-1762	s		-1763	$12_1^014_1^0$					

TABLE 30: Continued.

This Chapter					From Chapter IX		
SVLF		UV	Inferred[a]	Assignment	Vapor IR	Vapor Raman	Calculated[b]
-1815	m		-1814	$11_1^0 14_1^0$			
-1823	m		-1824	$9_1^0 46_1^0 48_1^0$			
-1837	m		-1836	44_2^0			
-1843	m		-1844	$15_1^0 18_1^0$			
-1849	s		-1851	$18_1^0 46_1^0 48_1^0 / 15_1^0 33_1^0$			
-1856	m		-1858	$33_1^0 46_1^0 48_1^0$			
-1919	w		-1918	$16_2^0 39_2^0 / 39_2^0 46_2^0$			
-1929	m		-1930	$14_1^0 34_1^0$			
-1989	s		-1990	$9_1^0 14_1^0$			
-2001	m		-2003	$44_2^0 25_1^0$			
-2014	s		-2017	$14_1^0 18_1^0$			
-2022	ms		-2014	$14_1^0 33_1^0$			

Abbreviations: s, strong; m, medium; w, weak; v, very.

[a] Inferred combination frequencies are based on assignments of individual vibrations.

[b] Calculated using the B3LYP/6-311++G(d,p) basis set with GAUSSIAN 03.

TABLE 31: Single Vibronic Level Fluorescence (SVLF) Frequencies (cm^{-1}) and Assignments From Various Excitation Bands of 1,4-Benzodioxan.

Excitation:		0_0^0	A'	B'	2A'	2C'	2B'	2A'+B'	4A'	A'+2B'
Assignment	Inferred[a]	0[b] vs	+80 w	+139 s	+159 s	+237 s	+278 m	+297 m	+318 m	+358 m
A	-104.3	-104 vw	-104 s							
B	-165.6	-166 s		-166 vs	-166 m	-166 w	-165 s	-166 vw	-165 vw	
2A	-207.7	-207 vw		-208 vw	-208 vs	-207 vs		-207 ms	-207 m	
A+B	-268.7		-271 m	-270 vw						-270 vw
C	-297.1	-297 vw	-296 s		-295 vw					
2B	-330.3	-330 ms		-332 s	-330 w		-332 s	-332 m	-328 s	
2A+B	-371.1			-374 vw	-374 m	-374 m		-373 s		
40_1^0		-377 w								-377 vs
A+C	-400.0	-400 m		-401 vw	-400 s	-400 m		-400 s	-399 s	
4A	-411.9	-412 vw			-412 w					-411 vw
16_1^0 / 46_1^0	-462.7	-464 m		-465 vw					-464 w	-462 w
3B / 39_1^0	-494.3	-494 m		-494 m	-494 w		-498 m	-496 w	-493 m	-493 vw
?				-499 m						
2A+2B	-538							-539 ms		-540 m
23_1^0		-553 m		-553 w					-553 m	
15_1^0		-562 s		-566 m	-566 m	-567 w		-566 s	-566 ms	
$46_1^0 48_1^0$		-569 s								
2C	-594.1	-594 w			-594 m	-594 s		-594 m	-594 m	
$16_1^0 25_1^0$ / $25_1^0 46_1^0$		-630 w		-631 w						
38_1^0		-643 w								
4B / $25_1^0 39_1^0$	-657.7	-659 w		-660 w			-659 w	-659 vw		

TABLE 31: Continued.

Excitation:		0_0^0	A'	B'	2A'	2C'	2B'	2A'+B'	4A'	A'+2B'
Assignment	Inferred[a]	0[b] vs	+80 w	+139 s	+159 s	+237 s	+278 m	+297 m	+318 m	+358 m
?			-665 m	-665 vw			-665 w			
A+2C	-697	-697 vw	-698 w					-697 w		
22_1^0 / $23_1^0 25_1^0$		-717 m		-717 w						
$15_1^0 25_1^0$		-727 m		-727 m						
14_1^0 / $25_1^0 46_1^0 48_1^0$		-735 vs		-734 s	-735 w	-734 w	-733 w	-733 m		

Abbreviations: s, strong; m, medium; w, weak; v, very.

[a] Frequency values inferred from the energy level diagram in Figure 48.

[b] The excitation of 0_0^0 is at 35,563.1 cm^{-1}; the frequencies of all other excitation bands are relative to the 0_0^0.

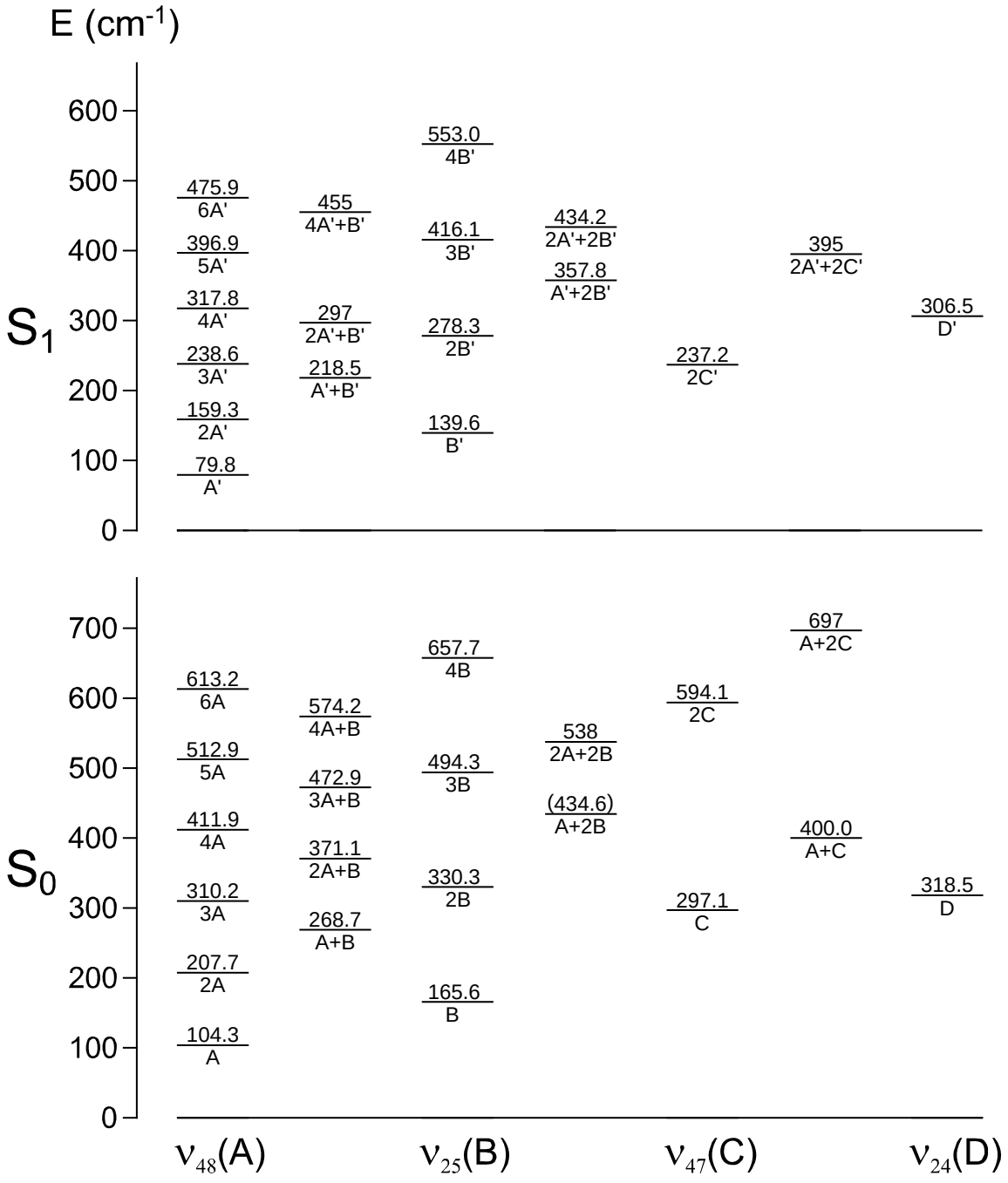

Figure 48. Energy level diagram for the low-frequency modes of 1,4-benzodioxan in its S_0 and $S_1(\pi,\pi^*)$ states.

$$V(\tau) = a\tau^4 + b\tau^2, \qquad (10.8)$$

where τ is the ring-twisting coordinate, as defined in Figure 39. This calculation can be done in either reduced coordinates[62] or dimensioned coordinates and the resulting calculated transition frequencies and barriers are the same in both cases. In reduced coordinates the function that best fits the data is

$$V(cm^{-1}) = 8.10(z^4 - 52.86z^2), \qquad (10.9)$$

where z is the reduced coordinate. This function, which is shown in Figure 49, has a barrier to inversion of 5672 cm^{-1}, and the calculated frequencies agree well with the observed values, as shown in Table 32 and Figure 49. The coordinate z can be transformed to the dimensioned coordinate τ using[62]

$$\tau = (2\mu A)^{-\frac{1}{2}}\hbar z, \qquad (10.10)$$

where $\mu = 1/g_{44}$ is the reduced mass. The reduced mass that was calculated for the simple twisting model is 30.0 au but this large-amplitude vibration is clearly much more complicated than this model. If this reduced mass value is used, the dimensioned potential function becomes

$$V(cm^{-1}) = (1.68\times10^3)\tau^4 - (6.18\times10^3)\tau^2, \qquad (10.11)$$

where τ is in radians. This function, however, has minima corresponding to ridiculously high twist angle values of ± 77°. Part of the discrepancy apparently is related to the fact that the extrapolated barrier is 40% higher than the *ab initio* value of 4095 cm^{-1} and thus

the minima are moved to higher τ values. The difficulty in having an accurate description of the vibrational model also contributes since a reliable reduced mass cannot readily be calculated. In addition to the twisting, the vibration no doubt also involves contributions from the out-of-plane and in-plane ring-bendings as well as CH_2 motions, particularly the rocking and twisting. In order to provide some perspective on the significance of the reduced mass, a reduced mass of μ = 100.0 au was utilized to recalculate the dimensioned potential function and this was found to be

$$V(cm^{-1}) = (1.87 \times 10^4)\tau^4 - (2.06 \times 10^4)\tau^2 . \qquad (10.12)$$

For this function the twisting angles are ± 42°, which are much closer to the *ab initio* values of ± 30°.

The experimental data in this case, therefore, do not do a particularly good job of determining the barrier as they only show the barrier to be very high. The experimental results can be stated to be 5000 ± 2000 cm^{-1} for the one-dimensional model. Prediction of the twisting angle is even worse. Again only the fact that there is a large twist angle can be ascertained.

In order to account for some of the vibrational coupling involving the ring-twisting mode, a two-dimensional calculation with the out-of-plane ring-bending coordinate added, was also carried out. Figure 50 presents a graphical view, based on the *ab initio* calculations, of the relative energies of the twisted (T), bent (B), and planar (P)

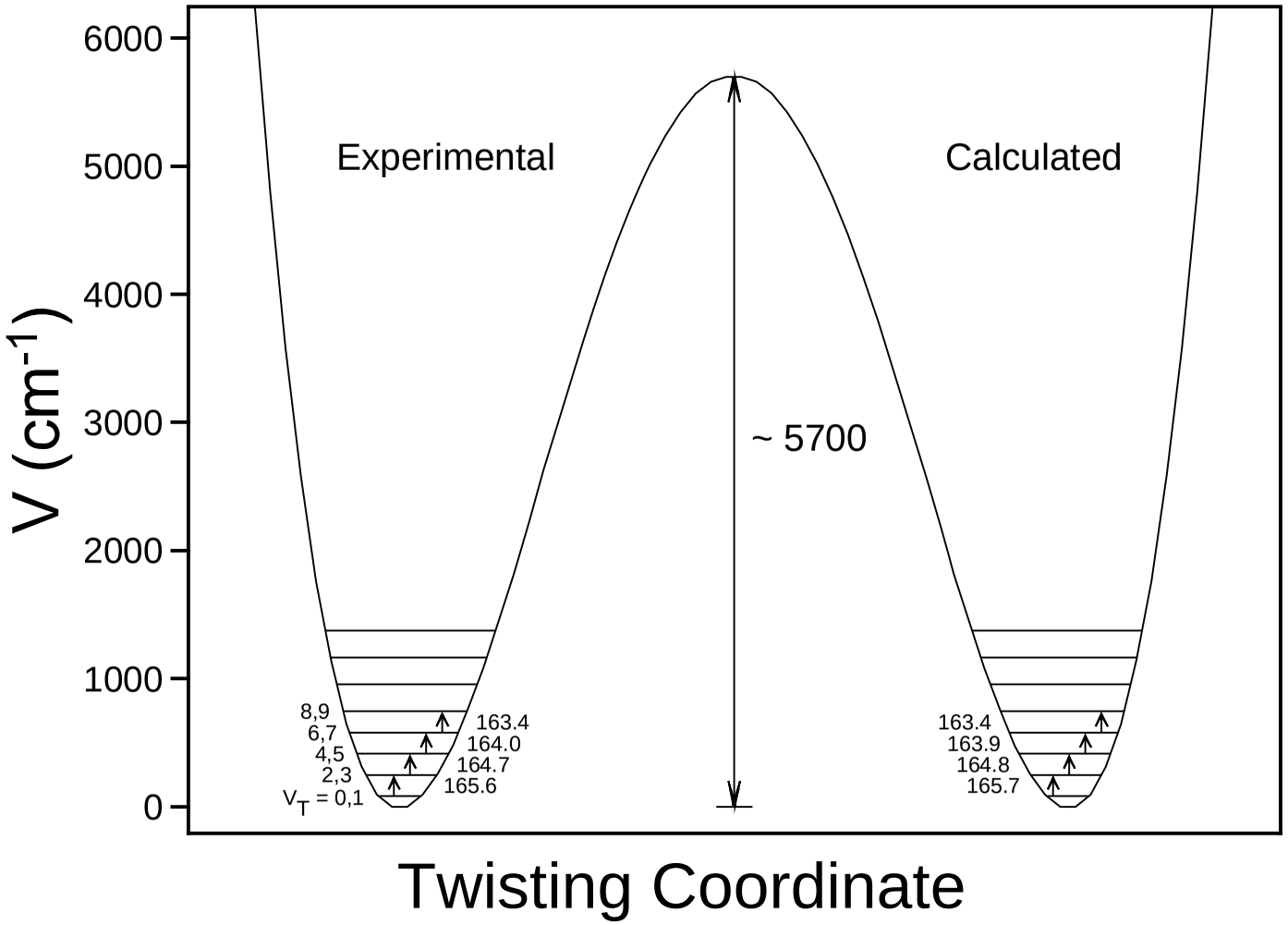

Figure 49. Experimental and calculated energy levels and the one-dimensional potential energy function of the ring-twisting vibration of 1,4-benzodioxan in the S_0 state.

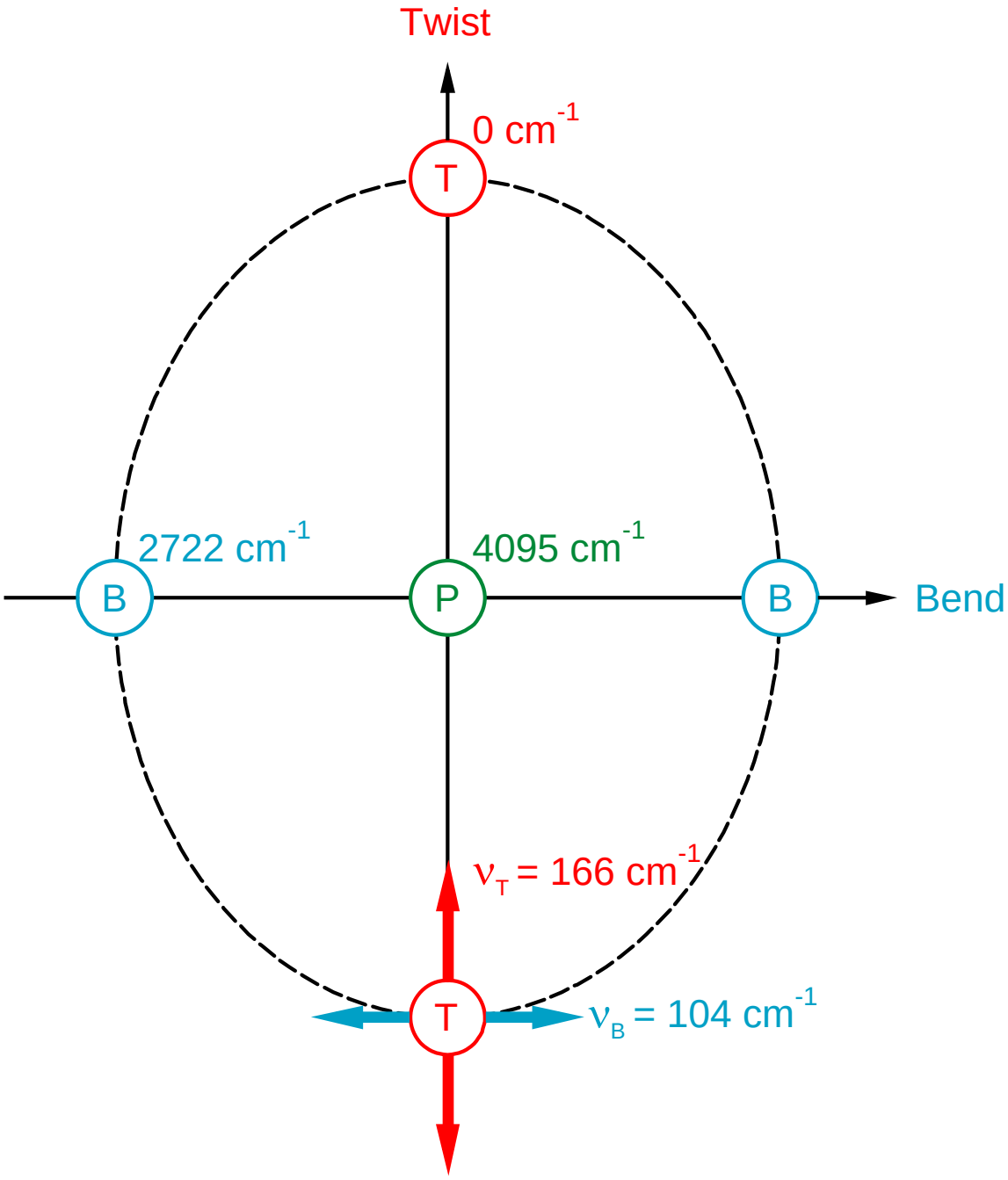

Figure 50. The two-dimensional potential energy diagram for the ring-twisting and ring-bending vibrations of 1,4-benzodioxan in the S_0 state.

TABLE 32: Observed and Calculated One-Dimensional and Two-Dimensional Transition Frequencies (cm^{-1}) and the Corresponding Potential Energy Parameters for 1,4-Benzodioxan S_0 Ground State.

Parameters	Observed	One-Dimensional[a]		Two-Dimensional[b]	
		Calc. I	Calc. II	Calc. III	Calc. IV
μ_{Twist}		30.0	100.0	29.9	84.3
a (cm^{-1}/rad^4)		1.68×10^3	1.87×10^4	6.4×10^3	3.7×10^4
b (cm^{-1}/rad^2)		-6.18×10^3	-2.06×10^4	-1.0×10^4	-2.8×10^4
c (cm^{-1}/rad^2)				2.8×10^3	2.8×10^3
d (cm^{-1}/rad^4)				1.0×10^3	2.3×10^3
A		8.10	8.10	12.68	11.43
B		-52.86	-52.86	-35.10	-43.23
BP (cm^{-1})		5672	5672	3906	5339
τ_{min} (rad)		1.35	0.74	0.88	0.61
τ_{min} (degree)		77°	42°	50°	35°
(0,0)-(2,0)	165.6	165.7	165.7	166.7	166.0
(2,0)-(4,0)	164.7	164.8	164.8	164.8	164.6
(4,0)-(6,0)	164.0	163.9	163.9	163.2	163.4
(6,0)-(8,0)	163.4	163.4	163.4	162.4	163.1
(0,1)-(2,1)	164.4			166.6	165.6
(0,2)-(2,2)	163.4			166.6	165.2
(0,0)-(0,1)	104.3			104.1	104.3
(0,1)-(0,2)	103.4			103.9	104.2
(0,2)-(0,3)	102.5			103.8	104.1
(0,3)-(0,4)	101.7			103.7	104.0
(0,4)-(0,5)	101.0			103.5	103.8
(0,5)-(0,6)	100.3			103.4	103.7
(0,6)-(0,7)	99.8			103.2	103.6
(2,0)-(2,1)	103.1			104.0	103.9
(2,1)-(2,2)	102.4			103.9	103.8
(2,2)-(2,3)	101.8			103.8	103.6
(2,3)-(2,4)	101.3			103.6	103.5
(4,0)-(4,1)	102.8			104.0	103.5
(4,1)-(4,2)	102.0			103.9	103.4

[a] The one-dimensional potential function is given by $V = a\tau^4 + b\tau^2$.

[b] The two-dimensional potential function is given by $V = a\tau^4 + b\tau^2 + c\theta^2 + d\tau^2\theta^2$.

conformations. The molecule is trapped in its twisted structure where the twisting frequency is 166 cm^{-1} and the bending frequency is 104 cm^{-1}. The molecule can undergo hindered pseudorotation and pass over a saddle point at 2722 cm^{-1} corresponding to a bent configuration. This is a lower energy pathway than ascending over the planar structure at 4095 cm^{-1}. Although the bent form is considerably lower in energy than the planar form, the data for the bending vibration, which extend to about 700 cm^{-1} above the ground state, are also not sufficient to yield a reliable experimental energy value for the bent structure. Therefore, the following two-dimensional form of the PES was utilized

$$V(\tau,\theta) = a\tau^4 + b\tau^2 + c\theta^2 + d\tau^2\theta^2 , \qquad (12.13)$$

where τ and θ are the ring-twisting and ring-bending coordinates defined in Figure 39, respectively. For this PES the *a* and *b* coefficients define the twisting energetics. The parameter *c* is the harmonic term for the bending since this motion is very nearly harmonic in the region of the twisting minima (T). The data do not allow a meaningful determination of the energy of the bent saddle points (B). Finally, the parameter *d* represents the interaction between the two modes. The two modes also interact through the g_{45} kinetic energy cross term discussed earlier. The parameters that best fit the data are

$$a = 6.4\times10^3\ \mathrm{cm^{-1}/rad^4},\ b = -1.0\times10^4\ \mathrm{cm^{-1}/rad^2},$$
$$c = 2.8\times10^3\ \mathrm{cm^{-1}/rad^2},\ \text{and}\ d = 1.0\times10^3\ \mathrm{cm^{-1}/rad^4},$$

and these correspond to a twisting barrier of 3906 cm^{-1}, which is much closer to the *ab initio* value of 4095 cm^{-1}. Here again, however, the energy minima depend on the reduced mass values. The computed two-dimensional value of 29.9 au for the twisting produces minima at ± 50°. A value of 84.3 au would be required to match the *ab initio* value of ± 30°.

The calculated frequencies for the two-dimensional PES are shown in Table 32 and Figure 51 shows this surface. The frequency agreement is excellent as it does not depend on the reduced mass values. Since no quadratic term was used in the potential energy function for the bending angle θ, this surface cannot show the presence of a saddle point along the bending axis although it is almost certainly present.

PES FOR THE $S_1(\pi,\pi^*)$ EXCITED STATE

Similar procedures were carried out for studying the $S_1(\pi,\pi^*)$ excited state, and the data in Table 29 and Figure 48 were used. The one-dimensional potential energy function for the ring-twisting vibration in reduced coordinate is

$$V(cm^{-1}) = 7.15(z^4 - 48.22z^2)\,. \qquad (10.14)$$

This function has a barrier of 4158 cm^{-1} and is shown in Figure 52. The *ab initio* barrier, which for an excited state calculation is not expected to be very reliable, is 7166 cm^{-1}. Table 33 shows the agreement between observed and calculated transition frequencies

and this is nearly perfect.

If the calculated reduced mass of 28.5 au is used to transfer to the dimensioned coordinate τ the potential energy function becomes

$$V(cm^{-1}) = (1.04 \times 10^3)\tau^4 - (4.17 \times 10^3)\tau^2, \qquad (10.15)$$

and this function has minima at ± 81°. The *ab initio* minima are at ± 29°. As shown in Table 33 a reduced mass of 100.0 au would produce twisting angle of ± 43°

A two-dimensional calculation based on Equation (10.13) was also carried out and the parameters determined are

$$a = 4.4 \times 10^3 \text{ cm}^{-1}/\text{rad}^4, \; b = -5.5 \times 10^3 \text{ cm}^{-1}/\text{rad}^2,$$
$$c = 2.1 \times 10^2 \text{ cm}^{-1}/\text{rad}^2, \text{ and } d = 3.2 \times 10^3 \text{ cm}^{-1}/\text{rad}^4.$$

For this case the calculated barrier is 1744 cm^{-1} and the energy minima are at ± 45°. The limited experimental data along with the inaccuracy of *ab initio* calculations for the excited state, however, do not give much confidence in these results. Since the twisting frequencies decrease from the 166 cm^{-1} in S_0 ground state to 140 cm^{-1} in S_1 excited state, this does indicate that the excited state barrier is lower. Moreover, the one-dimensional potential calculations, which yield a drop of 5672 cm^{-1} to 4158 cm^{-1}, strongly support this view. An educated guesstimate is that the S_1 excited state barrier is about 3600 ± 2000 cm^{-1} vs. 5000 ± 2000 cm^{-1} for the S_0 ground state.

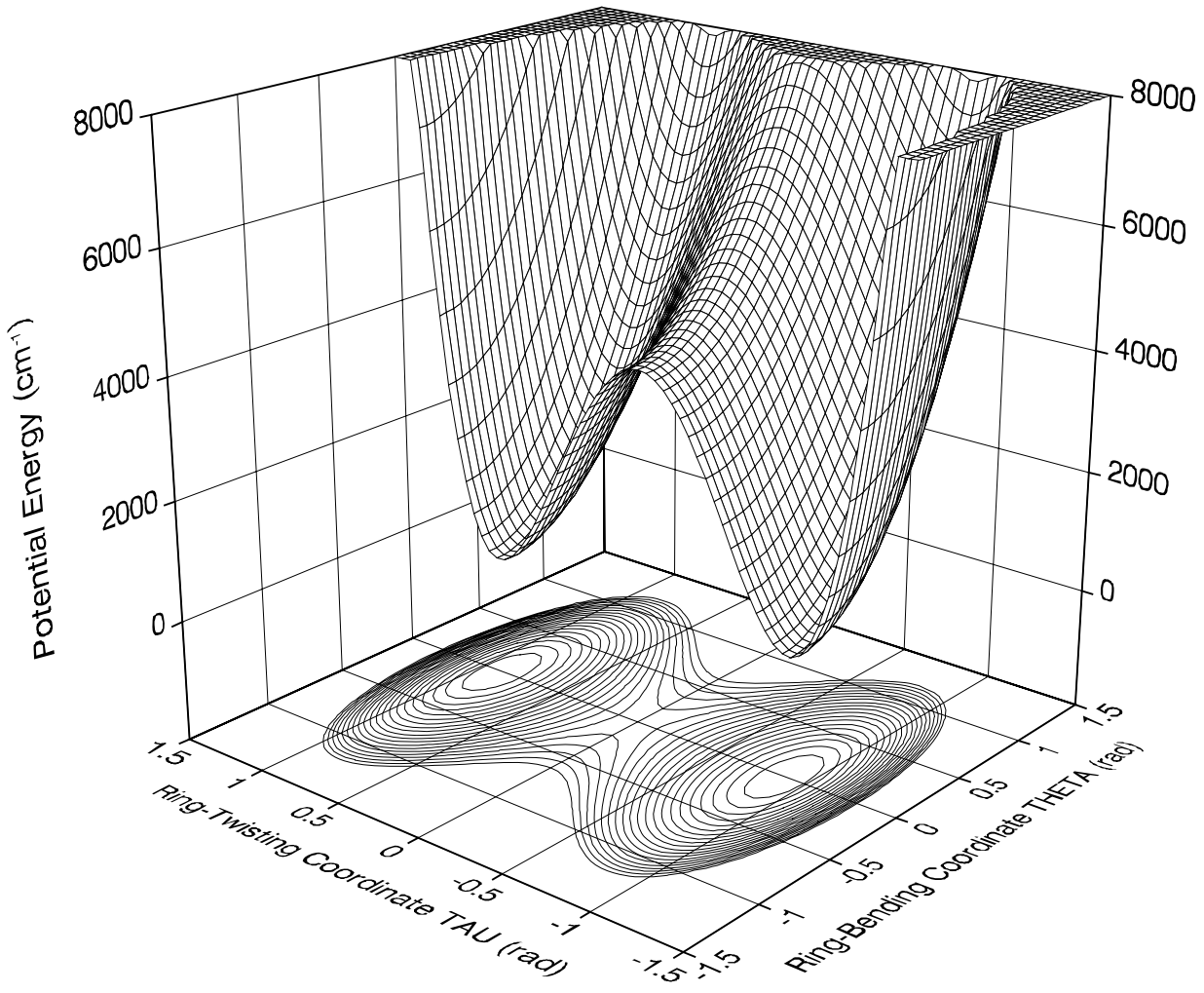

Figure 51. The two-dimensional potential energy surface for the ring-twisting coordinate τ and the ring-bending coordinate θ of 1,4-benzodioxan in the S_0 state.

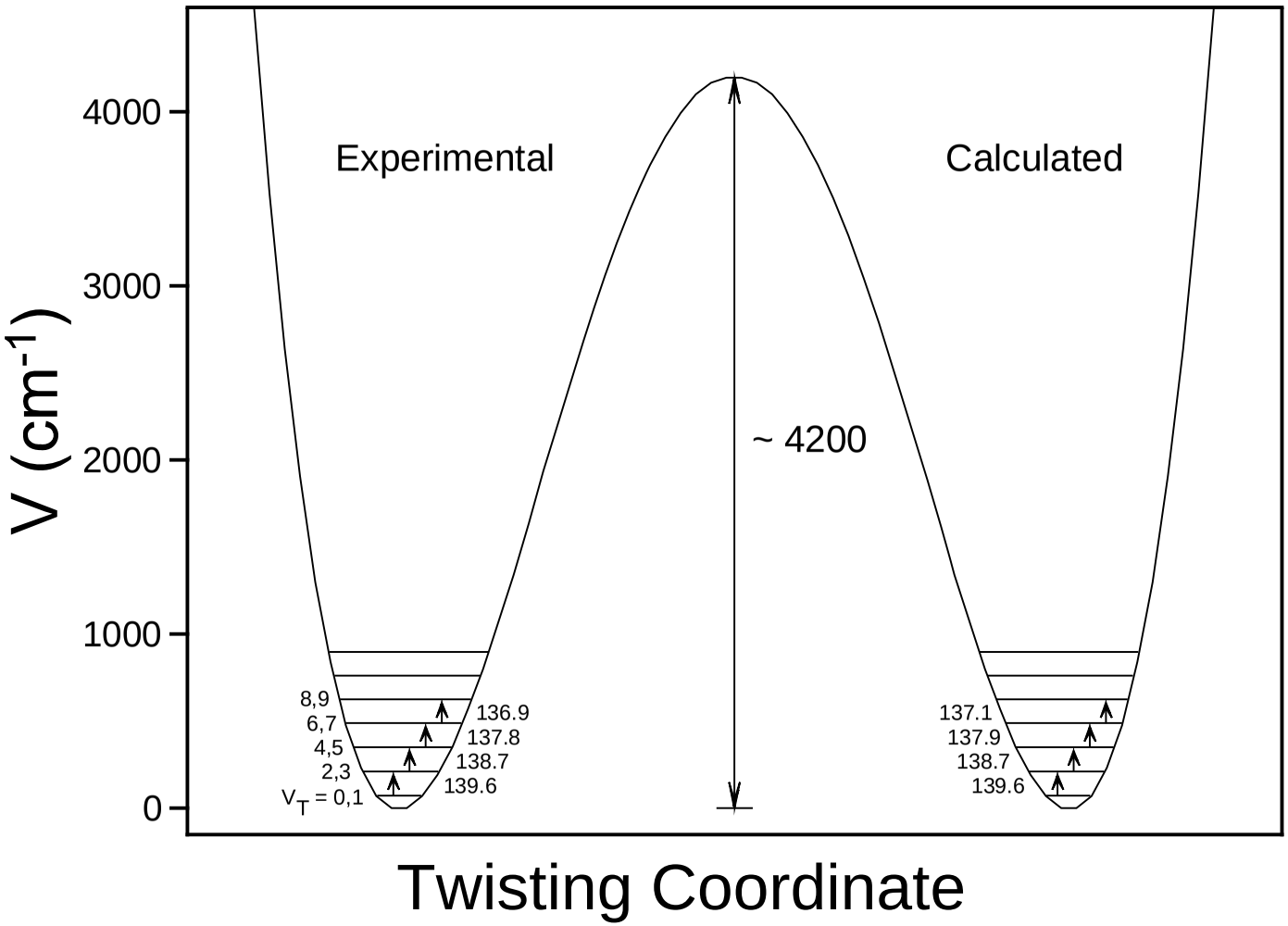

Figure 52. Experimental and calculated energy levels and the one-dimensional potential energy function of the ring-twisting vibration of 1,4-benzodioxan in the S_1 state.

TABLE 33: Observed and Calculated One-Dimensional and Two-Dimensional Transition Frequencies (cm^{-1}) and the Corresponding Potential Energy Parameters for 1,4-Benzodioxan $S_1(\pi,\pi^*)$ Excited State.

Parameters	Observed	One-Dimensional[a]		Two-Dimensional[b]	
		Calc. I	Calc. II	Calc. III	Calc. IV
μ_{Twist}		28.5	100.0	28.3	72.0
a (cm^{-1}/rad^4)		1.04×10^3	1.29×10^4	4.4×10^3	2.6×10^4
b (cm^{-1}/rad^2)		-4.17×10^3	-1.46×10^4	-5.5×10^3	-1.3×10^4
c (cm^{-1}/rad^2)				2.1×10^2	4.9×10^2
d (cm^{-1}/rad^4)				3.2×10^3	7.1×10^3
A		7.15	7.15	11.61	11.61
B		-48.22	-48.22	-24.51	-24.51
BP (cm^{-1})		4158	4158	1744	1672
τ_{min} (rad)		1.41	0.75	0.79	0.50
τ_{min} (degree)		81°	43°	45°	29°
(0,0)-(2,0)	139.6	139.6	139.6	139.5	140.3
(2,0)-(4,0)	138.7	138.7	138.7	138.9	138.7
(4,0)-(6,0)	137.8	137.9	137.9	137.8	137.2
(6,0)-(8,0)	136.9	137.1	137.1	136.9	136.4
(0,1)-(2,1)	138.7			138.4	139.2
(0,2)-(2,2)	137.7			137.3	138.0
(0,0)-(0,1)	79.8			80.3	80.5
(0,1)-(0,2)	79.5			79.9	79.9
(0,2)-(0,3)	79.3			79.4	79.4
(0,3)-(0,4)	79.2			79.0	78.9
(0,4)-(0,5)	79.1			78.6	78.4
(0,5)-(0,6)	79.0			78.2	78.0
(2,0)-(2,1)	78.9			79.2	79.3
(2,1)-(2,2)	78.5			78.7	78.8
(4,0)-(4,1)	79.5			77.7	78.0
(4,1)-(4,2)	76.4			77.3	77.5

[a] The one-dimensional potential function is given by $V = a\tau^4 + b\tau^2$.

[b] The two-dimensional potential function is given by $V = a\tau^4 + b\tau^2 + c\theta^2 + d\tau^2\theta^2$.

CHAPTER XI

FLUORESCENCE, ULTRAVIOLET ABSORPTION SPECTRA AND ASSIGNMENTS FOR 1,2,3,4-TETRAHYDRONAPHTHALENE

INTRODUCTION

The six-membered ring molecule cyclohexene[9,63] (CHX) has been studied previously. By carrying out a two-dimensional analysis of the ring-twisting and ring-bending vibrations, CHX was found to have a barrier to planarity of 4700 cm^{-1} with the lowest energy conformations at twist angles of ± 39°. With a benzene ring attached to the six-membered ring at the double bond, 1,2,3,4-tetrahydronaphthalene (tetralin or TET) is also expected to have twisted C_2 symmetry with a very high barrier to planarity.

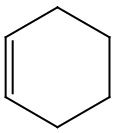

CHX

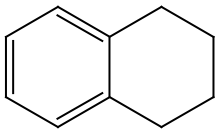

TET

The complete vibrational assignment of TET has already been made, as given in Chapter IX. In this chapter the ultraviolet (UV) absorption spectra, jet-cooled fluorescence excitation (FES) and single vibronic level fluorescence (SVLF) spectra are presented. The assignments for these spectra are compared to a previous study by Guchhait *et al.*[64] The FES spectra up to 2000 cm^{-1} higher than the 0_0^0 excitation are

reported and assigned in this work. SVLF spectra from thirteen different excitation lines confirm the assignments for those bands. The two-dimensional kinetic energy expansions of TET for both the S_0 ground and $S_1(\pi,\pi^*)$ excited states are presented in this chapter. However, the two-dimensional potential energy functions have not as yet been determined.

EXPERIMENTAL

The 1,2,3,4-tetrahydronaphthalene sample (99% purity) was purchased from Aldrich Chemical Company and further purified by vacuum distillation.

Ultraviolet absorption spectra of tetralin vapor were recorded on a Bomem DA8.02 Fourier-transform spectrometer using a deuterium lamp source, a quartz beamsplitter, and a silicon detector in the 20,000-50,000 cm^{-1} region. The sample was contained in a 20 cm glass cell with quartz windows. UV absorption spectra were collected at ambient temperatures and the vapor pressure within the cell was about 200 mTorr. A resolution of 0.5 cm^{-1} was used and more than ten thousand scans were averaged.

The FES and SVLF spectra were recorded using a Continuum Powerlite 9020 Nd:YAG laser which pumped a Continuum Sunlite OPO and FX-1 ultraviolet extension unit. FES spectra were obtained at a $\pm$ 0.5 cm^{-1} resolution and SVLF spectra were taken with a spectral resolution of $\pm$ 1 cm^{-1}. More details are provided elsewhere.[28-32]

CALCULATIONS

Theoretical calculations were carried out using the GAUSSIAN 03 package.[41] Bond lengths, bond angles, and vibrational frequencies were calculated for both planar C_{2v} and twisted C_2 structures in the $S_1(\pi,\pi^*)$ excited state. The configuration interaction-singles (CIS) method with the 6-311++G(d,p) basis set was used. The twisted C_2 symmetry was calculated to be the lowest energy conformation for the S_1 excited state.

Figure 53 shows the structures of TET for both C_{2v} and C_2 symmetries calculated with the MP2/cc-pVTZ basis set for the S_0 state and with CIS/6-311++G(d,p) basis set for the $S_1(\pi,\pi^*)$ state. The twisting angles for C_2 symmetry were calculated to be 31.4° for the S_0 ground state and 29.3° for the S_1 excited state. Table 34 lists the energies calculated with different theories and basis sets for the planar (C_{2v}) and bent (C_s) structures of TET in both S_0 ground and $S_1(\pi,\pi^*)$ excited states relative to the energy minima at twisted (C_2) conformations.

Table 35 compares the calculated frequencies for TET in its S_0 and $S_1(\pi,\pi^*)$ states. A scaling factor of 0.905 for the $S_1(\pi,\pi^*)$ excited state was determined from the average ratio of eight experimental and calculated fundamental frequencies, as presented in Table 36. The assignments for these eight fundamental bands in FES spectra are further confirmed by the corresponding SVLF spectra. Since no experimental frequencies were obtained for the C-H stretch region, 0.905 was also used for those stretching vibrations.

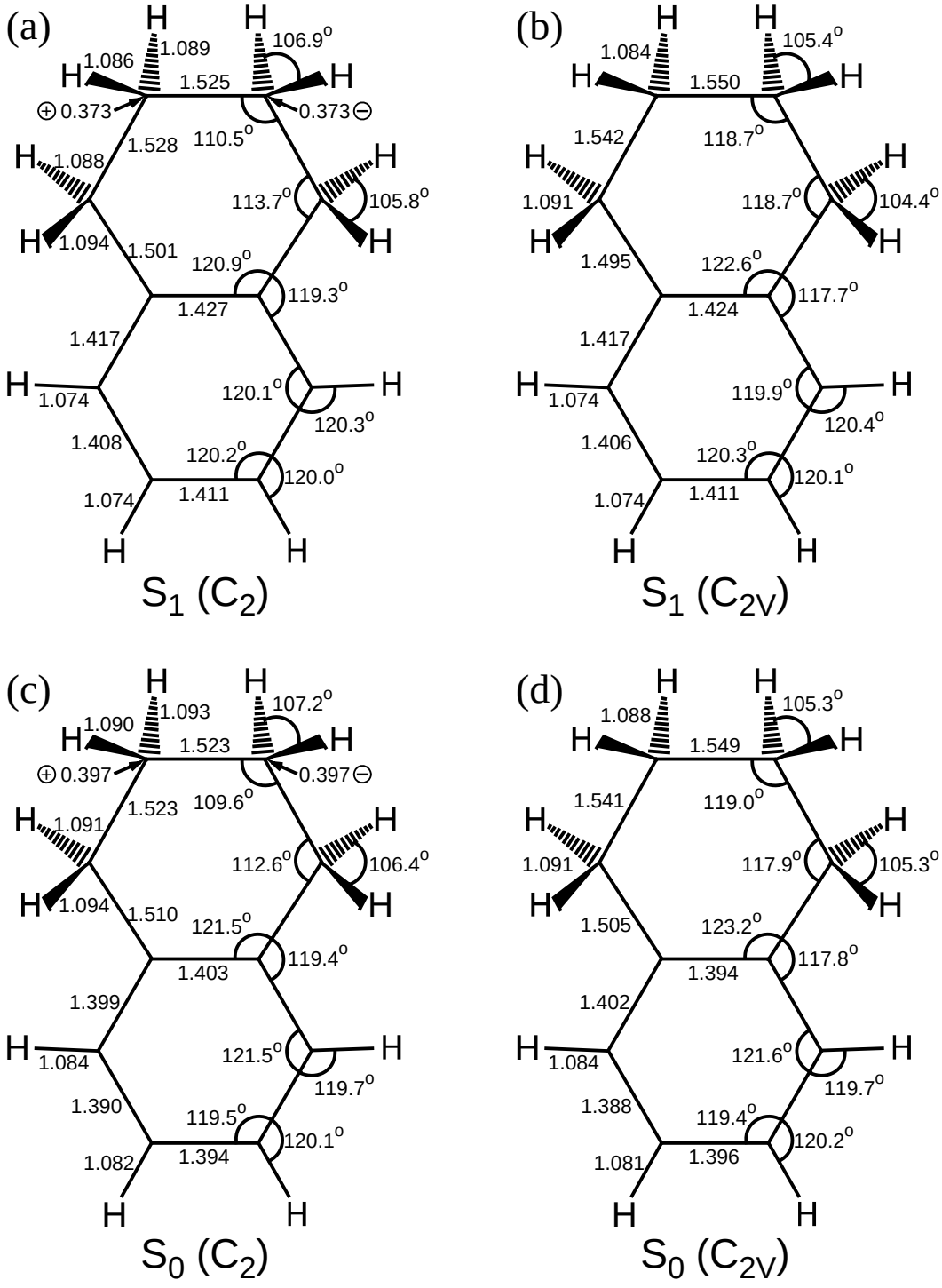

Figure 53. The calculated structures of tetralin (a) for C_2 symmetry and (b) for C_{2v} symmetry in the $S_1(\pi,\pi^*)$ state from CIS/6-311++G(d,p) calculations; (c) for C_2 symmetry and (d) for C_{2v} symmetry in the S_0 state from MP2/cc-pVTZ calculations.

TABLE 34: Calculated Relative Energies (cm^{-1}) for Different Structures of Tetralin in its S_0 Ground and $S_1(\pi,\pi^*)$ Excited States.

Structure	S_0				S_1
	HF	B3LYP	MP2		CIS
	6-311++G(d,p)	6-311++G(d,p)	6-311++G(d,p)	cc-pVTZ	6-311++G(d,p)
C_{2v} (planar)	4493	3938	5152	4811	5100
C_s (bent)	992	783	724	716	848
C_2 (twisted)	0	0	0	0	0

TABLE 35: Calculated Frequencies (cm^{-1}) for Tetralin in its S_0 Ground and $S_1(\pi,\pi^*)$ Excited States.

Sym.	ν		Description	S_0		S_1
$C_{2v}(C_2)$	C_{2v}	C_2		C_{2v}[a]	C_2[a]	C_2[b]
A_1 (A)	1	1	C-H sym. stretch (ip)	3069	3069	3048
	2	2	C-H sym. stretch (op)	3034	3037	3028
	3	5	CH_2 sym. stretch (ip, op')	2906	2899	2851
	4	6	CH_2 sym. stretch (ip, ip')	2943	2886	2794
	5	7	benzene C-C stretch	1602	1592	1531
	6	8	benzene C-C stretch	1504	1499	1435
	7	9	CH_2 deformation (ip, ip')	1507	1481	1469
	8	10	CH_2 deformation (ip, op')	1460	1453	1417
	9	11	CH_2 wag (op, ip')	1372	1365	1369
	10	13	benzene C-C stretch	1336	1309	1640
	11	15	sat. ring (C-C) stretch	1196	1200	1182
	12	16	CH_2 wag (op, op')	1268	1167	1160
	13	17	C-H wag (op, op')	1165	1164	1140
	14	19	sat. ring (C-C) stretch	1113	1064	1032
	15	20	C-H wag (op,ip')	1043	1038	968
	16	23	sat. ring (C-C) stretch	839	858	835[c]
	17	25	benzene C-C stretch	713	723	677
	18	27	benzene ring bend	584	581	489
	19	29	sat. ring bend	442	427	411
A_2 (A)	20	3	CH_2 asym. stretch (op, ip')	2948	2946	2894
	21	4	CH_2 asym. stretch (op, op')	2918	2936	2872
	22	12	CH_2 twist (ip, ip')	1291	1351	1350
	23	14	CH_2 twist (ip, op')	1259	1257	1229
	24	28	CH_2 rock (op, op')	1056	1085	1056
	25	21	C-H wag (op, op')	969	973	833[c]
	26	22	C-H wag (op, ip')	871	869	647
	27	24	CH_2 rock (op, ip')	818	819	800
	28	26	benzene ring bend	688	703	537
	29	28	benzene ring bend	483	504	335
	30	30	skeletal twist	*i*	301	288
	31	31	sat. ring twist	125	141	103
B_1 (B)	32	32	C-H asym. stretch (ip)	3054	3054	3038
	33	33	C-H asym. stretch (op)	3031	3033	3021

TABLE 35: Continued.

Sym.	ν		Description	S_0		S_1
$C_{2v}(C_2)$	C_{2v}	C_2		C_{2v}[a]	C_2[a]	C_2[b]
B_1 (B)	34	36	CH_2 sym. stretch (op, op')	2905	2905	2853
	35	37	CH_2 sym. stretch (op, ip')	2927	2885	2789
	36	38	benzene C-C stretch	1618	1618	1449
	37	40	CH_2 deformation (op, ip')	1482	1474	1460
	38	39	CH_2 deformation (op, op')	1459	1459	1425
	39	41	benzene C-C stretch	1454	1457	1406
	40	42	CH_2 wag (ip, op')	1361	1350	1349
	41	43	CH_2 wag (ip, ip')	1351	1346	1335
	42	45	C-H wag (ip, ip')	1251	1243	1174
	43	46	sat. ring (C-C) stretch	1204	1184	1146
	44	48	C-H wag (ip, op')	1118	1118	1062
	45	49	sat. ring (C-C) stretch	1007	981	954
	46	53	benzene ring bend	854	801	764
	47	55	benzene ring bend	728	587[c]	547
	48	56	sat. ring bend	477	450	407
	49	58	sat. ring bend	334	339	322
B_2 (B)	50	34	CH_2 asym. stretch (ip, ip')	2974	2949	2896
	51	35	CH_2 asym. stretch (ip, op')	2922	2935	2871
	52	44	CH_2 twist (op, ip')	1287	1294	1267
	53	47	CH_2 twist (op, op')	1219	1142	1104
	54	50	C-H wag (ip, op')	955	950	728
	55	51	CH_2 rock (ip,ip')	709	934[c]	908
	56	52	CH_2 rock (ip,op')	910	900	875
	57	54	C-H wag (ip, ip')	749	743	613
	58	57	benzene ring bend	429	432	288
	59	59	sat. ring flap	210	255	140
	60	60	sat. ring bend	*i*	94	93

[a] Calculated using the B3LYP/6-311++G(d,p) basis set with GAUSSIAN 03. The scaling factors are 0.985 for frequencies less than 1800 cm^{-1} and 0.964 for frequencies greater than 2800 cm^{-1}.

[b] Calculated using the CIS/6-311++G(d,p) basis set with GAUSSIAN 03. The scaling factors are 0.905 for the entire region.

[c] Vibrations that are strongly coupled.

TABLE 36: The Selected Experimental and Calculated Fundamental Frequencies (cm^{-1}) in $S_1(\pi,\pi^*)$ Excited State for Tetralin.

ν	Experimental[a]	Calculated[b]	Scaling Factor	Scaled Freq. (SF = 0.905)
17	680.5	748.1	0.910	677.0
18	480.3	540.5	0.889	489.1
19	417.3	454.3	0.919	411.1
28	521.4	593.1	0.879	536.8
29	329.5	370.2	0.890	335.0
30	294.7	317.8	0.927	287.6
31	94.5	113.8	0.830[c]	103.0
49	326.8	326.8	0.919	321.7

[a] Fundamental frequencies obtained from the FES spectra.

[b] Unscaled frequencies calculated using the CIS/6-311++G(d,p) basis set with GAUSSIAN 03.

[c] Not used in averaging the scaling factors.

KINETIC ENERGY EXPRESSIONS

Both TET and 1,4-benzodioxan (14BZD) can be included among molecules which have a symmetric saturated six-membered ring attached to a benzene ring. The definitions and components of the bond vectors for this type of molecule are given in Figure 39 and Table 28 in Chapter X. Using the calculated planar structures shown in Figure 53, the kinetic energy expressions for the S_0 ground state of TET was calculated to be

$$\begin{aligned} g_{44}^{S_0}(\tau,\theta) = {} & 0.030364480 + 0.001370494\tau^2 - 0.030386662\tau^4 + 0.023673542\tau^6 \\ & - 0.0002626730\theta^2 - 0.0012627220\theta^4 + 0.0020737160\theta^6 \\ & - 0.012152748\tau^2\theta^2 + 0.032310658\tau^4\theta^2 + 0.030804476\tau^2\theta^4 \end{aligned} , \quad (11.1)$$

$$\begin{aligned} g_{55}^{S_0}(\tau,\theta) = {} & 0.033206697 + 0.005837461\tau^2 + 0.002307415\tau^4 - 0.057934636\tau^6 \\ & - 0.0020079830\theta^2 - 0.0062677980\theta^4 - 0.0234937630\theta^6 \\ & - 0.022380782\tau^2\theta^2 + 0.011507498\tau^4\theta^2 + 0.032096665\tau^2\theta^4 \end{aligned} , \quad (11.2)$$

$$\begin{aligned} g_{45}^{S_0}(\tau,\theta) = {} & -0.003067150\tau\theta - 0.011746070\tau^3\theta \\ & - 0.011198683\tau\theta^3 + 0.051926726\tau^3\theta^3 \end{aligned} , \quad (11.3)$$

and these for the TET $S_1(\pi,\pi^*)$ excited state are

$$\begin{aligned} g_{44}^{S_1}(\tau,\theta) = {} & 0.030707558 + 0.001312939\tau^2 - 0.030119872\tau^4 + 0.023437577\tau^6 \\ & - 0.0000778160\theta^2 - 0.0015593210\theta^4 + 0.0023836980\theta^6 \\ & - 0.01360548\tau^2\theta^2 + 0.03493299\tau^4\theta^2 + 0.033849212\tau^2\theta^4 \end{aligned} , \quad (11.4)$$

$$\begin{aligned} g_{55}^{S_1}(\tau,\theta) = {} & 0.033184273 + 0.006131829\tau^2 - 0.001898866\tau^4 - 0.005376974\tau^6 \\ & - 0.0014236470\theta^2 - 0.0094940650\theta^4 + 0.0058156510\theta^6 \\ & - 0.026757097\tau^2\theta^2 + 0.039728795\tau^4\theta^2 + 0.062078983\tau^2\theta^4 \end{aligned} , \quad (11.5)$$

$$\begin{aligned} g_{45}^{S_1}(\tau,\theta) = {} & -0.002592500\tau\theta - 0.012784792\tau^3\theta \\ & - 0.012610571\tau\theta^3 + 0.056461188\tau^3\theta^3 \end{aligned} . \quad (11.6)$$

ASSIGNMENTS OF SPECTRA

Figures 54 and 55 compare the UV absorption spectra at ambient temperatures with the FES spectra of jet-cooled TET in the 0-900 cm^{-1} and 900-1800 cm^{-1} regions, respectively, relative to the 0_0^0 excitation at 36,789.3 cm^{-1}. Table 37 presents the frequencies and assignments for FES and UV absorption spectra. Since the observed UV absorption bands are weak and broad due to the weak dipole moment of TET, the assignments in Table 37 are made according to the FES frequencies. The FES frequencies and assignments reported by Guchhait *et al*.[64] are also listed in Table 37 for comparison. These authors numbered the vibrations simply from the lowest frequency to the highest frequency, without considering the symmetry of the molecule. The vibrational numbering used in this chapter, however, follows the convention adopted in Chapter IX, which is from the highest frequency to the lowest frequency according to the symmetry blocks in C_{2v} symmetry. The previous FES spectra and assignments only extended to 800 cm^{-1} higher than the 0_0^0 excitation. Spectra and assignments up to 2,000 cm^{-1} above the electronic origin are presented in this chapter. The FES spectra here have much better signal to noise ratio and are with much higher resolution than the spectra reported by Guchhait *et al*.[64]

Figure 56 shows the SVLF spectra with excitation of the 0_0^0 band at 36,789.3 cm^{-1}. The frequencies and assignments for these spectra are given in Table 38, compared to the

fundamental frequencies obtained from the vapor IR and vapor Raman spectra, as given in Chapter IX. Figure 57 shows the SVLF spectra with excitation of the 31_0^1 band at 94.5 cm^{-1} higher than the 0_0^0 band. The UV absorption spectra at ambient temperatures are also shown. The SVLF spectra were recorded from thirteen different excitation bands including 0_0^0 and 31_0^1. The frequencies and assignments from eight fundamental excitations are summarized in Table 39. The strongest bands shown in these SVLF spectra are always the corresponding transitions to the ground state levels of the same vibration as the excitation. For example, in the SVLF spectra with excitation of the 18_0^1 at 480.3 cm^{-1} and the 28_0^1 at 521.4 cm^{-1}, the strongest bands are observed at 579 cm^{-1} and 701 cm^{-1} lower than the excitation bands, respectively. The vapor-phase Raman spectra showed bands at 578 cm^{-1} and 699 cm^{-1} and these were assigned as fundamentals ν_{18} and ν_{28}, respectively. The nice agreement between the Raman and SVLF spectra further confirms the assignments of the FES bands 18_0^1 and 28_0^1. The eight fundamental excitation frequencies in Table 39 were compared with the corresponding calculated frequencies from CIS/6-311++G(d,p) calculations, and were used to determine the appropriate scaling factor for the $S_1(\pi,\pi^*)$ state, as shown in Table 35. Figure 58 presents the energy level diagram for both the S_0 and $S_1(\pi,\pi^*)$ states, based on the FES and SVLF spectra.

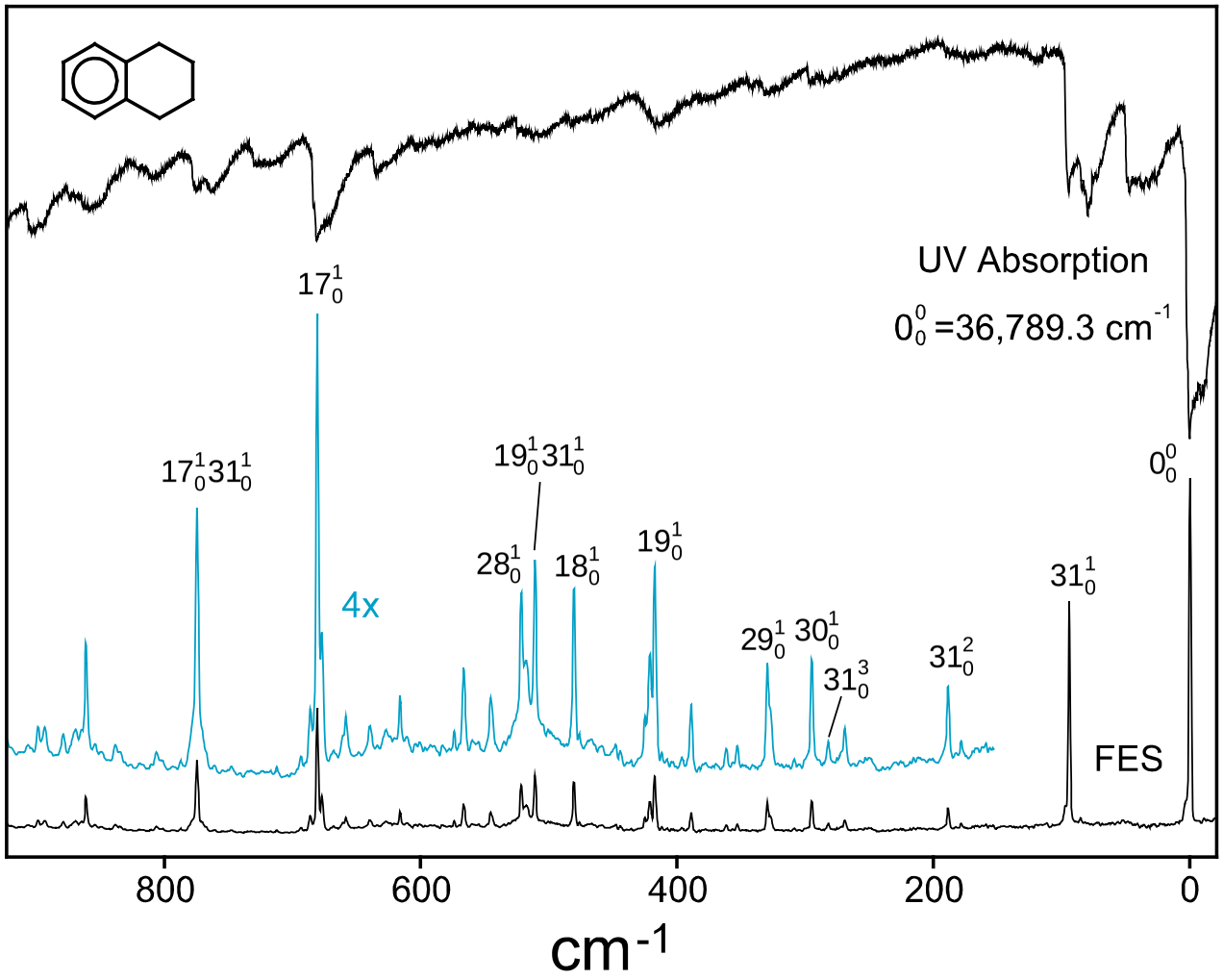

Figure 54. Fluorescence excitation spectra of jet-cooled tetralin and the ultraviolet absorption spectra at ambient temperature in the 0-900 cm^{-1} region.

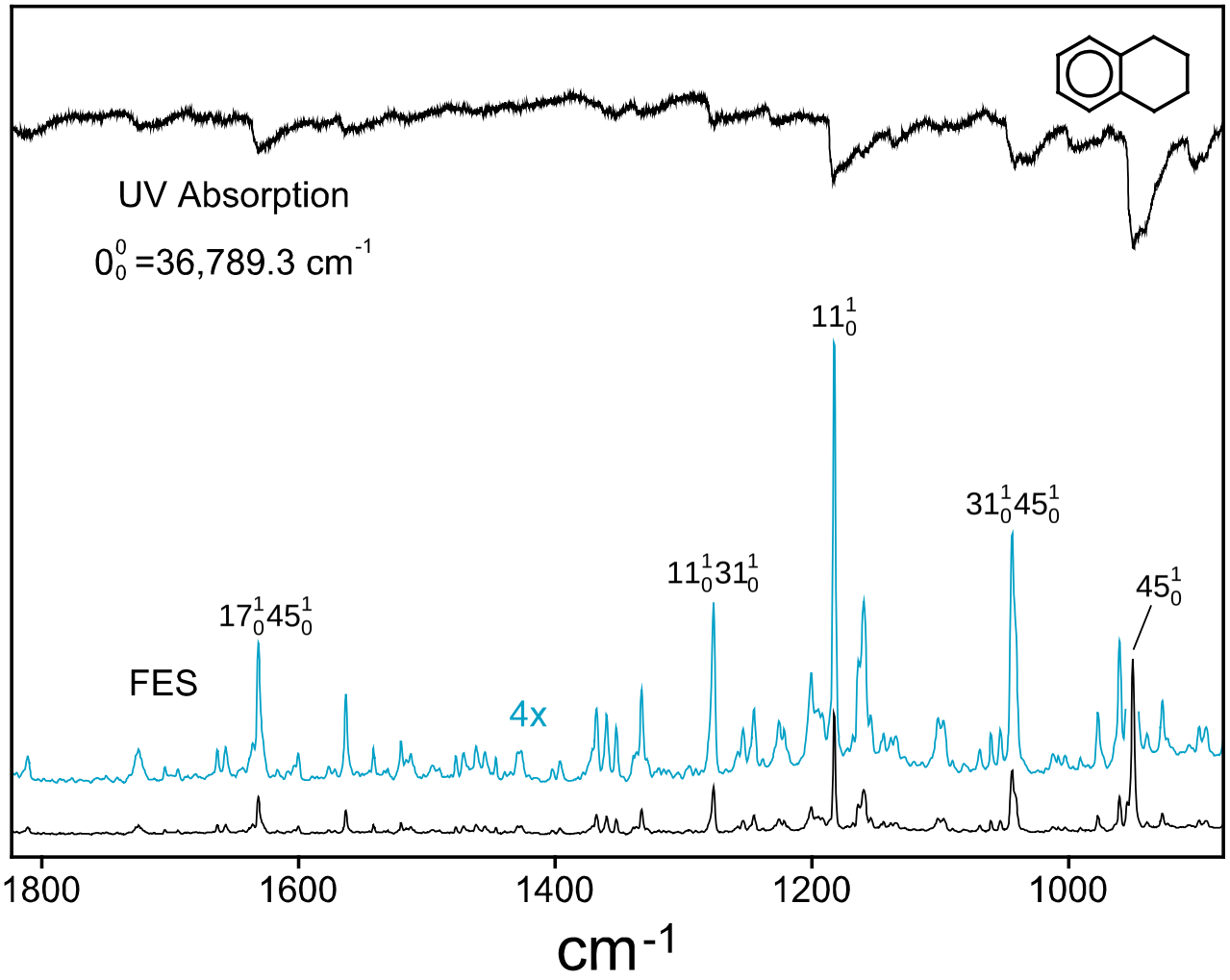

Figure 55. Fluorescence excitation spectra of jet-cooled tetralin and the ultraviolet absorption spectra at ambient temperature in the 900-1800 cm^{-1} region.

TABLE 37: Fluorescence Excitation (FES), Ultraviolet (UV) Absorption Frequencies (cm^{-1}) and Assignments for Tetralin.

This Work							GCMC[a]	
FES		UV		Calc.[b]	Inferred[c]	Assign.	FES	Assign.
		-283	vw			31_2^0		
		-141.4	m			31_1^0		
		-95	m,br			60_1^0		
		-57	m,br					
		-47.3	s			31_1^1		
		-10	s,br			60_1^1		
0.0	vs	0.0	vs			0_0^0	0	0_0^0
		46.9	s					
		79.5	s					
85.1	w			93		60_0^1		
94.0	vs	94.5	s	103		31_0^1	95	2_0^1
178.0	vw				179.1	$31_0^1 60_0^1$	179	1_0^2
188.4	m					31_0^2	189	2_0^2
268.9	w					$59_0^1 60_0^1$	270	$1_0^2 2_0^1$
281.9	vw	282	vw			31_0^3	282	2_0^3
294.7	m	295	vw	288		30_0^1	295	4_0^1
326.8	w			322		49_0^1		
329.5	m	331	w	335		29_0^1	329	3_0^1
353.0	vw				354.0	$59_0^1 60_0^2$	353	1_0^4
361.6	vw				362.9	$31_0^1 59_0^1 60_0^1$	363	$1_0^2 2_0^2$
							375	2_0^4
388.8	m				388.7	$30_0^1 31_0^1$	390	$4_0^1 2_0^1$
417.3	s	417	m	411		19_0^1	417	5_0^1
420.9	m				420.8	$31_0^1 49_0^1$	422	$3_0^1 2_0^1$
424.8	w				423.5	$29_0^1 31_0^1$		
							446	$1_0^4 2_0^1$
480.3	s			489		18_0^1	481	$4_0^1 2_0^2$
510.8	s	511	w		511.3	$19_0^1 31_0^1$	511	$5_0^1 2_0^1$ / $3_0^1 1_0^2$
517.6	m				517.9	$29_0^1 31_0^2$		
521.4	s			537		28_0^1	520	$3_0^1 2_0^2$
545.0	m			547		47_0^1	544	$1_0^4 2_0^2$

TABLE 37: Continued.

This Work							GCMC[a]	
FES		UV		Calc.[b]	Inferred[c]	Assign.	FES	Assign.
566.3	m			613		57^1_0	566	
573.7	vw				574.3	$18^1_0 31^1_0$	574	$4^1_0 2^3_0$
616.1	m				615.4	$28^1_0 31^1_0$		
627.1	vw							
		634	w					
639.5	vw				639.0	$31^1_0 47^1_0$		
658.1	w				660.3	$31^1_0 57^1_0$		
661.1	vw							
		671	m					
676.8	m			647		26^1_0		
680.5	vs	681	s	677		17^1_0	679	6^1_0
686.1	w							
693.5	vw							
		730	w					
		762	m					
767.4	vw							
770.4	w				770.8	$26^1_0 31^1_0$		
774.3	s	774	m		774.5	$17^1_0 31^1_0$	765	7^1_0
778.1	w				777.6	$30^2_0 31^2_0$		
780.7	vw							
		808	w					
860.9	ms	861	m	875		56^1_0		
		903	m					
927.2	m				928.1	$19^2_0 31^1_0$		
939.0	vw	940	m					
		946	m					
950.0	vs	950	s	954		45^1_0		
954.5	m				954.9	$31^1_0 56^1_0$		
960.4	ms				960.6	18^2_0		
963.8	vw							
977.3	m			968		15^1_0		
		996	w					

TABLE 37: Continued.

This Work							GCMC[a]	
FES		UV		Calc.[b]	Inferred[c]	Assign.	FES	Assign.
1041.6	m	1042	m		1042.8	28^2_0		
1044.2	s				1044.0	$31^1_0 45^1_0$		
		1136	w					
1159.8	ms	1160	vw		1160.8	$17^1_0 18^1_0$		
1164.0	m							
1182.8	vs	1183	m	1182		11^1_0		
1200.8	m				1201.9	$17^1_0 28^1_0$		
1276.8	ms	1277	w		1276.8	$11^1_0 31^1_0$		
1332.7	m	1333	w					
1352.5	w	1354	w					
1360.0	m				1361.0	17^2_0		
1367.8	m				1367.3	$19^1_0 45^1_0$		
1563.1	m				1563.0	28^3_0		
1631.3	ms	1631	m		1630.5	$17^1_0 45^1_0$		
1810.9	w				1810.9	$45^1_0 56^1_0$		
1863.1	w				1863.3	$11^1_0 17^1_0$		
1898.8	w	1899	w		1900.0	45^2_0		
		2133	w		2132.8	$11^1_0 45^1_0$		

Abbreviations: s, strong; m, medium; w, weak; v, very; br, broad.

[a] From reference 64.

[b] Calculated using the CIS/6-311++G(d,p) basis set with GAUSSIAN 03.

[c] Inferred combination frequencies are based on assignments of individual vibrations.

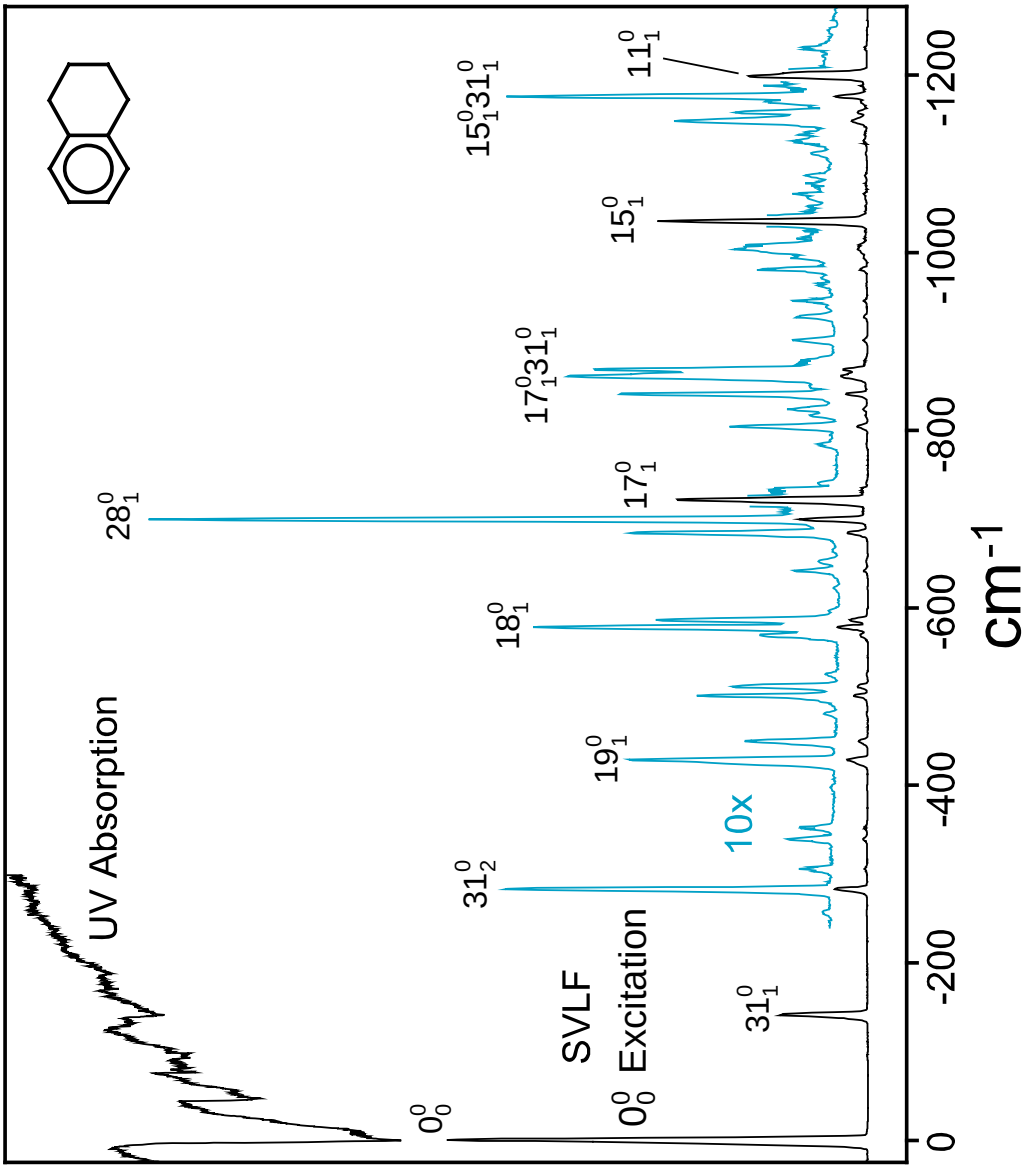

Figure 56. Single vibronic level fluorescence spectra of jet-cooled tetralin with excitation of the 0_0^0 band at 36,789.3 cm^{-1} and the ultraviolet absorption spectra at ambient temperature.

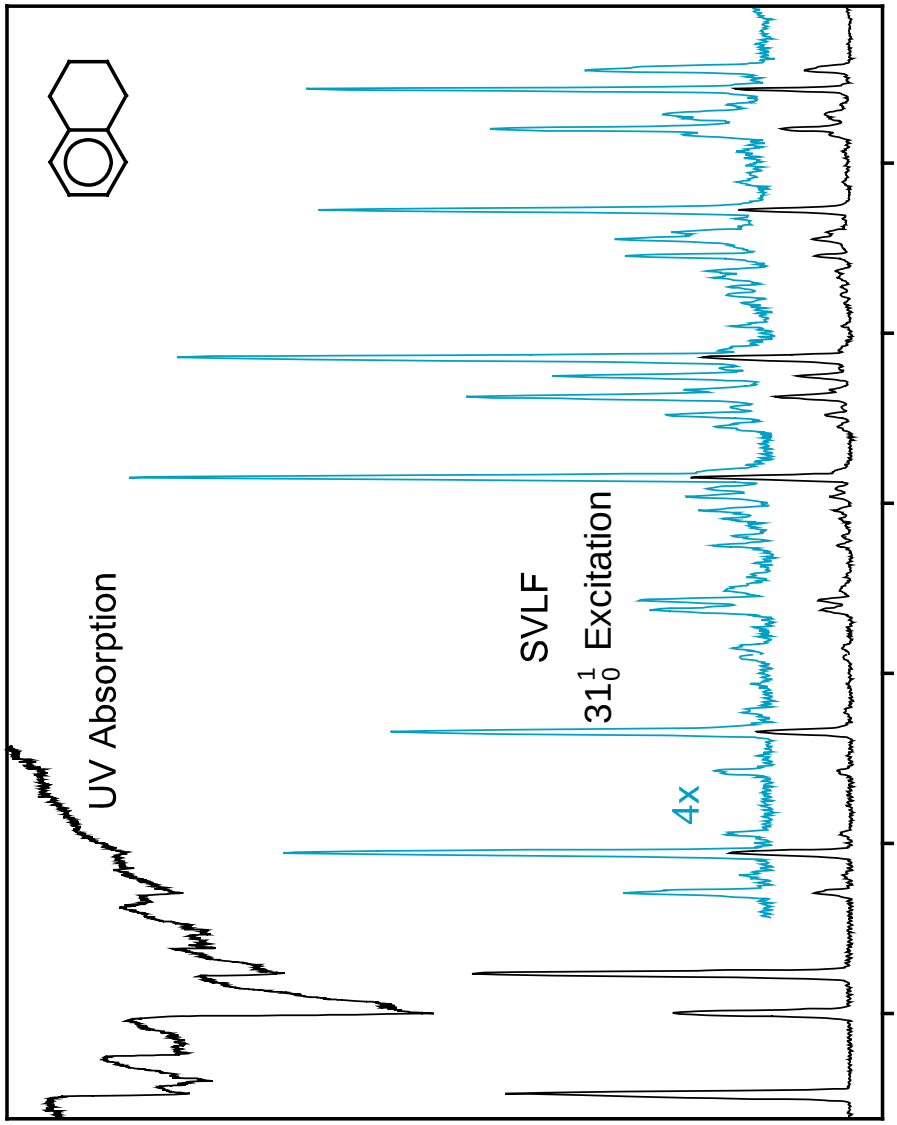

Figure 57. Single vibronic level fluorescence spectra of jet-cooled tetralin with excitation of the 31_0^1 band at 94.5 cm^{-1} higher than the 0_0^0 band and the ultraviolet absorption spectra at ambient temperature.

TABLE 38: Frequencies (cm^{-1}) and Assignments of Single Vibronic Level Fluorescence (SVLF) Spectra of Jet-Cooled Tetralin with Excitation of the 0_0^0 band at 36,789.3 cm^{-1}.

This Chapter						From Chapter IX			
SVLF		UV		Inferred[a]	Assignment	Vapor IR	Vapor Raman		Calculated[b]
0	vs	0.0	vs		0_0^0				
-95.3	vw	-95	m		60_1^0	---	~90	vw	94
-141.7	ms	-141	m		31_1^0	---	142	(11)	141
-256.7	vw				59_1^0	---	253	(1.6)	255
-283.0	m	-283	vw	283.4	31_2^0				
-306.0	w				30_1^0	---	298	(0.6)	301
-339.4	w				49_1^0	---	---		339
-352.1	w			352.0	$59_1^0 60_1^0$				
-397.4	vw			398.4	$31_1^0 59_1^0$				
-424.0	w,sh			425.1	31_3^0				
-428.5	m				19_1^0	---	427	(13)	427
-449.5	m				48_1^0	---	453	(2.1)	450
-480.7	vw			481.1	$31_1^0 49_1^0$				
-501.0	m				29_1^0	---	498	(6.2)	504
-511.6	m			513.4	59_2^0				
-524.8	vw				$58_1^0 60_1^0$				
-564.7	w,sh			566.8	31_4^0				
-569.1	m			570.2	$19_1^0 31_1^0$				
-578.0	m				18_1^0	---	578	(19)	581
-586.3	m				47_1^0	---	---		587

TABLE 38: Continued.

This Chapter					From Chapter IX				
SVLF		UV	Inferred[a]	Assignment	Vapor IR		Vapor Raman		Calculated[b]
-597.0	vw		596.1	$49_1^0 59_1^0$					
-622.1	vw		622.4	$31_2^0 49_1^0$					
-641.9	w		642.7	$29_1^0 31_1^0$					
-652.5	vw		653.3	$59_2^0 31_1^0$					
-684.6	m		685.2	$19_1^0 59_1^0$					
-699.7	ms			28_1^0	---		699	(5.9)	703
-721.5	s		719.7	17_1^0 /$18_1^0 31_1^0$	---		721	(83)	723
-804.0	m			46_1^0	805	w	805	(0.7)	801
-816.6	vw			27_1^0	817	w	815	(2.6)	819
-823.5	w			?					
-840.5	m		841.4	$28_1^0 31_1^0$					
-860.8	m,br		863.2/857.0	$17_1^0 31_1^0$ /19_2^0					
-868.4	m			26_1^0	868	w	---		869
-901.1	w			56_1^0	902	w	---		900
-928.2	w		929.5	$19_1^0 29_1^0$					
-945.7	w		945.7	$31_1^0 46_1^0$					
-981.5	m		982.7	$28_1^0 31_2^0$					
-1005.4	m		1004.5	$17_1^0 31_2^0$					
-1035.2	s			15_1^0	1038	w	1035	(57)	1038
-1148.5	m		1150.0	$17_1^0 19_1^0$					
-1158.5	m			13_1^0	---		1157	(1.4)	1164

TABLE 38: Continued.

This Chapter				From Chapter IX			
SVLF	UV	Inferred[a]	Assignment	Vapor IR	Vapor Raman		Calculated[b]
-1176.3 m		1176.9	$15_1^0 31_1^0$				
-1199.9 s			11_1^0	---	1199	(22)	1200

Abbreviations: s, strong; m, medium; w, weak; v, very; sh, shoulder, br, broad.

[a] Inferred combination frequencies are based on assignments of individual vibrations.

[b] Calculated using the B3LYP/6-311++G(d,p) basis set with GAUSSIAN 03.

TABLE 39: Single Vibronic Level Fluorescence (SVLF) Frequencies (cm^{-1}) and Assignments from Various Fundamental Excitation Bands of Tetralin.

Excitation:	0_0^0	31^1 (B')	30^1 (D')	49^1	29^1	19^1	18^1	28^1	17^1
Assignment	0.0[a] vvs	94.5 vs	294.7 m	326.8 w	329.5 m	417.3 s	480.3 s	521.4 s	680.5 vs
60_1 (A)	-95 vw	-95 s							
31_1 (B)	-142 ms	-142 vs				-141 vw			-141 m
31_160_1 (A+B)		-237 w							
31_2 (2B)	-283 m	-284 m							-283 w
30_1 (D)	-306 w	-306 vw	-305 s		-305 m	-305 w			
49_1	-339 w			-339 s					
59_160_1 (A+C)	-352 w		-352 w						
31_3 (3B)	-424 w	-424 m							
19_1	-428 m				-428 m	-429 vs		-428 w	-428 w
30_131_1 (B+D)			-447 m			-447 w			
48_1	-449 m								-449 vw
31_149_1	-481 vw			-480 w					
29_1	-501 m		-501 w		-501 s	-501 w	-501 m		-501 m
59_2 (2C)	-512 w				-512 w				-512 vw
31_4 (4B)	-565 w	-565 sh							
19_131_1	-569 m	-569 w				-570 m			
18_1	-578 m	-578 w			-579 vw	-579 w	-579 s	-579 s	-578 ms
47_1	-586 m								-586 w
30_131_2 (2B+D)			-589 vw						
31_249_1	-622 vw			-621 vw					
29_131_1	-642 w				-642 vw	-643 m			
28_1	-700 ms				-701 vw	-701 m	-701 m	-701 s	

TABLE 39: Continued.

Excitation:	0_0^0	31^1 (B')	30^1 (D')	49^1	29^1	19^1	18^1	28^1	17^1
Assignment	0.0[a] vvs	94.5 vs	294.7 m	326.8 w	329.5 m	417.3 s	480.3 s	521.4 s	680.5 vs
19_131_2						-712 w			
17_1 / 18_131_1	-722 s	-722 s			-721 vw		-721 m	-720 w	-721 s
28_131_1	-841 m	-841 m				-843 w			
19_2	-859 m					-858 m			
17_131_1	-862 m	-862 s							
26_1	-868 m								-864 ms
19_129_1	-928 w					-929 w			
19_159_2						-941 w			
28_131_2	-982 m	-982 w				-941 w			
17_131_2 / 28_130_1	-1005 m	-1005 w	-1007 w						-1006 m
17_130_1			-1028 m						
15_1	-1035 s	-1036 m							-1035 m
28_149_1				-1040 w					
17_149_1				-1062 m					
19_128_1						-1131 m			
17_119_1						-1152 s			
15_131_1	-1176 m	-1177							-1176 w
11_1	-1200 m	-1200							-1200 m

Abbreviations: s, strong; m, medium; w, weak; v, very; sh, shoulder.

[a] The excitation of 0_0^0 is at 36,789.3 cm^{-1}; the frequencies of all other excitation bands are relative to the 0_0^0.

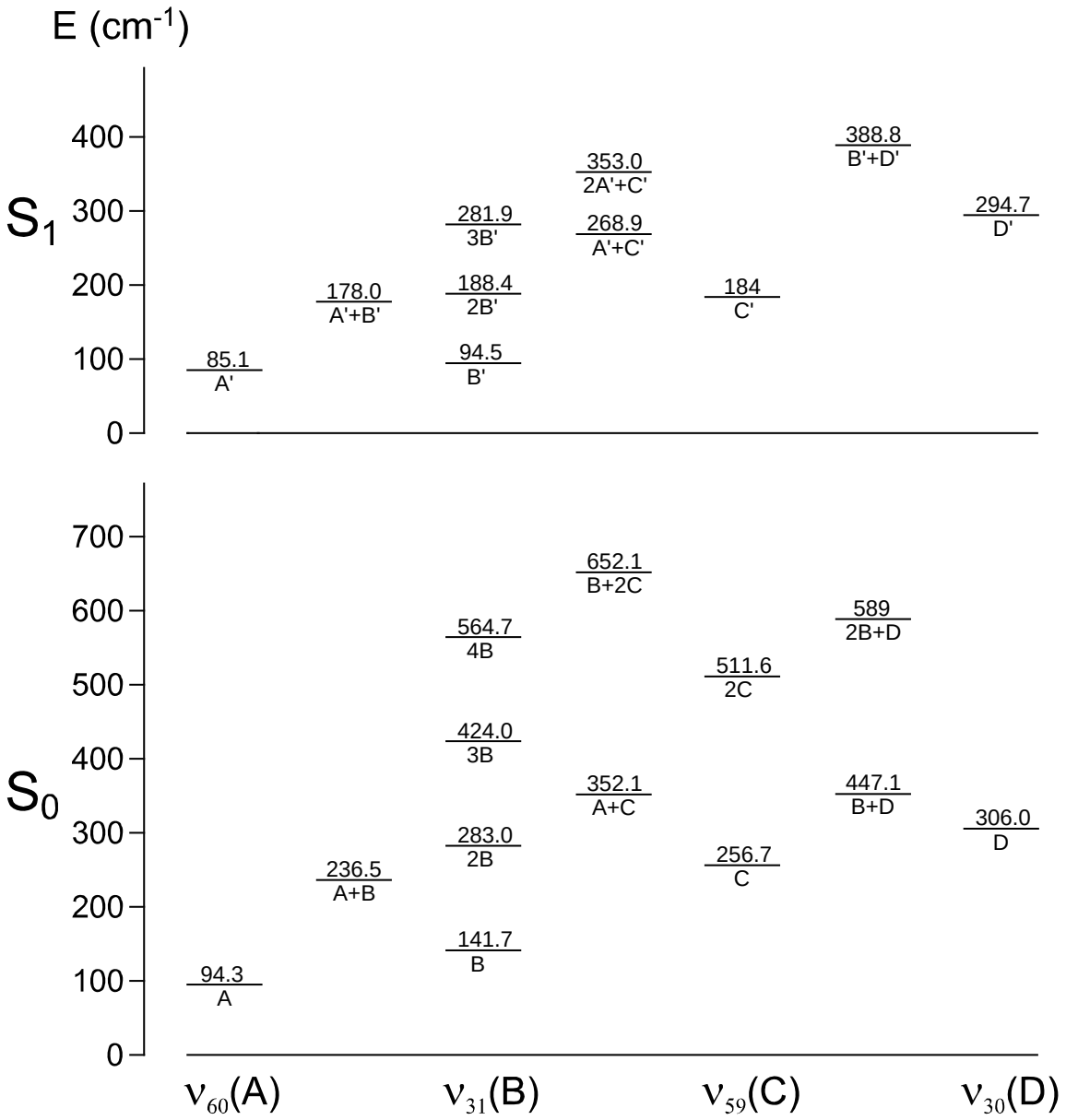

Figure 58. Energy level diagram for the low-frequency modes of tetralin in its S_0 and $S_1(\pi,\pi^*)$ states.

CHAPTER XII

PRELIMINARY INVESTIGATIONS OF 1,3-DITHIOLANE

INTRODUCTION

1,3-Dithiolane (13DTL) is related to the previously studied molecules cyclopentane[11] (CPT), 1,3-dioxolane[12,13] (13DOL), and 1,3-oxathiolane[14,15] (13OTL), which are all saturated five-membered ring molecules.

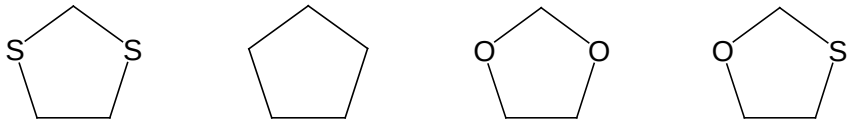

13DTL CPT 13DOL 13OTL

A saturated five-membered ring molecule has two out-of-plane ring vibrations, a twisting mode and a puckering mode. Accordingly, the lowest energy forms for this molecule are the twist form (half-chair, C_2 symmetry) and the bent form (envelope, C_s symmetry). There are a total of 10 twist and 10 bent forms. In order to interconvert between these forms, the molecule can go through other twist or bent forms instead of passing through the high-barrier planar form. This path is similar to a wave or a rotation, but it is actually a vibration. It is the so-called pseudorotational vibration, or pseudorotation. Therefore, the two out-of-plane twisting and puckering modes can be better described as pseudorotational and radial vibrations. The radial motion is primarily described by the out of plane amplitudes. Figure 59 shows the course of the

pseudorotation for a saturated five-membered ring molecule.

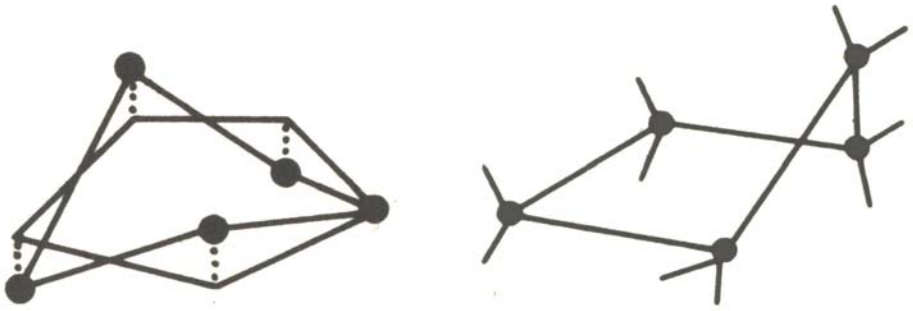

C_s, Bent (envelope) C_2, Twist (half-chair)

For cyclopentane with D_{5h} symmetry, the two out-of-plane ring vibrations are degenerate, so the twisting and the bending vibrations are of equal energy. The twisted and bent conformations also have nearly equal energies, and thus the molecule can easily interconvert between them but never needs to pass through the high barrier planar form. This is called free pseudorotation since there is no potential barrier hindering the interconversion process. However, for other five-membered ring molecules where the ring atoms are not all equivalent, the twist forms and the bent forms have different energies. Thus the pseudorotation is hindered. The PES for pseudorotation is a bowl-shaped surface with steep sides and a central circular hump, the height of which is the barrier to planarity. As examples, Figures 60 and 61 shows the potential energy surfaces (PESs) for the free pseudorotation in cyclopentane[11] and the hindered pseudorotation in 1,3-oxathiolane,[13] respectively. The potential energy function for pseudorotation can be best described in the one-dimensional form as

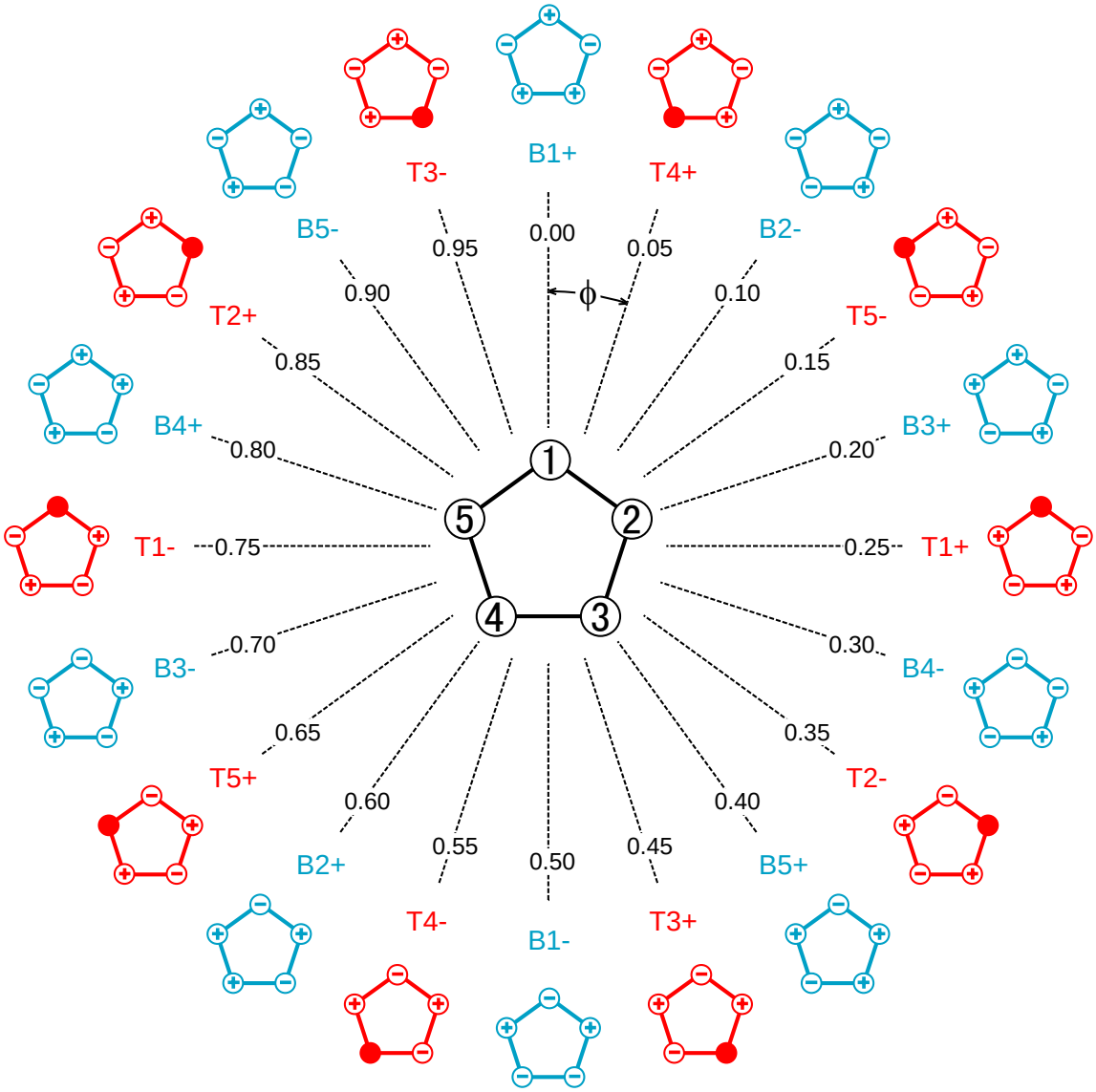

Figure 59. The course of the pseudorotational vibration for a saturated five-membered ring molecule.

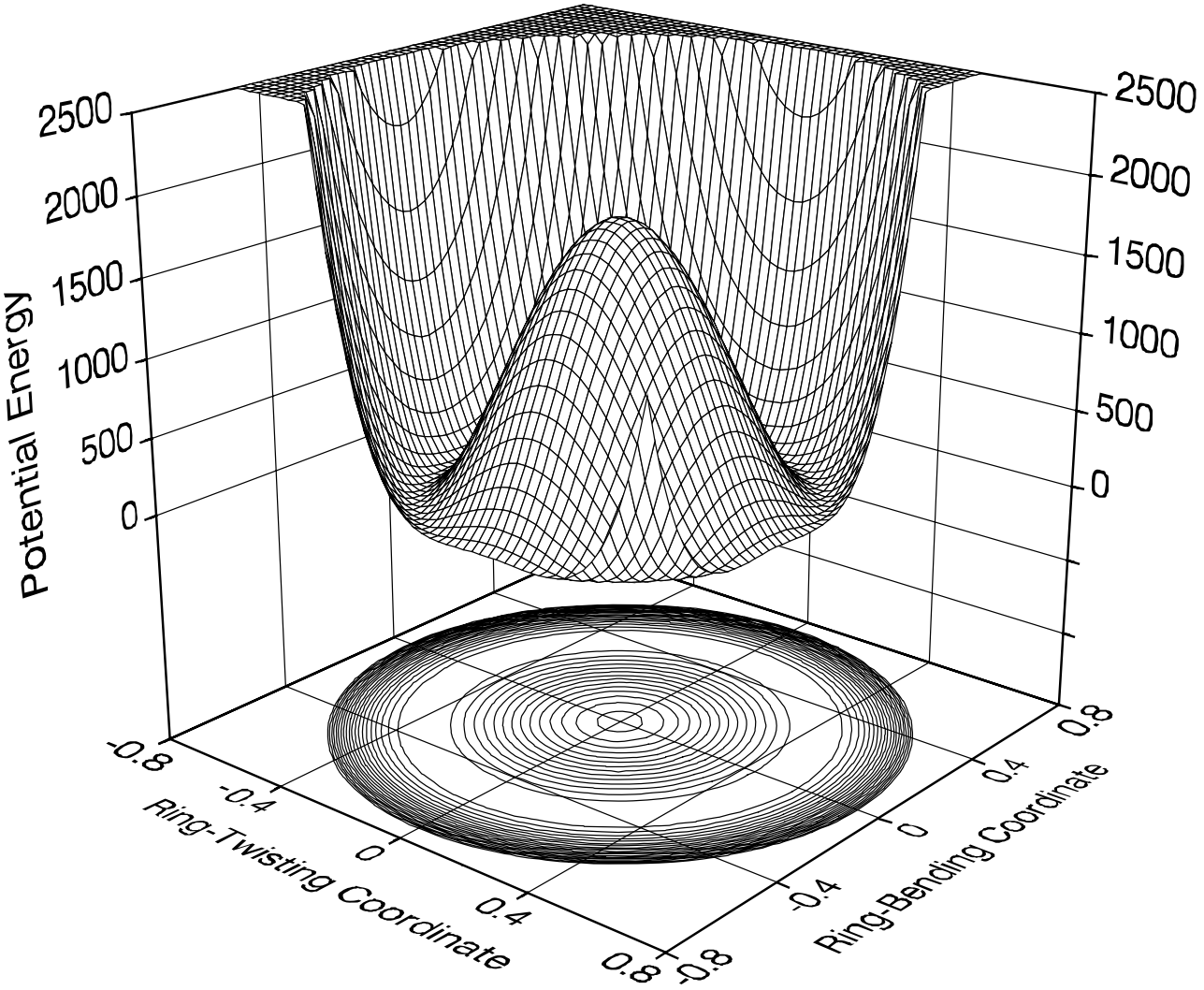

Figure 60. The two-dimensional potential energy surface for the free pseudorotation of cyclopentane.

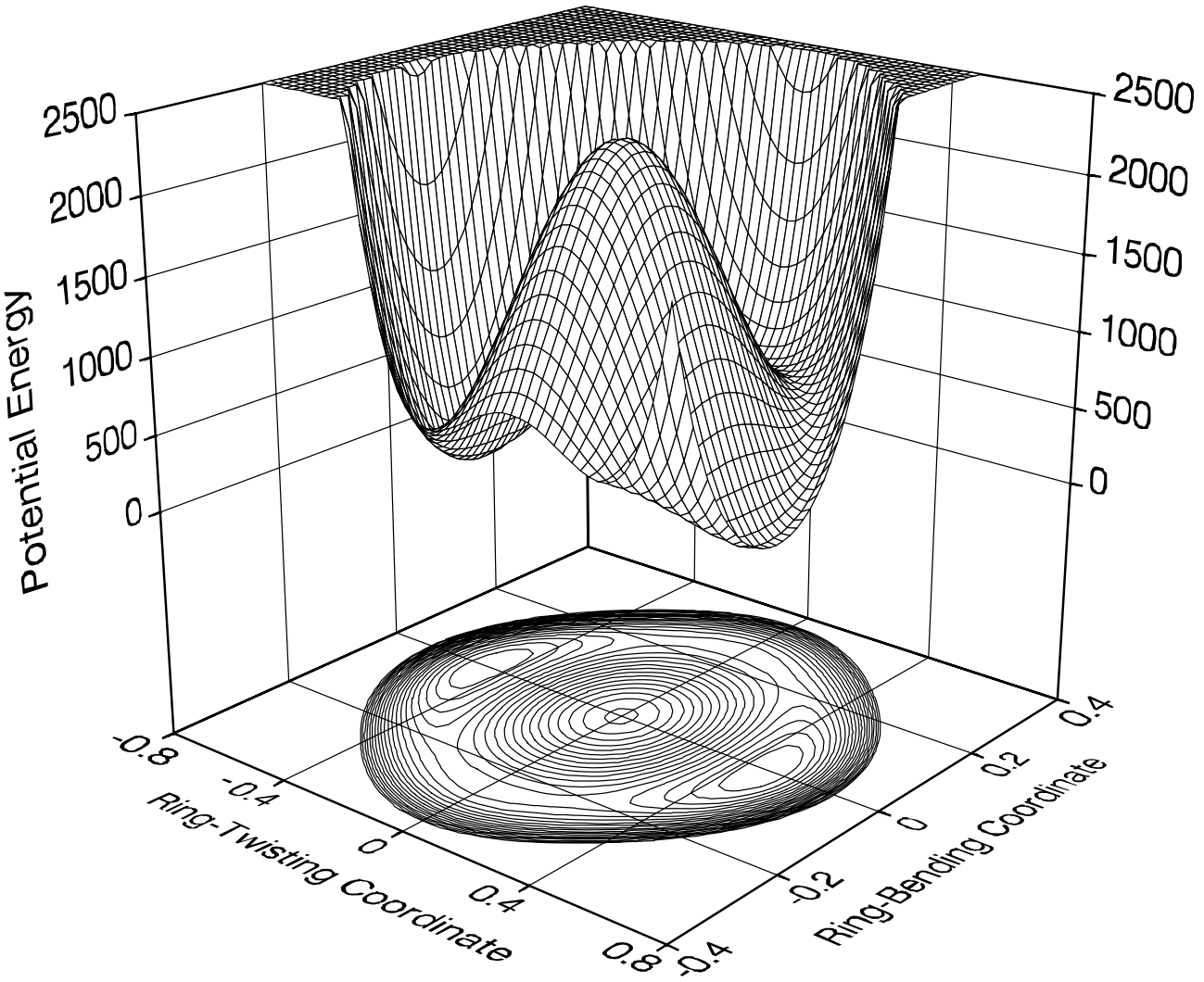

Figure 61. The two-dimensional potential energy surface for the hindered pseudorotation of 1,3-oxathiolane.

$$V(\phi) = \frac{1}{2}\sum_{n} V_n (1 - \cos n\phi), \qquad (12.1)$$

where ϕ is the phase angle of the pseudorotation, also as shown in Figure 59.

Previous studies showed that 1,3-dioxolane[13] is a nearly free pseudorotator with a less than 50 cm^{-1} pseudorotational barrier and 1,3-oxathiolane[14] has a pseudorotational barrier of 570 cm^{-1}. The study of the four lowest pseudorotational states of 1,3-dioxolane was also reported by Melnik *et al*.[65]

For 1,3-dithiolane, a previous study[13] assigned the pseudorotational frequencies in the ground and first excited radial states and showed that this molecule has a pseudorotational barrier of 296 cm^{-1}. In that study, the $0 \rightarrow 2$ transition was assigned at 54.6 cm^{-1}. However, later microwave spectra by Lopez and Alonso[17] showed a peak at 185.5 GHz, or 6.18 cm^{-1}, to be the $0 \rightarrow 2$ transition for the pseudorotation, which indicated that a small barrier (62 cm^{-1}) to pseudorotation occurs at the C_2 twisted configuration, and that the energy minima of 1,3-dithiolane is at the twisted and bent C_1 structure. Therefore, a careful reexamination of the potential energy function for the pseudorotation of 1,3-dithiolane is needed.

Only the preliminary results of 1,3-dithiolane are presented in this chapter. A complete vibrational assignment of the 1,3-dithiolane molecule has been made, based on the liquid and vapor-phase infrared and Raman spectra. The potential energy function of the pseudorotation, however, has not as yet been determined.

EXPERIMENTAL

The 1,3-dithiolane sample was initially synthesized by J. R. Villarreal from University of Texas-PanAmerican and later it was further purified by vacuum distillation.

The liquid-phase mid-infrared spectra were recorded on the Biorad FTS-60 Fourier-transform infrared spectrometer. The spectra were recorded at 1 cm^{-1} resolution and 64 scans were typically averaged.

Raman spectra were recorded on an Instruments SA Jobin-Yvon U-1000 monochromator with a liquid-nitrogen cooled charge-coupled device (CCD) detector. Liquid-phase Raman spectra were recorded at ambient temperatures. Excitation at 514.5 nm was achieved with a Coherent Radiation Innova 20 argon ion laser with a lasing power of 1 W. Depolarization measurements were taken using a polarizer and a scrambler to separate the scattered light into its parallel and perpendicular components. Vapor-phase Raman spectra were collected at temperatures at about 200 °C and at pressures typically 700-900 Torr. The sample was contained in a high-temperature Raman cell previously described.[24,25] Excitation at 514.5 nm was achieved with a Coherent Radiation Innova 20 argon ion laser operating at 5 W. The spectral resolution was about 0.7 cm^{-1}.

CALCULATIONS

Theoretical calculations were carried out using the Gaussian 98 package[51] at Hartree-Fock (HF), Moller-Plesset second-order perturbation (MP2), and density functional theory (B3LYP) with several different basis sets. The vibrational frequencies for planar (C_{2v}), bent (C_s), twisted (C_2), and non-symmetric (C_1) symmetries were obtained with the density functional (B3LYP) method and the 6-311++G(d,p) basis set. The infrared and Raman intensities were calculated for the C_1 symmetry. Based on previous work,[7,44,45] scaling factors of 0.964 for the 2900-3100 cm^{-1} region and 0.985 for the region below 1600 cm^{-1} were used.

Figure 62 shows the bond lengths and bond angles for C_2, C_s, and C_{2v} structures of 1,3-dithiolane from MP2/cc-pVTZ basis set calculations. The twisting angle for the C_2 structure was calculated to be 31.0° and the calculated bending angle for the C_s structure was 49.2°. The definition of the twisting and bending angles are also shown in Figure 62. Table 40 lists the calculated energies with different methods and basis sets for the planar (C_{2v}), bent (C_s), and twisted (C_2) structures of 1,3-dithiolane relative to the non-symmetric (C_1) structure. The energies obtained from microwave studies[17] for the bent, twisted, and non-symmetric structures of 1,3-dithiolane are also listed for comparison. All calculations predict very similar or equal energies for the C_2 and C_1 structures. Both HF and MP2 calculations show the twisted C_2 structure to be slightly higher in energy

than the C_1 structure, while DFT calculations predict the reverse case. However, by further calculating the vibrational frequencies from the optimized structures, DFT calculations show that there are 2, 1, 1, and 0 imaginary frequencies for the C_{2v}, C_s, C_2, and C_1 structures, respectively, which indicates that the non-symmetric C_1 structure corresponds to the real energy minimum for 1,3-dithiolane.

MOLECULAR VIBRATIONS

Considering the 1,3-dithiolane molecule has perturbed C_{2v} symmetry, a vibrational distribution of

$$9A_1 + 5A_2 + 7B_1 + 6B_2$$

can be obtained. In the twisted C_2 symmetry A_1 and A_2 symmetry species merge to become A symmetry, whereas B_1 and B_2 species merge to become B symmetry. Therefore, the vibrations are

$$14A + 13B\,.$$

In the non-symmetric C_1 symmetry, all 27 vibrations of 1,3-dithiolane merge to become totally symmetric A symmetry.

In the planar C_{2v} symmetry, the A_1, B_1, and B_2 vibrations will produce Type A, Type B, and Type C infrared bands, respectively. The A_1 bands will be Raman polarized while A_2, B_1, and B_2 bands will be Raman depolarized.

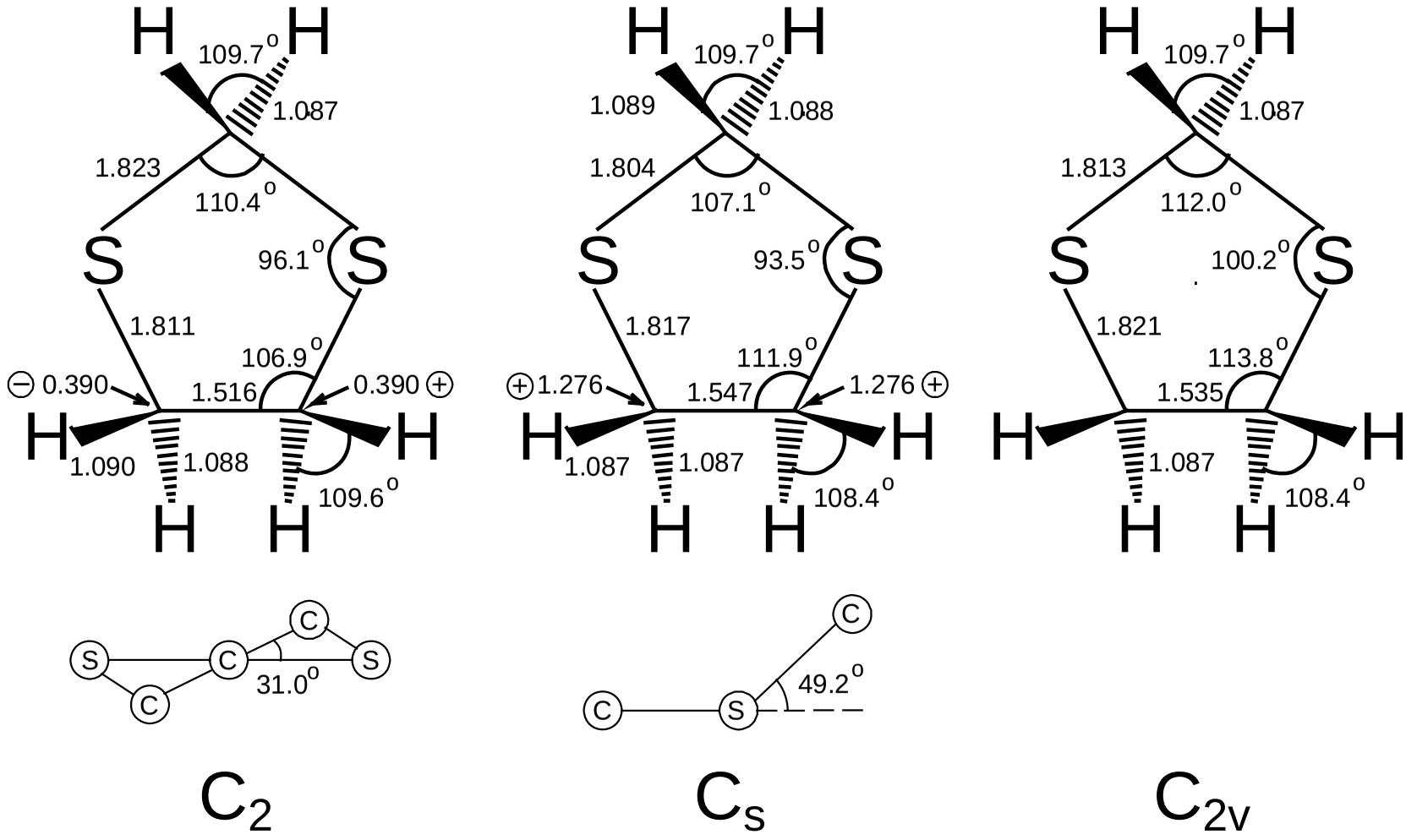

Figure 62. The calculated structures of 1,3-dithiolane for C_2, C_s, and C_{2v} symmetries and the corresponding twisting and bending angles from MP2/cc-pVTZ calculations.

TABLE 40: Calculated and Experimental Relative Energies (cm^{-1}) for Different Structures of 1,3-Dithiolane.

Structure	6-31G(d)			6-311++G(d,p)			cc-pVTZ	Exp.[a]
	HF	DFT	MP2	HF	DFT	MP2	MP2	
C_{2v} (planar)	2076	2137	2689	2148	2182	2843	2598	
C_s (bent)	1000	920	1068	1013	859	1062	910	599
C_2 (twisted)	0.1	-4.7	0.1	0.04	-2.4	0.02	0	62
C_1 (twisted & bent)	0	0	0	0	0	0	0	0

[a] Experimental energy differences relative to the energy minima at C_1 structure from Reference 17.

ASSIGNMENTS OF SPECTRA

Figure 63 presents the liquid-phase infrared and Raman spectra of 1,3-dithiolane. Figure 64 shows the Raman spectra with both parallel and perpendicular polarizations of the liquid sample. Figure 65 compares the vapor-phase Raman spectrum to the computed spectrum from density functional theory (DFT) with scaled frequencies.

Based on all those spectra, Table 41 lists the experimental and calculated frequencies for C_{2v}, C_s, C_2, and C_1 symmetries and the complete vibrational assignments of 1,3-dithiolane. The calculated frequencies for the non-symmetric C_1 symmetry do a better job of fitting the observed frequencies than those for the other symmetries, which further verifies the molecule actually has no symmetry at all. The calculation for the C_2 symmetry also fits the other experimental values very well except that it shows an imaginary frequency for the ring-bending vibration, which indicates that the twisted C_2 form corresponds to a saddle point on the two-dimensional surface with energy slightly higher than the non-symmetric C_1 minima. This agrees with the results derived from the microwave spectra by Lopez and Alonso.[17]

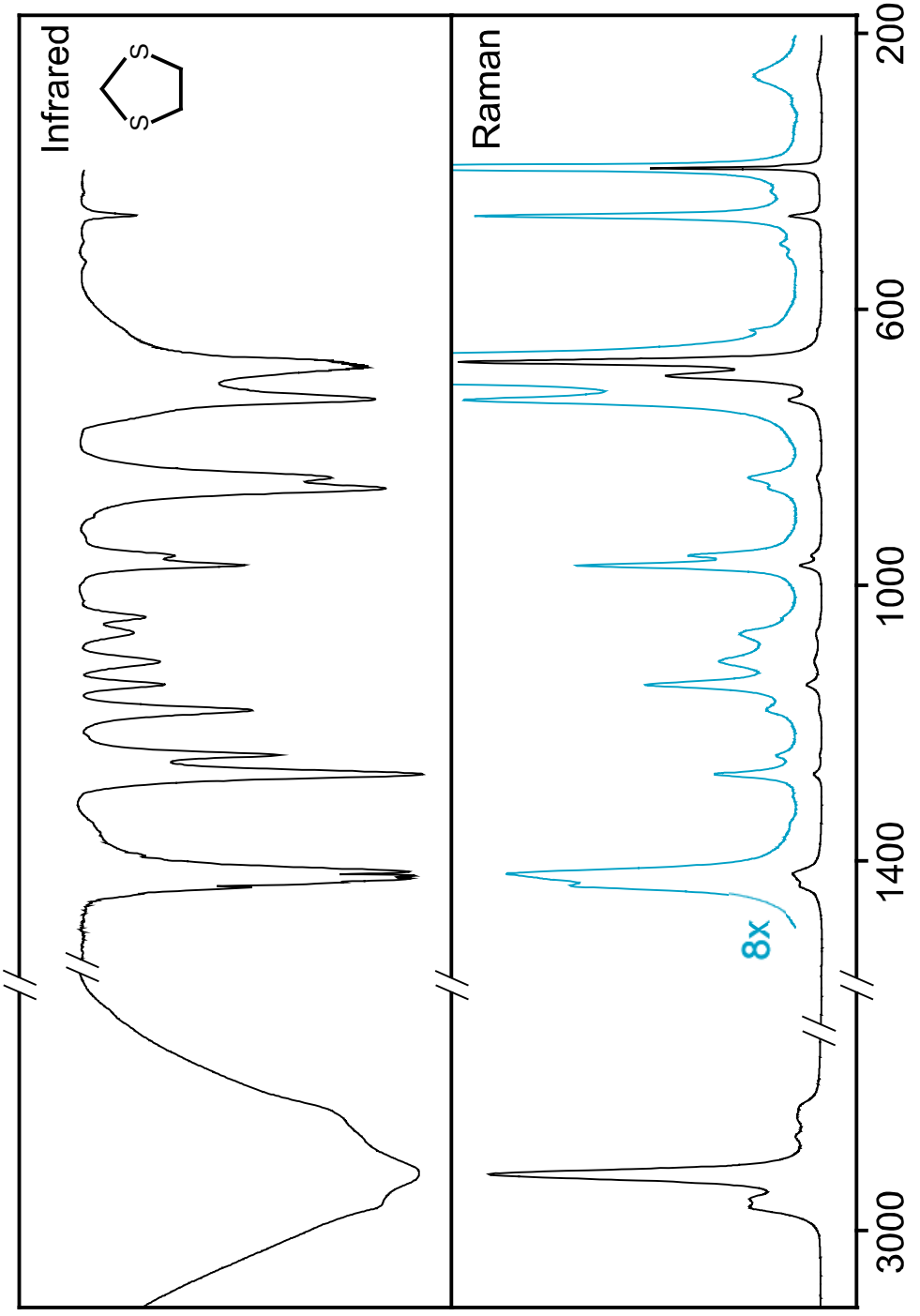

Figure 63. The infrared (top) and Raman (bottom) spectra of 1,3-dithiolane liquid.

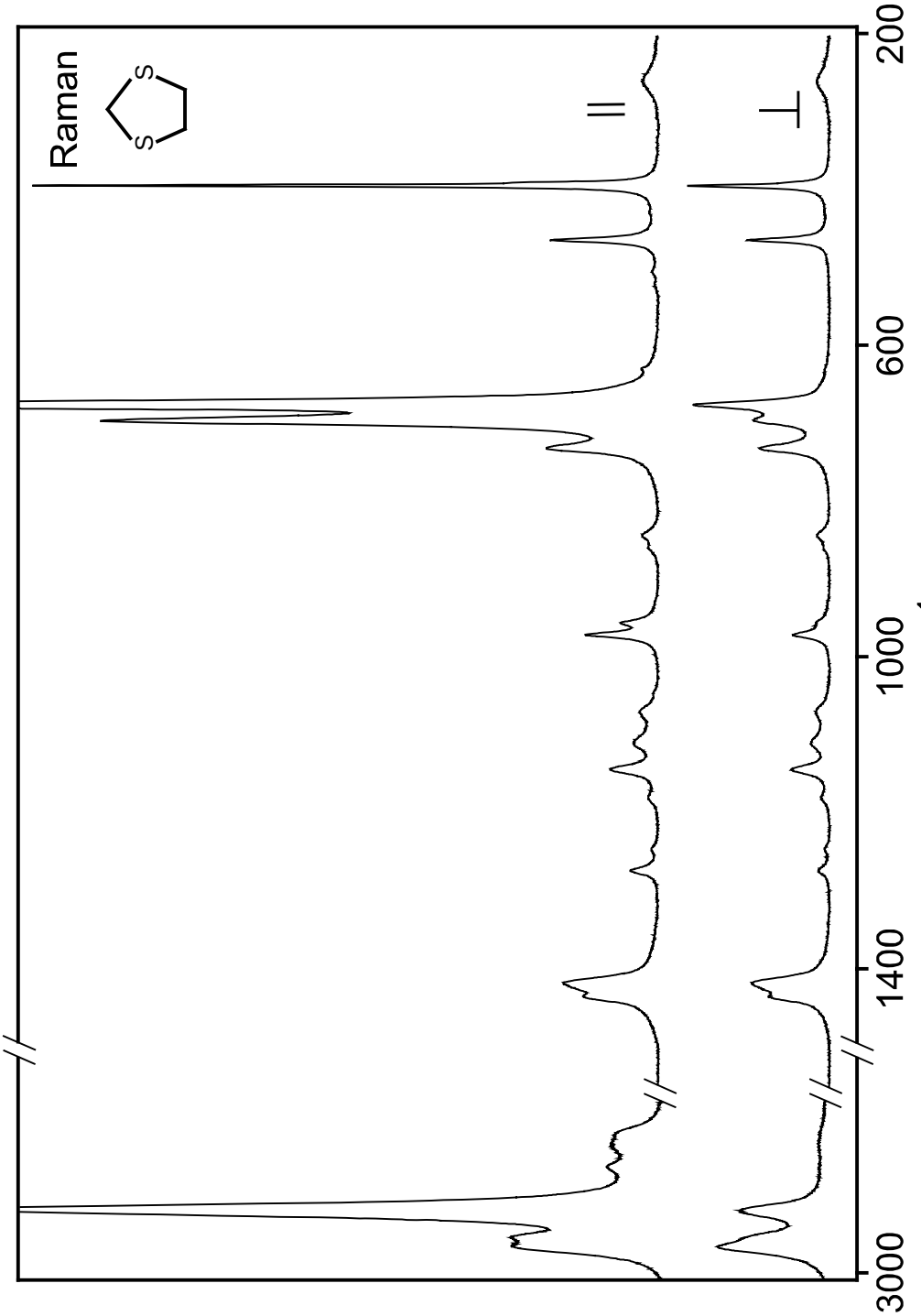

Figure 64. The Raman spectra with parallel (top) and perpendicular (bottom) polarizations of 1,3-dithiolane liquid.

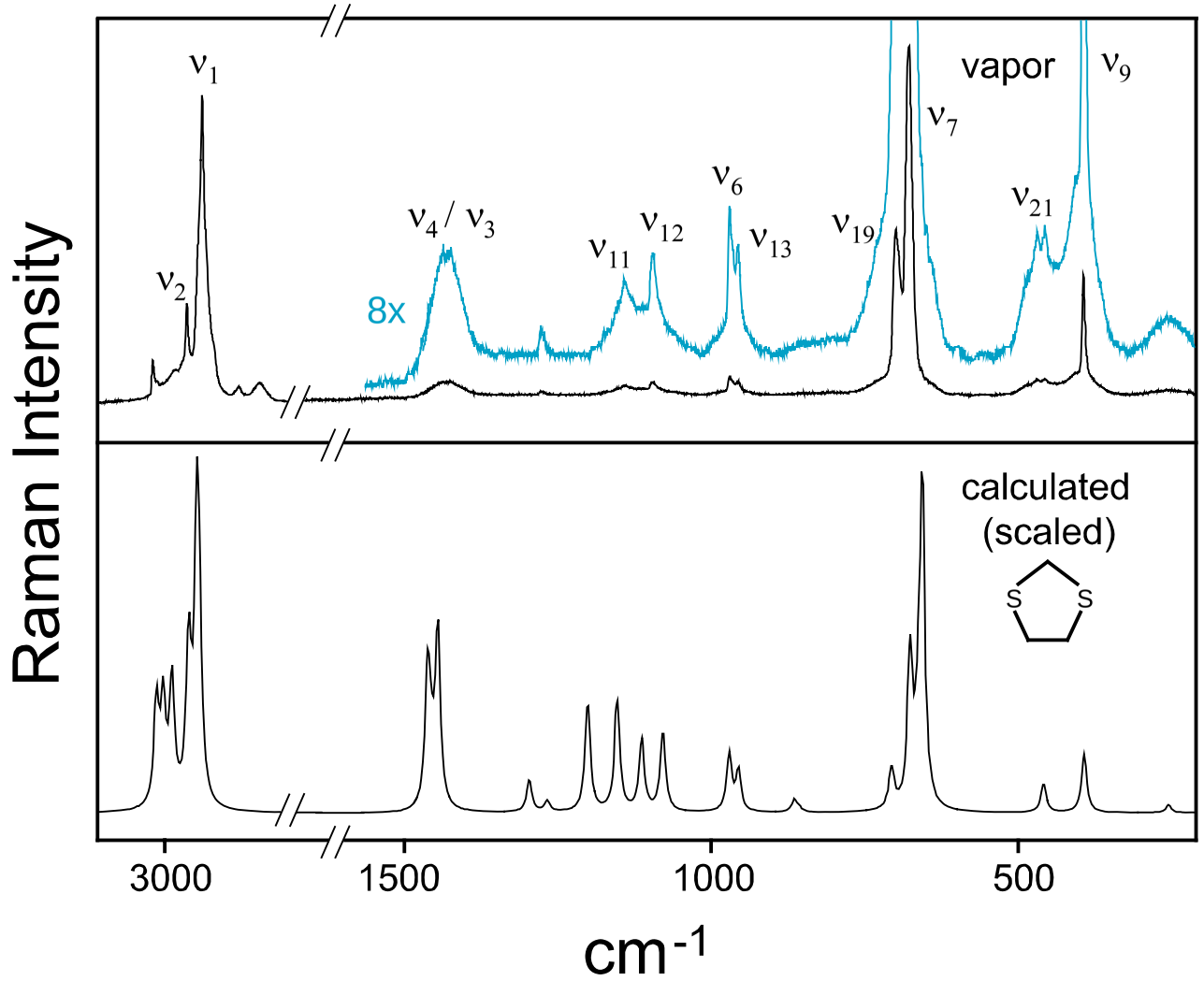

Figure 65. The vapor-phase Raman spectrum of 1,3-dithiolane (top) compared to the calculated DFT spectrum with scaled frequencies (bottom).

TABLE 41: The Experimental and Calculated Frequencies (cm^{-1}) and Vibrational Assignments of 1,3-Dithiolane.

Sym. C_{2v} (C_s, C_2)	ν			Description	Infrared	Raman		B3LYP/6-311++G(d,p)			
	C_{2v}	C_s	C_2		Liquid	Liquid	Vapor	C_{2v}[a]	C_s[a]	C_2[a]	C_1[a,b]
A_1	1	3	3	CH_2-CH_2 sym. stretch (ip)	2919 vs	2919 P	2939 vs	2960	2960	2947	2948 (100, 100)
(A', A)	2	4	2	CH_2 sym. stretch	-----	2933 P	2964 s	2958	2950	2961	2961 (67, 53)
	3	5	5	CH_2-CH_2 deformation (ip)	1425 m	-----	1425 m	1490	1479	1455	1456 (2.3, 1.1)
	4	6	4	CH_2 deformation	1438 w	1436 D	1438 m	1466	1436	1463	1462 (1.3, 4.8)
	5	7	6	CH_2-CH_2 wag (op)	1275 s	1275 P	-----	1246	1234	1296	1297 (43, 1.1)
	6	9	9	C-C stretch	971 m	971 P	970 m	994	953	970	971 (4.7, 1.9)
	7	12	11	S-C sym. stretch	-----	697 P	678 vs	683	686	680	676 (5.3, 5.2)
	8	13	12	S-C sym. stretch	681 s br	676 P	657 w	634	640	659	657 (5.7, 11)
	9	14	13	ring deformation	-----	395 P	394 s	406	392	393	393 (0.1, 1.9)
A_2	10	16	1	CH_2-CH_2 antisym. stretch (op)	-----	2955 P	2983 m	2984	2988	2988	2988 (2.0, 44)
(A", A)	11	20	7	CH_2-CH_2 twist (ip)	1144 m	1144 D	1142 m	1215	1216	1154	1154 (3.3, 3.8)
	12	22	8	CH_2 twist	1070 w	1071 D	1095 m	1085	1096	1082	1079 (3.0, 2.7)
	13	23	10	CH_2-CH_2 rock (op)	957 w	957 P	956 m	943	942	953	956 (3.0, 1.3)
	14	27	14	ring twist	-----	261 D	255 m	*i*	*i*	260	255 (2.0, 0.3)
B_1	15	17	17	CH_2-CH_2 sym. stretch (op)	-----	-----	2945 m	2949	2948	2943	2943 (40, 32)
(A", B)	16	18	18	CH_2-CH_2 deformation (op)	1419 s	1419 D	-----	1463	1455	1446	1446 (25, 6.1)
	17	19	19	CH_2-CH_2 wag (ip)	1247 m	1247 D	1275 w	1286	1279	1267	1267 (20, 0.3)
	18	21	20	CH_2 wag	1182 m	1182 D	-----	1210	1193	1200	1201 (11, 3.7)
	19	24	24	S-C antisym. stretch	731 s	732 D	700 s	763	751	704	707 (11, 1.4)

TABLE 41: Continued.

Sym. C_{2v} (C_s, C_2)	ν			Description	Infrared	Raman		B3LYP/6-311++G(d,p)				
	C_{2v}	C_s	C_2		Liquid	Liquid	Vapor	C_{2v}[a]	C_s[a]	C_2[a]	C_1[a,b]	
B_1	20	25	25	S-C antisym. stretch	665 vw	-----	-----	721	688	666	664	(10, 1.5)
(A", B)	21	26	26	ring deformation	464 w	465 D	463 m	484	472	460	459	(2.3, 1.0)
B_2	22	2	16	CH_2-CH_2 antisym. stretch (ip)	2966 s	2967 D	3004 w	3009	3011	3002	3003	(47, 35)
(A', B)	23	1	15	CH_2 antisym. stretch	-----	-----	3019 s	3006	3018	3013	3014	(3.0, 36)
	24	8	21	CH_2-CH_2 twist (op)	1112 m	1111 D	1112 w	1127	1130	1107	1113	(14, 2.4)
	25	10	22	CH_2 rock	860 s	859 D	-----	875	863	868	865	(19, 0.4)
	26	11	23	CH_2-CH_2 rock (ip)	844 s	844 D	857 w	780	767	860	858	(20, 0.1)
	27	15	27	ring bend	-----	-----	-----	*i*	195	*i*	29.4	(30, 0.04)

Abbreviations: ip, in-phase; op, out-of-phase; s, strong; m, medium; w, weak; v, very; br, broad; P, polarized; D, depolarized.

[a] Frequencies scaled with a scaling factor of 0.985 for frequencies less than 1600 cm^{-1} and 0.964 for frequencies greater than 2900 cm^{-1}.

[b] Relative intensities shown as (IR, Raman).

CHAPTER XIII

CONCLUSIONS

The vibrational potential energy surfaces (PESs) for the electronic ground and excited states of several ring molecules were investigated using several different spectroscopic methods, including far-infrared (IR), Raman, ultraviolet (UV) absorption, fluorescence excitation (FES), and single vibronic level fluorescence (SVLF) spectroscopies.

Based on new information obtained from SVLF and millimeter wave spectra, the far-IR spectra of coumaran were reassigned and the one-dimensional ring-puckering potential energy function for the S_0 ground state was determined to be

$$V(\mathrm{cm}^{-1}) = (8.91\times10^{5})x^{4} - (2.34\times10^{4})x^{2}, \qquad (13.1)$$

where x is the ring-puckering coordinate in Å. The barrier was found to be 154 cm^{-1} and the puckering angles to be ± 25°, in good agreement with the millimeter wave barrier of 152 cm^{-1} and puckering angles of ± 23°. The one-dimensional ring-puckering potential energy functions in the flapping and twisting vibrational excited states in the S_0 ground state were also determined.

The UV absorption, FES, and SVLF spectra of coumaran associated with its $S_1(\pi,\pi^*)$ electronic excited state have also been recorded and analyzed. The assignment of more

than seventy transitions allowed a detailed energy map of both the S_0 and S_1 states of the ring-puckering vibration to be determined in the excited states of nine other vibrations, including the ring-flapping and ring-twisting vibrations. The one-dimensional potential energy function for the ring-puckering

$$V(cm^{-1}) = (1.55 \times 10^6)x^4 - (1.46 \times 10^4)x^2 \qquad (13.2)$$

very nicely predicts the experimentally-determined energy level spacings. The puckering barrier is 34 cm^{-1} for the excited state and the puckering angles are ± 14°. As is the case for the related molecules in indan family, the angle strain in the five-membered ring increases upon the $\pi \rightarrow \pi^*$ excitation within the benzene ring and this increases the rigidity of the attached five-membered ring. Theoretical calculations predicted the expected increases of the carbon-carbon bond lengths of the benzene ring in the S_1 state, and predicted a barrier of 21 cm^{-1} for the excited state.

Several calculations with different basis sets have been carried out to better understand the unusual vibrational frequencies of cyclopropenone. It was shown that the bands at 1840, 1483, and 1026 cm^{-1} are predominantly the C=O, C=C, and symmetric C-C stretches and that there is strong interaction between the C=O and symmetric C-C stretching vibrations. The unexpectedly high and low frequencies arise from the unusual vibrational interactions. Similar results were also obtained for cyclopropenone-d_2. These results differ quantitatively from a previous normal coordinate calculation and

interpretation, which proposed that a very strong C=O bond and a very weak C=C bond were present.

The vapor-phase Raman spectrum of 3,7-dioxabicyclo[3.3.0]oct-1,5-ene was analyzed and compared to the predicted spectrum from density functional theory (DFT) calculations. This Raman spectrum confirmed the structure of the molecule and shows the skeleton of both rings to be planar with D_{2h} symmetry. Theoretical calculations were carried out to predict the bond distances and angles of the molecule, and these also showed the molecule to be planar.

The infrared and Raman spectra of vapor-phase and liquid-phase 1,4-benzodioxan and 1,2,3,4-tetrahydronaphthalene (tetralin) were collected and the complete vibrational assignments for both molecules were made. Theoretical calculations predicted the barriers to planarity to be 4095 cm^{-1} for 1,4-benzodioxan and 4809 cm^{-1} for tetralin. The twisting angles were calculated to be 30.1° for 1,4-benzodioxan and 31.4° for tetralin. DFT calculations for both planar (C_{2v}) and twisted (C_2) structures were carried out to predict the vibrational frequencies. After scaling, the agreement with the experimental values was excellent for C_2 symmetry.

The UV absorption, FES, and SVLF spectra of both 1,4-benzodioxan and tetralin were recorded and assigned. The energy level diagrams for the four lowest-frequency ring vibrations in S_0 ground and $S_1(\pi,\pi^*)$ excited states were made. The nearly harmonic

energy level spacings indicated very high energy barriers for molecules. Both a one-dimensional potential energy function in terms of the ring-twisting vibration and a two-dimensional PES in terms of the ring-twisting and ring-bending modes were carried out for the S_0 and $S_1(\pi,\pi^*)$ states of 14BZD, and these were also consistent with the high barriers calculated for both states. The low-frequency spectra of tetralin in both S_0 and S_1 states were also analyzed.

A complete vibrational assignment of 1,3-dithiolane was made based on the vapor and liquid-phase infrared and Raman spectra. Theoretical calculations at Hartree-Fock (HF), Moller-Plesset second-order perturbation (MP2), and density functional theory (DFT) with several basis sets were carried out. Energies, structural parameters, and vibrational frequencies for the planar (C_{2v}), bent (C_s), twist (C_2), and non-symmetric (C_1) structures were also obtained. Theoretical calculations predicted the C_1 structure to be the energy minima for 1,3-dithiolane, and this was consistent with the results from a recent microwave study for the pseudorotational vibration of this molecule.

REFERENCES

1. J. Laane, Quart. Rev. **25**, 533 (1971).
2. E. Bondoc, T. Klots, and J. Laane, J. Phys. Chem. A **104**, 275 (2000).
3. Z. Arp, M. Wagner, and J. Laane, unpublished results.
4. P. Ottoviani and W. Caminati, Chem. Phys. Lett. **405**, 68 (2005).
5. F. R. Brown, D. H. Finseth, F. A. Miller, and K. H. Rhee, J. Am. Chem. Soc. **97**, 1011 (1975).
6. E. C. Tuazon, D. H. Finseth, and F. A. Miller, Spectrochim. Acta **31A**, 1133 (1975).
7. D. Autrey, K. Haller, J. Laane, C. Mlynek, and H. Hopf, J. Phys. Chem. A **108**, 403 (2004).
8. D. Autrey, N. Meinander, and J. Laane, J. Phys. Chem. A **108**, 409 (2004).
9. V. E. Rivera-Gaines, S. J. Leibowitz, and J. Laane, J. Am. Chem. Soc. **113**, 9735 (1991).
10. M. M. J. Tecklenburg and J. Laane, J. Am. Chem. Soc. **111**, 6920 (1989).
11. L. E. Bauman and J. Laane, J. Phys. Chem. **92**, 1040 (1988).
12. J. A. Greenhouse and H. L. Strauss, J. Chem. Phys. **50**, 124 (1969).
13. E. Cortez, Ph.D. Dissertation, Texas A&M Unversity, 1994.
14. S. J. Leibowitz, J. Laane, R. Verastegui, and J. R. Villarreal, J. Chem. Phys. **96**, 7298

(1992).

15. S. J. Leibowitz and J. Laane, J. Chem. Phys. **101**, 2740 (1994).
16. L. A. Carreira, R. C. Lord, and T. B. Maloy, Jr., *Topics in Current Chemistry*, (Springer-Verlag, Berlin), 1979, Page 68.
17. J. C. Lopez, S. Blanco, A. Lesarri, J. L. Alonso, J. Laane, and J. R. Villareal, Abstract of the Sixteenth Colloquium on High Resolution Molecular Spectroscopy, Dijon, France, 1999, Page 315.
18. N. Meinander and J. Laane, J. Mol. Struct. **569**, 1 (2001).
19. M. A. Harthcock and J. Laane, J. Mol. Spectrosc. **91**, 300 (1982).
20. J. Laane, M. A. Harthcock, P. M. Killough, L. E. Bauman, and J. M. Cooke, J. Mol. Spectrosc. **91**, 286 (1982).
21. M. M. J. Tecklenburg and J. Laane, J. Mol. Spectrosc. **137**, 65 (1989).
22. R. P. Bell, Proc. R. Soc. London, **A183**, 328 (1945).
23. U. Toyotoshi and S. Takehiko, J. Chem. Phys. **49**, 470 (1968).
24. K. Haller, W.-Y. Chiang, A. del Rasario, and J. Laane, J. Mol. Struct. **379**, 19 (1996).
25. J. Laane, K. Haller, S. Sakurai, K. Morris, D. Autrey, Z. Arp, W.-Y. Chiang, and A. Combs, J. Mol. Struct. **650**, 57 (2002).
26. C. M. Cheatham, M.-H. Huang, and J. Laane, J. Mol. Struct. **377**, 81 (1996).
27. C. M. Cheatham, M.-H. Huang, N. Meinander, M. B. Kelly, K. Haller, W.-Y. Chiang,

and J. Laane, J. Mol. Struct. **377**, 93 (1996).

28. K. Morris, Ph.D. Dissertation, Texas A&M University, 1998.
29. Z. Arp, Ph.D. Dissertation, Texas A&M University, 2001.
30. Z. Arp, N. Meinander, J. Choo, and J. Laane, J. Chem. Phys. **116**, 6648 (2002).
31. J. Laane, J. Phys. Chem. A **104**, 7715 (2000).
32. S. Sakurai, N. Meinander, K. Morris, and J. Laane, J. Am. Chem. Soc. **121**, 5056 (1999).
33. T. Klots, S. Sakurai, and J. Laane, J. Phys. Chem. **108**, 3531 (1998).
34. S. Sakurai, N. Meinander, and J. Laane, J. Chem. Phys. **108**, 3537 (1998)
35. E. Bondoc, S. Sakurai, K. Morris, W.-Y. Chiang, and J. Laane, J. Chem. Phys. **103**, 8772 (1999)
36. J. Laane, E. Bondoc, S. Sakurai, K. Morris, N. Meinander, and J. Choo, J. Am. Chem. Soc, **122**, 2628 (2000).
37. D. Autrey, and J. Laane, J. Phys, Chem. A **105**, 6894 (2001).
38. M. J. Watkins, D. E. Belcher, and M. C. R. Cockett, J. Chem. Phys. **116**, 7855 (2002).
39. R. Ahlrichs, M. Bär, M. Häser, H. Horn, and C. Kölmel, Chem. Phys. Lett. **162**, 165 (1989).
40. F. Furche and R. Ahlrichs, J. Chem. Phys. **117**, 7433 (2002).

41. M. J. Frisch, G. W. Trucks, H. B. Schlegel, G. E. Scuseria, M. A. Robb, J. R. Cheeseman, J. A. Montgomery, Jr., T. Vreven, K. N. Kudin, J. C. Burant, J. M. Millam, S. S. Iyengar, J. Tomasi, V. Barone, B. Mennucci, M. Cossi, G. Scalmani, N. Rega, G. A. Petersson, H. Nakatsuji, M. Hada, M. Ehara, K. Toyota, R. Fukuda, J. Hasegawa, M. Ishida, T. Nakajima, Y. Honda, O. Kitao, H. Nakai, M. Klene, X. Li, J. E. Knox, H. P. Hratchian, J. B. Cross, V. Bakken, C. Adamo, J. Jaramillo, R. Gomperts, R. E. Stratmann, O. Yazyev, A. J. Austin, R. Cammi, C. Pomelli, J. W. Ochterski, P. Y. Ayala, K. Morokuma, G. A. Voth, P. Salvador, J. J. Dannenberg, V. G. Zakrzewski, S. Dapprich, A. D. Daniels, M. C. Strain, O. Farkas, D. K. Malick, A. D. Rabuck, K. Raghavachari, J. B. Foresman, J. V. Ortiz, Q. Cui, A. G. Baboul, S. Clifford, J. Cioslowski, B. B. Stefanov, G. Liu, A. Liashenko, P. Piskorz, I. Komaromi, R. L. Martin, D. J. Fox, T. Keith, M. A. Al-Laham, C. Y. Peng, A. Nanayakkara, M. Challacombe, P. M. W. Gill, B. Johnson, W. Chen, M. W. Wong, C. Gonzalez, and J. A. Pople, *GAUSSIAN 03*, Revision C.02, Gaussian, Inc., Wallingford, CT, 2004.

42. J. Laane, J. Phys. Chem. **95**, 9246 (1991).

43. L. E. Bauman, P. M. Killough, J. M. Cooke, J. Villareal, and J. Laane, J. Phys. Chem. **86**, 2000 (1982).

44. D. Autrey, Z. Arp, J. Choo, and J. Laane, J. Chem. Phys. **119**, 2557 (2003)

45. D. Autrey, J. Choo, and J. Laane, J. Phys. Chem. **105A**, 10230 (2001).

46. R. Breslow and G. Ryan, J. Am. Chem. Soc. **89**, 3073 (1967).

47. R. Breslow and M. Oda, J. Am. Chem. Soc. **94**, 4787 (1972).

48. R. C. Benson, W. H. Flygare, M. Oda, and R. Breslow, J. Am. Chem. Soc. **95**, 2772, (1975).

49. F. R. Brown, D. H. Finseth, K. H. Rhee, and F. A. Miller, 28th Symposium Molecular Structure and Spectroscopy, Ohio State University, Paper D2, June, 1973.

50. J. Laane, unpublished results.

51. M. J. Frisch, G. W. Trucks, H. B. Schlegel, G. E. Scuseria, M. A. Robb, J. R. Cheeseman, W. G. Zakrzewski, J. A. Montgomery, Jr., R. E. Stratmann, J. C. Burant, S. Dapprich, J. M. Millam, A. D. Daniels, K. N. Kudin, M. C. Strain, O. Farkas, J. Tomasi, V. Barone, M. Cossi, R. Cammi, B. Mennucci, C. Pomelli, C. Adamo, S. Clifford, J. Ochterski, G. A. Peterson, P. Y. Ayala, Q. Cui, K. Morokuma, D. K. Malick, A. D. Rabuck, K. Raghavachari, J. B. Foresman, J. Cioslowski, J. V. Ortiz, B. B. Stefanov, G. Liu, A. Liashenko, P. Piskorz, I. Komaromi, R. Gomerts, R. L. Martin, D. J. Fox, T. Keith, M. A. Al-Laham, C. Y. Peng, A. Nanayakkara, C. Gonzalez, M. Challacombe, P. M. W. Gill, B. Johnson, W. Chen, M. W. Wong, J. L. Andres C. Gonzalez, M. Head-Gordon, E. S. Replogie, J. A. Pople, *GAUSSIAN 98*, Revision A.3, Gaussian, Inc., Pittsburgh, PA, 1998.

52. C. Mlynek, H. Hopf, J. Yang, and J. Laane, J. Mol. Struct. **742**, 161 (2005)

53. J. Laane, Int. Rev. Phys. Chem. **18**, 301 (1999).

54. J. Laane, Annu. Rev. Phys. Chem. **45**, 179 (1994).

55. J. Laane, M. Dakkouri, B. van der Veken, and H. Oberhammer(Eds.), *Structures and Conformations of Non-rigid Molecules*, (Kluwer, Amsterdam), 1993, Chapter 4.

56. D. Autrey, Ph.D. Dissertation, Texas A&M University, 2003.

57. J. Choo, S. J. Han, and Y. S. Choi, Bull. Korean Chem. Soc. **18**, 1076 (1997).

58. R. D. Gordon and J. M. Hollas, J. Mol. Struct. **293**, 193 (1993).

59. R. D. Gordon and J. M. Hollas, J. Mol. Spectrosc. **163**, 159 (1994).

60. R. W. Schmude, M. A. Harthcock, M. B. Kelly, and J. Laane, J. Mol. Spectrosc. **124**, 369 (1987).

61. M. M. Strube and J. Laane, J. Mol. Spectrosc. **129**, 126 (1988).

62. J. Laane, Appl. Spectrosc. **24**, 73 (1970)

63. J. Laane and J. Choo, J. Am. Chem. Soc. **116**, 3889 (1994).

64. N. Guchhait, T. Chakraborty, D. Majumdar, and M. Chowdhury, J. Phys, Chem. **98**, 9227 (1994).

65. D. G. Melnik, T. A. Miller, and F. C. De Lucia, J. Mol. Spectrosc. **221**, 227 (2003).

VITA

Juan Yang graduated from Beijing University, China and received her Bachelor of Science degree in chemistry in July 2001. She began her graduate studies in the Department of Chemistry at Texas A&M University in August 2001. Later that year she joined the research group of Professor Jaan Laane, and her principal research project was the investigation of the vibrational potential energy surfaces in electronic ground and excited states using molecular spectroscopy. She received her Doctor of Philosophy degree in chemistry in May 2006.

Juan Yang's permanent address is HuKeng Tungsten Mine Hospital Building 2-52, Anfu County, Jiang Xi Province 343205, China. She may also be reached at the Department of Chemistry, Texas A&M University, College Station, TX 77840. Her email address is yjtamu@yahoo.com.cn.